Development of two in vitro organotypic models for the oral tumour ameloblastoma

Tuula M I Eriksson

Biomaterials and Tissue Engineering

UCL Eastman Dental Institute

University College London

Thesis submitted for the degree Doctor of Philosophy

May 2016

Declaration

I, Tuula M I Eriksson, confirm that the work presented in this thesis is my own. Where information has been obtained from other sources, I confirm that this has been indicated in the thesis.

Tuula Eriksson

Supervisors

Dr Stefano Fedele, Oral Medicine Unit, Eastman Dental Institute

Dr Richard M Day, Applied Biomedical Engineering Group, Division of Medicine

University College London

and

Dr Vehid Salih, Plymouth University Peninsula School of Medicine and Dentistry, Plymouth

Acknowledgements

This has been an interdisciplinary project and has, as such, come with numerous people without whom this work would have been impossible. I would like to express my gratitude towards the following people: the funders of my UCL Impact scholarship, Adele and Roger of the Biss-Davies charitable trust and Sarah Medd-Phillips at the UCL Development Office for managing it all. It has been a joy to work on a project where the funders have been so excited about it and involved throughout.

My supervisors, Drs Richard Day, Stefano Fedele and Vehid Salih for their respective areas of expertise, help and support with this project.

Prof. Hidemitsu Harada and his research group at Iwate University for allowing use of the AM-1 cell line during this project. BTE staff members, in particular Dr Nicky Mordan for her unfailing helpfulness. A lot of the experiments in this thesis would not have happened without her. Prof Jonathan Knowles and Drs Isabel Kingston, George Georgiou and Graham Palmer for all their technical help and support.

Thank you also to Prof Stephen Porter and Dr Shahid Chaudhry for their ideas for model development, Dr Aviva Petrie for running an excellent statistics course and Dr Celia Murray-Dunning for her encouragement.

Thank you to all of the staff, and in particular Christopher Evagora and Pauline Levey, at the Blizard Core Pathology facility (QMUL) for their expertise with histology.

I would also specifically like to thank Dr James Phillips for the talks, ideas and troubleshooting both in the lab and the pub. The benefit of an interdisciplinary project is that you end up with many friends from many different labs: the students both in Biomaterials and Tissue Engineering and in Applied Biomedical Engineering have all been a joy to work with and a fantastic group of people.

My sincere thanks are directed to the following people, who have in their various ways made my life these past 3,5 years more fun: Dr Adam “Columbo” Day for lab giving me someone to laugh with in the lab, and useful advice on experiments, cells and theses. Dominique Thomas, without whom I probably wouldn’t have made it through the early days. Dr Nasser Alqhtani for always being helpful, having all the random reagents I urgently required and keeping the office supplied with tea, coffee and chocolates. Dr Caitriona O’Rourke for her never-ending questions and help with a variety of things.

Friends and family for getting me out of the lab. I should probably have listened to Dr Neil Sinclair’s advice more.

Most importantly, I would like to express my gratitude to my parents and sisters for their attempts to understand what it is I do, their unfailing support and love. Henry - I wouldn’t even have started this project without you, and I certainly wouldn’t have made it this far.

Abstract

Ameloblastoma is the most common odontogenic tumour worldwide. It is a locally invasive yet benign tumour, with bone destructive capacity. Up to 70% of cases are estimated to recur and some of these form tumours in the soft tissues surrounding the original tumour sites.

There are many unanswered questions around the cellular events leading up to the growth of an ameloblastoma tumour, how ameloblastoma cells invade the bone tissue surrounding it, how the disease progresses and if there are any suitable biomarkers to potentially be used for disease diagnosis and/or prevention.

This study used tissue engineering techniques to create two distinct models for ameloblastoma tumours. The first involved the development of bone-like compressed collagen constructs, which were co-cultured with ameloblastoma cells from the AM-1 cell line. These constructs were examined for cell proliferation, invasion, cell-to-cell contacts and gene expression. The second construct involved modelling AM-1 cell behaviour together with an organotypic soft tissue model, so that recurrent ameloblastoma behaviour could be investigated. For this, co-cultures of gingival fibroblasts in compressed collagen scaffolds were developed. Using this construct, it was found that AM-1 cells upregulated matrix metalloproteinase (MMP-2) expression.

It was found that AM-1 cells rapidly proliferated in both constructs, and cell-to-cell interactions and some invasion were also observed.

Finally, based on gene expression data obtained for the two constructs, potential therapeutic agents were tested. Application of either Alendronate or Doxycycline was found to reduce AM-1 cell survival within the models.

The models developed during this project are the first to provide an organotypic *in vitro* setting for the examination of ameloblastoma cells. They effectively mimic the *in vivo* tissue by providing appropriate extracellular matrix factors and cell types. The behaviour of AM-1 cells in these models was close to that observed in *in vivo* tumours.

Contents

List of Figures

List of Tables

List of abbreviations

2D	Two-dimensional
3D	Three-dimensional
ADAM-12	A disintegrin and metalloproteinase (ADAM) domain 12
AF	Alexa Fluor secondary antibodies used for immunocytochemical staining
ALN	Alendronate
ALP	Alkaline phosphatase
AM	Ameloblastoma
AM-1	Cells from the first ameloblastoma cell line
AM-2	Cells from the second ameloblastoma cell line
AM-3	Cells from the third ameloblastoma cell line
AMBN	Ameloblastin, enamel encoding gene and ameloblastoma marker
AME-1	Cells from the Brazilian ameloblastoma cell line
AMEL	Amelogenin
AR	Alizarin red stain for mineralisation
ARAF	A-isoform of the RAF molecule in the mitogen-activated protein kinase pathway
ATP	Adenosine triphosphate
BCL-2	B-cell lymphoma-2, apoptosis preventer
BM	Basement membrane
BMP-2	Bone morphogenic protein-2
BRAF	B-isoform of the RAF molecule in the mitogen-activated protein kinase pathway
BRAF V600E	Mutation in B-RAF at amino acid 600
BSA	Bovine serum albumin
CAF	Cancer activated fibroblast
CAM DR	Cell adhesion mediated drug resistance
CCND1	Gene encoding for β-catenin
CDK(4)	Cyclin-dependent kinase (4)
cDNA	Complimentary deoxyribonucleic acid
CK (-14/-19)	Cytokeratin (-14/-19), epithelial cell markers
CLSM	Confocal light scanning microscope
cm	Centimetre
CO_2	Carbon dioxide
CRAF	C-isoform of the RAF molecule in the mitogen-activated protein kinase pathway
C_t	Threshold cycle
CT	Cell Tracker assay
CTG	Cell Tracker green
CTR	Cell Tracker red
DA	Desmoplastic ameloblastoma
DAPI	4',6-diamidino-2-phenylindole, fluorescent DNA stain
dH_20	Distilled water
DM IRB	Inverted computer-controlled conventional wide-angle (non-confocal) microscope
DMA	Dynamic mechanical analysis
DMEM	Dulbecco's Modified Eagle Medium
DMSO	Dimethyl sulfoxide
DNA	Deoxyribonucleic acid
Dox	Doxycycline
DPX	Distyrene, plasticiser and xylene mountant for histology
ECM	Extracellular matrix
EGF	Epidermal growth factor

EGFR	Epidermal growth factor receptor
EHS	Engelbreth-Holm-Swarm cells
EMT	Endothelial-mesenchymal transition
ELISA	Enzyme-linked immunosorbent assay
ERK	Mitogen-activated protein kinase
FAM	Fluorescein dye, used as detector in quantitative real time polymerase chain reaction
FAP	Fibroblast activation protein
FBS	Fetal bovine serum
FGFR2	Fibroblast growth factor receptor 2
FPP	Farnesyl pyrophosphatase
FRZ	Frizzled
FSP	Fibroblast surface protein
G	Gauge, size of needles
g	Gram
GAPDH	Glyceraldehyde-3- Phosphate Dehydrogenase
gDNA	Genomic deoxyribonucleic acid
GF	Gingival fibroblast(s)
GF + AM-1	Co-culture of GF soft tissue model and ameloblastoma model
GFR	Growth factor reduced, type of Matrigel basement membrane
Gli	Glioblastoma
GPa	GigaPascal
GTP	Guanosine-5'-triphosphate
h	Hour
HA	Hydroxyapatite
H&E	Haematoxylin and eosin histological stain
HOB	Human primary osteoblast cell(s)
HOB + AM-1	Co-culture of HOB bone-like model and ameloblastoma model
HOS	Human osteosarcoma cell(s)
HOS + AM-1	Co-culture of HOS bone-like model and ameloblastoma model
HPV	Human papilloma virus
hTERT	Human telomerase reverse transcriptase
Hz	Hertz, unit of frequency
ICC	Immunocytochemistry
IGF	Insulin-like growth factor
IF	Interface of the co-culture models
IL	Interleukin family molecules
IMS	Industrial methylated spirit
KCl	Potassium chloride
kDa	KiloDalton
kPa	KiloPascal
KSFM	Keratinocyte serum-free medium
L	Litre
M	Molar
MAPK	Mitogen-activated protein kinase
MEM	Modified Eagle's medium
mg	Milligram
Min	Minute

ml	Millilitre
mm	Millimetre
MMP	Matrix metalloproteinase
MMP-2	Matrix metalloproteinase-2, collagenase
MMP-9	Matrix metalloproteinase-9, collagenase
MPa	MegaPascal
mRNA	Messenger ribonucleic acid
μg	Microgram
μl	Microlitre
μm	Micrometre
μM	Micromolar
N	Newton, unit of force
NaCl	Sodium chloride
NaOH	Sodium hydroxide
NFκB	Nuclear factor kappa B, factor in osteoclast activation pathway
nm	Nanometre
nM	Nanomolar
ODAM	Odontogenic, ameloblast-associated protein
OM	Osteogenic medium
OPG	Osteoprotegrin, bone marker, also known as TNFRSF11B
OPN	Osteopontin, bone marker
OSCC	Oral squamous-cell carcinoma
p53	Phosphoprotein 53, tumour suppressor
PA	Peripheral ameloblastoma
PBS	Phosphate buffered saline, magnesium and calcium free
PBST	Phosphate buffered saline with added Triton X-100
PDGF	Platelet-derived growth factor
PGA	Polyglycolic acid
PI3K	Phosphoinositol-3 kinase
PLA	Polylactic acid
PLGA	Poly(lactic-co-glycolic) acid
PLGA-PCL	Poly(lactic-co-glycolic) acid poly-caprolactone blend
pNPP	para-Nitrophenylphosphate, chromogenic substrate for alkaline phosphatase
PTCH-1	Patched-1, cell developmental gene, part of sonic hedgehog pathway
qRT-PCR	Quantitative real time polymerase chain reaction
RAF	Rapid Accelerated Fibrosarcoma molecule, serine-threonine kinase
RANKL	Receptor activator of nuclear factor kappa B ligand, also known as TNFSF11
RAS	Oncogene, member of the GTPase superfamily
RECK	Reversion-inducing cystein-rich protein with Kazal motifs
RGD	Arginine-Glycine-Aspartic acid motif for cell adhesion
RNA	Ribonucleic acid
ROX	Passive reference dye used in quantitative real time polymerase chain reaction
rpm	Revolutions per minute
RT	Room temperature

Sec	Second
SEM	Scanning electron microscope / microscopy
sFRP	Secreted Frizzle-related protein
SHH	Sonic hedgehog
SMA	Solid/multicystic ameloblastoma
SMO	Smoothened, part of the SHH pathway
TAF	Tumour activated fibroblast
TCP	Tissue culture plastic
TEM	Transmission electron microscope / microscopy
TGFβ1	Tumour growth factor family member β1
TIMP	Tissue inhibitor of matrix metalloproteinases
TNF(α)	Tumour necrosis factor (-α)
TNFRSF	Tumour necrosis factor receptor superfamily
TRAF-6	Tumour necrosis factor receptor-associated factor 6, mediator in NFκB activation
TRAIL	TNF-related apoptosis-inducing ligand, also known as TNFRSF1
UA	Unicystic ameloblastoma
ULA	Ultra low-attachment
UV	Ultraviolet light
v/v	Volume by volume
VK	Von Kossa histological stain
w/v	Weight by volume
w/w	Weight by weight
WHO	World Health Organisation
Wnt	Wingless-related integration site protein
x *g*	Times gravity, used in centrifuging

Chapter 1

Introduction and literature review

The first part of this chapter provides an introduction to the ameloblastoma family of tumours, current knowledge about these tumours and their causes. The second part then details the native tissue environments, extracellular matrix compositions of bone and the soft tissues, and how tissue-engineered models may aid in understanding oral diseases in complex, organotypic settings. Finally, current tissue engineering techniques and methods are reviewed with the aim of using these to develop the models as the focus of this thesis.

This thesis describes the development of bone-like and soft tissue scaffolds using human fibroblasts, bone cells and compressed collagen scaffolds. The organotypic models made during this project will provide information on tumour growth, but also on the interactions ameloblastoma cells have with bone cells, fibroblasts and their surroundings. In addition, these scaffolds will lend themselves to testing of therapeutic agents, as standardising scaffold synthesis will allow for a reproducible model for inhibition of cell growth and any relevant pathways within the cells.

1.1 Ameloblastoma

Ameloblastoma is a rare, odontogenic tumour, which occurs either in the maxilla or mandible. While it is the most common of all odontogenic tumours (Philipsen and Reichart, 2004), its rarity did for a long time mean that there was a lack of samples in tissue banks appropriate for genomic studies (Jamshidi et al., 2015). However, recent advances in DNA extraction and genome sequencing from histological specimens has led to some major developments in ameloblastoma research. The molecular pathogenesis of these tumours was only characterised in 2014, in a series of high-throughput genetic studies (Brown et al., 2014; Kurppa et al., 2014; Sweeney et al., 2014).

The limited knowledge is partly due to the rarity of the tumour, but also due to the complex physiological behaviour it exhibits (Heikinheimo et al., 2015).

1.1.1 Ameloblastoma incidence

Ameloblastoma incidence was recently estimated to be 0.5 cases per one million person years (McClary et al., 2014). Even though it is rare, ameloblastoma is the most common clinically significant odontogenic tumour (Bachmann and Linfesty, 2009), with 11.7% of all odontogenic tumours worldwide being classed as ameloblastoma (Philipsen and Reichart, 2004). When odontomas, which are often considered to be either developmental abnormalities or benign tumours, are discounted from this figure, different types of ameloblastoma form 48.5% of odontogenic tumours (Buchner et al., 2006).

However, this high figure may be biased by several factors including the lack of symptoms, by ameloblastomas being treated as large aggressive tumours at cancer hospitals instead of being recognised within dental clinical settings, and by cases not being recorded or sent for examination (Avelar et al., 2011).

1.1.2 Tumour locations

Benign but invasive odontogenic tumours are rare and much remains unknown about their formation, aetiology and cellular events. Up to 80% of ameloblastoma tumours occur in the mandible (Gardner et al., 2005; Reichart et al., 1995). The high proliferation rate in the posterior region of both mandible and maxilla (molar-ramus area) is thought to account for the high occurrence rate in this region (Reichart et al., 1995).

Specifying successful methods for therapy is therefore difficult, and the prognosis for some ameloblastoma subtypes is poor, in part because of the lack of therapies other than surgery, but also due to the complex anatomy of the head and neck region (Gardner et al., 2005).

1.1.3 Tumour formation and appearance

Radiographs and computerised tomography scans of suspected ameloblastomas often show an expansive, radiolucent, uni- or multilocular cystic lesion, with a characteristic soap bubble-like appearance (Bachmann and Linfesty, 2009). The lack of bone matrix calcification is also visible, and sometimes even tooth root erosion can be visualised using radiographs (Bachmann and Linfesty, 2009). A computerised tomography scan of an ameloblastoma tumour invading the jaw bone and the surrounding tissues is seen in fig. 1.1, where the tumour (grey mass within the jaw bone) has degraded most of the jaw bone (in white) and deformed the facial structure. The tumour has also invaded one of the orbits (yellow arrow) and some of the sino-nasal passages.

1.1.4 Ameloblastoma growth and symptoms

Ameloblastomas originate from the odontogenic epithelium, from unerupted third molars, or the tooth bud (Harada et al., 1998; Mendenhall et al., 2007; Kibe et al., 2013). Despite being histologically benign, ameloblastomas exhibit locally invasive properties, and can reach a large size before the patient reports any symptoms (Reichart et al., 1995; Gardner et al., 2005). The average size of the tumour upon removal is 4.3cm, with tumours larger in females (5.2cm) than males (3.6cm) (Reichart et al., 1995). The average age of

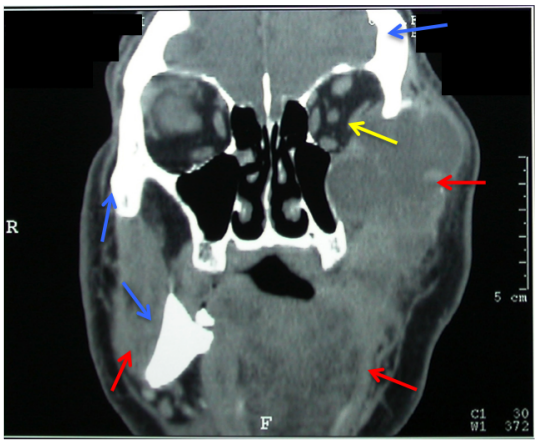

Figure 1.1: A computerised tomography scan of an advanced ameloblastoma tumour as seen in the frontal plane. The jaw and skull bones are visible in white (blue arrows), whereas the soft tissues and the ameloblastoma tumour are in grey and the nasal cavity is in black. Large parts of the mandible and maxilla have been resorbed by the ameloblastoma tumour (red arrows). The tumour has also infiltrated the left orbit (yellow arrow). Image provided by Dr S. Fedele (UCL Eastman Dental Institute).

a patient when the ameloblastoma tumour is discovered is 36 years (Reichart et al., 1995).

The ameloblastoma tumour grows slowly, often causing no early symptoms, which contributes to the difficulties in accurate diagnosis and the large size when removed. All subtypes, which are discussed in section 1.2, mainly present as a painless swelling or a slow-growing mass, and always require biopsy for diagnosis confirmation (Gardner et al., 2005). The ameloblastoma tumour is often noticed during a routine dental examination. Some patients may also present with malocclusion, loose teeth and paraesthesia (Bachmann and Linfesty, 2009), as well as delayed tooth eruption and in some cases pain (Reichart et al., 1995).

Diagnosis takes anywhere between months to years from the onset of symptoms, with the average time reported as 27 months (Reichart et al., 1995; Mendenhall et al., 2007). During this time, it is possible for the tumour to erode most of the maxilla or mandible. Eggshell cracking of the bone proximal to the tumour is often reported - this is due to pressure from the growing tumour leading to expansion and stretching of the surrounding bone (Cawson and Odell, 2008). However, in some cases, the slow growth of the tumour allows the periosteum to develop a sheet of bone to expand with it, leading to a greatly distorted jaw (Cawson and Odell, 2008). Cupping or saucerisation, which involves superficial erosion of the peripheral or superficial bone surrounding the tumour, can also occur (Mendenhall, 2011).

1.1.5 Tumour invasion

In some cases, ameloblastoma can continue to grow beyond the bone tissue and infiltrate both the medullary cavity and the surrounding soft tissue and anatomical structures of the head and neck. The proximity of the skull base and thinner bone in this region is thought to allow for easy tumour spread to the anatomical structures in the head and neck (Sampson and Pogrel, 1999; Ferretti et al., 2000). Primarily, this infiltration occurs in the gingivae, alveolar mucosa and facial muscles due to their proximity to the tumour (Arora et al., 2009; Gardner et al., 2005; Mendenhall et al., 2007). Some authors postulate that pressure resorption caused by the tumour on the surrounding bone is the major mechanism by which the tumour grows to a large size -

rather than specific tissue invasion or the invasive properties of the tumour cells themselves. A report in 2011 included a case with exophytic growth without cortical expansion with superficial erosion (saucerisation) of the bone (Sanjay et al., 2011). The authors postulated this may have indicated tumour growth through pressure resorption rather than resorptive invasion (Sanjay et al., 2011).

However, as continuously applied compressive pressure has been shown to reduce osteoblast function and increase osteoclast pre-cursor activity (Imamura et al., 1990), both pressure resorption and the potentially bone resorptive properties of ameloblastoma cells appear to function through the same turnover pathways.

1.1.6 Tumour recurrence

In the majority of cases, the benign ameloblastoma tumour does not recur. Hard tissue recurrences of ameloblastoma are rare, as a large piece of the affected jaw bone including the tumour is resected as a standard initial treatment. Soft tissue recurrence is thought to be caused by incompletely excised primary tumours appearing to use the surrounding soft tissues as an access point for further invasion (Al-Bayaty et al., 2002). Indeed, most recurrences are thought to be due to inadequate removal of the primary tumour (Mendenhall et al., 2007). The average time for recurrence development is 7.2 years, but can span decades (Reichart et al., 1995).

Overall, recent reports estimate approximately 30% of all ameloblastoma tumours recur (McClary et al., 2014). However, depending on the tumour subtype and treatment technique, varying recurrence rates have been reported: curettage or conservative treatment results in recurrence rates up to 70% (Gardner, 1984; Jaaskelainen et al., 2002; McClary et al., 2014), whereas recurrence rates after resection have been reported in approximately 15% of cases (Jaaskelainen et al., 2002; Chapelle et al., 2004; McClary et al., 2014). The recurrence rates for the different tumour subtypes are outlined in section 1.2.

Rarely, recurrent tumours cause extensive damage to the head and neck, and spread into vital organs in the vicinity of the original tumour. Maxillary tumour recurrences have been reported to have spread to the palate, nasopharynx and sinuses, as well as occasionally into the orbit, which is associated with impaired vision (Brazis et al., 1995).

1.2 Ameloblastoma classification

Currently, four different clinical variants of ameloblastoma have been classified: solid or multicystic ameloblastoma (SMA), unicystic ameloblastoma (UA), peripheral ameloblastoma (PA) and desmoplastic ameloblastoma (DA). These four different variants were standardised by the World Health Organization in 2005 (Gardner et al., 2005), making comparisons of cases before and after difficult, as different tumour types would be presented with varying names and the reclassification of the subtypes led to a changed disease picture (Mosqueda-Taylor, 2008).

All four variants are described histologically at length in major reviews and other reference books on ameloblastoma, such as those by Gardner et al. (2005); Mendenhall (2011); Philipsen et al. (2001a,b). All types of

ameloblastoma need biopsy for diagnosis confirmation, and histological examination of the tumour is used to distinguish between the different ameloblastoma subtypes. It is not known, whether there are differing cellular events or mutations, which underlie the different ameloblastoma subtypes. Some forms are prone to metastasis, but the metastasising variants display no specific features to distinguish them from non-metastatic forms of the disease, making prognosis difficult (Gardner et al., 2005).

1.2.1 Solid / multicystic ameloblastoma

Solid/multicystic ameloblastoma (SMA) is the most commonly occurring tumour type and second most common odontogenic tumour, making up approximately 80% of all ameloblastoma tumours (Bachmann and Linfesty, 2009). Tumours are intraosseous (central) and have the typical ameloblastoma qualities of slow growth and local invasiveness, with infiltrative growth into surrounding osseous tissue (Mendenhall, 2011). Rarely, intracranial spread is seen after destruction of the maxillary sinus (Gardner et al., 2005).
80% of tumours of this subtype involve the mandible, predominantly the posterior region (Bachmann and Linfesty, 2009). Similarly, maxillary tumours also involve the posterior region, which is thought to be due to the presence of aberrant tooth germ and the continuous proliferation of the dental lamina in this region (Mendenhall, 2011).

Histologically, this subtype presents as a unilocular or multilocular radiolucent lesion with soap-bubble appearance and irregular configurations of tumour tissue (Philipsen and Reichart, 1998; Mendenhall, 2011). Root resorption of proximal teeth is sometimes seen (Philipsen and Reichart, 1998). Two histological patterns are the most common: follicular (with islands of odontogenic epithelium) and plexiform (with branching strands of epithelium) in a connective tissue stroma, with both patterns infrequently seen in the same lesion (Bachmann and Linfesty, 2009). Recurrences are “not uncommon”, and can be seen more than ten years post-treatment, which is why long-term follow up is recommended (Gardner et al., 2005).

1.2.2 Unicystic ameloblastoma

Unicystic ameloblastoma (UA) is characterised by the presence of a single well-defined cystic lesion, with a lining partly consisting of odontogenic epithelium (Philipsen and Reichart, 1998). This subtype accounts for between 5-22% of all ameloblastomas, and is sometimes considered to be a variant of SMA (Philipsen and Reichart, 1998).
Up to 90% of tumours are associated with an impacted tooth (dentigerous variant; often impacted mandibular third molar), in which case it can be indistinguishable from a dentigerous cyst (Mendenhall, 2011). However, a study comparing 20 dentigerous cysts and unicystic ameloblastomas found that 81.5% of UA samples stained for calretinin, whereas none of the dentigerous cysts did, indicating calretinin as a potential diagnostic marker in UA (Coleman et al., 2001). Lesions arise anywhere, predominantly within the mandible body, and external root resorption can occur. Histologically, three or four different subtypes have been categorised, depending

on whether luminal, intraluminal and mural involvement is seen (Philipsen and Reichart, 1998).
Recurrence is documented as 6% for tumours without mural involvement and 37% for tumours with mural involvement (Mendenhall, 2011). The involvement of intramural tumour growth should be used to guide surgery, with aggressive resectioning and potential removal of adjacent bone in cases with invading tumour islands (Philipsen and Reichart, 1998; Mendenhall et al., 2007).

1.2.3 Desmoplastic ameloblastoma

Desmoplastic ameloblastoma (DA) is a recently defined subtype and although it is currently considered a distinct type of ameloblastoma, it may be a subtype of SMA (Philipsen et al., 2001b). The desmoplastic subtype accounts for around 3-13% of all ameloblastomas (Mendenhall, 2011).
The characteristic presentation of DA is as islands of ameloblastoma tissue within dense fibrous connective tissue, with abundant collagen of moderate cellularity (Philipsen et al., 2001b). Desmoplastic ameloblastoma is found with equal frequency in the maxilla and mandible (maxilla:mandible ratio 1:0.9) (Philipsen et al., 2001b). Radiological differences exist between this class and SMA, as desmoplastic tumours can be either radiolucent or radiopaque in appearance, with new bone reported in several cases (Philipsen et al., 2001b). Desmoplastic tumours have also been reported to have the weakest Ki-67 staining, and thereby the lowest cell proliferation rate, reinforcing the differences between this and the other ameloblastoma subtypes (Gomes et al., 2010). This subtype also invades the surrounding osseous tissue, characterised by irregularly shaped islands of odontogenic epithelium (Philipsen et al., 2001b). Defined tumour borders have been found present in only 7% of cases (Philipsen et al., 2001b). Collagen type IV and tumour growth factor (TGF)-β staining are seen in DA using immunohistochemical techniques, both of which are not seen in SMA (Mendenhall, 2011). Fibroblasts are also seen present within the tumour stroma; there is also an increased amount of stroma seen surrounding the tumour (Mendenhall, 2011).
Treatment is recommended as for SMA, with complete resection of the tumour with a 1-2cm margin to account for the diffuse tumour border, and long-term follow-up is recommended (Philipsen et al., 2001b).
Recurrence rates are difficult to determine, as this subtype is very rare, and the Philipsen review, with 100 patients' data is the largest one to date (Philipsen et al., 2001b).

1.2.4 Peripheral ameloblastoma

Peripheral ameloblastoma (PA) is a soft tissue (extraosseous) variant of ameloblastoma, forming lesions in the gingival or alveolar mucosa without bone involvement (Philipsen et al., 2001a). However, it is possible, that PA is in fact a variant of intraoral basal cell carcinoma, and these two lesions should be regarded as a single entity rather than as two separate tumours (Philipsen and Reichart, 2004). PA lesions arise either from remnants of the dental lamina proximal to tooth-bearing areas, or from the epithelial surface (Philipsen et al., 2001a). Lesions can also merge with the epithelial surface during growth (Philipsen et al., 2001a). PA accounts for 2-10% of all ameloblastomas, and is predominantly found in the mandible (Philipsen et al.,

2001a; Mendenhall, 2011). The average age for diagnosis is 52 years, approximately 15 years later than for other, intraosseous ameloblastomas (Philipsen et al., 2001a).

The lesions are painless and firm with a smooth swollen appearance, although local trauma, e.g. mastication, can give rise to an ulcerated surface (Philipsen et al., 2001a). Despite no bone involvement, the pressure exerted by the tumour on the underlying bone tissue may in some cases cause saucerisation (Philipsen et al., 2001a).

The histology of this tumour is similar to SMA, but no stellate reticulum involvement is seen. The majority of lesions exhibit a follicular pattern when examined histologically, although plexiform patterning is also seen (Philipsen et al., 2001a). The tumour stroma consists of mature stromal tissue (Philipsen et al., 2001a). As this subtype does not invade the bone, local surgical excision (conservative supraperiosteal excision) with disease-free margins is usually effective when combined with long-term follow-up (Philipsen et al., 2001a). It should be noted that due to the term ameloblastoma being included in the name of the lesion, there is a risk of the growth being treated with more extensive surgery than would be needed (Gardner et al., 2005). This subtype has a low recurrence rate, with only rare examples of malignant PA reported (Mendenhall, 2011).

1.2.5 Malignant ameloblastoma

As a rare exception, malignant or metastatic variants of the tumour occur in approximately 2% of ameloblastomas (Gardner et al., 2005). These cases are severe as they are not limited to being locally invasive and include metastasis to a distant site (Brazis et al., 1995; Lin et al., 2014). Malignant tumours are similar to non-metastatic ones when examined histologically, and can only be diagnosed retrospectively (Gardner et al., 2005; Bachmann and Linfesty, 2009). Malignant forms of the tumour can result in lesions in the skin, lymph nodes and parapharyngeal region (Kranz, 2015; Lin et al., 2014; Xavier et al., 2013). Case reports outline spread to more distant sites, with the primary location being the lungs, but this is rare (Hirshberg and Buchner, 1995; Klapsinou et al., 2013; Lin et al., 2014). Most literature on this type of ameloblastoma is in the form of case reports, which are sporadic and variable in quality - incidence rates, causes and recurrence rates for metastatic ameloblastoma are currently unknown.

1.2.6 Ameloblastic carcinoma

Ameloblastic carcinoma (AC) is a rare, malignant variant of the ameloblastoma tumour, which develops either from a pre-existing ameloblastoma tumour or *de novo* (Carinci et al., 2004; Ram et al., 2011). While metastatic ameloblastoma exhibits a benign histology, ameloblastic carcinomas exhibit both ameloblastoma-like and carcinoma-like malignant histology, with or without metastasis (Gardner et al., 2005; Bedi et al., 2010). AC is characterised by significant bone resorption and tooth resorption (Ram et al., 2011). The main symptom is a fast growing swelling, typically in the mandible (Ram et al., 2011).

Although AC is rare, its incidence has been reported to be twice that of metastatic ameloblastoma (Bedi et al., 2010).

1.3 Current treatment

1.3.1 Surgery

The mainstay treatment is surgical removal of the tumour. The large size of the tumour often leads to the need for a large amount of surplus tissue excision to ensure complete removal of all tumour cells in order to prevent or minimise recurrences (Gardner et al., 2005; Mendenhall, 2011).

At least a 1cm margin around the radiographic edge is recommended in most subtypes (Mendenhall, 2011), although many authors recommend a margin of 1.5-2cm to ensure all microcysts (tumour tissue remnants) are removed (Mosqueda-Taylor, 2008). This radical surgical excision requires removal of a potentially large part of the jaw bone to ensure complete excision. In all cases, the complex anatomy of the head and neck region provides an additional challenge. In the maxilla, the surgery is limited by the proximity or involvement of vital structures including, but not limited to, nerves, blood vessels and orbits (McClary et al., 2014). Where soft tissue involvement is evident, this should also be excised to prevent recurrences (Chapelle et al., 2004).

Early resection is recommended for especially maxillary tumours, as the bone surrounding the tumour in this location is thinner than in the mandible and therefore acts as less of a barrier to tumour spread (Chae et al., 2015). Furthermore, maxillary ameloblastoma is potentially lethal, as its potential for intracranial spread can make the complete removal of the tumour difficult even with modern surgical techniques (Bachmann and Linfesty, 2009; Mendenhall, 2011).

For mandibular tumours, vascularised free grafts are the standard replacement for the excised bone tissue (McClary et al., 2014). Reconstruction of the jaw bones is predominantly carried out by autologous bone transplantation from the fibula, iliac crest or scapula (Dandriyal et al., 2011). Some authors recommend conservative resectioning for low-risk unicystic ameloblastoma tumours, which have a lower infiltrative capacity and therefore a lower recurrence rate (Chapelle et al., 2004; McClary et al., 2014).

Quality of life post-operatively is limited by functional and cosmetic problems, such as malocclusion, masticatory dysfunction, abnormal jaw movement and facial deformities, as well as increased site morbidity and mortality. Several studies suggest the treatment method as an important prognostic factor, specifically implicating under-treatment and conservative tumour excision without use of appropriate margins as the main causes of recurrence (Mendenhall et al., 2007; Bachmann and Linfesty, 2009). Recurrences often present over 5 years after initial treatment, so follow-up is essential (Mendenhall, 2011).

However, more efficient diagnosis and treatment methods are needed, as a large part of the harmful effects of ameloblastoma could be avoided if there was a suitable method of diagnosis prior to the tumour reaching a large size inside the patients jaws, or an alternative to surgical treatment.

1.3.2 Radiotherapy

Radiotherapy should be considered for ameloblastoma tumours in patients with incompletely resectable tumours or in patients not amenable to re-resection (Koukourakis et al., 2011). However, radiation therapy is

generally not considered a valid treatment option, as ameloblastoma tumours have been classified as radioresistant for decades (Gardner, 1984; Mendenhall, 2011). Despite this, some studies have still reported treatment with radiation therapy, with an average recurrence rate of 45% when combined with surgery (McClary et al., 2014).

1.3.3 Chemotherapy

Recently, two studies have been published on treating B-rapidly accelerated fibrosarcoma (BRAF)-mutated ameloblastoma tumours. The first one was a late-stage ameloblastoma tumour (stage IV invasion with intrapulmonary metastasis), which was reduced in size using the BRAF V600E-inhibiting therapeutic agents dabrafenib and trametinib (Kaye et al., 2015). In the second one, the BRAF inhibitor dabrafenib was applied to a mandibular ameloblastoma tumour with the BRAF mutation, which resulted in a 90% reduction in tumour volume, although the tumour within the bone appeared less responsive to treatment and squamous cell maturation among the tumour cells was noted (Tan et al., 2016). The authors also reported on a pending clinical trial application on the use of a BRAF inhibitor for the treatment of ameloblastoma (Tan et al., 2016). Other authors have recently also advocated the use of similar BRAF-inhibiting agents, such as vemurafenib, to treat ameloblastoma tumours (Brown et al., 2014; Diniz et al., 2015; Heikinheimo et al., 2015; Sweeney et al., 2014).

1.4 The molecular and genetic background of ameloblastoma

This section introduces some of the current research on how ameloblastoma tumour cells are thought to become tumourigenic, able to grow within the jaw bones and invade surrounding tissues.

Until recently, most ameloblastoma research was concentrated on small studies of unquantifiable histological examinations of excised tumours, case reports of single tumours, as well as follow-up studies and population incidence studies. This is still the case to an extent, with case reports and histological observations of ameloblastoma published weekly. Histological examination of tumour samples is variable, as staining of the same sample can appear different to different people, and therefore great care must be taken to calibrate the people examining the stained samples. The staining is often not reliably quantifiable, and comparisons between different studies where different people assessed the staining levels are difficult.

Furthermore, a lot of studies would benefit from increased sample numbers, which as ameloblastoma is a rare tumour, have been low in a lot of studies (n = 2 (Lim et al., 2006), n = 5 (DeVilliers et al., 2011)), thereby contributing very little reliable, reproducible data to the field. Additionally, consensus should be reached on the type of tissue to be used as a default control or controls when examining ameloblastoma tumours, as studies use a variety of other odontogenic tumour tissues, gingival tissues, tooth buds, making comparisons between the various studies impossible (Heikinheimo et al., 2002; Carinci et al., 2003; Lim et al., 2006; DeVilliers et al., 2011).

Some studies have attempted to increase variation, and have included data from other methods, such as qRT-

PCR in their published studies. However, in some cases, this is found lacking due to the inexperience of the authors in these techniques. An example of this is the RANKL study by Qian and Huang (2010) *et al*, where essentially raw qRT-PCR data is offered without normalisation or calculations, and the reader is expected to calculate it themselves.

Due to advances in high-throughput screening, there have been a handful of larger studies on causative molecular mutations found in ameloblastoma tumours (Brown et al., 2014; Kurppa et al., 2014; Sweeney et al., 2014), as well as earlier microarray studies highlighting some common mutations (Heikinheimo et al., 2002; DeVilliers et al., 2011). These recent findings have shed light on the previously unknown molecular pathogenesis of ameloblastoma tumours, and proven that ameloblastoma tumours have some characteristic genetic abnormalities, including dysregulation of two main developmental pathways, the mitogen-activated protein kinase (MAPK) and sonic hedgehog (SHH) pathways, which are described in detail below, starting with the most significant mutations.

Furthermore, bone turnover genes which have been implicated in ameloblastoma tumours and tumour invasion are also discussed in this section. Potential matrix metalloproteinase involvement in the expansion and local invasion of this tumour is also described.

The major pathways implicated in ameloblastoma pathogenesis have been described separately for clarity, but as with any biochemical pathways, there is a great degree of overlap and interplay between different proteins; and different aberrantly expressed genes and proteins may be able to activate different pathways not discussed here. Therefore, not all molecules implicated in e.g. cell motility are considered under the 'motility' heading.

1.4.1 Mitogen-activated protein kinase (MAPK) pathway

The mitogen-activated protein kinase (MAPK, also known as ERK) is responsible for cell growth, differentiation and survival, by amplifying extracellular signals the cell receives through the RAS-RAF-MEK phosphorylation cascade (Sandra et al., 2006b; Kumamoto and Ooya, 2007b; Cargnello and Roux, 2011). A simplified schematic of the MAPK pathway is depicted in fig. 1.2. Early studies into the involvement of this pathway in ameloblastoma pathogenesis showed high epidermal growth factor (EGF) expression and activated (phosphorylated) MAPK1/2 in the tumour stroma, used by the tumour cells to induce cell proliferation and tumour growth (Siqueira et al., 2010). EGF and its receptor EGFR, as seen at the top of the pathway in fig. 1.2, have been studied in relation to ameloblastoma cell motility and invasion. The EGFR gene was found upregulated in an oligonucleotide microarray study of ameloblastoma tumours (Lim et al., 2006). Addition of EGF was found to increase ameloblastoma cell migration in an *in vitro* Transwell invasion study (Pinheiro da Rosa et al., 2014), although this study was only carried out on primary cells from one tumour sample. EGFR was prior to this abundantly expressed in 13 tumour biopsies (Siqueira et al., 2010), indicating that this pathway may be used by ameloblastoma cells for migration and potential invasion.

As depicted in fig. 1.2, the transcription factors RAS and RAF are situated between EGFR and MAPK

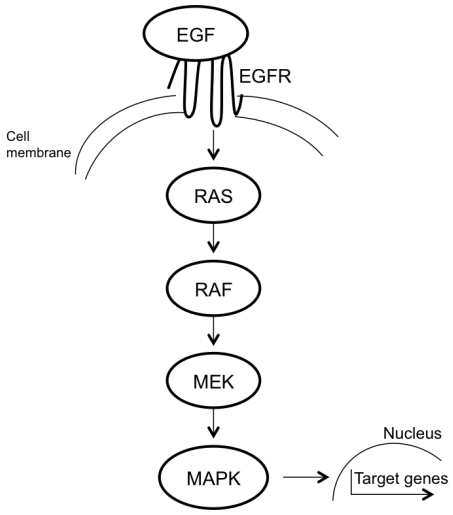

Figure 1.2: A simplified schematic of the normal MAPK pathway, which activates transcription of several genes in the cell nucleus, which are involved in at least cell differentiation and survival. The kinase cascade phosphorylates RAS, RAF and MEK in order to activate them. MAPK is also known as ERK. RAF is present in one of three isoforms, A-RAF, B-RAF or C-RAF. Image adapted from Garnett and Marais (2004); Wan et al. (2004).

in the signalling pathway. The RAF family of proteins includes three isoforms: ARAF, BRAF, and CRAF, where each isoform acts as an intermediary in the RAS-RAF pathway. In an immunohistochemistry study by Kumamoto and Ooya (2007b), MAPK expression was found elevated in 45 out of 47 ameloblastoma samples compared to no expression seen in ten tooth germ controls. Since then, mutations within the MAPK pathway have been found in the majority of ameloblastoma cases: FGFR2 (fibroblast growth factor receptor-2, another tyrosine kinase), RAS and BRAF mutations have been found in 78-88% of ameloblastoma tumours (Brown and Betz, 2015).

RAF is the most commonly mutated oncogene in human cancers,leading to increased MAPK activity (Cully et al., 2006; Garnett and Marais, 2004). Up to 100% of hairy cell leukaemias, 70% of malignant melanomas, 22% of colorectal cancers, 53% of thyroid and 3% of lung cancers have been documented to harbour a RAF mutation (Garnett and Marais, 2004; Lito et al., 2013).

The most common mutation is a single-site missense mutation, often in the kinase domain of the RAF protein. Wan *et al* found that a valine to glutamine by a thymidine to adenosine transversion at residue 600 accounted for 90% of BRAF mutations in cancers (Wan et al., 2004).

Mutations in the MAPK pathway have been described as mutually exclusive driver mutations; it appears these mutations activate the same oncogenic pathway (Wan et al., 2004). In ameloblastomas, the significance of this BRAF mutation was only discovered in 2014 (Sweeney et al., 2014).

BRAF V600E

The V600E (valine to glutamine substitution) mutation in the protein leads to enhanced cell proliferation, survival and neoplastic transformation (Brown et al., 2014). When comparing the frequency of this BRAF mutation in odontogenic carcinomas and ameloblastomas, 36% of odontogenic carcinomas were found to

have the mutation, compared to 82% of ameloblastomas (Diniz et al., 2015). In mandibular tumours, 72% cases were positive for BRAF mutations, whereas 19% of maxillary tumours were positive (Sweeney et al., 2014). Ameloblastomas with BRAF mutations were found to develop earlier than tumours without this mutation (median age 34.5y vs 53.6y respectively) (Sweeney et al., 2014).

Additionally, BRAF mutations are common in several other epithelial tumours. Therefore, inhibitors of BRAF V600E are clinically available, and are commonly used as treatments for melanomas with this mutation. The previously discussed case report of a stage-4 ameloblastoma tumour reported by Kaye et al. (2015), was also found to harbour a BRAF V600E mutation, and therefore responded to the anti-BRAF treatments. This treatment was seen to be effective despite previous treatment regimes, although there appeared to be a resistant tumour cell population at the original site after treatment (Kaye et al., 2015).

RNA interference (RNAi) could also be used as a potential therapeutic solution, as application of it on BRAF was reported to reduce MAPK activity and increased apoptosis in treated cells (Garnett and Marais, 2004).

Mutations in the MAPK pathway appeared to be critical in ameloblastoma pathogenesis in most cases (Brown et al., 2014). Based on these results, the MAPK pathway is currently likely to be the most important causative pathway for the activation of ameloblastoma tumour growth.

1.4.2 Sonic hedgehog (SHH) pathway

The sonic hedgehog (SHH) pathway and parts of it play a role in normal tooth development, especially during epithelial cell proliferation (Zhang et al., 2006; Mishra et al., 2015), and it has therefore been widely studied in ameloblastoma biopsies for its potential role in tumour growth and invasion. Aberrant SHH activation has been related to tumour formation, with constitutive activation in adulthood associated with many malignancies (Gurgel et al., 2010). A simple diagrammatic view of the SHH pathway is seen in fig. 1.3.

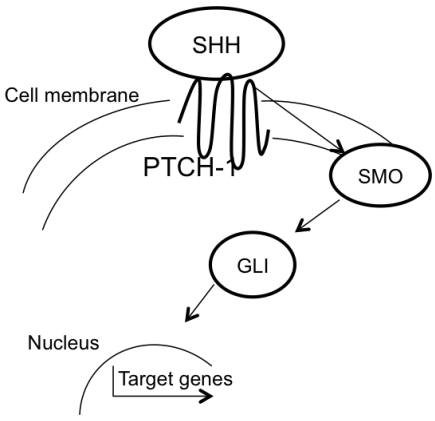

Figure 1.3: A simplified schematic of the Sonic Hedgehog (SHH) pathway. PTCH-1 (Patched-1), when unbound to SHH inhibits SMO (Smoothened) function and activation of the SMO pathway. When bound to SHH, the SHH-PTCH complex activates SMO and the downstream GLI (Glioblastoma) cascade to act on target genes in the nucleus. Image adapted from McMahon (2000); Kanda et al. (2013).

All 36 ameloblastoma biopsies investigated in an immunohistochemistry study by Kumamoto *et al* were found to have increased expression of SHH, patched-1 (PTCH-1), smoothened (SMO) and glioblastoma-

1 (GLI1) (Kumamoto et al., 2004b). Similar results for expression of other factors downstream of SHH, namely SMO, PTCH-1, GLI1, BCL-2, have been reported in other studies using both histological staining and qPCR (Gurgel et al., 2010; Zhang et al., 2006, 2010b). Confirmation of SHH pathway involvement in ameloblastomas was reported in 2014, with the SHH downstream factor SMO predominantly mutated in maxillary ameloblastoma tumours (Sweeney et al., 2014).

However, other odontogenic tumours, such as nine samples of calcifying epithelial odontogenic tumours, ten samples of adenomatoid odontogenic tumours and nine samples of calcifying odontogenic cysts showed similar SHH pathway expression patterns in a small immunohistochemical study as 15 ameloblastoma samples (Zhang et al., 2006). Considering the important function of SHH during tooth development, and the tissue remnants ameloblastomas and other odontogenic tumours are thought to arise from, this expression in most, if not all, odontogenic tumours should be expected. AM-1 proliferation has been shown to be significantly inhibited by the addition of a SHH-neutralising antibody, and the apoptotic response of the treated cells was restored (Kanda et al., 2013). All parts of the SHH pathway are therefore candidates for contributing to the development and the biological behaviour of ameloblastoma, as well as potential therapeutic targets.

Patched-1

As seen in the schematic in fig. 1.3, patched-1 (PTCH-1) a signalling factor involved with activating the SHH pathway when bound in a complex with SHH. The PTCH-1 protein on its own is an inhibitor of the SHH pathway as it represses SMO receptor signalling (Gurgel et al., 2010). A mutation (polymorphism) in the PTCH-1 gene has been suggested as a predisposing factor (Kawabata et al., 2005). Two studies, one of which used 8 ameloblastoma biopsies and 20 tooth germs as controls (Heikinheimo et al., 2002) and another with total genomic DNA from 14 ameloblastoma patients and 35 controls with no odontogenic disease (Kawabata et al., 2005), found abnormal PTCH-1 expression in the ameloblastoma samples but not in the control tissues, strengthening the possible role of a PTCH-1 mutation as predisposing in ameloblastomas. In a small microarray study, PTCH-1 was found aberrantly expressed in all five ameloblastoma samples examined (DeVilliers et al., 2011).

Smoothened

The SMO molecule is normally inhibited by unbound PTCH-1, and it has long been thought that mutations and polymorphisms in PTCH-1 affect ameloblastoma risk (Heikinheimo et al., 2002; Kawabata et al., 2005). The latest research has implicated SMO, a downstream factor of SHH in ameloblastoma tumours of the maxilla, indicating two distinct subclasses of ameloblastoma tumours with different molecular expression patterns of SMO and BRAF (Sweeney et al., 2014). Over half of maxillary ameloblastomas were found positive for SMO mutations, whereas only approximately 6% of mandibular origin tumours were SMO positive (Brown et al., 2014). A subsequent study found a SMO mutation in 39% of ameloblastoma cases (Brown and Betz, 2015). The SMO mutation most commonly identified was a L412F mutation (leucine to phenylalanine at

amino acid 412), with another common SMO mutation being a F412E (phenylalanine to glutamic acid) substitution (Brown and Betz, 2015; Diniz et al., 2015).

Over half of tumours where SMO was found mutated and approximately 15% of BRAF-mutated tumours recurred within 3 years of initial treatment Sweeney et al. (2014). Currently, SMO inhibitors are only effective in tumours which have a specific mutation to inactivate PTCH-1, as extensive resistance to therapies has been reported when SMO-only inhibitors have been used on ameloblastomas (Sweeney et al., 2014).

1.4.3 Wingless-type (Wnt) pathway

Mutations in parts of the canonical Wingless-type (Wnt) pathway have also been reported in ameloblastoma, and this pathway is, together with the MAPK and SHH pathways, currently one of the main pathways implicated in ameloblastoma pathogenesis (MacDonald et al., 2009; Sathi et al., 2009, 2012). The pathway is visualised in a simplified schematic in fig. 1.4. Many of the proteins in this pathway are also involved in osteoblastic differentiation (Sathi et al., 2012). Secreted frizzled-related protein (sFRP), which is an antagonist to the Wnt pathway, has been found expressed by ameloblastoma cells, and shown to inhibit osteoblastogenesis by preventing the normal function of β-catenin (Sathi et al., 2009).

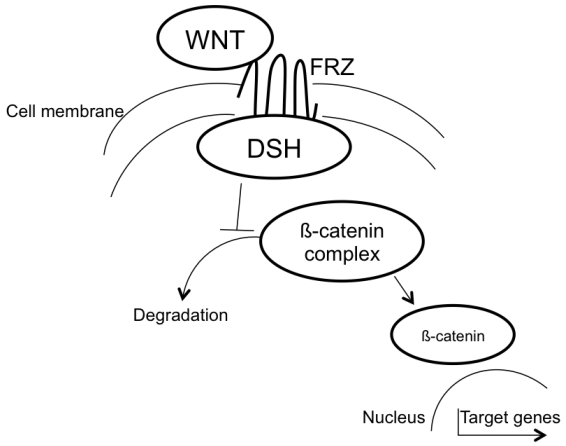

Figure 1.4: A simplified schematic of the WNT pathway. WNT binds to Frizzled (FRZ), which then binds to Dishevelled (DSH). This then inhibits degradation of the β-catenin complex, allowing β-catenin translocating to the nucleus and transcription of target genes. Pathway image adapted from (MacDonald et al., 2009).

β-catenin

The *CTNNB1* gene codes for β-catenin within the Wnt pathway, and some studies have implicated both the gene and the resulting protein as responsible for increased ameloblastoma cell survival and motility (Kumamoto and Ooya, 2005). The molecule is also involved in bone turnover: when Wnt expression is disrupted, β-catenin is ubiquinated for destruction, resulting in a reduction of osteogenesis (Sathi et al., 2012). A few studies have examined the involvement of β-catenin in ameloblastomas, although these have generally involved a hand-full of samples; thus more extensive studies with more samples would be needed on β-catenin expression in ameloblastoma tumours. However, immunostaining of β-catenin in biopsy samples has shown consistent expression in all samples (Kumamoto and Ooya, 2005). β-catenin has also been found expressed

in both primary and recurrent ameloblastoma tumours, and may thus contribute to the increased local invasion of ameloblastoma tumours (Siar et al., 2015).

1.4.4 Bone turnover in ameloblastoma

The main concepts of bone biology, proteins and genes involved in the synthesis and resorption of bone tissue *in vivo* are discussed in more detail in section 1.10. Here, some of the bone signalling pathways which have been found aberrantly expressed in ameloblastoma tumours and implicated in tumour-mediated bone resorption are considered.

Osteoprotegerin

Osteoprotegerin (OPG) is a decoy receptor for receptor activator of nuclear factor-κB ligand (RANKL), and prevents RANKL from binding to its target and activating osteoclasts as seen in fig. 1.5. Lower levels or a lack of the OPG molecule leads to osteoclastogenesis, as the lack of this decoy receptor allows for activation of RANKL. The OPG molecule has consistently been found expressed in ameloblastoma samples, and often at higher levels than RANKL (Kumamoto and Ooya, 2004; Iakovou et al., 2015). However, OPG can also, instead of binding to RANKL, bind to TNF-related apoptosis-inducing ligand (TRAIL), limiting its apoptotic potential, while simultaneously rendering RANKL able to activate osteoclastogenesis in bone tissues and potentially also in ameloblastoma tumours (Sandra et al., 2006a).

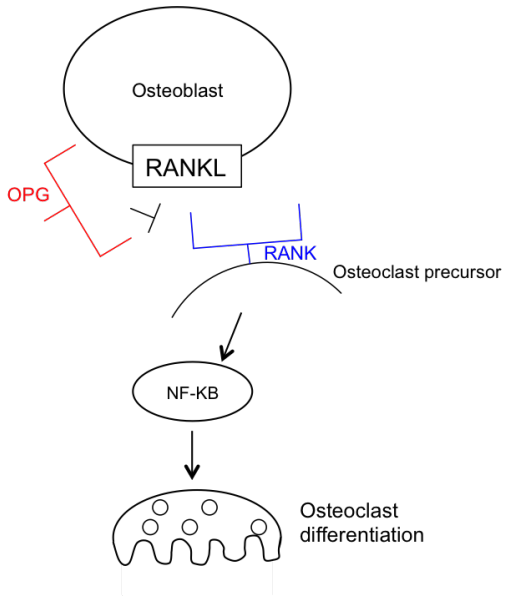

Figure 1.5: A simplified schematic of the osteoclast activation pathway. RANKL is expressed on osteoblasts, as well as on some other cell surfaces. OPG (in red) and RANK (in blue) both bind to RANKL, but only RANKL binding induces osteoclast precursor activation and osteoclast formation. OPG, by inhibiting RANKL, therefore promotes bone synthesis whereas RANKL promotes bone resorption. Adapted from (Boyce and Xing, 2006).

RANKL

The receptor activator of nuclear factor-κB ligand (RANKL) is an essential cytokine for regulating tumour-bone interactions, bone metastases and tumour invasion into bone tissues in several types of tumours; notably those of the facial skeleton (Tay et al., 2004; Tekkesin et al., 2011). In an immunohistochemistry study on primary ameloblastoma samples, RANKL staining was seen in both tumour and stromal cells in solid ameloblastoma tumours (Iakovou et al., 2015). Osteoclasts were found to appear on the ameloblastoma tumour border, which suggests that the tumour cells secrete factors to induce osteoclastogenesis (Sandra et al., 2005a).

Studies carried out on ameloblastoma samples indicate that the tumour cells have an ability to recruit and promote the differentiation of osteoclasts through RANKL signalling, enabling the tumour cells to resorb the bone around them (Sandra et al., 2005a; Wang et al., 2008; Qian and Huang, 2010). RANKL-induced osteoclastogenesis has been shown to play an important role in tumours with higher local invasion capacity and more aggressive behaviour, such as oral squamous cell carcinoma (Kearns et al., 2008; Jimi et al., 2011; Quan et al., 2012). Expression of RANKL and OPG especially in the mesenchymal cells within the tumour stroma have been found to regulate bone metabolism locally, potentially aiding local tumour invasion (Kumamoto and Ooya, 2004; Sathi et al., 2008).

Nuclear factor-κB

Nuclear factor-κB (NFκB) is a transcription factor responsible for a variety of cellular functions, including cellular survival (Hendarmin et al., 2008), and bone turnover as a downstream factor of RANKL (Hofbauer and Heufelder, 2000; Ghosh and Karin, 2002; Karin, 2006). NFκB has been found to be constitutively activated in oral squamous cell carcinomas and to promote the invasion of these tumour cells (Furuta et al., 2012).

83% of ameloblastoma tumour biopsies were found to stain positive for NFκB in a study, with stronger staining found on cells on the surface of the tumours, indicating a stronger anti-apoptotic potential in these cells in all 24 samples studied (Hendarmin et al., 2008). NFκB was also found to promote cell survival by preventing apoptosis in AM-1 cells (Hendarmin et al., 2008).

1.4.5 Ameloblastoma cell-mediated extracellular matrix breakdown

Some genes implicated in ameloblastoma pathogenesis have a clear effect on the ability of the tumour cells to locally invade the tissues surrounding it. The roles of various MMPs and other proteins involved with ECM breakdown in ameloblastoma tumours is summarised in table 1.1. It should however be noted that a majority of the studies outlined here have been carried out using immunohistochemical techniques, which give no indication of the MMPs enzymatic activity; MMP activity studies should be performed in addition to IHC staining for MMP localisation within the ameloblastoma tumours.

The EGF and EGFR mutations discussed in section 1.4.1 have also been linked with increases in MMP

synthesis and activity (Pinheiro da Rosa et al., 2014). A major source for MMP activity in tumours are stromal cells, which are recruited to the vicinity of the tumour cells, which can then aid tumour cell invasion and growth (Sahai, 2005; Kessenbrock et al., 2010).

Table 1.1: Expression of molecules involved in cell-mediated ECM breakdown in ameloblastoma tumours. Details of the experimental set-up and normal function of the molecule in question are also given. 'N' is the number of ameloblastoma samples used in the study. 'Control' details the tissue or cell type used as a control. MMP - matrix metalloproteinase, AOT - adenomatoid odontogenic tumour, CCOT - calcifying cystic odontogenic tumour, KCOT - keratocystic odontogenic tumour, IHC - immunohistochemistry, RECK - reversion-inducing cysteine-rich protein with Kazal motifs, WB - western blotting, ICC - immunocytochemistry

Name	**Function**	**N, control**	**Study type**	**Finding**	**Location**	**Authors**
MMP-1	ECM breakdown, mediating osteoclastogenesis in ameloblastoma	20, AOT	IHC	Expressed in all AM samples	Central cells of tumours	Ribeiro et al. (2009)
MMP-2	ECM breakdown Cleaves collagen IV, cell motility and tissue expansion	1) 22, tooth germ 2)20, AOT	IHC	1) Weak expression in tumour cells, strong in mesenchymal components, 2) Strong expression due to interactions between epithelial and mesenchymal AM tumour components, not present in controls	1) Stromal cells, 2) Peripheral tumour cells, central portion of odontogenic epithelial cells	1) Kumamoto et al. (2003) 2) Ribeiro et al. (2009)
MMP-9	Cell motility, tissue expansion	1) 24 2) 13, CCOT	1) IHC and qRT-PCR 2)	1) Expression in all AM types, 2) Detected using both methods	1) Cells in tumour periphery, 2) Epithelial component, stromal cells surrounding tumour	1) Qian and Huang (2010) 2)Siqueira et al. (2010)
RECK	Inhibits MMP matrix breakdown	1) 69, KCOT 2) Cell line	1) IHC, qRT-PCR, 2) qRT-PCR, WB, ICC	1) Expression lower in recurrent tumours enabling invasion, 2) Overexpression inhibited invasion	1) Tumour periphery, 2) Cytoplasm of individual cells	1) Zhang et al. (2009b) 2) Liang et al. (2014)

Generally, the findings agree that MMP-2 is present in the mesenchymal cells surrounding the tumour, and on the tumour periphery, where it is thought to aid with local invasion. MMPs present in ameloblastoma tumours may mediate bone resorption and the tumour cells may use growth factors released from absorbed bone to grow further (Siqueira et al., 2010). As MMPs mediate changes to the ECM during tumour progression, they can clinically be considered targets of anti-cancer therapy. Tissue inhibitors of matrix metalloproteinases (TIMPs) are the major physiological inhibitors of MMPs; but they are also thought to play a role in the activation of MMPs at lower concentrations (Curran and Murray, 2000; Egeblad and Werb, 2002). A study by Wang et al. (2008) examined MMP inhibition in ameloblastoma tumours by applying MMP-2-inhibiting TIMP-2 to AM-1 cells *in vitro*, and found that invasion of the cells was inhibited in an *in vitro* Transwell invasion study (Wang et al., 2008). A subsequent study induced the TIMP-2 gene in nude mice with human ameloblastoma, resulting in a reduction in tumour size (Zhang et al., 2010a).

1.4.6 Mutations to cell adhesion molecules

Studies have mapped out various mutations to cell adhesion molecules, such as integrins, in ameloblastoma. These are detailed in table 1.2.

Table 1.2: Mutations to cell adhesion molecules in ameloblastoma samples. Expression of various molecules involved with cell adhesion is detailed together with the experimental set-up and normal function of the molecule in question. 'N' is the number of ameloblastoma samples used in the study. 'Control' details the tissue or cell type used as a control. IHC = immunohistochemistry, AOT = adenomatoid odontogenic tumour, CCOT = calcifying cystic odontogenic tumours, OOT = other odontogenic tumours.

Name	**Function**	**N, control**	**Study type**	**Finding**	**Location**	**Authors**
Integrin: $\alpha2\beta1$, $\alpha3\beta1$, $\alpha5\beta1$	Mediate cell binding to ECM, increase MMP-2 synthesis	AOT, tooth germ	IHC	$\alpha2\beta1$ and $\alpha5\beta1$ expression higher in AM than in controls, $\alpha3\beta1$ expression in AM but not in controls	Intercellular and periphery of tumour	de Souza Andrade et al. (2008)
Integrin: NOTCH1	Disintegrin, involved in cell proliferation and motility	20, CCOT and dental follicle	IHC	AM cells positive for NOTCH1	Strong expression in parenchymal AM cells	da Costa et al. (2016)
Integrin: ADAM-12	Disintegrin, cell invasion and migration	20, CCOT and dental follicle	IHC	Upregulated in AM cells, may increase AM cell invasion	Cytoplasms and cell membranes of AM cells	da Costa et al. (2016)
Glypican	Involved in both SHH and Wnt pathways, role in cell adhesion	80, normal tooth germs	IHC	100% of DA, 66% of PA, 51.2% of SMA and 47.2% of UA stained positive, suggesting association between expression and AM subtype	tumour cells, fibroblasts, stroma, extracellular space	Bologna-Molina et al. (2015)
E-Cadherin	Cell-to-cell adhesion, reduction increases cell motility	1) 24, tooth germs 2) 21, toothgerm 3) 25,	1) IHC 2) IHC 3) IHC	1) Reduction in more malignant tumours, 2) cell adhesion promoted in distant cells by normal levels in, 3) AM tumours positive	1) cell-to-cell boundaries, 2) cell membrane of stellate reticulum cells and peripheral cells, 3) Cell membrane, lower levels at invasive fronts	1)Kumamoto and Ooya (1999), 2)Alves Pereira et al. (2010), 3)Siar et al. (2015)
β-catenin	Wnt pathway, cell-to-cell adhesion	21, tooth germ	IHC	Half stained, mixed results	Peripheral cells, stellate reticulum	Alves Pereira et al. (2010)

1.4.7 Ameloblastoma apoptosis prevention

Ameloblastoma cells in parts of tumours proximal to bone tissue have been found to proliferate faster than cells elsewhere in the tumours (Pinheiro et al., 2004). The increased expression of BCL-2 in cells on the periphery of the ameloblastoma tumours, as detailed in table 1.3, may in turn increase cell proliferation (Mitsuyasu et al., 1997; Sandra et al., 2001). Furthermore, BCL-2 and SHH expression have been found to co-localise in histological ameloblastoma samples to cells with a high proliferation rate within the tumours, indicating an increase in cell viability and apoptosis prevention in these cells (Kanda et al., 2013).

Table 1.3: Summary of expression of molecules involved in apoptosis prevention in ameloblastoma tumours, together with the experimental set-up and normal function of the molecule in question. 'N' is the number of ameloblastoma samples used in the study. 'Control' details the tissue or cell type used as a control. Tumour necrosis factor (TNF)-α,TNF-related apoptosis-inducing ligand (TRAIL), IHC = immunohistochemistry, WB = western blotting, ELISA = enzyme-linked immunosorbent assay,

Name	**Function**	**N, control**	**Study type**	**Finding**	**Location**	**Authors**
TNFα	Mediating osteoclastogenesis in ameloblastoma	24, none	IHC, WB, ELISA	Expression seen using all methods. Increased TNF levels induce MAPK phosphorylation	Epithelial cells of tumours	Hendarmin et al. (2005)
TRAIL	Neoplastic transformation of the epithelium, cell growth	1) 40, none 2) 15, none 3) 32 and AM-1, none	1) IHC, 2) IHC, apoptosis assay, 3) IHC, WB, apoptosis assay	1) 87.5% positive 2) expressed in AM 3) TRAIL induces apoptosis in AM	1) Epithelial cells proximal to the basement membrane 2) cytoplasms of neoplastic epithelial cells	1) Iakovou et al. (2015) 2) Rizzardi et al. (2009) 3) Sandra et al. (2005b)
BCL-2	Apoptotis inhibitor	1) 25 2) 40, none	IHC	Mostly positive staining	1) Increasing in cells on the periphery of tumours 2) Cytoplasmic, in peripheral epithelial cells	1) Mitsuyasu et al. (1997) 2) Neves-Silva et al. (2016)

1.4.8 Other proteins

Details of other proteins found aberrantly expressed in some ameloblastoma tumour samples are shown in table 1.4. These include various inflammatory factors but also genes involved in enamel formation in developing teeth.

Again, the wide variety of control choices is seen in these studies, with no consensus making comparison difficult as actual staining levels remain unknown. Furthermore, studies such as the one by Iezzi *et al* detailed in table 1.4, which group ameloblastoma into tumour less and more likely to recur, without controls for staining nor data on patient follow-ups (i.e whether the tumours did occur or not), clearly lack in experimental design.

To summarise, a few major pathways currently appear to play significant roles in ameloblastoma pathogenesis, with the BRAF mutation in the MAPK pathway appearing to be the major causative mutation (Sweeney et al., 2014), with SHH/SMO pathway mutations a close second (Brown and Betz, 2015). However, many researchers have previously attempted to uncover causative mutations, and therefore there is a wide range of studies available. Many of these have found under- or overexpression of genes and proteins involved with cell-to-cell attachment and cell-to-matrix attachment, leading to increased cell motility, which is especially relevant for the locally invasive ameloblastoma tumour.

Mutations have also been uncovered in apoptosis prevention, leading to increased survival of the mutated tumour cells (Gomes et al., 2010; Brown and Betz, 2015), as well as mutations in interleukins, TNF-α and other molecules, which can all lead to increased RANKL levels and thereby increased osteoclast activation, further contributing to tumour progression and bone resorption (Sathi et al., 2008; Jimi et al., 2011). As with

Table 1.4: Expression of enamel matrix proteins, vascular markers, immune factors in ameloblastoma tumours and the experimental set-up and normal function of the molecule in question. 'N' is the number of ameloblastoma samples used in the study. 'Control' details the tissue or cell type used as a control. IHC = immunohistochemistry, OT = other odontogenic tumours, NOM = normal oral mucosa CCOT = calcifying cystic odontogenic tumour.

Name	**Function**	**N, control**	**Study type**	**Finding**	**Location**	**Authors**
AMBN	Matrix protein expressed during enamel formation	4, OT and dental follicles	IHC	No expression	N/A	Perdigao et al. (2004); Crivelini et al. (2012)
ODAM	Odontogenic ameloblast-associated protein	4, OT and dental follicles	IHC	No expression	N/A	Crivelini et al. (2012)
AMEL	Mineral	4, OT and dental follicles	IHC	No expression	N/A	Crivelini et al. (2012)
P53	Tumour suppressor	1) 46, tooth germs 2) 23, OT and NOM	1) IHC and DNA sequencing, 2) IHC	1) No DNA alterations, positive staining in half of AM 2) Expressed in all samples; minor role in neoplastic change in the odontogenic epithelium	Peripheral tumour cells	1)Kumamoto et al. (2004a) 2)Gadbail et al. (2012)
PI3K	Akt pathway, regulates apoptosis, increases cell survival	40, tooth germ	IHC	Expression higher in plexiform than follicular AM, overall similar to control expression	Throughout neoplastic cells	Kumamoto and Ooya (2007a).
HIF-1α	Cell survival in hypoxia	20, CCOT and dental follices	IHC	Positive in central cells, weak in stroma	Predominantly nuclei of tumour cells	da Costa et al. (2016)
TGFβ1	Cell invasion, wound healing, immune responses	29, none	IHC	Increased expression in tumours more likely to recur, increased AM invasion	Peripheral cells and stromal cells	Iezzi et al. (2008)
Interleukins	Inflammation, interactions between tumour cells and fibroblasts	AM-3 co-culture	AM-3 cells	Upregulation of IL-6, IL-8 and TNF by fibroblasts, ILs and TNF contribute to local tumour invasion	N/A	Fuchigami et al. (2014)

other tumours, many individual ameloblastomas also appear to have unique mutations, enabling individual tumours to improve their invasion and survival, and making the disease picture more complex.

1.5 Knowledge gap

There have recently been a few of ground-breaking studies looking at the potential genetic and molecular causes of ameloblastoma, relating to a few pathways and putative genetic causes. However, little is known about the cellular events leading up to the growth of the tumour, its initial developmental stages, how the tumour invades its surrounding ECM and bone tissue and how this all could be detected.

Whereas potential genetic abnormalities and aberrant signalling mechanisms could be used to indicate predisposition to the tumour, and potentially to aid prognosis, inhibiting the growth and stopping bone and soft tissue invasion of the tumour will be critical in treating ameloblastoma tumours and improving the quality of life of patients. Attempting to answer some of these questions by developing an *in vitro* scaffold in which ameloblastoma can be modelled formed the basis of this study.

1.6 The need for an in vitro ameloblastoma model

Numerous *in vitro* 2D studies of ameloblastomas have been carried out, mostly using the AM-1 cell line, as well as studies on ameloblastoma biopsies, with most of these being immunohistochemical analyses of various proteins in the tumours. Currently, a wide variety of methods are used for characterising ameloblastoma *in vitro*. These are summarised in table 1.5, along with some of the major positives and negatives for using each type of model.

As ameloblastoma initially forms inside the jaw bones, which it then invades, a bone-like organotypic model was one of the two models developed during this project. The models developed here sought to improve on the past models by incorporating the best aspects of each of them in one model, i.e. organotypic, 3D, mineralised, collagen-based bone-like scaffolds with bone-like cell behaviour for modelling ameloblastoma within the jaw bones, and a collagen-based soft tissue mimic to model ameloblastoma growth within the soft tissues.

By using tissue engineering techniques to achieve a reproducible and cheap biomimetic *in vitro* model for ameloblastoma, large numbers of ameloblastoma tumour samples could ultimately be examined for gene expression, protein production and cell behaviour to provide large, reliable data sets on the tumour. Tumour cell growth, progression and local invasion could also be monitored, specifically with the aim of elucidating which pathways and molecules the tumour cells use to reach a larger size within their native tissues. Additionally, *in vitro* organotypic scaffolds also allow for testing of potential therapeutic agents, which could also be useful for ameloblastoma research.

However, a *post hoc* model made with cells from excised tumours and ECM factors will not be able to find out the causes of ameloblastoma. The models developed during this study can therefore only be used for

Table 1.5: Summary of *in vitro* ameloblastoma models. The type of model used is summarised, along with whether the model includes the cells in 2D or 3D. The major positives as well as negative sides for each model are also included.

Model type	**2D / 3D**	**Studies carried out**	**Positives**	**Negatives**	**Authors**
Cell lines, AM-1, AM-3, AME-1	2D on plastic	Protein expression, gene expression	Quick, reproducible	2D cell behaviour different to native cells, potential cancerous effects of cell lines	Harada et al. (1998); Tao et al. (2009); Alves Pereira et al. (2010)
Transwell studies	2D or 3D	Invasion study, conditioned media effects	Quantifiable, reproducible, controllable	Cells only in contact through media	Fuchigami et al. (2014); Zhang et al. (2010c); Chantravekin and Koontongkaew (2014)
Explant co-cultures	3D	Effects on other cells	3D, organotypic	Co-culture cells were murine, not human	Caton et al. (2012)
Co-cultures using conditioned media	2D	Protein synthesis, cell behaviour	Interactions between the different cell types	Mostly on 2D plastic, cells only in contact through media	Fuchigami et al. (2014)
Co-cultures within the same matrix	3D	Cell-to-cell interactions, proteins and other effects	3D, co-culture effects on cells	Soft matrix, not organotypic	Chantravekin and Koontongkaew (2014)
Matrigel	3D	Mostly Transwell invasion studies, 3D characterisation, potential for co-culture	3D, various ECM factors	Cancerous matrix, batch-to-batch variation, soft matrix	Wang et al. (2008); Chantravekin and Koontongkaew (2014)
AM-1 on dentine	2D	Bone resorption assay	Quick, includes osteoclasts	Dentine is not bone	Qian and Huang (2010)
Hydrated collagen matrix	3D	Ultrastructural AM observation, IHC	3D environment	Not organotypic as matrix hydrated, single protein scaffold	Yasuda et al. (1991a)

determining sone molecular events and aberrant signalling pathways which may contribute to tumour growth, progression and tissue invasion, and attempt to control these to make the tumour easier to treat in a clinical situation.

Due to difficulties in obtaining either another cell line for use in this system or fresh ameloblastoma tissue, this model was only developed using one cell line, AM-1. In order to successfully engineer a suitable scaffold and successfully develop organotypic ameloblastoma models, the properties of healthy native tissues need to be considered.

To ensure the scaffolds used are biomimetic, the decellularised mineralised bone substrate Bio-Oss will be used to make a compressed collagen and bone granule composite. This set-up provides the bone-like scaffolds with mineral without the cellular component. By additionally incorporating human cells to the constructs, the co-cultures are provided with human proteins and cell-to-cell interactions. Similarly, soft tissue models with compressed collagen and Matrigel will be developed in order to develop soft tissue ameloblastoma co-culture models.

After ameloblastoma (AM-1) cell addition, these two co-culture models with ameloblastoma tumour cells and bone cells or fibroblasts could provide a useful tool for observing tumour growth in 3D, cell motility inside the tissue models, and the rate of bone turnover and matrix degradation caused by the ameloblastoma cells. By creating these 3D *in vitro* models for ameloblastoma using human cell lines, the findings can be more directly applied to human patients rather than if animal models or 2D culture had been used. Furthermore, by incorporating more than one cell type in the culture models, the relevance of the models is increased.

A number of recent studies have begun to assess the effects of novel anti-cancer drugs within organotypic 3D models (Smalley et al., 2008; Nyga et al., 2011). Potential therapeutic agents will therefore also be tested on this co-culture model to attempt to inhibit the progress of the disease, provided the model is sufficiently like the *in vivo* structure, and an improved, targeted treatment for ameloblastoma could be developed.

The three-dimensional models presented here also provide an improved environment compared to traditional *in vitro* studies with regards to drug actions and diffusion through tissues and organs. Cells in 2D environments are easily disrupted by therapeutic agents, however the efficacy of therapeutics applied is already greatly reduced in a simple 3D model (Weigelt et al., 2014). This change in efficacy and function of therapeutic agents is partly due to the different cell conformations in 3D matrices, but also due to the presence of extracellular matrix factors, proteins and fibres in 3D matrices, which are able to physically inhibit the actions of the drug molecules (Weigelt et al., 2014).

1.7 Tissue engineering organotypic models

Tissue engineering is the use of a combination of scaffolds, proteins and cells *in vitro* to synthesise complex cellular constructs for tissue replacement or as models of tissues and disease (Langer and Vacanti, 1993). The second part of this introductory chapter considers the background to tissue engineering, specifically for the development of bone-like and soft tissues, as well as suitable scaffolds and cells to use to achieve organotypic

scaffolds *in vitro*.

Organotypic models aim to capture complex biological and physiological interactions *in vitro*. This is achieved by closely modelling physiological mechanics and architecture of tissues, cellular complexity and cell-to-cell interactions. Organotypic models are currently favoured as a method to establish a more *in vivo*-like environment for cell growth *in vitro* (Weigelt et al., 2014).Two-dimensional (2D) cell cultures of monolayers on tissue culture plastic (TCP), which are conventionally used for cell cultures, drug efficacy studies and pre-animal models, provide the cells in culture with no environmental cues (Burdett et al., 2010). Furthermore, traditional cell culture also suffers from a lack of stroma, leading to a lack of cellular architecture and cell-to-cell and cell-to-matrix interactions (Kim et al., 2004). Culturing cells in three-dimensional (3D) matrices has been shown to have an tissue-like effect on cellular behaviour, including adhesion, mechanotransduction, contraction, differentiation and survival (Lutolf and Hubbell, 2005; Griffith and Swartz, 2006). Cells in 2D often exhibit remarkably different behaviour to more complex 3D tissues, with some major differences between 2D and 3D cell culture, including cell appearance and survival, as well as anti-cancer agent function (Weaver et al., 1997; Santini and Rainaldi, 1999).

The 3D environment is also advantageous for scaffold remodelling and other morphogenic events over a longer culture time (Griffith and Swartz, 2006; Tsuda et al., 2007).

Additionally, cell proliferation in 3D cultures has been shown to be more physiologically relevant, i.e. slower (Hutmacher, 2000). Cell polarity, especially in epithelial cell lines, has been shown to persist in 3D cultures, which is important for *in vivo*-like cell behaviour (Kim et al., 2005).

The use of 3D tissue models makes it possible to obtain close-to-physiological responses and processes, especially to (novel) drug therapies (Astashkina and Grainger, 2014). In general, 3D modelling provides the cells cultured within the scaffold with a well defined geometry, cell-to-cell and cell-to-matrix interactions, support from stromal elements and cellular heterogeneity (Kim et al., 2004). In addition, cultures of cells with heterogeneous phenotypes can be similar to intact tumours, with the 3D scaffolds providing the cells with an *in vivo*-like environment (Kim et al., 2004). Therefore, what is required for basic organotypic model development is a simple, predictable and reproducible scaffold, designed to mimic specific aspects of a tissue (Brown, 2013).

However, establishing true and reliable *in vitro* models is difficult, as the *in vivo* cell microenvironment consists of a variety of cell-to-cell interactions, cell-ECM interactions and cell-soluble factor interactions, which make up a complex array of physical, chemical and electrical information about their surroundings (Friedl and Brocker, 2000; Hakanson et al., 2014).

It should also be remembered that perfect *in vitro* models do not exist - an ideal model is an intact, native tissue (Kim et al., 2004; Villasante and Vunjak-Novakovic, 2015). It is also difficult to achieve perfect physiological models, as different *in situ* tissues and *in vitro* tissue models have different nutrient gradients, often lack blood flow and exhibit differences in oxygen perfusion (Hakanson et al., 2014).

1.7.1 Tumour models as organotypics

Tumour engineering has been defined as the construction of complex models of the *in vivo* tumour microenvironment to study tumour development, progression and therapy (Ghajar and Bissell, 2010). In short, engineering organotypic tumour models makes use of tissue engineering techniques to study complex environments in cancer biology (Gill and West, 2014). In 1889, the importance of the tumour microenvironment was noted in Paget's "seed and soil" hypothesis, where the tumour and its microenvironment appeared connected (Langley and Fidler, 2011; Villasante and Vunjak-Novakovic, 2015). Tumour microenvironment instability has been linked to increased tumour progression, i.e. invasion, and the microenvironment also further contributes to the instability of the tumour itself (Bindra and Glazer, 2005). Indeed, the microenvironment is now recognised as is a crucial regulator in the evolution of the tumour, progression of tumour growth, as well as the outcome of treatment (Polyak et al., 2009; Hakanson et al., 2014).

Organotypic models allow for systematic investigation into unknown regulatory feedback mechanisms between tumour cells and other cells present in the microenvironment (Kim et al., 2004). Organotypic tumour models can be used to mimic tumour-stromal interactions, interactions between different cell types and protein signalling in the tumour (Chioni and Grose, 2008; Szot et al., 2011; Villasante and Vunjak-Novakovic, 2015). Evidence suggests that unpredictable changes in and a dysfunction of the tumour stroma are as important in the formation of a tumour, as the initial cellular mutations which caused the tumour to form (Albini and Sporn, 2007).

Important things to consider when developing organotypic tumour models include the different cell types in and around the tumours, the co-localisation of these cells, any cell-cell interactions and exchange of growth factors (Kim et al., 2004). Additionally, tissue-engineered organotypics also lend themselves to co-culture development and the exploration of cell-to-cell interactions with the stroma playing an important part here, as it maintains populations of fibroblasts, macrophages, and endothelial cells (Hutmacher, 2000; Burdett et al., 2010).

More predictive organotypic models have the potential to decrease costs for drug development for both target validation as well as screening, and to reduce the use of animals in research (Hakanson et al., 2014). More representative and reproducible *in vitro* models will enable more reliable biomarker detection (Burdett et al., 2010). 3D tumour models also allow for improved pre-clinical drug candidate testing, as optimised 3D culture systems enable high-throughput imaging and screening of compounds using e.g. microarrays of the tumour cells within an organotypic co-culture environment (LaBarge et al., 2014; Roth and Singer, 2014).

Today, 3D culture models range from cancer spheroids to multiple cell line models used to mimic the tumour microenvironment (Nyga et al., 2011). In the head and neck region, 3D tumour models have previously been made for e.g. oral squamous cell carcinoma using collagen-based 3D cultures with cancer cells and fibroblasts(Che et al., 2006; Chaudhry et al., 2013), and tongue squamous cell carcinoma in another

collagen-based co-culture with fibroblasts (Nurmenniemi et al., 2009).

Tumour nutrients and oxygen

Due to the lack of vasculature in this type of tissue-engineered tumour construct, oxygen and nutrient supply is crucial. Especially oxygen availability is critical and it is often the first factor to become limiting (Liu et al., 2003). Without a blood supply, only simple nutrient and oxygen diffusion is possible; this can greatly affect the behaviour of the cells in the scaffold and is something which needs to be considered when modelling tissues and tumours *in vitro*. The limiting size for tissue-engineered constructs is around 200μm (Carmeliet and Jain, 2000; Liu et al., 2003). This is around the same maximum distance from capillaries that cells can be under physiological conditions (Radisic et al., 2006; Malda et al., 2008; Lovett et al., 2009). Despite this, physiological oxygen and cell numbers have been reported to exist in only the first 128μm of a tissue-engineered construct (Radisic et al., 2006).
Of course, this small distance does not only provide the cells with oxygen, but also with nutrients as well as a mechanism for removing waste products - a lack of any of these may cause an increase in dead or dying cells within the tissue-engineered constructs.

1.8 The extracellular matrix

Cells in tissues and tumours exist surrounded by a complex mixture of proteins and molecules which together form the extracellular matrix (ECM). In the following sections, the native compositions of ECM and bone tissue are considered in order to provide a background to the type of tissues the organotypic constructs developed during this study attempt to mimic. Subsequently, suitable scaffold materials for tissue engineering ameloblastoma models are discussed.

Normal ECM is made up insoluble hydrated macromolecules, consisting of different types of collagens (mainly types I and II, but also IV, XV and XVIII), non-collagenous glycoproteins (laminin and fibronectin), as well as sulphated glycosaminoglycans and soluble factors of different kinds (Lutolf and Hubbell, 2005; Hynes, 2009). In addition to these insoluble proteins, there are also soluble macromolecules, such as growth factors, chemokines and other signals, secreted by the cells within the matrix, as well as proteins on the surfaces of cells, which provide cues to the other cells within the ECM (Lutolf and Hubbell, 2005).
The main ECM molecules are conserved through evolution and are synthesised by fibroblasts, endothelial cells, pericytes and leukocytes (Hubbell, 2003). These different cell types and the varying quantities of ECM fibres they secrete lead to tissue-specific cellular microenvironments. Explanted ameloblastoma cells and cells from the AM-1 cell line have been shown to produce abundant ECM proteins in 2D culture (Harada et al., 1998).
The main function of the ECM is to anchor the cells in the tissue and provide them with their appropriate growth environment, structural support, nutrients and macromolecular cues about the tissue state and bio-

chemistry (Hubbell, 2003). Cues both from the ECM to the cell nucleus and the nucleus to the ECM maintain tissue integrity. Discrete domains in the ECM also act as a reservoirs for growth factors, which are released at appropriate times enabling patterning during development (Hynes, 2009).
Cell adhesion to ECM ligands is critical for mediation of signals for numerous physiological processes. This signalling is mostly carried out by integrins, which are transmembrane receptors that bind the cell cytoskeleton to the ECM. Matrix properties such as dimensionality and rigidity affect cell attachment, so the ECM also plays a role in tissue remodelling as well as cell invasion (Harjanto and Zaman, 2009).

It is increasingly recognised that the tumour stroma is an integral part of tumour development and growth processes (Pietras and Ostman, 2010). A variety of ECM components, such as collagen type I and proteoglycans, are present in tumour ECM at higher concentrations than in normal tissues, and the architecture of these proteins has been shown to change within tumours with disease severity and increased risk of metastasis (Martin and Boyd, 2008; Ulrich et al., 2010). This important role of the microenvironment in tumour development and progression can to a large extent be explained by domains within the ECM proteins, which act as growth factor receptor ligands, as well as the aforementioned reservoirs for growth factors released upon ECM breakdown (Hynes, 2009).
Increased stiffness of the substrate further induces greater tumour cell migration and invasion (Ulrich et al., 2010). In some cases, the stroma has been found to provide prognostic and response-predictive information, and novel treatment targets within the microenvironment of tumours have been identified (Pietras and Ostman, 2010).

1.9 Scaffolds for tissue engineering

Scaffolds used for organotypic tissue engineering need to mimic the cell-to-ECM interactions and support reciprocal, bi-directional signalling from both the cells to the ECM and the ECM to cells (Hubbell, 2003; Lutolf and Hubbell, 2005). 3D tumour models benefit from an as *in vivo*-like ECM composition as possible, and in practice one or two different matrix materials are often combined to produce organotypic models.

Biomaterials currently used for bone tissue engineering can be characterised in several groups: ceramics, such as strontium releasing bioactive glasses; hydroxyapatite (HA) mineral containing scaffolds; synthetic polymers; and natural polymers such as collagen type I sponges, porous foams, gelatin scaffolds and demineralised bone matrices (Koh and Atala, 2004; Place et al., 2009; Williams et al., 2010; O'Brien, 2011).
Various commercially available bone biomaterials have been developed in the last few decades, including osteoinductive materials such as composites of poly(lactic-coglycolic acid) (PLGA) and HA; hybrid synthetic and natural scaffolds, co-polymers (PLGA-PCL) and HA-collagen or HA-gelatin composites (Place et al., 2009; Amini et al., 2012).

For soft tissue engineering, synthetic polymer scaffolds, such as those discussed in section 1.10.2, and natural polymers such as collagen, fibrin, hyaluronan and agarose are used. These are modified in various ways, mostly at the point of synthesis, to suit the potential applications, by methods such as electrospinning (Bonzani et al., 2006); plastic compression (Brown et al., 2005); or used as hydrogels of various compositions (Brown and Phillips, 2007). Collagen scaffolds are discussed in more detail in section 1.10.3.

1.10 Bone biology

Bone ECM is a nanocomposite, made up of roughly 60% inorganic mineral, 30% organic material, and 10% water (Currey, 2002; Jayakumar and Di Silvio, 2010). Collagen makes up 85-90% of the protein in the non-mineralised, organic component. Most of the collagen found in the tissue is type I, but small amounts of collagen type IV are also present. Collagen inside bone is more cross-linked than in other tissues, contributing to the strong and inert structure (Jayakumar and Di Silvio, 2010). Large spaces within the structure allow for mineral deposition onto the collagen fibres, thus also reinforcing the structure (Currey, 2002).
The mineral is deposited in the form of hydroxyapatite (HA; $Ca_{10}(PO_4)_6(OH)_2$) crystals, which also forms the non-organic component (Stevens, 2008). HA crystals are small, 2-3nm thick plates, which precipitate onto the collagen fibres (Mistry and Mikos, 2005). Additionally, there are some non-collagenous matrix proteins present in the bone structure, such as proteoglycans and sialoproteins, which contribute to the signals in the bone environment, as well as water to contribute to its mechanical properties (Currey, 2002).
The mechanical properties of bone are one of its defining features, with the structure of the mineralised matrix important for its mechanical integrity. Because of the interaction of the rigid HA crystals providing compressive strength and the collagen fibres providing tensile properties, bone is tough and flexible, enabling it both to withstand a high degree of compression and to be resistant against fractures (Mistry and Mikos, 2005).

Macroscopically, cortical bone has a compressive stiffness of 12-20GPa, whereas cancellous bone has one of less than 1GPa (Froehlich et al., 2008). Importantly, bone is a directionally stiff material which enables it to function *in vivo*; the long axis of cortical bone has been measured to have a Young's modulus of 17GPa, but only 9.6GPa when measured in the transverse direction (Froehlich et al., 2008).

Two cell developmental lineages are responsible for the development and maintenance of bone: cells from the osteoblastic lineage include active osteoblasts, as well as osteocytes. Osteoblasts are well adapted to synthesise and secrete copious amounts of bone matrix, collagens, and cytoskeletal proteins in order to maintain bone tissue (Jayakumar and Di Silvio, 2010). Osteocytes are osteoblasts with a lower metabolic activity, and reside inside lacunae in bone (Gartland et al., 2012b). They make up 90% of the cells inside bone in a normal skeleton (Jayakumar and Di Silvio, 2010).
The second developmental lineage is a haematopoetic one, with osteoclasts originating from a macrophage-derived lineage. *In vivo*, the mineralised ECM is synthesised by osteoblasts, which produce most of the

organic components in the tissue. The function of osteoclasts is to resorb bone both during normal development and disease (Jayakumar and Di Silvio, 2010; Gartland et al., 2012b).

Bone turnover has been documented to vary in different anatomical locations, with a higher rate found in the jaws, specifically the mandible (Aghaloo et al., 2010). Maxillary and mandibular bones are made up of a thin layer of cortical bone around a centre of cancellous bone, and the higher turnover in these bones is thought to be caused by mastication (Aghaloo et al., 2010). Mastication can in this instance be thought of as a type of cyclic loading, which has the ability to increase bone turnover (Imamura et al., 1990).

Bone turnover regulation

The main molecular pathway involved in bone turnover regulation is the OPG / RANKL pathway, with RANKL implicated in all steps of the bone resorption process, as well as in osteoclasts avoiding apoptosis (Kearns et al., 2008). As seen in the schematic in fig. 1.6, OPG promotes the formation of new bone by activating osteoblasts and inhibiting osteoclast formation by inhibiting RANKL. OPG, which is secreted by osteoblasts, but also by other cell types, supresses bone resorption by binding its TNF domain to the RANKL molecule as seen in fig. 1.5 (Kearns et al., 2008). Furthermore, osteoblasts also express RANKL on their surfaces to facilitate osteoclastogenesis (Iakovou et al., 2015).

Conversely, the main function of RANKL is to activate osteoclasts for increased bone resorption and to inhibit the bone forming activity of osteoblasts. RANKL exhibits the dominant role in bone resorption (Kearns et al., 2008). RANKL induces osteoclast formation via the NFκB pathway, which induces transcription of genes involved in osteoclastogenesis, and after successful bone resorption, the osteoclasts apoptose (Kearns et al., 2008).

The entire process is a fine balance between bone synthesis and resorption, and is easily brought off balance, resulting in various diseases associated with increased bone resorption, such as osteoporosis.
In addition to inhibiting RANKL, OPG is also able to bind to TRAIL to inhibit apoptosis, which effectively blocks OPG-induced inhibition of osteoclastogenesis (Iakovou et al., 2015).

Bone turnover inhibition

Various therapeutic agents have been developed to control diseases caused by excessive bone synthesis or resorption. Bisphosphonates have been used clinically as osteoclast-mediated bone-resorption blockers for over 30 years to treat diseases such as osteoporosis (NICE, 2008). Bisphosphonates specifically act on geranylgeraniol in the mevalonate pathway, which is a metabolic pathway within eukaryotic cells (Keller and Fliesler, 1999; Schott et al., 2015). The bisphosphonate alendronate (ALN) prevents osteoclast activation through this pathway, altering osteoclast activation and function by acting on farnesyl pyrophosphatase (FPP)

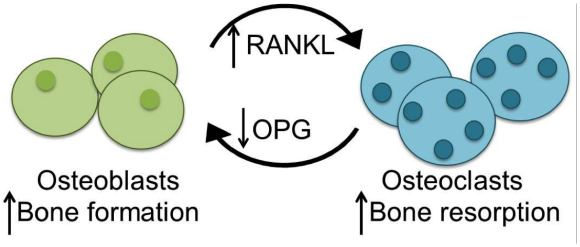

Figure 1.6: Interactions between OPG and RANKL in bone turnover. An increase in OPG results in a decrease in RANKL levels and an upregulation of bone synthesis, whereas an increase in RANKL results in a decrease in OPG levels and an upregulation of osteoclast activity leading to more bone resorption in both healthy and diseased tissues. Whereas osteoblasts and other cell types secrete RANKL to activate bone resorption, osteoclasts do not secrete OPG to activate bone synthesis, which leads to osteoclast activation being the preferred outcome of the bone turnover pathway. In diseased tissues, the mechanism is out of balance in favour of either OPG or RANKL.

in the mevalonate pathway, rather than through the OPG / RANKL pathway (Gertz et al., 1993; Keller and Fliesler, 1999; Fisher et al., 1999; NICE, 2008). FPP is required for normal cell function, and ALN may induce apoptosis of osteclasts by acting on this pathway (Fisher et al., 1999; Keller and Fliesler, 1999).

The clinical, systemic dosage of ALN is as a weekly 70mg preparation or as a daily 10mg tablet (NICE, 2008), with 50% of the dose being excreted within 72h after administration and with an estimated half life of the drug being 10 yrs (Gertz et al., 1993).

However, studies have also indicated that in addition to inhibiting osteoclast-mediated bone resorption, bisphosphonates are also able to inhibit osteoblast synthesis and therefore effectively preserve bone rather than repair it (Schott et al., 2015).

Other, more novel means of inhibiting turnover include the use of antibodies specific to actors of the RANKL pathway, such as the high-affinitiy anti-RANKL antibody denosumab (Kearns et al., 2008; Schott et al., 2015).

1.10.1 Bone-like tissue-engineered ameloblastoma models

As the majority of ameloblastoma tumours originate within the jaw bones, the major focus of this study was to construct a bone-like tissue-engineered scaffold, with which growth of the ameloblastoma tumour could be modelled *in vitro*. Bone-like tissue-engineered scaffolds aim to mimic the native properties of bone as described above. In this section, potential suitable scaffolds and other means to achieve *in vivo*-like bone mimetic constructs are briefly discussed.

Bone tissue engineering is a complex and dynamic process and several factors need to be considered (Sikavitsas et al., 2001; Bose et al., 2012). The basic requirements of a bone tissue-engineered construct are: 1) a biocompatible scaffold; 2) osteogenic cells which are able to mineralise the scaffold; 3) presence of morphogenic signals to direct cell phenotype and growth; 4) vasculature to support cells or growth factors to promote vascularisation (Vacanti et al., 1993; Amini et al., 2012). However, the lack of specific minimal requirements for a tissue-engineered bone construct has resulted in a wide variety of available scaffolds (Froehlich et al., 2008).

As cells respond to the stiffness of their substrate (Discher et al., 2005), the stiffness of the scaffold

used for bone-like scaffolds also needs to be considered. Cell proliferation is also greatly influenced by the stiffness of the substrate (Ghosh and Ingber, 2007). Ideally, the scaffold used should exhibit mechanical properties close to the native tissue. However, while bone is a mechanically stiff material, the scaffold used should not be the stiffest available, as this does not correspond to the natural properties of bone tissue, which also yields to some mechanical strains when required (Hutmacher, 2000; Froehlich et al., 2008).

Table 1.6: Stiffness measurements of various scaffolds used for bone tissue engineering and tissue culture plastic. Values for HA, titanium and tissue culture plastic from Bose et al. (2012); Bio-Oss in rabbits from Orr et al. (2001); compressed collagen from Hadjipanayi et al. (2009).

Bio-Oss (*in vivo* study in rabbits)	6.9 ± 1.4MPa
Compressed collagen scaffolds	1-2MPa
Hydroxyapatite scaffolds	35MPa
Porous titanium	24-463MPa
Tissue culture plastic	2.8GPa

Biomaterials with varying porosity used in bone augmentation have been measured for mechanical stiffness, and the some resulting values are detailed in table 1.6. It should be noted that these stiffness measurements have been obtained by various different experimental methods and are therefore not strictly comparable, but no consensus on how to measure the mechanical properties exists and often little data is provided by authors on the exact parameters used for mechanical testing. The compressive strengths of various biomaterials used in bone augmentation are commonly between 10-20MPa (Bose et al., 2012), whereas the elastic modulus of *in vivo* bone has been reported to be approximately 23.3GPa (Nomura et al., 2005). Additionally, bone tissue engineering commonly makes use of growth factors added to the cell-seeded scaffolds to aid differentiation and mineralisation of the scaffold (Froehlich et al., 2008). Both cell seeding density (higher densities allowing for earlier bone formation), as well as supplemented growth media (notably with dexamethasone), have been shown to improve scaffold mineralisation and bone synthesis *in vitro* (Holy et al., 2000).

As discussed in section 1.10, the ECM of bone is a nanocomposite, with 60% hydroxyapatite (HA) crystals and 30% collagen type I (Currey, 2002; Stevens et al., 2008). Additionally, non-collagenous matrix proteins contribute to the signals in the bone environment. Bone tissue-engineered scaffolds are typically porous and degradable, with the pores contributing to the micromechanical strength of the scaffolds (Bose et al., 2012). Pores within the structure allow for mineral deposition, thus also reinforcing the structure (Jayakumar and Di Silvio, 2010). A porous HA-gelatin nanocomposite has previously been found to be cytocompatible and to promote osteoblast growth (Kim et al., 2005). Of the two bone types found in the jaws, cortical bone is made up of a up to 30% porous outer layer, and cancellous bone is composed of up to 90% pores (Bose et al., 2012). Therefore, the ideal bone construct should mimic this composition.

1.10.2 Soft tissue-engineered ameloblastoma models

Since up to 19% of ameloblastoma tumours recur in soft tissue (Xavier et al., 2013), a soft tissue model of ameloblastoma would also be valuable to provide insight into the soft tissue-invading ameloblastoma pheno-

type. Both soft and hard tissue recurrences are destructive, but soft tissue invasion can also result in lesions in the skin, orbit or brain (Mendenhall et al., 2007; Xavier et al., 2013). This study therefore partly focussed on developing a suitable soft tissue scaffold for modelling ameloblastoma growth within soft tissues, and specifically, the gingival tissues, into which ameloblastoma often initially spreads to from its original location within the jaw bones. The gingivae are composed of a population fibroblasts, which synthesise an environment specific to the gingivae (Hasseil and Stanek, 1983).

Soft tissue engineering is in many ways less challenging than bone tissue engineering, and a variety of different scaffolds are commonly used to mimic different ECM compositions and tissues. Common scaffolds include FDA-approved polyesters of different kinds, such as polyglycolic acid (PGA), polylactic acid (PLA), and poly(lactic-co-glycolic acid) (PLGA) (Koh and Atala, 2004; Levenberg et al., 2005); and hydrogels, such as those made from fibrin (Linnes et al., 2007).

Here, a soft tissue model will be made by incorporating gingival fibroblasts (Mariotti and Cochran, 1990) into a compressed collagen scaffold to mimic the gingival environment.

This will allow for modelling of the invasion mechanisms of the tumour cells when incorporated, as well as examining any potential interactions the ameloblastoma cells may have directly with the fibroblasts. Importantly, the scaffolds used for both bone-like and soft tissue engineering should mimic the native ECM composition.

1.10.3 Collagen in tissue and tumour engineering

Collagen is widely used for tissue engineering purposes, mainly due to its availability and biocompatibility. This section discusses the use of collagen as a scaffold in tissue engineering. Collagen provides biological and structural integrity of various tissues including bone (Pedraza et al., 2010). As collagen type I is found in high amounts in native bone and soft tissues, it is an optimal scaffold material for tissue-engineered organotypic scaffolds (Hutmacher, 2000). Furthermore, it is also easily tailored to suit different approaches, sizes, collagen protein content, stiffness and co-cultures (Hutmacher, 2000). Biocompatibility of collagen hydrogels allow for reproduction of the conditions of a solid tumour (Szot et al., 2011). Collagen fibres contain a RGD peptide sequence, making it ideal for cell binding and facilitating immediate cellular growth (Hubbell, 2003; Szot et al., 2011).

Collagen scaffolds

Native protein scaffolds have been shown to have improved cell adhesion and growth properties compared to synthetic scaffolds (Villasante and Vunjak-Novakovic, 2015). Collagen type I is essential for bone tissue matrix formation, as the collagen fibres provide a framework for mineral crystal deposition within bone and are a source for mechanical strength within bone (Cen et al., 2008).

Collagen hydrogels, often used as tissue engineering scaffolds, are random meshes with abundant fluid. In 2005, Brown *et al* developed a compressed collagen scaffold, in which closely packed collagen fibres pro-

vided a mechanically improved environment to previously synthesised collagen matrices (Brown et al., 2005). When the collagen matrix is compressed to a form a more rigid structure, the distribution of proteins available for cell adhesion changes to a more tissue-like conformation (Chen et al., 2004). The plastic compression technique has been reported to rapidly remove up to 98% of the fluid from collagen gels, resulting in mechanically stronger and denser scaffolds when compared to hydrated collagen constructs, thus enabling the development of more *in vivo*-like scaffolds (Abou Neel et al., 2006; Bitar et al., 2007). Compression increases both the cell and collagen density in these gels, with densities up to 20% collagen achieved, an increase more *in vivo*-like than previous collagen matrices (Brown, 2013). Other authors have reported collagen densities of approximately 13% as a result of compression (Pedraza et al., 2010).
The instant plastic deformation of collagen has been shown to have an improved effect on cell mechanotransduction and the environment for cell growth for osteochondral tissue engineering (Brown et al., 2005; Bitar et al., 2008). Collagen networks are highly organised and dynamic, and these dense collagen scaffolds have been shown to be better at guiding cell differentiation and scaffold mineralisation than hydrogels are (Bitar et al., 2008; Buxton et al., 2008; Cen et al., 2008; Pedraza et al., 2010). Compression of the collagen scaffold results in a layered structure, which is an ideal lamellar bone mimic (Abou Neel et al., 2006).

Adhesion to collagen fibrils promotes cell survival and increases differentiated function (Fassett et al., 2006). Cells in collagen matrices are able to penetrate the matrix and remodel the fibrils, whereby the ECM molecules can be stretched and reorganised by cellular action (Rhee and Grinnell, 2007).
Collagen scaffold thickness, fibre density and cell seeding density all play a role in the levels of hypoxia experienced by the cells within the tumour engineered scaffolds (Szot et al., 2011).

Osteoblasts have previously been reported to mineralise collagen matrices *in vitro* (Rattner et al., 2000; Domaschke et al., 2006; Coyac et al., 2013). Mineralised bone-like structures have been demonstrated to form within two weeks of cell culture in a 3D environment with dexamethasone (Holy et al., 2000). Von Kossa staining showed mineralisation in another study on days 15 and 30, with the best mineralisation achieved by administering β-glycerophosphate as a single dose between days 0 and 3 of culture (Rattner et al., 2000). Previous work has also shown that cellularised collagen constructs mineralise within 28 days in collagen culture using osteogenic media with dexamethasone and β-glycerophosphate (Rattner et al., 2000; Pedraza et al., 2010).
Collagen fibrils in compressed collagen gels examined using scanning electron microscopy have previously been shown to appear randomly oriented with varying sizes and shapes of interfibrillar pores, with the compression process not resulting in a greater degree of fibril alignment within the scaffolds (Cheema et al., 2007; Pedraza et al., 2010). Furthermore, no change was observed in collagen morphology or network structure in compressed scaffolds incubated with either normal cell culture media or with osteogenic media (with dexamethasone) (Pedraza et al., 2010).

The addition of inorganic phosphates to the culture media is considered necessary as a source of inorganic phosphorus for scaffold mineralisation - 10nM phosphate corresponds to the *in vivo* plasma phosphate concentration and is therefore recommended for *in vitro* use (Rattner et al., 2000).

The benefits of using collagen

During this study, compressed collagen scaffolds were used to form the basis of both the bone-like and soft tissue organotypic models. Collagen was chosen as an ideal starting point for these models for several reasons:

- Collagen is the most abundant ECM protein *in vivo*, and is therefore both biocompatible and biodegradable.
- Collagen type I fibres are important in maintaining tissue structures, without which it is difficult to recapture an accurate *in vivo*-like environment using *in vitro* models (Nyga et al., 2011).
- Collagen is readily available, with a conserved structure between species, and a high degree of biologically functional groups (Hubbell, 2003; Kim et al., 2005).
- Cells within the collagen matrices, as with other ECM substitutes, experience cell-to-cell and cell-to-matrix interactions (Burdett et al., 2010), which is a great improvement on 2D tissue culture plastic.
- Cells within the collagen matrices are able to remodel the scaffolds (Cheema et al., 2003).

The biological, chemical and mechanical properties of collagen scaffolds can further be tailored to the specific tissues. Compression of the collagen scaffold results in physiologically relevant collagen density, with approximately 20% of collagen in compressed structures. The initial collagen protein concentration of the collagen used in this study was 2.01 mg/ml.
It should be noted that due to the collagen used in scaffold development originating from animals, some immunogenic concerns remain (Hubbell, 2003).

1.10.4 Decellularised bone substrates

In order to add more bone-like properties, commercially available, clinically used matrices will also be added to the collagen scaffold.
There are many commercial products which are used as scaffolds in bone tissue engineering (Place et al., 2009). Ideally, the addition of other matrix substrates provide the scaffolds with mineral without the cellular components. Therefore, a commercially available decellularised bovine bone-substitute, Bio-Oss®, was added to the bone-like scaffolds to provide the constructs with hydroxyapatite mineral, porosity and improved mechanical properties. Bio-Oss has been documented to have a porosity of approximately 70%, with a pore size of 200-900μm (Walsh et al., 2011). It is widely used in the dental clinic for e.g. repair of periodontal defects (Hartman et al., 2004), as well as for research into bone regeneration and bone-mimicking scaffolds

(Tapety et al., 2004; Liu et al., 2006; Dashti et al., 2010; Mastrangelo et al., 2013).

Bio-Oss is available as two construct types: Bio-Oss granules and Bio-Oss + collagen blocks. Bio-Oss granules are different sized granules of decellularised bone, whereas the blocks comprise 90% Bio-Oss granules with 10% of added collagen to shape the constructs as blocks. The collagen in the Bio-Oss + collagen blocks is porcine (Hartman et al., 2004). As with other decellularised bone materials, Bio-Oss has reduced osteoinductive properties due to the decellularisation and sterilisation processes used during manufacture (Amini et al., 2012). While the stiffness of Bio-Oss *in vivo* has been documented as approximately 7MPa (as seen in table 1.6), reliable mechanical studies on *in vitro* Bio-Oss have not been carried out.
As these products are mineralised and are widely used in the dental clinic, it was thought these scaffolds would provide a suitable starting point for the development of a bone-like scaffold in this study.

1.10.5 Matrigel extracellular basement membrane

Natural ECMs provide powerful means for controlling the biological performance of regenerative materials. Cell and tissue-derived ECMs retain their complexity *in vitro*, and as in natural matrices, growth factors interact with surrounding macromolecules, such as laminin, type IV collagen, chondroitin and heparan sulfate proteoglycans (Astashkina and Grainger, 2014).

The commercially available multi-component ECM product Matrigel® is a mixture of basement membrane proteins deposited by cultured murine Engelbreth-Holm-Swarm (EHS) cells (Kleinman and Martin, 2005). Proteins which engage in cell-matrix interactions are found in Matrigel to regulate migration, attachment and spread of cells (Nyga et al., 2011). These include laminin, collagen IV and entactin, which provide the cells within the matrix with a basement membrane-like environment (Kleinman and Martin, 2005; Hughes et al., 2010). The growth factor reduced (GFR) version has been specifically formulated to reduce the levels of growth factors, which may cause cells seeded in the matrix to change their behaviour (Hughes et al., 2010). The GFR version of the product is more purified and characterised than the original. The major components of the gel - laminin, collagen type IV and entactin - are conserved throughout the purification process. The manufacturers report levels of insulin-like growth factor (IGF) 3-fold reduced, platelet-derived growth factor (PDGF) 2.5-fold reduced, and TGF-β and heparan sulphate proteoglycan levels halved.
However, several hundred unique proteins and cell components including nuclear proteins have been found present even in the growth factor reduced version, indicating that these are also extracted from the mouse tumours when Matrigel is prepared (Hughes et al., 2010). This could also to some extent explain the large batch-to-batch variation found, especially with respect to growth factors. Indeed, the major disadvantage of Matrigel is the significant amount of batch-to-batch variation, both in protein composition and the subsequent cell behaviour (Astashkina and Grainger, 2014).
The mechanical properties of the scaffolds used in tissue engineering are important for correct cellular func-

tion. For reference, table 1.7 lists the mechanical properties of Matrigel compared to the gingivae. Collagen construct stiffness, as seen in table 1.6, has been measured to be up to 2MPa.

Table 1.7: Stiffness measurements of native gingivae, as well as Matrigel, which is often used for soft tissue engineering, compared to tissue culture plastic. Matrigel stiffness from Zaman et al. (2006), fibrin from Linnes et al. (2007), gingival mechnical properties from Goktas et al. (2011), TCP from Bose et al. (2012).

Gingivae	19.75 ± 6.20MPa
Fibrin scaffolds	185kPa
Matrigel	180Pa
Tissue culture plastic	2.8GPa

Matrigel provides the cells in the organotypic models with a basement membrane-like (BM) matrix. However, normal (growth factor-rich) Matrigel also provides various tumour-associated growth factors instead of only BM proteins such as laminin and collagens (Kleinman and Martin, 2005), which is why this study used the growth factor-reduced product. Any tumour-associated factors in the model should therefore originate from the ameloblastoma cell part of the soft tissue tumour constructs.

1.11 Cells for tissue engineering

Cell lines are often the first point of call when including cells in a model due to their ease of use, availability and quick and uniform growth. However, cell lines are altered both genotypically, often using viral vectors, and phenotypically, as they have been selected as the fittest to survive in a 2D environment (TCP) lacking most native environmental cues (Hakanson et al., 2014).

To date, there have been a handful of cell lines made from ameloblastoma tumours in order to aid research into ameloblastoma *in vitro*. The cell lines AM-1, AM-3 and AME-1 are discussed in more detail below. There is also an AM-2 cell line (Tao et al., 2009), however accessible data on this remains sparse. There have also been reports of cell lines created by researchers at Birmingham University Alabama (Dr Hope Amm, *personal communication*), however so far much research has not been carried out on these. It should be noted, that cell lines are made from a homogeneous cell population within the tumour cell population, and do therefore not contain the other cell types which may be present within the tumour environment, such as stromal fibroblasts. This renders the cell line population representative only up to a point.

Primary cells, which have not been genetically altered, selected for their ability to survive on tissue culture plastic, nor grown continuously for several generations, increase the predictivity of *in vitro* assays and models. The cell lines and primary cells used during this project and a selection of other available cells for further study are briefly described below.

AM-1

The ameloblastoma cell line AM-1 was established in 1998 as an aid for studying ameloblastoma development (Harada et al., 1998). These cells are from a mural, plexiform ameloblastoma of the mandible, which were immortalised by transfection of viral human papillomavirus HPV-16DNA (plasmid pMHPV16d, size

22.4kb) (Harada et al., 1998). The use of the HPV-16DNA viral vector may slightly change the behaviour and properties of these cells compared to those in a native ameloblastoma tumours of a similar subtype.

This cell line grows as islands in 2D culture and has a tendency to not grown in a monolayer. The cells from this cell line exhibit heterogenous morphologies with mainly small polygonal, cobblestone-like cells with some larger flattened cells and some spindle-shaped ones, with the numbers of the latter two increasing as the cells in culture age and develop. AM-1 cells resemble *in situ* ameloblastoma tumour cells both in their morphology and tendency to grow in clusters (Harada et al., 1998).

The AM-1 cells also produce abundant extracellular matrix factors and therefore stick to the culture dish. They have been reported to express vimentin and E-cadherin (Harada et al., 1998; Kibe et al., 2013). Several cytokeratins, anti-apoptosis factor BCL-2 and MMPs were also found expressed, with MMP-2 moderately elevated and MMP-9 highly expressed (Harada et al., 1998; Kibe et al., 2013). When in collagen-only 3D culture, AM-1 cells were shown to degrade the gel and form a depression on the surface (Harada et al., 1998).

This cell line was donated by Prof Harada (Iwate University, Japan) for use with this project.

AM-3

The HPV plasmid used to immortalise the AM-1 cell line may predispose to oral cancers, including ameloblastoma, and may affect the reliability of results obtained using AM-1 cells, and an alternative immortalisation method for ameloblastoma cells was sought (Kibe et al., 2013). The AM-3 cell line was established in 2013 using a lentiviral vector CSII-CMV-RfA with mutant CDK4, cyclin D1, a dominant negative form of p53 (p53C234) and human telomerase reverse transcriptase (hTERT) (Kibe et al., 2013).

This cell line can, according to the authors, be passaged for months without any apparent changes to the cell morphology (Kibe et al., 2013). MMP-2 and MMP-9 were found upregulated in these cells, and β-catenin expression was also increased, and the cells were reported to be able to induce osteoclastogenesis (Kibe et al., 2013). Efforts were made to obtain this cell line as a comparison to AM-1 during this project, however the cells did not survive the transit.

AME-1

A third report of an ameloblastoma cell line was published in 2014, when a group in Brazil made the AME-1 cell line. This cell line, from a mandibular SMA tumour, was transfected with E6/7 oncogenes from HPV-16 (as AM-1) with a pLXSN retroviral vector (Pinheiro da Rosa et al., 2014). Again, the choice of transfection factor used for this cell line may lead to artefacts when examining the ameloblastoma tumour using these, as the HPV-16 virus predisposes to oral cancers and can be a factor in ameloblastoma development. The ameloblastoma sample examined was immunoreactive for vimentin, α-smooth muscle actin (α-SMA) and epithelial cell markers CK-14 and -19. AME-1 cells also expressed MMP-2 and -9 as well as EGF. The expression of α-SMA and vimentin is not typical for the epithelial cells used for this cell line, and could be due to the HPV-16 transfection. The addition of EGF was found to increase the migration of AME-1 cells in

a 2D scratch assay and a migration assay (Pinheiro da Rosa et al., 2014).

Human gingival fibroblasts

Fibroblasts are non-vascular, non-epithelial and non-inflammatory cells of the connective tissues (Kalluri and Zeisberg, 2006; Xouri and Christian, 2010). The main function of fibroblasts is to maintain tissue homeostasis by synthesising collagen fibres, laminin and fibronectin for both the ECM and the basement membrane, and they therefore play crucial roles in many tissue functions (Mariotti and Cochran, 1990). Fibroblasts also secrete matrix metalloproteinases to remodel the ECM (Xouri and Christian, 2010).

In normal stroma, minimal numbers of fibroblasts are seen within a physiological ECM. However, in the reactive stroma of tumours, increased numbers of fibroblasts are seen, with enhanced capillary density, collagen I and fibrin deposition, all of which are thought to provide increased tumourigenic signals to the surrounding cells (Kalluri and Zeisberg, 2006). Fibroblasts in tumours have been shown to be a heterogeneous population, where different cells produce different levels of ECM molecules such as collagen, growth factors and cytokines, and stain for different markers e.g. vimentin, α-smooth muscle actin (α-SMA) and fibroblast surface protein (FSP) (Orimo and Weinberg, 2007). Within these fibroblast populations, senescent fibroblasts are also present (Orimo and Weinberg, 2007). Populations of activated fibroblasts, or myofibroblasts, have also been shown to play important roles in tumour progression, invasion and development (Orimo and Weinberg, 2007; Xouri and Christian, 2010).

Fibroblasts were used in this project for the soft tissue scaffolds and co-cultures. Cells from a gingival fibroblast (GF) cell line were used for soft tissue-like fibroblast-seeded collagen scaffolds. The choice of fibroblasts influences the type of soft tissue model, as fibroblasts from different sites appear different in both *in vivo* and in *in vitro* culture. The model developed in this project was therefore a gingival co-culture model. Distinct tissues give rise to fibroblasts with differing functions, e.g. periodontal ligament fibroblasts have been found to have higher levels of alkaline phosphatase, collagen and protein production than gingival fibroblasts (Mariotti and Cochran, 1990). GF cells are larger than periodontal ligament cells, and they synthesise collagen and non-collagenous proteins including glycosaminoglycans (Mariotti and Cochran, 1990). GF cultures have been shown to be 57% collagen and 42% fibronectin positive, although this content varied with cell cycle phase (Mariotti and Cochran, 1990).

The properties of fibroblast cells have been documented to change significantly during long term culture on tissue culture plastic (Mariotti and Cochran, 1990). The GF cells cultured during this project exhibited exponential growth for the first 4 days. In the GF cells used here, cell proliferation was noted to decrease after approximately a month of culture (8-10 passages), and a fresh culture of cells was therefore started at least every three weeks from original stocks. The cells used in the co-culture models developed here were in passage 4-6. This property of fast genetic and behavioural change, and eventually senescence may result in

slightly altered experimental results, however regular reseeding of stock cells from an earlier passage number minimised these changes and the resulting fibroblast population was uniform enough to produce significant results.

Human osteosarcoma cells (HOS)

The human osteosarcoma (HOS) cell line is a cancerous cell line of osteoblasts, which were used for initial synthesis of the bone-like models and experiments with AM-1 co-cultures. Advantages of using this cell line, although cancerous, include quick proliferation and doubling times in culture on tissue culture plastic. These cells exhibit a heterogenous, mostly osteoblastic morphology, with some fibroblast and epithelial-like cell morphologies present.
The HOS cells express osteoblastic genes and synthesise bone matrix proteins, although the oncogenic potential of these cells may affect some genes and pathways (Gartland et al., 2005).

Human osteoblast cells (HOB)

As an alternative bone cell, primary human osteoblasts (HOB) were also used. Primary osteoblasts have been extensively used in tissue-engineered scaffolds (Jayakumar and Di Silvio, 2010), and was used in this project for synthesis of the bone-like scaffolds for later co-culture experiments with AM-1 cells. This is a slow growing cell line on tissue culture plastic; the manufacturer states a cell doubling time of 19 hrs.
Morphology of these cells is cobble stone-like and uniformly osteoblastic. The cell morphology, behaviour and osteoblastic phenotype were guaranteed for 10 passages by the manufacturer; cells used in this project were between passages 6 and 8.

1.12 Therapeutic agents

Ameloblastoma researchers have only recently begun testing whether therapeutic agents may improve therapeutic outcomes or reduce the extent of surgery required for tumour removal. Although some publication bias may exist in not reporting negative trial data, the recent reports on anti-BRAF treatments for ameloblastoma may lead to future clinical trials (Kaye et al., 2015; Tan et al., 2016).

Some recent research into MMP inhibition in ameloblastoma tumours has utilised knowledge of tissue inhibitors of matrix metalloproteinases (TIMPs; (Kumamoto et al., 2003)). While using TIMPs to deactivate or limit ameloblastoma tissue invasion is an exciting therapeutic prospect, it also has its limitations. For example, TIMP-2 serves as an activator as well as a suppressor of MMP-2 and systemically administered TIMPs may even promote tumour formation, making it a difficult class of molecules to use for this purpose (Egeblad and Werb, 2002; Zhang et al., 2009a).

For this study, Doxycycline (Dox) was used as a potential therapeutic agent. Doxycycline is a clinically used tetracycline antibiotic, but when used at concentrations below antibiotic levels it is also a known inhibitor

of MMPs in tissues, by inhibiting the conversion of pro-MMPs to MMPs and blocking their enzymatic activity (Hanemaaijer et al., 1998; Shen et al., 2010; Stechmiller et al., 2010). It is clinically used to treat chronic wounds such as pressure ulcers, to inhibit inflammatory cytokines and MMPs, as well as in oral conditions such as periodontitis (as Periostat®) (Stechmiller et al., 2010). Dox has also been used in breast cancer treatment, where it was shown to be osteotropic and reduced metastatic tumours in bone (Foroodi et al., 2009). Dox has previously been applied to a model of oral squamous-cell carcinoma (OSCC), where a 10μg/ml of Dox concentration achieved a significant reduction in cell viability in 2D *in vitro* studies and a reduction in tumour size in *in vivo* mouse models (n = 10) (Shen et al., 2010).

Alendronate (ALN), as outlined in section 1.10, is clinically used for treatment of osteoporosis and other disorders involving bone turnover with associated high levels of bone resorption. The potential to use this clinically available agent to inhibit the growth of ameloblastoma cells within the organotypic co-culture models was also explored during this study.

1.13 Study hypothesis

The starting hypothesis behind the research undertaken during this project was that cellularised collagen-based scaffolds mineralise to provide a bone-like environment for the tumour model. Further hypotheses included:

Ameloblastoma cells can be added to create a reproducible *in vitro* model with viable cells exhibiting ameloblastoma-like behaviour.

By adding potential therapeutic agents to the *in vitro* models, ameloblastoma cell survival can be decreased using therapeutic agents.

1.14 Aims and objectives

The main aim of this project was to develop both a bone-like tissue model and a soft-tissue model into which cells from the odontogenic tumour ameloblastoma could be incorporated and analysed in an organotypic environment. Furthermore, by using these scaffolds, the aim was to develop suitable disease models to assess the progress of the tumour and any potential genes or biomarkers, which may be involved in ameloblastoma growth and invasion.

The following objectives were used to guide this study:

- Establish a bone-like construct *in vitro*, made with bone cells and plastic compressed collagen type I in order to mimic the native ameloblastoma growth environment.
- Characterise this scaffold to ensure appropriate bone-like properties are achieved.

- Determine the optimal method in which ameloblastoma cells could be incorporated into this bone-like model.
- Develop a soft tissue model using fibroblasts and a collagen-based scaffold for modelling what occurs to the ameloblastoma cells when they invade the soft tissues surrounding the jaw bone.
- Manufacture suitable ameloblastoma co-culture models *in vitro* using tissue engineering techniques by incorporating ameloblastoma cells from the AM-1 cell line into the scaffolds.
- Standardise the model assembly process so reproducible models can be manufactured enabling reliable, consistent studies.
- Analyse these two models for changes in gene expression over time, and where possible, also for differences between the models, which could be used to determine what makes the cells switch from bone-destroying cells to being invasive in soft tissue.
- Analyse cell invasion and cell-to-cell interactions present in the models.
- Inhibit growth and spread of AM-1 cells in the *in vitro* models by testing potential therapeutic compounds on them.
- Relate discoveries back to current knowledge of ameloblastoma tumours and ensure model is as *in vivo*-like as possible to better mimic the ameloblastoma tumour.

The first results chapter (chapter 3) describes the initial development of a bone-like tissue-engineered scaffold, and the analysis of this for its suitability for ameloblastoma co-culture. The second results chapter (chapter 4) then details the co-culture of the bone-like scaffold with ameloblastoma cells and the results obtained from these co-cultures.

The third results chapter (chapter 5) first describes the development of a soft tissue-mimicking collagen-based scaffold, which is then also used in co-culture with ameloblastoma cells. Finally, the fourth results chapter (chapter 6) concerns the application of potential therapeutic agents to both of these co-culture scaffolds and what effects application of Alendronate and Doxycycline had on the co-culture models. The last chapter (chapter 7) brings together the findings from this study and discusses them in the wider context of ameloblastoma research and tissue engineering.

Chapter 2

Materials and Methods

2.1 Mammalian cell culture

All cell culture and collagen gel manufacture was carried out in a class II laminar flow tissue culture cabinet observing standard sterile technique. All reagents were purchased sterile or sterile filtered through 2μm filters (Merck Millipore, Darmstadt, Germany) prior to use. All surfaces and cell culture instruments were wiped with 70% industrial methylated spirit (IMS) to ensure sterility. Instruments for gel manufacture were sterilised by autoclaving and immersing them in IMS prior to placing them in the flow hood. Cells and collagen gels were cultured in incubators at 37°C with 5% CO_2, 90% humidity and atmospheric oxygen.

2.1.1 Cell lines used for co-culture manufacture

Cells from the human osteosarcoma cell line HOS (ATCC in partnership with LGC Standards, Teddington, UK), human primary osteoblasts (HOB; NHOst-Osteoblasts, Lonza Walkersville Inc., MD, US), cells from a human gingival cell line (GF; ATCC; in partnership with LGC Standards, Teddington, UK), as well as cells from the AM-1 ameloblastoma cell line were used during this project. AM-1 were donated for this project by Prof Harada (Iwate University, Japan).

2.1.2 Culture media and supplements

Three different types of growth media were used for experiments carried out, depending on cell type as detailed below.

Normal growth media

Low glucose (1g/l) Dulbecco's Modified Eagle's Medium (DMEM; Life Technologies, Paisley, UK) was used for subculturing HOS, HOB and GF cells on tissue culture plastic and GF-cellularised three-dimensional collagen constructs before co-culture.

All media used contained L-glutamine, which is essential for cell energy production and protein and nucleic

acid synthesis. DMEM was supplemented with 10% fetal bovine serum (FBS; Life Technologies, Paisley, UK) and 100U/ml penicillin and 100μg/ml streptomycin (PAA, GE Healthcare, Buckinghamshire, UK) for both cell expansion and collagen construct incubation.

Osteogenic media

Mineralising or osteogenic media (OM) was used for inducing mineralisation in the HOS- and HOB- cellularised collagen constructs prior to co-culture. This was made up of low glucose DMEM (with 10% FBS and 100U/ml penicillin and 100μg/ml streptomycin as before) by adding stocks of 10M β-glycerophosphate, 0.1M ascorbate-2-phosphate and 1mM dexamethasone solutions (all from Sigma-Aldrich Company Ltd, Gillingham, UK), which had previously been made up in DMEM and stored at -20°C. All osteogenic stock solutions were passed through 0.22μm Millipore filters (Merck Millipore, Darmstadt, Germany) to ensure their sterility when adding them to the final media. The final concentrations in the media were: 10mM β-glycerophosphate, 50μM ascorbate-2-phosphate and 10nM dexamethasone.

These three additives promote mineralisation and osteoblast differentiation (Rattner et al., 2000). Dexamethasone has been shown to increase osteoblast proliferation, but other glucocorticoid family agents have been implicated in a reduction of bone formation and osteoblast proliferation (Kearns et al., 2008). Therefore, osteogenic media was only used on single-cell HOS and HOB cellularised collagen cultures, and the co-cultures were kept in AM-1 growth media, keratinocyte serum-free media.

The supplemented osteogenic media was stable at 4°C for approximately one week. For increased reagent stability, aliquots of osteogenic media were stored at -20°C and thawed at 4°C before use. The thawed aliquots were stored at 4°C and used within two days.

Keratinocyte serum-free media

Keratinocyte serum-free medium (KSFM; Life Technologies, Paisley, UK) was used to culture the AM-1 cell line (Harada et al., 1998). A vial of KSFM growth supplement (1ml) provided by the manufacturer was added to the media prior to use according to the manufacturer's instructions.

The media was supplemented with 100U/ml penicillin and 100μg/ml streptomycin (PAA, GE Healthcare, Buckinghamshire, UK). AM-1 cells were subcultured in KSFM for approximately 7 days until confluent. All co-cultures and single-cell type controls for these were also cultured in KSFM.

2.1.3 Cell passaging

HOS and GF cells were cultured on tissue culture plastic (TCP) in T75cm^2 or T150cm^2 flasks for 2-7 days until in a 80% monolayer, at which point they were passaged. AM-1 cells were cultured in T75cm^2 flasks for up to 7 days before passage. HOB cells were cultured in T75cm^2 flasks for two weeks before passage. Details for the passaging process for each cell line are shown in table 2.1.

For passaging of all cells, the cells were gently washed with pre-warmed Mg^{2+}- and Ca^{2+}-free phosphate

Table 2.1: Passaging details for the cell lines used in this project.

Cell type	Media	Trypsinisation time	Centrifugation speed, time	Time between passages
HOS	DMEM	2-3min	85x g, 5min	2-3 days
HOB	DMEM	5min	190x g, 10min	2 weeks
GF	DMEM	2-3min	85x g, 5min	5-7 days
AM-1	KSFM	3min + scraping	190x g, 10min	1 week

buffered saline (PBS; Life Technologies, Paisley, UK) to remove excess matrix proteins and serum; this time was increased to 5min for AM-1 as the cells secreted more matrix proteins. Cells were then detached using trypsin-EDTA (0.25% trypsin; Life Technologies, Paisley, UK) - 1ml for cells grown in T75cm^2 and 2ml for cells in T150cm^2 flasks - at 37°C (3min for HOS, HOB and AM-1 cells, 5min for GF cells). Trypsin digests linkages the cells use to attach to the flask or ECM with, while EDTA chelates Ca^{2+} needed for cell attachment; prolonged incubation times will make the cells unable to reform these linkages and therefore results in cell death.

HOS, HOB and GF cells were fully detached by gently tapping the side of the flask. A cell scraper (Corning, VWR International Ltd, Lutterworth, UK) was used to detach the rounded AM-1 cells from the flask, as the trypsin-EDTA was not sufficient for detaching all cells and the time taken for the cells to detach using chemical means would have resulted in extensive cell death; this combination of chemical and mechanical detachment provided the maximum amount of cell detachment with the minimal amount of damage caused to the cells.

Fresh DMEM was added in a ratio of 3:1 medium to trypsin volume; serum in the medium neutralises the digestive activity of trypsin. The cell suspension was then pipetted into 15ml tubes (TPP, Helena Biosciences, Gateshead, UK) and centrifuged as detailed in table 2.1. The supernatant was then discarded and the cell pellet resuspended in fresh growth medium (DMEM for HOS, HOB and GF; KSFM for AM-1) and transferred into new flasks.

Media was changed every 2-3 days in all flasks until the cells were passaged, frozen or seeded in collagen gels. Light microscopy was used to examine the cells in culture flasks to determine cell health and confluence.

2.1.4 Cell storage and retrieval

Freezing media for GF and HOS cells was made up of 90% normal growth media (including 10% FBS) and 10% dimethyl sulfoxide (DMSO; Sigma-Aldrich Company Ltd, Gillingham, UK). Freezing media for AM-1 and HOB cell lines was made up of 90% FBS and 10% DMSO. Sensitive cell lines, like AM-1 and HOB, have been shown to withstand cryopreservation better when frozen in abundant serum (Gartland et al., 2012b). Both of these were made up on the day of use and sterile filtered through a 2μm filter (Millipore, Molsheim, France).

All cell types were frozen in 1ml of respective freezing media. No more than 500,000 cells were frozen per aliquot. Cryovials (Starlab, Milton Keynes, UK) were first placed in -80°C for a gradual freezing process in

a Nalgene Mr Frosty freezing container (Thermo Fischer Scientific, Loughborough, UK) with the outer layer filled with isopropanol, and moved to liquid nitrogen storage after a minimum of 24 hours. This ensured a gradual, cell-friendly freezing process, where the rate of freezing was around 1°C per hour. The DMSO added to the freezing media prevents ice and crystal formation inside the cells, improving preservation and survival. Typical survival rates of around 80% viable cells were observed for all cell types.

Cell retrieval from liquid nitrogen was carried out by rapidly defrosting the cryovials in a 37°C water bath for a few minutes. The cell suspension was then gently pipetted into 10ml of pre-warmed cell growth media using Sterilin single-use transfer pipettes (VWR International Ltd, Lutterworth, UK). The resulting cell suspension was then added to fresh flasks, routinely with a 1:2 split.

2.1.5 Cell counting

Prior to using the cells for experiments, the cells were counted using a Scepter automated cell counting pipette (Merck Millipore KGaA, Darmstadt, Germany). In this pipette, the cells are counted by passing the cell suspension (or particles in suspension) through a channel in the counting pipette tip. The passing cells create a change in voltage in the channel and the pipette then arranges the cells by size.

For counting, the cell suspension was diluted 1:10 in 900μl PBS. A 60μm channel pipette tip, suitable for cells in the 6μm to 36μm range, was used for counting GF and HOS cells. A 40μm channel pipette tip, suitable for cells in the 3μm to 17μm range, was used to count HOB and AM-1 cells. The total cell number was obtained by multiplying the reading with the dilution factor (10) and the total volume of cell suspension. The Scepter cell counter also creates a histogram of the cells, which allows estimates of cell health. This is again based on approximations of cell volume and size; with cell volume changing in apoptosis (Kerr et al., 1972), resulting in a smaller size for dead or dying cells. Further narrowing down the field of counting based on the expected size of a specific cell type in suspension is also possible, e.g. to reduce the amount of cell or matrix debris present in the sample. A representative image of the resulting histogram and associated cell count can be found in appendix section B.

2.1.6 AM-1 tumour sphere synthesis

Tumour spheres are commonly used in tumour research and modelling. Spheres form a suitable organotypic environment for tumour cells to grow in with *in vivo*-like gradients of nutrients and oxygen from the surface towards the core (Deakin, 1975; Sutherland, 1988; De Wever et al., 2010; Hirschhaeuser et al., 2010). If cells do not have a surface (plate or substrate) to attach to, they will attach to each other and this will happen in a matter of days, as most cells require attachment to survive (De Wever et al., 2010). Therefore, synthesis of AM-1 spheres from cultured AM-1 cells was attempted. Multicellular spheres are commonly made using one of three methods: the hanging drop method, the low attachment plate method and the swirling flask method (Friedrich et al., 2009). The latter two were attempted for AM-1 sphere culture during this project.

Low attachment cell plates

Corning Ultra-Low Attachment (ULA) plates (Corning, Amsterdam, Netherlands) are made hydrophilic by a covalently bound hydrogel layer on the plates. They therefore prevent cell attachment by inhibiting non-specific immobilisation of proteins and biomolecules.
HOS cells, being cancerous, are known to form spheres (Rimann et al., 2014) and were used as a control. 6-well ULA plates were seeded with 20,000 HOS or AM-1 cells and 4ml media (DMEM for HOS, KSFM for AM-1) was added to the wells. All plates were incubated for up to 6 days, with HOS cell sphericalisation as a guide for incubation time. Media was partially removed and replaced with fresh media every 2-3 days. The cultures were examined using a light microscope every 24 hours.

Erlenmeyer flasks

Cells in suspension were counted and 100,000 AM-1 cells were used, with the aim of synthesising 100 spheres. 30ml of cell suspension in KSFM was placed in a 125ml sterile conical Erlenmeyer flask (BD Falcon, Bedford, MA, US). HOS cells were again used as a control due to their sphere-forming ability, and because of their larger size which enabled better visualisation under a light microscope. A sterile Spinbar magnetic stirrer (Bel-Art, Pequannock, NJ, US) was included per flask and the flasks were rotated at 70rpm for up to five days on a gyratory shaker set up inside an incubator. Every 24 hours, the cells were checked for sphere formation using a light microscope.
After incubation, the cell suspension was gently pipetted out of the flask to a sterile 50ml tube and the cells were left to sediment to the bottom of the tube for 30min - centrifuging the aggregates causes them to break up or to further aggregate, using only gravity allows for a gentle sedimentation. The supernatant was then removed without disturbing the cell pellet. Cell aggregation was then analysed using histology and light microscopy.

2.2 Organotypic three-dimensional models

Free-floating collagen scaffolds and models were used throughout the project for all experiments. Prior to analysis, the co-culture models were removed from the wells they were grown in to new culture plates, in order to minimise any effect of cells which had migrated from the collagen to the bottom of the well (and had thus been grown in a 2D environment on TCP).

A timeline for culture of the cells, collagen constructs and co-cultures is seen in fig. 2.1, detailing the culture of the organotypic scaffolds. Single-cell type cultures were cultured for 1-28 days as a standard and analysed during various time points during this organotypic culture. Co-culture constructs were assembled on day 14 of single-cell organotypic culture. In the case of co-culture models, day 0 refers to the day the two cell types were combined; both HOS and GF gels had by this point been in culture for 14 days. Co-culture

constructs were cultured for up to 14 days and analysed at regular intervals throughout this culture time.

Single-cell type cultures used as controls were analysed on the same day as their co-culture equivalents; a 'day 7' single cell control is therefore a day 14 + day 7 single-cell control.

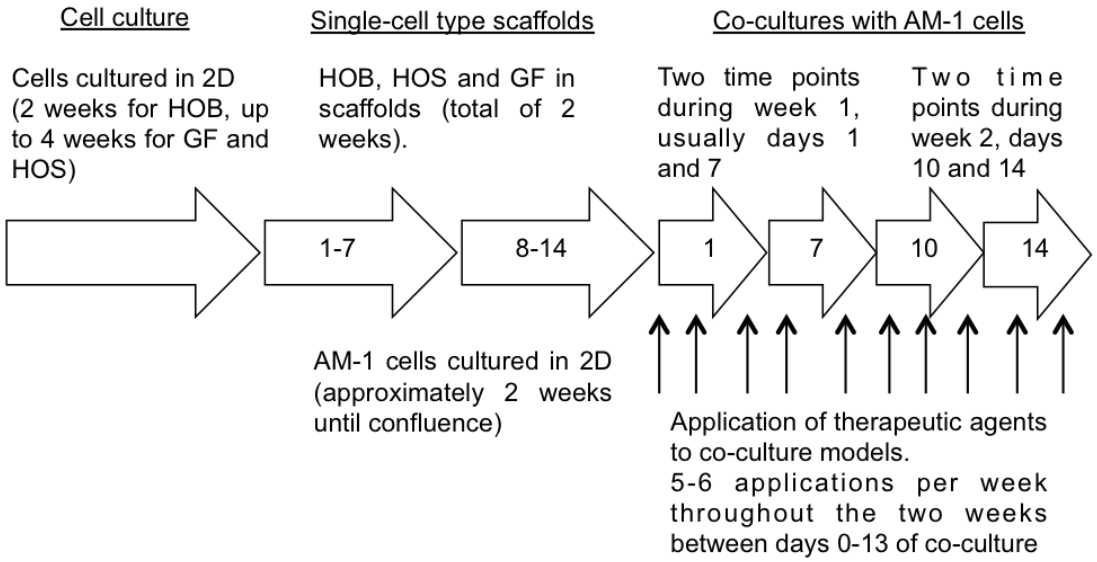

Figure 2.1: Schematic representation of co-culture timelines. The cells for the tissue-like models were initially cultured on tissue culture plastic in 2D before incorporation in the organotypic scaffolds. The organotypic scaffolds were cultured as single-cell type cultures for two weeks. During this time, AM-1 cells were cultured in flasks until confluence. Co-cultures were made on day 0 of AM-1 collagen scaffold culture and cultured for a total of two weeks. Both single-cell type controls and co-culture models were typically analysed on days 1, 7, 10 and 14 of co-culture. If therapeutic agents were applied, these were applied 5-6 times per co-culture week from day 0 of co-culture onwards.

2.2.1 Collagen type I gel manufacture

1M and 5M NaOH solutions for neutralising the collagen solution were made up from NaOH stock powder (Sigma-Aldrich Company Ltd, Gillingham, UK) and distilled water (dH_20). Both solutions were passed through a 2μm Millipore filter to ensure sterility before use.

Cellularised collagen type I gels were prepared observing sterile technique in a grade II laminar flow hood using 2.01mg/ml of 4°C rat-tail collagen (First Link, UK) and adding 10% v/v of 10X non-supplemented Minimum Essential Medium (MEM, Life Technologies, Paisley, UK) as a colourimetric indicator of pH (yellow at acidic pH, fig. 2.2A). Typically, 6ml of collagen solution was mixed with 600μl of MEM. A rise in pH and thereby gelling of the collagen, was achieved using 5M NaOH in 1 x 40μl aliquots and 6-8 x 40μl aliquots of 1M NaOH. This was visualised by a change in the solution colour, where the gel turned a magenta colour, which did not disappear when mixed (fig. 2.2B and C).

The appropriate volume of cell suspension to incorporate the desired number of cells was quickly pipetted and mixed with the gel before setting. Mixing in the cells before polymerisation bypasses initial steps in cell adhesion (and invasion / motility, i.e. where cells have to penetrate the matrix in order to adhere to it), as the

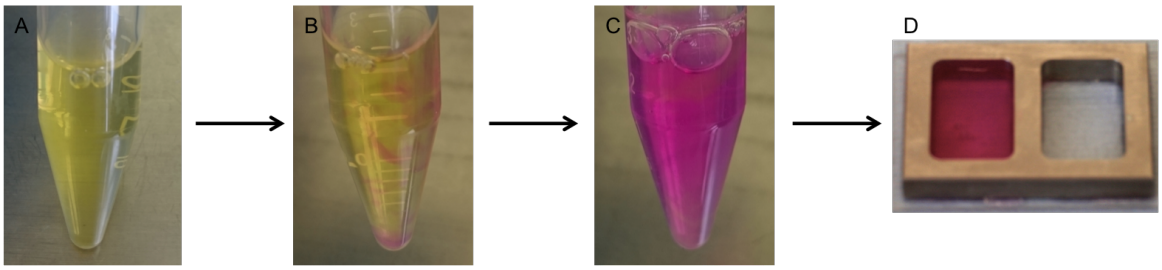

Figure 2.2: A) Collagen type I solution with 10% added 10X MEM as a colourimetric indicator (yellow at acidic pH). B) Addition of NaOH caused a gradual colour change to the collagen solution, and is ready for cell incorporation once a magenta colour at pH 7. C) The neutralised collagen solution was pipetted into a steel mould (D) for gelling for 20min.

cells are effectively trapped between the collagen fibres in the gel (Friedl and Brocker, 2000).

The mixture was then pipetted into sterilised moulds (2cm x 3cm, approximate volume 4ml) and incubated at room temperature (RT; 21°C) in the flow hood for 20min to crosslink the gel (fig. 2.2D). Plastic compression (Brown et al., 2005) was carried out as described below in section 2.2.2 and the resulting constructs were cut into 12-24 parts using a sterile scalpel (Swann-Morton, Fisher Scientific, Loughborough, UK).

Ideally, the same samples would have been analysed in longitudinal studies to minimise variation and better mimic an *in vivo* tumour in terms of growth and invasion. However, this was not possible for all analysis techniques used either due to necessary cell lysis, cytotoxicity or potential infections outside of the tissue culture environment. Therefore, cutting the gels in smaller parts enabled fast manufacture of a large amount of samples and minimised the use of reagents and experimental variation.

The constructs were then placed in tissue culture plate wells (TPP, Helena Biosciences, Gateshead, UK) and ensured to be free-floating. All gels were then incubated in culture media at 37°C, 5% CO_2 and 95% humidity for up to 14 days prior to analysis or co-culture manufacture. Media was changed every 1-3 days. The cells within the gels were inspected using a light microscope throughout the culture.

Cell numbers in organotypic scaffolds

300,000 HOS and HOB cells per ml collagen gel suspension were used for the bone-like gels and the AM-1 cellularised gels. These figures were based on previous, similar cellularised collagen gel studies (Bitar et al., 2008; Pedraza et al., 2010). Cells in the GF-cellularised constructs varied between 25,000 and 300,000 cells per ml collagen. 25,000 GF cells per ml collagen gel were used for the soft tissue co-culture models, based on collagen contraction experiments carried out in this project and described in section 2.2.5.

Addition of Bio-Oss granules to bone-like model

In order to improve the properties and mineralisation of the bone-mimicking constructs, commerically available Bio-Oss spongiosa granules (Geistlich Biomaterials, Manchester, UK) were added to the collagen scaffolds. Bio-Oss granules are made from bovine long bones, and were decellularised and sterilised by sintering by the manufacturer. The particle size varied, with a typical batch containing particles between 10-200μm in size (fig. 2.3). For a more uniform size distribution, the granule size could have been reduced further by

mechanical action, i.e. crushing, and subsequent sieving though e.g. a 70μm strainer. However, this was not done here.

Approximately 125μg of Bio-Oss granules was added per 3ml collagen gel. In the clinic, where Bio-Oss is used as a bone substitute, the manufacturers recommend mixing Bio-Oss with patient blood prior to implantation to the defect site. However, it was found to be difficult to mix the granules thoroughly with the cell suspension prior to setting the collagen. The Bio-Oss granules were therefore added to the top of the cellularised collagen mixture immediately once it had been placed in the moulds for setting. An approximately equal distribution of the granules throughout the gel area was achieved by mixing the granules into the collagen solution briefly with a pipette tip (without pipetting). Due to the difference in granule weight, some of the larger granules sank to the bottom of the construct during gel setting. However, as these were the approximate size (thickness) of the final compressed collagen gel, it was assumed that the distribution of granules throughout the collagen construct post-compression was equal.

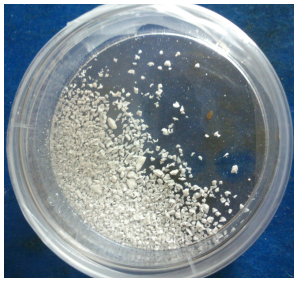

Figure 2.3: Bio-Oss granules, as seen here in a 34mm cell culture dish, were incorporated in the bone-like model collagen gels to add mineral into the scaffold and improve mechanical properties and overall structure. The granules varied in size, with the largest approximately 200μm in diameter.

Bio-Oss blocks as an alternative bone-like model

10% collagen and 90% Bio-Oss rectangular blocks (Geistlich Biomaterials, Manchester, UK) were used to test whether HOS cells would survive on these, produce more mineral, and thus provide a better alternative to the compressed collagen structures. Bio-Oss collagen blocks were cut in three, thus the initial size of the Bio-Oss Collagen blocks was 5 x 5 x 5mm (as calculated in ImageJ). The initial weight was approximately 100mg per block. The blocks were placed in the wells of a 24 well plate and 50,000 cells per block added to the surface of the blocks by pipetting a concentrated suspension of HOS cells in DMEM on the top of the block. The cells were left to attach for 30min. The process was repeated once with the block at a 90° angle. The blocks were then placed at 37°C for 30min in order to allow the cells to attach to the surface of the block and to avoid washing them off when media was added. Fresh osteogenic media was then gently added to cover the blocks and the blocks incubated at 37°C, 5% CO_2 and 95% humidity for up to two weeks.

Addition of Matrigel to soft tissue models

For the soft tissue constructs, the reconstituted basement matrix product Matrigel (BD Biosciences, Corning, Bedford, MA, US) was added to the collagen prior to setting. For these models, growth factor reduced (GFR) phenol red-free Matrigel was used, as Matrigel is extracted from Engelbreth-Holm-Swarm cells from sarcomas in mice and therefore contains numerous tumour-specific growth factors.

By using the GFR version, the effects of tumour-specific growth factors on the growth of the ameloblastoma tumour cells were therefore minimised whilst Matrigel still provided a selection of proteins (other than collagen) normally present in soft and connective tissues. Two production lots of Matrigel were used (no. 3270646 and no. 4160010) in order to minimise batch-to-batch variation. Upon receipt, Matrigel was aliquoted to 1ml aliquots and stored in -20°C to mimise freeze-thaw cycles. The aliquots to be used were placed to thaw at 4°C overnight prior to use.

Collagen gels were made and cellularised with gingival fibroblasts as above. 1ml of Matrigel was added per 2ml of collagen solution. This ratio was based on previous, similar oral organotypic tissue models (Chaudhry et al., 2013). Ice-cold Matrigel was added to the collagen immediately before pipetting into the mould to set, so that the volume of Matrigel added was one third of the total gel volume. The mixture was gently pipetted with pre-cooled pipette tips and left in the mould to set. GFR Matrigel gels above 10°C, so all work was carried out using chilled (4°C) pipette tips. The collagen gel mixture at this point was still below 10°C as it was quickly neutralised at RT with 4°C NaOH. The gels were then compressed.

2.2.2 Top-down plastic compression of collagen scaffolds

Top-down plastic compression was the main method for achieving compressed, organotypic collagen constructs during this project. This compression method was carried out with autoclaved and ethanol-wiped equipment as previously described with 0.12kPa compression for 5 minutes (Brown et al., 2005; Bitar et al., 2008). The set-up for the gel is visualised in fig. 2.4, which shows the gel placed between of layers of nylon and steel mesh on top of absorbent paper. The weight used is placed on top of the gel to compress it. All gels were then cut using a sterile scalpel and incubated at 37°C with a change of media (DMEM or OM) every three days. Constructs were cultured for up to 28 days.

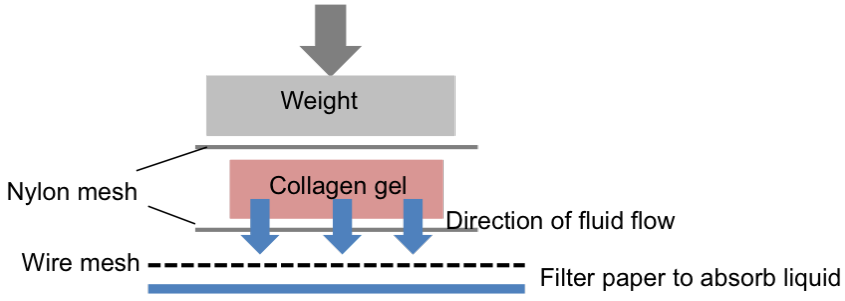

Figure 2.4: Compression set-up with the cellularised gel on top of filter paper and metal wire mesh. The collagen gel was sandwiched between two layers of nylon mesh. Liquid flow was towards the bottom of gel (and to the absorbent paper layer) when a weight was applied as indicated by the arrows.

2.2.3 Bottom-up plastic compression of collagen scaffolds

Bottom-up plastic compression was only used for the collagen contraction assays. In bottom-up plastic compression, plunger rolls are placed on top of the collagen gels in well plates to absorb the liquid from the collagen constructs. For this construct assembly technique, Whatman filter paper (4cm x 100m, GE Healthcare Life Sciences, Amersham, UK) was rolled up using a custom-made plunger-making machine seen in fig. 2.5A (lent for use during this project by D Thomas, EDI BTE and Institute of Orthopaedics, UCL) to make custom made plungers to remove the liquid within the collagen hydrogels. Similar compression kits are commercially available e.g. RAFT 3D Cell Culture Systems (Lonza, Cologne, Germany).

Approximately 80cm of Whatman filter paper was used for a roll to fit the well of a 24-well plate (fig. 2.5). Discs to fit the bottom of the plate (1.6cm in diameter) were also cut out to be placed at the bottom of the well in order to make the surface of the gel flat as the ends of the paper roll tended to undulate.

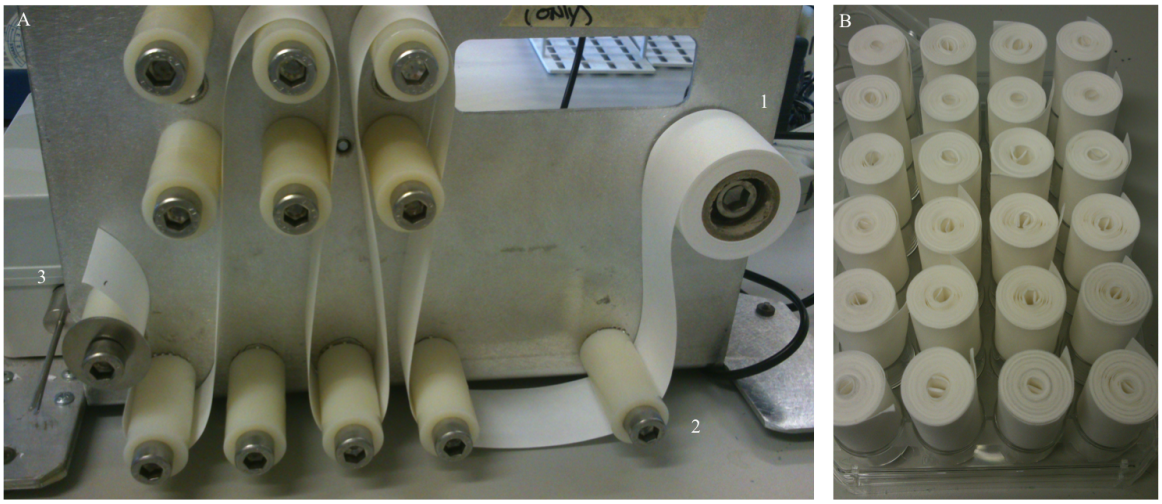

Figure 2.5: A) The custom-made machine to roll filter paper. 1, as indicated on the image, was the paper roll attachment point. A mark was made in the paper roll at point 2, and the plunger (start point attached to the rod at 3) was the correct size when this mark reached point 3. B) Filter paper plungers set up in a 24 well plate. Plungers were secured with autoclave tape and autoclaved to ensure sterility before compression.

Collagen gels were neutralised and GF cells were added to these as described in section 2.2.5. For compression, three discs of autoclaved filter paper were placed in the well on top of each collagen gel. On top of this, a sterilised filter paper plunger (fig. 2.5B) was placed to remove the liquid expelled during the compression process. A weight of 22g per gel (i.e. a total of 528g or 0.12kPa) was used to compress the gels for 5 minutes. The fluid flow in this type of compression is upward, as seen in fig. 2.6.

After compression, the weight was removed and the plungers and filter paper were gently removed and discarded. The gels were incubated for 14 days and used for a contraction assay as described in section 2.2.5.

2.2.4 Co-culture model manufacture

AM-1 cellularised gels were incorporated in co-culture models with either HOS, HOB or GF cellularised gels. The bone-like HOS and HOB constructs were incubated in osteogenic media for up to 14 days to pre-mineralise the constructs. GF gels were incubated for 14 days before AM-1 cell addition in DMEM.

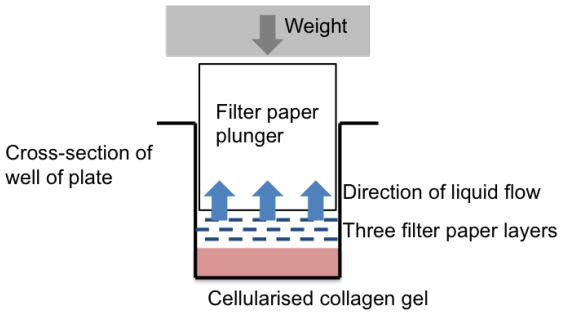

Figure 2.6: Set-up for compressing collagen gels using the 'bottom-up' method. Using this method, liquid flowed upwards from the collagen gel through the three filter paper layers into the paper plunger, when the filter paper plunger was placed in the well and a weight was applied.

Initial attempts

Initially, two methods were used to create co-cultures:

Firstly, an area in the middle of each bone-like pre-cellularised construct was removed to accommodate AM-1 cellularised gels. For this, Harris Uni-core 3 and 6mm biopsy punchers (Qiagen, Manchester, UK) were used. Collagen gels were cellularised with 300,000 AM-1 cells/ml collagen as before, and were cut small enough to fit the resulting hole in the pre-cellularised gels. The two gels were then combined by compressing the constructs again. The removed part of the pre-cellularised construct was discarded. The Uni-core instrument was sterilised by autoclaving between uses.

Secondly, AM-1 cell suspension was injected into collagen constructs. 0.7mm (22G) and 1.1mm (19G) thin-walled, hypodermic Microlance needles (Becton Dickinson, Oxford, UK) and 1ml Terumo syringes (Terumo Medical, Somerset, NJ, US) were used for this. 200,000 AM-1 cells in KSFM were drawn up in the syringe. This approximately 500μl suspension was then carefully injected in several places on 3ml acellular collagen gels.

Final co-culture assembly

The final co-culture assembly set-up as seen in the schematic in fig. 2.7 was as follows: 2ml acellular non-compressed support gels were made and set at RT immediately prior to co-culture manufacture. One 2ml acellular gel, when cut to smaller rectangles, provided support gels for 4-8 co-cultures, depending on the size of the co-culture gels. The AM-1 cellularised collagen type I gels were made as above, with 300,000 cells/ml and allowed to set at room temperature before cutting to the appropriate size using a sterile scalpel.

Pre-cellularised and pre-cultured bone-like or soft tissue collagen scaffolds were placed next to non-compressed, AM-1 cellularised collagen gels. The two gels were assembled as shown in fig. 2.7, where the lighter square is the pre-cellularised bone-like construct, and the other darker half of the rectangular co-culture construct is the AM-1 cellularised construct. The construct was then compressed again as before, with the acellular gel holding the two gels in place, acting as glue. Multiple constructs were assembled at once in order to reduce the time the cells were out of media and at room temperature (fig. 2.8), as well as to streamline the

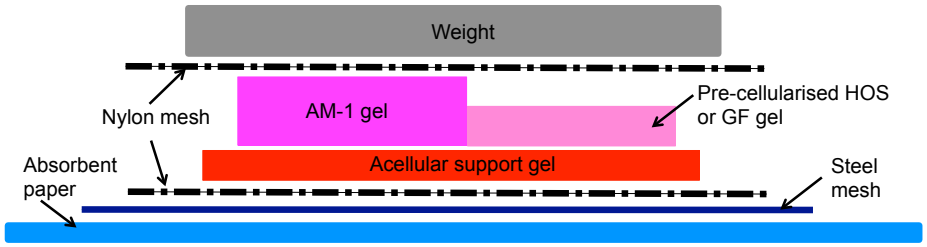

Figure 2.7: Co-culture model set-up, with the two different gels next to each other for top-down compression. The two constructs were placed on top of an acellular gel, which acted as a glue.

Figure 2.8: Multiple co-culture models were made at any one time to reduce variation between the organotypic models. Here, 12 co-cultures were assembled simultaneously. The long edge of one co-culture construct is 10mm. Non-compressed acellular gels were first placed on the nylon mesh. Then, the pre-cultured organotypic bone-like or soft tissue model was placed on top of this (here, the lighter-coloured part of the construct is the bone-like model with Bio-Oss granules). Then, the AM-1 cellularised gel was placed next to the first gel. The two gel parts were placed in close proximity to each other. The whole constructs were then compressed and cultured.

compression process and to minimise variation between co-culture models. The compressed co-cultures were gently moved to media-filled wells without separating the different components.

The co-culture gels were incubated in 1-3ml KSFM up to 14 days at 37°C, 5% CO_2 and 90% humidity prior to analysis.

Co-culture parts

For most analysis techniques, the constructs were cut in three parts: one for the AM-1 part of the construct, one from the middle between the two cell types and one for the organotypic construct with HOS, HOB or GF cells only. The area in the middle was denoted as “interface” (IF) in further analysis. This was done in order to compare cell growth, gene expression and protein levels in the different parts of the gels.

Imaging techniques followed the set up described in section 2.9.3, where two images of the interface, two from the opposite edges of the gels with least cell type mixing and one in the middle of each gel were taken. For single-cell type controls, three images were routinely taken, with two from the edges and one in the middle.

2.2.5 Collagen gel contraction in soft tissue models

Cells within constructs are known to exert forces on the collagen fibrils surrounding them, resulting in remodelling of the fibrils (Rajan et al., 2006). Cell motility and proliferation in the soft tissue scaffolds generated deformation as illustrated in the schematic in fig. 2.9B-C. In order to seed the maximum number of cells into the collagen gels while minimising contraction of the gels, contraction curves for a range of cell seeding densities were calculated.

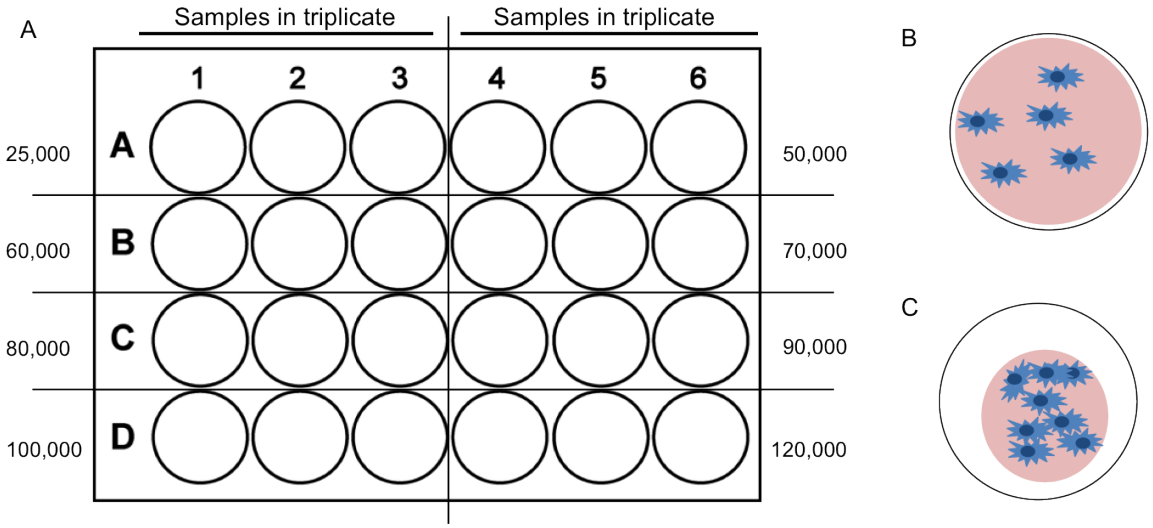

Figure 2.9: A) Plate set-up for the collagen contraction assay. Samples were set up in triplicate with different cell concentrations ranging from 25,000 to 120,000 cells per gel. The gels were top-compressed in the 24-well plate. Gels were then imaged macroscopically to determine the cell-induced collagen gel contraction taking place. B) Schematic of a cellularised gel as seen from the top of the well. A few cells (blue) are initially present. The gel has not yet contracted. C) Schematic of a cellularised gel which has contracted in the well. This is due to cellular action as well as cell proliferation within the gel, which increases the contraction effect.

GF cells were counted as before using the Scepter Cell Counter with 60μm channel tips and the appropriate volume of cell suspension to include in each gel was calculated. The final amounts of cells per 1 ml gel were as follows: 25,000, 50,000, 60,000, 70,000, 80,000, 90,000, 100,000 and 120,000.

Collagen gel was neutralised using 1M and 5M NaOH as before, with 1ml of collagen used per gel and the cell suspension included before pipetting into a 24-well plate. All cell densities were assayed in triplicate and collagen was therefore neutralised in batches. Due to having to neutralise several batches of collagen, the gels were left to polymerise at room temperature for between 20-30 minutes. Once all gels had polymerised, they were compressed using the 'bottom-up' method seen in fig. 2.6. The resulting compressed gels were detached from the walls and bottoms of the wells using a pipette tip to achieve free-floating cultures and incubated in 1ml normal DMEM. The media in the wells was changed every 1-2 days, as for other collagen gels.

In order to assay gel contraction over time, the gels were macroscopically imaged daily for 14 days (Sony Xperia P camera and iPhoto software). Photos were taken at a distance of 15cm from the bottom of the wells. The area of the gels for each time point was calculated using ImageJ (National Institutes of Health, Bethesda, US). The known diameter of the well (15.4mm) was used to set the scale on each image before measuring. A detailed description of the ImageJ processing can be found in appendix fig. 2.12. The variability of tracing

the outside of the gel on the images on different days resulted in some minor variability between the samples. Gels from day 0 were used to measure the starting area. The compression process resulted in some uneven or folded gels, which were difficult to flatten out due to the sticky nature of the collagen gels and were thought to reflect the "top-down" compression process and the variation resulting from the cutting used to make the models. The difference in area for each day was calculated as a percentage of the initial area and plotted in GraphPad Prism 6.

2.3 Mechanical testing of bone-like models

The mechnical properties of the bone-like scaffolds were tested in order to ascertain that these gels were an appropriate environment for bone formation. In order to test the stiffness of these constructs, dynamic mechanical analysis (DMA) was carried out using a Bose 3220 Series III dynamic tester with associated WinTest 7 DMA software (Bose Ltd, Carrickmacross, Co Monaghan, Ireland).
Cellularised bone-like collagen constructs with and without Bio-Oss granules, as well as acellular collagen-only and collagen + Bio-Oss constructs in PBS, DMEM and OM were tested.

In order for the software to correctly calculate the Elastic (Young's) modulus of a sample, the sample thickness was first measured by contact angle (CAM200 optical contact angle and Attension Theta software (KSV Instruments Ltd, Biolin Scientific, Stockholm, Sweden)), where the sample was placed onto the sample holder and viewed and imaged side-on using the software. A 0.16mm thick coverslip (VWR International, Lutterworth, UK) was used as a known constant for thickness. Sample thickness was measured in ImageJ using the "set scale", "line drawing" and "measure" tools. The thickness of the sample and the diameter of the sample (as measured using a ruler) were input in the WinTest software prior to DMA measurement; this enabled the software to accurately calculate the elastic modulus (E).

Distilled water was applied to around the sample, but not on top of it, once it had been placed in the sample plate shown in fig. 2.10. The hydrated environment was designed to stop the expulsion of liquid from within the collagen constructs and thereby a change in the sample properties and a change in the reading. The sample was placed on the instrument and the top part of the probe was brought into contact with the sample surface. The dynamic amplitude used was 3% of the total sample thickness, which equated to 0.012mm based on the average thickness of the measured samples. This amplitude was chosen as previous users had advocated an arbitrary amplitude of 6-12% of sample thickness, but this range was found during this study to cause stiffness measurements of the plate, not the sample.
DMA was performed at frequencies between 0.5-1 Hz. The value for samples stiffness (elastic modulus; E) was measured by the software from the slope of the linear part (the elastic region) of the stress-strain curve according to:

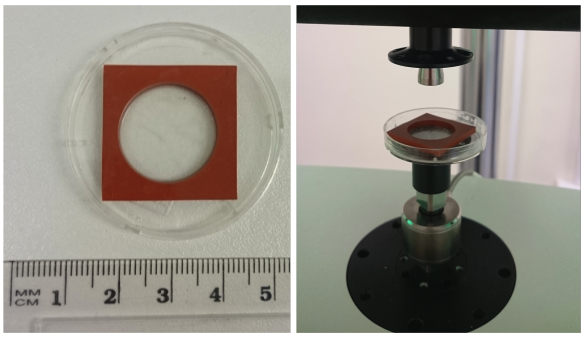

Figure 2.10: Image of the plate used for dynamic mechanical analysis. The sample (approximately 9mm across) was placed in the brown well inside the Petri dish. Distilled water was added around the sample to keep the sample hydrated. The plate was then placed on top of the DMA testing unit and the top probe was lowered until it was in contact with the sample.

$$E^* = \Delta\Sigma \div \Delta\varepsilon$$

i.e. the change in stress (Σ, grams of force) divided by the change in strain (ε, mm), which was automatically calculated by the WinTest 7 software. The output value (*E**, g/mm^2) was then converted to a stiffness measurement in MPa according to the following:

$$E^*(g/mm^2) \div 98.07 = E^*(N/mm^2)$$

$$1N/mm^2 = 1MPa$$

Where *E** is the stiffness value calculated by the WinTest 7 software (g/mm^2) and N/mm^2 is the unit for pressure. 98.07 is the value for gravity (9.807m/s^2). Figures were plotted in MS Excel and GraphPad Prism 6. Statistical significances were calculated using GraphPad Prism 6 as detailed below in section 2.11.

2.4 Cell survival in the co-culture scaffolds

Cell survival was assessed using two metabolic assays to give an indication of cell numbers within the collagen constructs. The Alamar Blue assay was used for cell monolayers and cellularised gels, and the Cell Titre Glo ATP assay was used on cellularised gels.

2.4.1 Alamar Blue cell viability assay

Alamar Blue is an assay used to determine the number of cells in culture based on their metabolic activity. Metabolical activity and cell growth in the sample results in a chemical reduction of the blue assay reagent, which then turns more red in colour. The reduced form of the reagent is also fluorescent. Conversely, in samples with little or no cell metabolic activity, the assay reagent remains blue in the absence of a reducing reaction. The major advantage of this assay is that it does not have major cytotoxic effects, and can therefore be used on the same cell population on subsequent assay times, reducing intra-sample variability as well

as sample production costs. The measurement of metabolic activity obtained is often used as a measure of proliferation as these two are correlated in some cell types. It should however be noted that cell metabolic activity can change independent of the proliferation status of the cells.

Cell metabolic activity was measured in the collagen gels throughout the incubation period. For standard curve construction, known quantities of cells (measured using the Specter Cell Counter) were incubated in triplicate overnight. For HOS and GF cells 0-500,000 cells per well and for HOB and AM-1 cells 0-100,000 cells per well were used. For the samples, Alamar Blue reagent (AbD Serotec, Kiddlington, UK) was incubated at 10% v/v of medium for 4 hours at 37°C, before transferring 200μl of each sample well to a black 96-well plate. The plate was read using a fluorescence spectrophotometer (BioTek Flx800, BioTek, Swindon UK) at absorbance wavelength 530nm and emission wavelength 590nm. Both standards and samples were measured in triplicate and normalised for background fluorescence using wells with 100μl media and Alamar Blue reagent only.

In between measurements, the reagent and media mixture was removed, the culture media was changed and the cellularised gels were incubated in 37°C. For the standard curve, the fluorescent reading was plotted against the known cell number. The resulting standard curves used to calculate the cell numbers in the samples can be found in appendix fig. B.3. The equation for the standard curve was then used to calculate the approximate number of cells present in the samples based on the fluorescent reading.

2.4.2 Cell Titre Glo ATP cell viability assay

Cellular ATP levels can be used to estimate the number and proliferation of cells in culture (Maehara et al., 1987). The Cell Titre Glo 3D assay (Promega Corporation, Madison, WI, US) was specifically developed by Promega for 3D cultures, and may therefore produce more reliable results from the models shown here than other assays due to improved reagent penetration. It is based on quantitation of the amount of ATP present in lysed cells in 3D microtissues. ATP is a marker of cell metabolic activity, but can be used to estimate the number of cells in a construct, as the amount of ATP directly correlates with the number of cells present (Crouch et al., 1993). The assay was performed in white, opaque 96-well plates in order to reduce signal cross-over.

The reagent, which is a homogeneous mixture, results in cell lysis and generates a “glow-type” luminescent signal as illustrated in fig. 2.11. This signal is proportional to the number of metabolically active cells in the culture.

For the standard curve, ATP powder (Sigma-Aldrich Company Ltd, Gillingham, UK) was first diluted to 10mM in sterile PBS and then to 10μM in OM and KSFM. The standard curve was constructed with 0, 0.625, 1.25, 2.5, 5 and 10μM ATP solution in duplicate, as well as a set of media blanks to discount for any background luminescence.

Cell standard curves for all cell types were constructed as those for Alamar Blue by incubating a known quan-

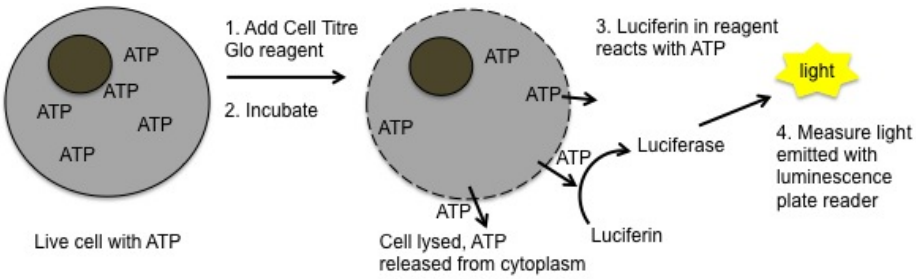

Figure 2.11: 1. The live cells in the 3D culture models were lysed when Cell Titre Glo reagent was added and (2) incubated for 30min at RT. The reagent caused ATP release from the cytoplasm. 3. Luciferin in the Cell Titre Glo 3D reagent reacted with the released ATP to produce luciferase. The luciferase reaction produced light (4), which was measured using a plate reader with luminescence reading capacity. Schematic adapted from manufacturer's protocol.

tity of cells (HOS and GF: 0-500,000; AM-1 and HOB: 0-100,000 cells per well in triplicate) on TCP plates, adding the Cell Titre Glo reagent to these and reading the luminescence emitted. Cell numbers in the samples were correspondingly calculated based on the standard curve equation obtained. Representative images of the standard curves produced can be found in appendix fig. B.4.

The co-culture and single-cell type samples were cultured as normal in either osteogenic media or KSFM for a variety of time points up to 28 days with the total sample number per condition per time point equalling three or six samples (n = 3 or 6). Co-culture samples were cut in three parts (AM-1, interface region, other cell type (HOS/HOB/GF)) and placed in the wells of the same opaque 96-well plate with 100μl media with the appropriate controls.

100μl of Cell Titre Glo reagent was added to all wells, upon which the wells turned various shades of yellow. The plate was placed on a Biometra WT I 6 plate shaker for 10min to ensure lysis of all cells in the samples. The samples were then incubated for a further 10-15min at RT to ensure reagent stabilisation.

After incubation, sample luminescence was read using a BioTek FLx800 plate reader and associated software. The values for background luminescence (0μM ATP) were subtracted from all the sample readings and standards and the standard curves were plotted. Cell numbers in the samples were calculated in MS Excel by using the equation obtained from the standard curve for the specific cell type and media used. The data was then entered into GraphPad Prism 6, where a histogram was plotted and statistical analysis was carried out.

2.5 Therapeutic compounds applied to co-culture models

Prior to application of the therapeutic agents tested here, their cytotoxicity was assayed in 2D on HOS and AM-1 cells (using alendronate) as well as GF and AM-1 cells (using doxycycline). These pilot tests were carried out over 72 hours in well plates and their main aim was to ensure the application of the therapeutic agent did not cause the non-AM cells to not survive in the models. The resulting histograms detailing cell viability in both HOS and AM-1 as well as GF and AM-1 cultures are visualised in the appendix.

Alendronate and doxycycline were then applied to the co-culture models to study their effect on the ameloblastoma tumours in the cultures.

2.5.1 Alendronate addition to bone-like models

Nitrogen-containing bisphosphonates such as alendronate (ALN) have been used for over 30 years to treat bone loss caused by excessive bone resorption in diseases such as osteoporosis (Fisher et al., 2013). As the ALN in this study was applied locally to the culture medium with direct contact with the cellularised scaffolds, and previous studies indicated osteoblast-favourable outcomes with reduced ALN amounts, greatly reduced concentrations were used.

Alendronate sodium trihydrate (Sigma-Aldrich Company Ltd, Gillingham, UK) was initially diluted to a 10mM stock solution in PBS and stored at -20°C until applied to the cultures. The concentrations tested on the co-culture models during this brief study were 10nM and 100nM. These values were based on previous research (10nM to 100μM (Alqhatani, 2014), 0.5-5μM (Schott et al., 2015) and others), as well as the brief cytotoxicity study carried out over 72 hours (appendix fig. B.11). In this case, HOS and AM-1 cells were cultured in a two-dimensional environment in a 24-well plate with cell culture media, and ALN was applied to the media of these wells at a range of 10nM-100μM. The Spectre Cell Counter was used to quantify live and dead cells based on the size distribution of the cells in the supernatant and cell suspension.

For addition to the co-culture models, 10nM and 100mM ALN in PBS was pipetted to 1ml of culture medium every 1-2 days (fig. 2.1) from the day of co-culture assembly (day 0).

The co-cultures were examined on days 7 and 14 after ALN application for cell survival using Live/Dead staining, and for cell proliferation using Cell Titre Glo several times throughout co-culture.

Additionally, in HOB + AM-1 co-cultures, ALN was also applied to 'established' tumour models. For this, co-cultures were maintained in culture for one week after assembly, and ALN was added every 1-2 days from day 7 of co-culture. Live/Dead staining was carried out on these models on days 3 and 7 of co-culture (d7 + 3 and d7 + 7), and cell viability was measured using Cell Titre Glo on days 1, 5, 10 and 14.

2.5.2 Doxycycline addition to soft tissue models

Based on the gene expression results for MMPs found in the GF + AM-1 co-culture models in this study, Doxycycline (Dox) was chosen as a potential therapeutic agent to inhibit AM growth in the soft tissue models.

Previous studies where Dox has been used for its anti-MMP properties in oral tumour research have included as treatment for oral squamous cell carcinoma (Shen et al., 2010). This and similar studies used concentrations ranging from 5-40μg/ml (Shen et al., 2010). Previous studies have found a 37% decrease in MMP-2 levels with 5μg/mL of doxycycline, a 80% decrease with 10μg/mL, and a 97% decrease with 20μg/mL (Liu et al., 2003). In patients, a standard dose of doxycycline (2-3 mg/kg/day) resulted in measured serum doxycycline levels of 2-6μg/mL (Liu et al., 2003).

A cytotoxicity study was carried out on GF and AM-1 cells with a range of concentrations prior to drug application to the 3D models to ensure that fibroblast cells were not affected by the concentrations used. This brief study was carried out on tissue culture plastic over 72hrs (appendix fig. B.12) with 5-40μg/ml of

Doxycycline hydrochloride (Sigma-Aldrich Company Ltd, Gillingham, UK) applied daily.

Based on the results from the cytotoxicity study (fig. B.12), 10μg/ml (21μM) and 20μg/ml (42μM) Dox was applied to the co-culture models every 1-2 days from day 0 of co-culture. Cell viability was measured using the Cell Titre Glo ATP assay at several time points throughout co-culture.

Additionally, Dox was applied to 'established' GF + AM-1 models which had been co-cultured for 7 days. For these, Dox was applied from day 7 and cell viability was measured using Cell Titre Glo on days 1, 4, 7 and 14. Immunocytochemical staining was also carried out on Dox treated models.

2.6 Histology on organotypic scaffolds

All histology was carried out on site at the Blizard Institute Core Pathology facility (Queen Mary University, London) and followed their standard operating procedures. All staining solutions (apart from silver nitrate, which was freshly made up) had previously been made up by the Blizard staff, or were commercially available. In preparation for histology staining, the samples were removed from culture medium, washed briefly in warm PBS and fixed in 10% formal saline for at least 24 hours at room temperature in order to crosslink the collagen gels, prior to processing.

All wax embedding, sample cutting and mounting on slides was carried out by trained staff at the Blizard Institute facility. All samples were dehydrated in alcohol, cleared in xylene and soaked in paraffin wax using an automated process. The samples were then embedded onto wax blocks, and oriented so that the specimens were 'on edge' to cut through the middle of the sample. Tissue sections of 3μm in thickness were cut from each sample using a rotary microtome.

The sections were then mounted on standard histology slides and dried at 60°C for a minimum of 30min. All sections were brought back to being compatible with the water-based stains by washing them first for 2x 3min in xylene, then 2x 3min in ethanol and finally for 5min in running tap water. Staining was then carried out as described in the sections below.

After staining, all histology slides were examined and imaged using a Leica light microscope and associated software (TS View 7, Tucsen Photonics, Fujian, China).

2.6.1 Haematoxylin and eosin

The haematoxylin and eosin (H&E) stain is used in histology to examine general tissue architecture. The haematoxylin dye is positively charged, and therefore reacts with negatively charged components within cells, such as nucleic acids. Conversely, eosin is a negatively charged dye and therefore reacts with positively charged parts of the cells, such as proteins in the cytoplasm. With this double stain, nuclei are coloured blue or black by haematoxylin and the cytoplasms of the cells are coloured pink by eosin. Collagen structures are also coloured light pink.

H&E staining of samples was carried out using a standard automated slide stainer (Varistain Gemini, Thermo

Fisher Scientific, Loughborough, UK). Cover slips were mounted on the slides with a xylene-based mountant using an automated process (Clearvue, Thermo Fisher Scientific, Loughborough, UK).

2.6.2 Assessing mineralisation of bone-like constructs: Von Kossa

The Von Kossa histological stain is based on the reaction between phosphate ions in the calcified tissue sections examined and silver nitrate in the stain (Meloan and Puchtler, 1985), when the tissue section is exposed to strong (ultra violet) light. A positive control in the form of calcified tissue (human trabercular bone, supplied by Blizard staff) was used for each staining procedure.

Sections were dewaxed in xylene for 2x 3min, 2x 3min in alcohol and rehydrated in distilled water. They were then placed in a Coplin jar with 0.5% aqueous silver nitrate (Merck Millipore KGaA, Darmstadt, Germany) and exposed to ultra violet light for one hour. This developed the calcified phosphate deposits, which stain dark brown or black. The sections were then washed thoroughly in distilled water and fixed in 5% sodium thiosulphate for 5min. They were then washed with tap water and the cell nuclei were counterstained with 1% Neutral Red for 10-15sec.

The sections were then blotted dry using several layers of filter paper, dehydrated in ethanol, cleared in xylene and mounted by hand using DPX glue before viewing and imaging under a light microscope.

2.7 Assessing mineralisation of bone-like constructs

2.7.1 Alkaline phosphatase activity assay

Alkaline phosphatase (ALP) levels in the bone-like samples were measured quantitatively using a commercially available ALP activity kit to indicate bone formation and osteoblast activity in the constructs. A Sensolyte pNPP alkaline phosphatase assay kit (AnaSpec Inc, Fremont, CA, US) was used for this. This particular assay was colourimetric.

For the ALP standard curve, 0ng/ml to 100ng/ml of the provided ALP standard solution was made up as a serial dilution in dilution buffer. 1X dilution buffer was made up by diluting the supplied 10X dilution buffer in dH_20. 20μl of Triton X-100 (Sigma-Aldrich, UK) was added to the 1X dilution buffer to make lysis buffer. Collagen gels were first minced with sterile scalpel blades to facilitate better digestion and 1ml of lysis buffer was then added to each sample. These were briefly shaken and centrifuged at 9,500x *g* for 15min at 4°C. 50μl of all samples and standards were then added in triplicate to a 96-well plate. 50μl of pNPP substrate was added to all wells, covered from light and incubated at room temperature for 45min. 50μl of stop solution was then added to each well.

Absorbance was read at 405nm using a Tecan M200 plate reader and Infinite 200 software (Tecan Infinite 200 PRO microplate reader (Tecan, Mannerdorf, Switzerland)).

The standard curve was plotted and the curve equation calculated in MS Excel, and the resulting ALP sample values were calculated in MS Excel and plotted in GraphPad Prism 6. The ALP activity was plotted as units

per litre (U/mL; the calculation is shown in the appendix), which is a standard unit for ALP activity. The definition of a unit (U) is the amount of enzyme required for hydrolysis of 1μM of pNPP substrate per minute at pH9.8 and 37°C. Native ALP in adults is between 20-140 U/L according to the manufacturer's protocol.

2.7.2 Alizarin Red

Alizarin Red S (AR) is a semi-quantitative stain for examining mineralisation in tissues and *in vitro* constructs. This was done in the bone-like cellularised collagen gels. 2% Alizarin Red staining solution was made up by dissolving 1g of AR powder (Sigma Aldrich Company Ltd, Gillingham, UK) in 45ml dH_20. The pH of the solution was adjusted from pH3.4 to 4.25 with 1M NaOH and the volume of the solution finalised to 50ml with dH_20. The made-up solution was stored covered from light.
For staining, samples were washed three times in PBS. 2% AR solution was added to cover each sample and incubated for 10min. The dye was then removed, samples washed 3 times with PBS and air-dried. The samples were turned over once during drying to aid this. Samples were then imaged macroscopically to assess mineral staining.

2.8 Quantification of gene expression in co-culture models

Quantitative real-time polymerase chain reaction (qRT-PCR) allows real-time detection of a gene of interest through the amplification of fluorescence in the target samples. Like other forms of PCR, the process is used to amplify DNA samples using the enzyme DNA polymerase. PCR amplifies DNA exponentially, doubling the number of molecules present with each amplification cycle, although in practice the amount of reagents available in the reaction limits the number of amplifications. The reaction is highly accurate in determining the starting template copy number (of copies of DNA).
First, the total RNA from test and control samples needed to be isolated. Then, the RNA was reverse transcribed to cDNA, which is used as the template for the PCR reactions. qRT-PCR was then performed on the target and reference genes for the controls and samples.

To reduce contamination, all RNA extraction, cDNA synthesis and PCR set-up steps were performed using sterile pipette tips with filters (Starlab, Milton Keynes, UK). All equipment and surfaces were cleaned prior to starting and RNAses removed with application of RNAse Zap spray (Life Technologies, Paisley, UK). In order to reduce pipetting errors and variability between samples, the same calibrated pipettes were used throughout.

2.8.1 RNA extraction and quantification

HOS samples for gene expression analysis were stabilised in RNAlater reagent (Qiagen GmBH, Hilden, Germany) at the desired time points. Reagent was applied dependent on the size of the sample; generally

500μl was used for single-cell gels and 700μl for larger co-culture gels. GF and HOB co-cultures were stabilised in Trizol reagent (Life Technologies, Paisley, UK) at the desired time points. 500μl Trizol reagent was used for all samples.

Co-culture RNA extraction: Fibrous tissue RNeasy extraction kit

RNA extraction for the HOS-only and HOS + AM-1 co-culture models and control samples was performed using a Fibrous Tissue RNeasy kit (Qiagen GmBH, Hilden, Germany) according to the manufacturer's protocol.

Ready-to-use lysis (RLT) buffer was made up by adding β-mercaptoethanol (Sigma-Aldrich Company Ltd, Gillingham, UK) at 10μl per ml buffer to the RLT buffer supplied in the kit prior to use. Four volumes of 96% ethanol (Sigma-Aldrich, UK) was also added to wash buffer RPE prior to use.

For RNA extraction, the samples stored in RNAlater reagent were removed to clean 1.5ml Eppendorf tubes (Fischer Scientific, Loughborough, UK) and 300μl of lysis buffer was added. The samples were homogenised by passing them through a 1ml pipette tip and vortexed, with these two steps repeated until the collagen gel had dissolved when examined by eye; this took approximately 10min. For most parts, the Bio-Oss particles in the samples did not dissolve completely using this method; however, as they are porous it was assumed that sufficient amounts of lysis buffer was passed through even the larger granules to lyse the cells and extract the nucleic acids.

Once samples were homogenised, 590μl nuclease-free water (Qiagen, Germany) and 10μl proteinase K solution (provided with the RNeasy kit) were added to further help digest the collagen fibres in the samples and samples were mixed thoroughly. Samples were then heated in a 55°C dry heating block (Grant BT3, Grant Instruments Ltd, Royston, UK) for 10min and centrifuged for 3min at 10,000x *g* using a table top microfuge (MSE Laboratory Equipment, London, UK). The resulting supernatant was transferred to a new Eppendorf tube without disturbing the pellet at the bottom (to avoid clogging the spin column later on). 450μl of 96% ethanol (Sigma-Aldrich, UK) was added to all tubes and mixed. 700μl of sample was then pipetted to a RNeasy spin column, centrifuged at 8000x *g* for 15sec, the flow-through was discarded and this step repeated with the remaining 650μl of sample. The samples were then washed once with 350μl RW1 buffer, centrifuged at 8000x *g* for 15sec, 80μl of DNase solution was added per sample and the samples were incubated at RT for 15min. The RW1 wash was then repeated, after which all samples were washed twice with 500μl buffer RPE by first centrifuging the samples with the buffer for 15sec and then for 2min at 8000x *g*. The RNA was then eluted from the spin column using a total of 50μl of RNase-free water and centrifuged for 1min at 8000x *g*. RNA content and purity was then measured as detailed below and the purified RNA stored at -80°C.

Co-culture RNA extraction: Trizol extraction

RNA extraction from the soft tissue and HOB + AM-1 models and controls was carried out using the Trizol extraction method. Trizol (Life Technologies, Paisley, UK) is a phenol and guanidine isothiocyanate solution,

which preserves the RNA in the samples, while disrupting the cellular structures during sample homogenisation. Single-cell type and co-culture samples of GF + AM-1 and HOB + AM-1 were placed in 500μl of room temperature Trizol reagent in 1.5ml RNAse-free Eppendorf tubes (Fischer Scientific, Loughborough, UK) and processed for total RNA extraction immediately or frozen in -20°C for storage. Samples, which had previously been stored in RNAlater reagent, were thawed and removed to a fresh Eppendorf tube with 500μl of Trizol reagent and processed.

Samples were homogenised in Trizol by pipetting them up and down using a 1ml RNAse-free filter tip (Starlab, Milton Keynes, UK) and vortexing briefly, repeating these steps until all collagen had dissolved when examining by eye. Phase separation was carried out by adding 100μl of chloroform (Sigma-Aldrich Company Ltd, Gillingham, UK) to the tubes, the samples were shaken vigorously by hand (15sec) and incubated at RT for 3min. They were then centrifuged in a pre-cooled centrifuge at 12000x *g* for 15min at 4°C. The aqueous phase of the separated samples, which contained the nuclei acids, was then carefully pipetted to a fresh Eppendorf tube. 250μl of isopropanol (Sigma-Aldrich Company Ltd, Gillingham, UK) was then added to the aqueous phase to precipitate the RNA, the tubes were briefly mixed and incubated at room temperature for 10min before centrifuging at 12000x *g* for 10min (4°C).

The resulting RNA pellet was then washed twice with 500μl of 75% ethanol (Sigma-Aldrich, UK) in DEPC-treated, nuclease-free water (Fischer Scientific, Loughborough, UK) and centrifuged at 7500x *g* for 5min (4°C). The additional wash step was found to result in a purer final RNA product. The RNA pellet was then air dried for up to 5min at room temperature and resuspended in 50μl of RNase-free water (Qiagen, Germany). All samples were then heated in a 55°C dry heating block for 10min to dissolve the RNA and the RNA concentration and purity was measured. The purified RNA was then stored at -80°C until used for gene expression experiments.

RNA quantification and quality measurements

The purity of the RNA product and any potential contamination caused by using either RNA extraction method was measured using a NanoQuant 16-well plate in a Tecan M200 colourimetric plate reader and associated iControl software (Tecan Infinite 200 PRO microplate reader (Tecan, Switzerland)). The NanoQuant plate was cleaned by immersion in a sonic waterbath (Elmasonic S10H, Elma Schmidbauer GmbH, Singen, Germany) at 40°C for 20min and further wiped with RNase Zap spray (Qiagen GmbH, Hilden, Germany). The NanoQuant plate was blanked using 2μl of RNase-free water. 2μl of RNA sample was added to each sample well and the plate was read.

Absorbance was read at 260nm/280nm, with 260nm as the absorbance wavelength for nucleic acids and 280nm for protein contamination. The ratio of absorbance calculated by the software provided a measure of RNA purity (i.e. protein contamination); a ratio between 1.9-2.1 indicate pure RNA which is ready for further processing. Values less than this range indicated impurities in the sample, particularly DNA and proteins, rendering this RNA impure and unusable. Readings of more than 2.5 indicate potential phenol carry-over or

ethanol carry-over from washing the samples. These contaminants may have an inhibitory effect of further downstream PCR amplification, and samples with values outwith this range were discarded.

Typical readings obtained using the Qiagen column extraction method were 1.9-2.1, and using the Trizol extraction method were 2.1-2.3. The lower purity yield in Trizol extracted samples may have been due to precipitation of small polysaccharide fragments in the aqueous phase of the extraction procedure. This, as well as entrapment of nucleic acids by larger polysaccharides (leading to accidentally discarding of some of the RNA during washing steps, contributing to lowered yields), are a well-documented problem with Trizol extraction (Wang and Stegeman, 2010). The silica membrane in the Qiagen RNeasy kits is thought to reduce this problem to an extent (Wang and Stegeman, 2010); indeed, more purified RNA was obtained using this method. Even though the Qiagen kit was shown to be more efficient at purifying the RNA, the Trizol kit was nevertheless more cost-effective for the large amount of samples processed during this project.

2.8.2 cDNA synthesis

The purified RNA was converted to single-stranded, complimentary DNA (cDNA) using Applied Biosystems High Capacity RNA-to-cDNA reverse transcription kits (Life Technologies, Paisley, UK). Sterile, filtered pipette tips were used as before for all reactions. In order to keep the pipetting errors to a minimum and minimise variation between cDNA and PCR processing lots, the same recently calibrated pipettes were used throughout.

Table 2.2: The components of the 2X Mastermix used to transcribe RNA to cDNA. RT buffer is the reverse transcriptase buffer and dNTP is a premixed deoxynucleotides solution required for cDNA synthesis. 10μl of Mastermix was then pipetted to tubes with 10μl of RNA to make a 1X RNA-Master mix solution.

Reagent	**Amount (μl)**
10x RT buffer	2
dNTP mix	0.8
Random primers	2
Reverse transcriptase enzyme	1
Nuclease-free water	4.2

Table 2.2 lists the reagents and amounts used in the 2X cDNA master mix. The master mix was made up as n+1, where n is the number of samples and the extra reaction mix allows for pipetting errors. The reaction mix was kept on ice until used.

In order to normalise RNA amounts, RNA was diluted in nuclease-free water (Life Technologies, Paisley, UK) and made up to 10μl reaction volumes in 500μl Eppendorf tubes. 100ng of purified RNA was used per PCR primer reaction, so at least 400ng of RNA was used for one cDNA reaction. For each 10μl of cDNA solution, 10μl of cDNA Mastermix (table 2.2) was added to the tube. The tubes were vortexed to mix and briefly centrifuged to collect the liquid at the bottom of the tube.

All reaction tubes were then placed in the slots of a 60-well tube holder in a programmable thermal cycler (PTC-100; MJ Research, Bio-Rad laboratories Ltd, Hemel Hempsted, UK). The outside wells were avoided in case of uneven temperatures. cDNA was synthesised according to the manufacturer's instructions using a

pre-programmed reverse transcription cycle, outlined in table 2.3.

Table 2.3: Reverse transcription (RNA-to-cDNA) reaction in PTC-100.

Time	**Degrees (°C)**	**Step description**
10 min	25	Reaction equilibrated
120 min	37	Reverse transcription
5 min	85	Enzyme degraded
Up to 99 h	4	Storage (if required)

At the end of the reverse transcription reaction, cDNA was cooled down and temporarily stored in the machine at 4°C (usually overnight, table 2.3) and removed to storage in -20°C if used within a few days, or -80°C for longer term storage, or used immediately for further gene expression analysis.

2.8.3 Quantitative real-time PCR gene expression analysis

The amount of mRNA present for the desired genes was quantified using quantitative real-time polymerase chain reaction (qRT-PCR) analysis. The qRT-PCR technique is based on a fluorescent signal emitted by the primer during the PCR cycle in a reaction with the cDNA synthesised during the previous step.

For qRT-PCR, Applied Biosystems Taqman-labelled gene specific PCR primers were used (Life Technologies, Paisley, UK). These are highly-sequence specific primers with a fluorescent FAM (fluorescein) reporter at the 5′ end and quencher at the 3′ end. When intact, the reporter fluorescence is quenched due to the proximity of the quencher. During annealing (at 55-60°C), the probe is hybridised to the target gene sequence and the reporter is cleaved off by exonuclease activity. As the reporter is no longer proximal to the quencher, a fluorescent signal is produced, which is proportional to the amount of product amplified. A ROX passive reference dye is used in all Taqman primers to normalise signal variation caused by e.g. pipetting errors.

GAPDH

The expression of the gene of interest is compared to the expression of an endogenous (internal) control gene in the samples. The expression levels of the endogenous control should remain constant in the all experimental samples throughout the time points. However, in practice this is difficult to achieve, and there is no single gene appropriate for this purpose (Vandesompele et al., 2002).

During this study, levels of glyceraldehyde-3-phosphate dehydrogenase (GAPDH) were used as an endogenous (internal) control for all samples, as this is a commonly used control for qRT-PCR experiments. Although this is a commonly used endogenous control gene, the levels of this may vary (Vandesompele et al., 2002). Ideally, several endogenous controls would have been used, however, GAPDH had been previously optimised to be used with the AM-1 cell line with the current experimental set-up (C. Raison, *unpublished data*).

Target genes were normalised to GAPDH levels automatically after the PCR run by the Applied Biosystems software.

Reaction efficiency

PCR assay optimisation can be evaluated using the equation of the linear regression line and Pearson's correlation coeffient (r), with evenly spaced amplification curves producing a linear standard curve. The linear standard curve is calculated as follows:

$$E = 10^{-1/slope}$$

where *E* is the amplification efficiency and *slope* is the standard curve y coefficient. For a 10-fold serial dilution, the C_t values should be separated by 3.32 cycles (i.e. a slope of -3.32, although values between -3.58 and -3.10 are within the accepted range). Therefore, the reaction efficiency is calculated as follows:

$$10^{-1/slope} = -3.32$$

The percentage efficiency of the reaction is then calculated as:

$$(E - 1) \times 100 = (\%)$$

$$(2 - 1) \times 100 = 100\%$$

Where a reaction efficiency (*E*) equalling 2 indicates a perfect doubling (i.e. 100%) of the PCR product on each cycle and therefore a 2-fold increase of copy number per cycle. The efficiency of all Taqman probes was verified by Applied Biosystems to be $100 \pm 10\%$, which is within the accepted efficiency range.

Calibrator samples

For final analysis of several separate plates within the same study, a calibrator sample to which all other samples are compared is required. Calibrator samples can be one of the control samples, a pool of all samples, or an altogether unrelated sample; the only condition is that all assayed genes must be expressed in the calibrator. Different experimental runs (and at different times or cohorts) should each have the same calibrator to enable comparisons later on.

PCR reaction set-up

For the qRT-PCR reactions, Taqman Gene Expression Master Mix (Life Technologies, Paisley, UK) was used. The 1X Master Mix protocol is detailed in table 2.4. The PCR Master Mix solutions were made up in separate 1.5ml Eppendorf tubes for each gene analysed as n+2, where n was the number of samples analysed. These were all kept on ice until needed.

The primers used for the genes of interest were as follows: alkaline phosphatase (ALP) and bone morphogenic protein-2 (BMP2) were used to probe mineralisation and osteoblast activity within the bone-like scaffolds. OPG, RANKL, TRAIL and NFκB were all used to assess bone turnover in the bone-like co-

Table 2.4: Table of Mastermix (MM) reagents used for qRT-PCR gene expression analysis. The reagents shown here make up a 20μl MM solution per sample well. These were multiplied by n+1, where n is the sample number, for each gene to be analysed to get the final amount added to the MM.

Reagent	**Amount (μl)**
20x Master Mix	12.5
Nuclease-free water	6.25
Primer	1.25

cultures. MMP-2 and MMP-9 was used to probe the levels of matrix metalloproteinase-2 and -9 in the scaffolds. PTCH1 and SMO are common mutations present in ameloblastoma tumours.

Taqman Gene Expression assay primers used in this study are shown in table 2.5. All gene expression assay primers were purchased from the range at Applied Biosystems, none were custom made for this study. Assay primers which are labelled '_m1' at the end of the primer name, span an exon-exon junction, which makes them specific for cDNA, ie. they should not detect genomic DNA contaminants. Freeze-thaw cycles were avoided by aliquoting the primers upon receipt. All primers were stored in the dark at -20°C to avoid degrading the fluorescent probe.

Table 2.5: Details of primers used for genes of interest during this study. The primer names, numbers, lot numbers and amplicon length are included for reference.

Primer	**Name**	**Lot number**	**Amplicon length**
GAPDH	Hs03929097_g1	P140716-004 E08	58
ALP (ALPL)	Hs01029144_m1	762138 G12, P140328-011 B09	79
BMP2	Hs00154192_m1	P140117-007 A01	60
MMP-2	Hs01548727_m1	1287510 G8	65
MMP-9	Hs00234579_m1	1361372 A12	54
NFκB1	Hs00765730_m1	1334081 D7	66
OPG (TNFRSF11B)	Hs00900358_m1	1310710 G6	74
PTCH1	Hs00181117_m1	P130816-004 A12	72
RANKL (TNFSF11)	Hs00243522_m1	1272548 C5, P140721-006 B02	67
SMO	Hs01090242_m1	1341910	54
TRAIL (TNFRSF1)	Hs00366278_m1	1346129 F6	62

A plate holder and MicroAmp optical 96-well reaction plates (Life Technologies, Paisley, UK) were pre-cooled on ice before reaction set-up. 5μl of each cDNA sample was added to the wells of the plate. cDNA from a pool of untreated, single-cell type samples from day 0 of culture was used as a calibrator sample. The same calibrator sample was used for all plates which would subsequently be used in one study. The calibrator sample ensured normalisation of the gene expression levels between plates.

Running controls used for each plate included: a well without cDNA to control for any contamination present in the reaction solutions, a well without primer to control for any genomic DNA contamination and a calibrator sample. All controls and samples were run in triplicate.

20μl of Master Mix solution was added to the primer-specific wells, so the total volume in all reaction wells was 25μl. The plate was covered with MicroAmp optical adhesive PCR-compatible film (Applied Biosystems) and briefly centrifuged to mix and collect all of the reagents at the bottom of the wells.

The qRT-PCR reactions were run on an Abi Prism 7300 RT PCR system with associated software and the run was set up according to the details in table 2.6. TaqMan PCR reagents include Uracil DNA glucosylase (UDG), which is an enzyme used to reduce DNA carry-over contamination in the samples, as it cleaves the uracil residues present in any contaminants leaving the target cDNA template unaffected. The first step in the PCR reaction is designed to activate this enzyme.

The optimised standard qRT-PCR run included 40 cycles of annealing and extension as detailed in table 2.6. Data acquisition was carried out in step 2 of stage 3. A representative image of an amplification plot can also be found in the appendix fig. B.1.

Table 2.6: Table detailing the thermal cycler profile used for qRT-PCR in this study. A total of 40 amplification cycles were used.

Stage	**Temperature**	**Time and repeats**	**Function**
Stage 1	50°C	2 minutes, 1 repeat	UDG activation
Stage 2	95°C	10 minutes, 2 repeats	Polymerase activation
Stage 3	95°C 60°C	15 seconds, then 1 minute, 40 repeats of each	Denaturing Annealing / Extension

To analyse the resulting qRT-PCR data, the following two parametres were defined on the software:

1) The threshold, which is the cycle number within the exponential part of the amplification curve at which fluorescence accumulation in samples becomes detectable. The intersection of the threshold line with the amplification plot is the C_t (threshold cycle) value. Small amounts of starting template lead to more amplification cycles needed for detectable, above background, levels of fluorescence.

2) The baseline, which is the value for background fluorescence before gene amplification starts; fluorescence is subtracted from the results when the baseline is set.

Once the qRT-PCR run was complete, the baseline and threshold values were manually adjusted for each gene.

For calculating changes in gene expression levels in the samples, changes in gene expression were expressed as the relative fold difference in expression (ddCt; Livak method). This is the ratio of the gene of interest, relative to the calibrator gene expression, and normalised to the endogenous gene levels between the two samples. This method is especially useful for small quantities of starting product. The ddCt method assumes that the assay efficiency for both target and reference genes was 100% ($\pm$ 5% of each other).

In order to calculate the ddCt value of the reaction, the target gene is first normalised to the reference gene for both test and calibrator samples:

$$\Delta C_{t(test)} = C_{t(target,test)} - C_{t(ref,test)}$$

$$\Delta C_{t(calibrator)} = C_{t(target,calibrator)} - C_{t(ref,calibrator)}$$

Then, the ΔC_t of the test sample is normalised to the ΔC_t of the calibrator

$$\Delta\Delta C_t = \Delta C_{t(test)} - \Delta C_{t(calibrator)}$$

Finally, the normalised expression ratio is calculated. C_t is on a log scale (base 2), so to find the linear fold change in expression between the sample and calibrator, the formula is:

$$2 - \Delta\Delta C_t = \text{normalised expression ratio}$$

The normalisation compensates for any differences in the starting amount of sample.
These values were automatically calculated by the Abi Prism software and were plotted using GraphPad Prism 6, and the significance levels were calculated as detailed in section 2.11.

2.9 Examining the co-culture models using microscopy

One of the benefits of using collagen as the main scaffold material is that it was possible to examine the scaffolds and the cells within it using microscopy techniques. This also enabled examination of the cells *in situ* and of any cell-to-cell interactions, as well as migration.

2.9.1 Transmission Electron Microscopy

In transmission electron microscopy (TEM), electrons pass through an approximately 100nm thick slice of the sample, resulting in an image of the specimen at very high magnification. After sample preparation and cutting, staining of the samples further increases the contrast between the different parts of the sample. This increased contrast is due to an increase in electron scattering due to the presence of the heavy metal ions (commonly lead or iron) in the stains used.
For sample preparation, 3% glutaraldehyde in 0.1M cacodylate buffer (Agar Scientific, Essex, UK) was used to fix the samples for at least 24 hours at 4°C. Samples were then processed by embedding them in resin as previously described by Richardson et al. (2009). Briefly, the samples were first dehydrated in a graded series of ethanol alcohols (15 minutes each in 20%, 50%, 70% and 90%) and then infiltrated with hard-grade acrylic LR white resin (London Resin Company, Reading, UK) as follows: 1:1 LR white:90% alcohol for 30min, pure LR white for 1 hour, overnight in LR white (at 4°C) and one further incubation in LR white for 30min the following day.

The samples were embedded in resin using 15μl of cold accelerator (London Resin Company, Reading, UK) for every 10ml of fresh LR white resin. The embedding was done in tin foil containers with cold reagents and containers, as the reaction was exothermic. Air was excluded from the top of the resin by placing Parafilm (Agar Scientific, Essex, UK) over the exposed surface; any resin in contact with air does not set. The samples were left to set at 4°C for a minimum of 24 hours before removal to room temperature for two hours before cutting.

The samples were cut out from the resin using an ultramicrotome (Ultra-cut 710710, Reichert-Jung). Approximately 85-90nm thick sections were cut from all samples using a diamond knife (Ultra-cut Diatome

45°, Reichert-Jung) and mounted on 3.05mm gold electron microscope grids (Agar Scientific, Essex, UK) and air dried. The grids were then briefly stained in uranyl acetate (5min) and washed twice in absolute alcohol (5min per wash), before viewing and imaging in the TEM at 80kV, with associated software (CM12 Transmission Electron Microscope, Philips, Eindhoven, The Netherlands).

2.9.2 Scanning Electron Microscopy

Scanning electron microscopy (SEM) is a surface scanning technique, where electrons are focused to a beam and used to scan the sample to produce an image. The samples are first dried and coated with an electrically conducting material to allow imaging, and are imaged in a vacuum. However, as the processing removes all water from the samples, cellular and three-dimensional structures are difficult to image.
In this project, SEM was carried out to examine the structure of the cellularised gels, and to assess cell movement in the vicinity of the Bio-Oss particles, cell infiltration into the pores of the particles, cell growth on the collagen gels and collagen degradation over culture time.

Samples were first cut so as to expose the desired area of examination, e.g. the centre of a collagen gel or the interface between two gels in a co-culture model, as the SEM only images the surface of a sample. They were then fixed in 3% glutaraldehyde in 0.1M cacodylate buffer (Agar Scientific, Essex, UK) at 4°C. Samples were first dried in a graded series of ethanol alcohols as for TEM (15min each in 20%, 50%, 70%, 90% ethanol and 3x 10min in absolute alcohol) and then immersed in hexamethyldisilazane (HMDS; Sigma-Aldrich Company Ltd, Gillingham, UK) for critical point drying. Samples were left to dry for at least an hour in the fume hood before mounting. Samples were mounted on 0.5cm SEM stubs (Agar Scientific, UK) using a thin layer of wood glue (Evo Stik, Bostik, Leicester, UK) for increased drying speed. All stubs were then sputtered-coated with a gold-palladium coating in a vacuum (Polaron E500, Quorum Technology, UK). Samples were viewed at a voltage of 5kV using a JEOL 5410LV SEM (JEOL UK, Welwyn Garden City, UK) and associated software.

2.9.3 Confocal Laser Scanning Microscopy

Confocal laser scanning microscopy (CLSM) enables fluorescent 3D visualisation of cells and proteins within samples. Samples were stained as detailed below and then moved to 6-well plates with approximately 4ml PBS per well for viewing under the CLSM using a 40X water objective. For viewing under a 10X objective, the samples were placed on microscope slides (VWR International, Lutterworth, UK), with a small amount of PBS surrounding the sample to prevent it from drying out during imaging. A Bio-Rad Radiance 2100 confocal microscope, fitted to an Olympus BX51 upright microscope and ProScan II X-Y stage (Olympus, Essex, UK), with associated Lasersharp 2000 software (Bio-Rad, Hemel Hempsted, UK), was used for imaging the fluorescently stained samples.
The lasers used were an Argon laser at wavelength 488nm producing a blue light and emitting green flu-

orescence and a Helium Neon (HeNe) laser at wavelength 543nm producing a green light and thus a red fluorescence.

Lambda scanning was used throughout for imaging the samples. This mode excites the samples separately by separating the fluorochromes and records the image slices obtained separately. This minimises the amount of bleed-through from the other wavelength in the samples and thus reduces artefacts. For imaging, three to five areas of the sample were selected in all samples for consistency as visualised in fig. 2.12.

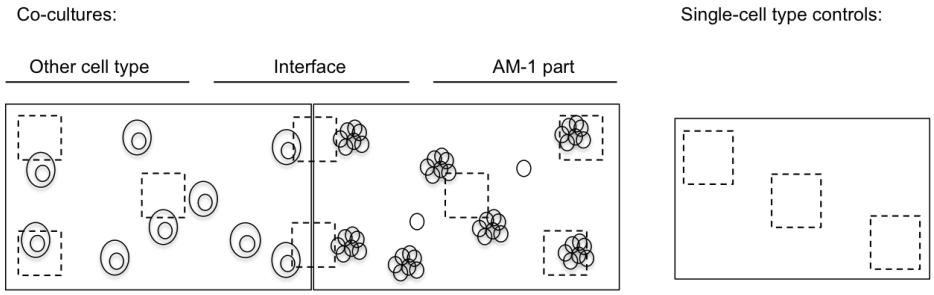

Figure 2.12: Schematic visualising the areas routinely imaged during fluorescent microscopy. Two areas on the co-culture construct interface were routinely imaged, as well as one in the middle of each co-culture part, and two on each separate construct edge. Three areas of the control constructs were also imaged.

2.9.4 Fluorescent microscopy

For the Cell Tracker assays (section 2.10.1) the samples were imaged using a DM IRB inverted fluorescent microscope (Leica Microsystems Ltd, Milton Keynes, UK) with associated software to localise the cells within the samples and identify the two populations. Cell Tracker-stained GF + AM-1 samples were imaged at 2h, 24h, 48h, 72h and 96h after co-culture production. HOB + AM-1 samples were imaged every 24h from 2h after seeding for up to 14 days.

Typical exposure times for the different filters when using the DM IRB were as follows: green channel - 462ms, blue channel - 50ms, light channel - 1-2ms.

2.9.5 Nuclear stains

Cell nuclei were stained with a selection of different stains depending on the different antibodies and other stains used at the same time and the wavelengths of these.

All staining for fluorescent microscopy was carried out in tin-foil wrapped plates in order to minimise photo-bleaching during stain incubation and sample washing.

DAPI

The DAPI (4',6-diamidino-2-phenylindole) stain emits blue light under UV light when bound to DNA. DAPI is a semi-impermeant stain, which associates with the minor groove of double-stranded DNA in mostly dead cells and, depending on the cell line, live cells (Dellinger and Geze, 2001). Due to the potential cytotoxic effects of the stain, it was not used with primary osteoblasts. On the other cell lines, it was used at a low

concentration due to its potential cytotoxic effects.
For staining of co-cultures, 180μM DAPI stock from a SelectFX Nuclear Labelling Kit (Invitrogen, Paisley, UK) was diluted in PBS. 300nM of DAPI stain in 1ml PBS per sample was incubated for 15 min at RT. DAPI staining was viewed using the UV filter on a DM IRB inverted 2D fluorescent wide-angle microscope (Leica Microsystems, Milton Keynes, Germany).

Sytox green

The Sytox green stain is a cell impermeant cyanine dye, which binds to nucleic acids in dead cells. This stain was used as a counterstain for some immunofluorescence (ICC) experiments. The Sytox green stain (from a SelectFX Nuclear Labelling Kit (Life Technologies, Paisley, UK)) was diluted in PBS. A final concentration of 250nM of solution was applied as a nuclear counterstain to methanol-fixed and permeabilised cells during immunostaining. The dye was incubated for the last 20min of secondary antibody staining and then washed three times with PBS prior to viewing the samples in the CLSM.

2.9.6 Live/Dead staining

Live/Dead staining, which allows live cells and dead or dying cells within tissues to be imaged simultaneously, was carried out using a 2μM calcein AM and 4μM Ethidium homodimer-1 (EthD-1) solution (both from Life Technologies, Paisley, UK). EthD-1 is a nuclear stain and fluoresces red at 555nm. The calcein AM stain stains the cytoplasms of live cells and fluoresces green at 488nm. Calcein AM can also stain the cytoplasms of dying cells, but the resulting stain is granular due to ongoing apoptosis in that cell.

The staining solution was made up in 10ml of sterile, 37°C PBS according to manufacturer's protocol and incubated with the samples on a Biometra WT I 6 shaker for 20-30min. After staining, the gels were washed once in PBS to rinse off excess stain and placed in PBS for imaging using confocal microscopy as detailed in section 2.9.3 or fluorescent microscopy as detailed in section 2.9.4.

The red EthD-1 stain was also used as a nuclear counterstain during immunocytochemical staining.

2.9.7 Immunocytochemistry

Immunocytochemistry (ICC) is a highly specific technique, which involves fluorescently labelling proteins and molecules within constructs with first a primary antibody to the desired protein (epitope) (Hayes et al., 2008). This primary antibody is then bound to a secondary antibody, which is linked to a fluorophore. The fluorescence emitted by the secondary antibody can be viewed under fluorescent microscopes, enabling viewing of both the presence or absence of the target protein, as well as the location of the target within the cell nucleus, cytoplasm or extracellular matrix.

In this project, the fibroblast and tumour-associated fibroblast markers fibroblast surface protein (FSP) and fibroblast activation protein (FAP) were used to label fibroblasts within the co-culture scaffolds. The bone cells within the constructs were labelled using osteopontin (OPN). AM-1 cells were labelled with ameloblastin (AMBN), as vimentin, which is sometimes used to label ameloblastoma cells in histological studies is also abundantly expressed by fibroblasts, and could therefore not reliably be used as a label to differentiate the two cell types from each other in co-culture. Matrix metalloproteinase-2 was labelled with an MMP-2 antibody.

All steps for both double and single ICC of the co-culture models were carried out on a plate shaker to ensure even mixing and thorough washing. First, media was removed from co-culture samples and the samples were fixed using ice-cold methanol (Fisher Scientific UK Ltd, Loughborough, UK) for 15min. Samples were then washed three times at 5min each with ice-cold PBS.

Cells in the samples were then made permeable using PBS with 0.25% Triton-X100 (PBST; 0.01M phosphate buffer, 0.0027M KCl, 0.14M NaCl both from Sigma-Aldrich Company Ltd, Gillingham, UK) for 10min. The methanol used for fixing causes some permeability, but this additional step ensured the scaffolds were fully permeable to the antibodies used.

Non-specific binding sites within the constructs were blocked using freshly made up 1% BSA in PBST (Sigma-Aldrich Company Ltd, Gillingham, UK) for 30min.

For single ICC, one primary antibody was diluted in PBST + BSA according to the dilution details in table 2.7. For double ICC, two primary antibodies were diluted according to table 2.7 and mixed in one tube of PBST. The antibodies used for double ICC were raised in different species to avoid cross-reactivity. All antibodies used for ICC detailed in table 2.7 were purchased from Abcam (Cambridge, UK).

Table 2.7: Details of primary antibodies used for immunofluorescence. The antigen column specifies the protein the antibody reacted with. The species column specifies the species the antibody was raised in, and therefore which secondary antibody bound to the primary antibody used. The clonality is specified in the mono/poly-clonal column; monoclonal antibodies are raised in a single animal and therefore have a very specific reactivity, whereas polyclonal antibodies are raised in several animals of the same species and provide a more sensitive but less specific reactivity. The dilution used for the immunofluorescence assays is specified in the dilutions column, and the final concentration of the antibody when diluted in PBST is specified in the final concentration column.

Antigen	**Species**	**Clonality**	**Epitope**	**Dilution**	**Final concentration**
AMBN	Rabbit	Polyclonal	IgG	1:500	2μg/ml
OPN	Mouse	Monoclonal	IgG2a	1:500	2μg/ml
MMP-2	Mouse	Monoclonal	IgG1	1:500	2μg/ml
FSP	Mouse	Monoclonal	IgM	1:200	1μg/ml
FAP	Rabbit	Polyclonal	IgG	1:200	5μg/ml

Each sample was incubated with 500μl of primary antibody solution for 1h on a plate shaker at RT. After incubation, samples were washed three times with PBS for 5min each. Control samples were stained simultaneously, with one or both of the primary antibodies omitted to ensure antibody specificity.

The species which the primary antibody was raised in dictated the secondary antibody species as detailed

in table 2.8. The following secondary antibodies were used for each primary antibody:

AMBN: goat anti-rabbit IgG AF555

OPN: goat anti-mouse IgG AF488

MMP2: goat anti-mouse IgG AF488

FSP: rabbit anti-mouse IgM AF488

FAP: goat anti-rabbit IgG AF555

For the single ICC stained samples, one secondary Alexa Fluor (AF) antibody was diluted in PBST and used for fluorescent staining. For single ICC staining, the secondary antibody was incubated for 40min at RT. Then, for AF488-stained samples, EthD-1 was added and for AF555-stained samples Sytox green was added to the staining solution in order to counterstain nuclei in the samples. Samples were incubated for an additional 20min with this double stain for a total secondary antibody incubation time of 1 hour.

Table 2.8: The secondary antibodies used for immunofluorescence studies during this project are detailed here. The columns detail the excitation / emission (ex/em) wavelengths of the two different Alexa Fluor antibody types, the species they were raised in, the species they react with, the dilution of antibody used for staining, as well as the final concentration of the secondary antibodies when diluted in PBST for staining.

Name	**Wavelength (ex/em), nm**	**Host species**	**Target species**	**Immunogen**	**Dilution**	**Final concentration**
Alexa Fluor 488	495/519	Rabbit	Anti-Mouse	IgM μ-chain	1:200	10μg/ml
Alexa Fluor 488	495/519	Goat	Anti-Mouse	IgG heavy chain	1:200	2mg/ml
Alexa Fluor 555	555/565	Goat	Anti-Rabbit	IgG	1:200	10μg/ml

For the double ICC experiments, two secondary AF antibodies were mixed together in PBST; again, the two secondary antibodies were raised in different species. Secondary antibody incubation for double ICC staining using both AF488 and AF555 was carried out for 1 hour at RT on a plate shaker to ensure even antibody penetration throughout the constructs.
All secondary antibody incubation was carried out in the dark in order to minimise photobleaching of the fluorochromes.

After secondary antibody staining, the samples were washed three times with PBS at 5min each. Targets stained with AF488 were visualised as green staining, and targets stained with AF555 were visualised as red staining under the confocal microscope. Composite images of the two channels were created in ImageJ software (National Institute of Health, USA) as detailed in section 2.11.

2.10 Monitoring cell invasion in the models

Cell Tracker dyes enable fluorescent staining and thereby visualisation of distinct cell populations within 3D scaffolds over long periods of time. In addition to the Cell Tracker assay, immunocytochemistry with confocal

microscopy was also used to assess cell interactions in the co-culture models.

2.10.1 Cell Tracker

The Cell Tracker assay was used for tracking cells in mixed populations in the collagen co-cultures. Two dyes were used in this project: CellTracker Green CMFDA (5-chloromethylfluorescein diacetate) and the red CellTracker CM-DiI (Chloromethylbenzamido-DiI) (both from Life Technologies, Paisley, UK). Both are fluorescent dyes which are retained by the cells for multiple generations and for over 72 hours, allowing for long-term imaging of cells in separate populations and tracking of cells within constructs. The dyes, which were added to the cells prior to incorporation in the collagen scaffolds, do not transfer to adjacent cells, only to daughter cells, with diminishing fluorescent signal. Therefore, faster dividing cells have a shorter window for successful staining.

By incorporating a larger number of cells into the collagen co-culture scaffolds when using Cell Tracker, and effectively making the gels confluent to start with, the division of the cells can be limited and the fluorescent signal maintained for longer. The basic process for labelling the two cell populations is shown in fig. 2.13 (image adapted from Iyer et al. (2009)).

Both Cell Tracker dyes were solubilised to a concentration of 10nM in sterile filtered DMSO (Sigma-Aldrich Company Ltd, Gillingham, UK) according to the manufacturer's protocol before use.

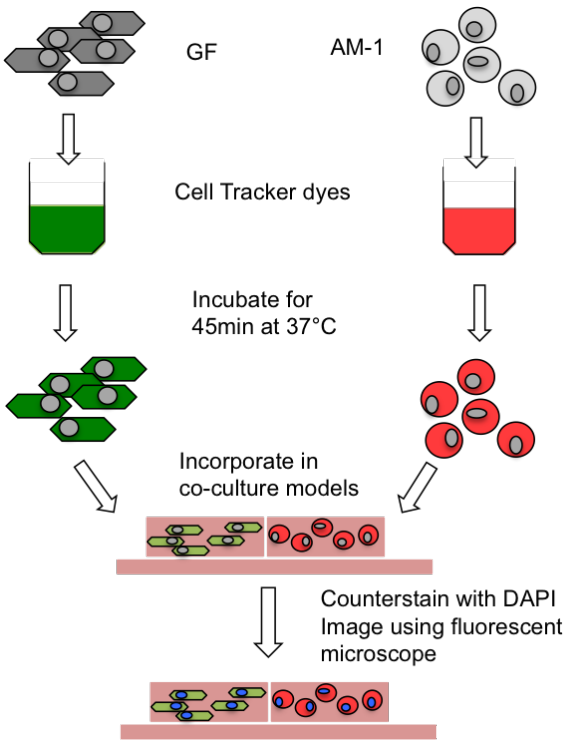

Figure 2.13: Schematic for Cell Tracker labelling of the 3D GF + AM-1 co-cultures for an invasion study. Note that only the cytoplasms are stained with Cell Tracker, enabling counterstaining of the nuclei. Parts of image adapted from (Iyer et al., 2009).

Cell Tracker Green

For GF + AM-1 co-cultures, GF cells were stained with the green Cell Tracker dye (CTG). GF cells in a 75cm^2 flask were washed once with PBS and 2mM of CTG (ex/em 492/517nm) in DMSO in 10ml KSFM was added per flask to stain the cells. The stain was incubated for 45min at 37°C. After incubation, the cells were washed, detached, counted and incorporated into collagen-Matrigel gels as normal. 300,000 cells/ml collagen were used. GF + AM-1 constructs were counterstained with DAPI 30min before imaging on day 0 as detailed in section 2.9.5.

For HOB + AM-1 co-cultures, the AM-1 cells were stained with the green stain, as this was found to be the more prominent stain and monitoring of AM-1 invasion was desired. 300,000 cells per ml of collagen gel were incorporated as before and made into co-cultures after the constructs had set. HOB + AM-1 co-cultures were incubated up to 14 days, as it was found that these slow dividing cell types in this co-culture retained the fluorescence for a longer time period.

Cell Tracker Red

For GF + AM-1 co-cultures, AM-1 cells were stained with Cell Tracker Red (CTR). The AM-1 cells were washed, detached and resuspended as normal in 2ml KSFM in a 15ml tube. A final concentration of 40μM CTR (ex/em 553/570) was then added to the cell suspension, and the cells were incubated for 45min in the suspension with occasional mixing at 37°C.

The suspension was then centrifuged to pellet the cells and to remove the CTR dye, washed once in fresh KSFM, counted and incorporated into collagen gels as normal. The standard protocol for GF co-culture compression was then followed to make 16 co-culture gels. 30min before imaging on day 0, GF + AM-1 constructs were counterstained with DAPI as above.

For HOB + AM-1 co-cultures, HOB cells were stained with the CTR stain as above, and collagen + Bio-Oss constructs were made as normal. 12 co-culture constructs were assembled immediately after the gels had set.

Quantification of invasion

Cell Tracker-labelled cell invasion was quantified using ImageJ using a zonal system - i.e. three zones to indicate the proportion of cells within the constructs which had at a given time point migrated to the zones. This methods enabled both a quantification of migrated cell number as well as a rough measure of how far the cells had travelled (and whether with time, more cells travelled further).

Initially, both the light micrograph and the fluorescent image were opened up next to each other, and the light micrograph (with the interface between the two constructs clearly visible) was used to label the interface area in the fluorescent image. The interface was indicated with a line. Then, two lines were used at an (arbitrary) 1cm distance away from the interface line to denote the borders between zones 1-2 and 2-3, so that the distance between lines 2 and 3 was also 1cm. A 1cm zone size was used for all 1024 x 1024 pixel images. Then, the cells in each zone were counted using the ImageJ 'Cell Counter' plug-in. Only AM-1

cells (green in the HOB + AM-1 Cell Tracker study) were counted, and only distinct cells were counted, i.e. only those which were in focus within the constructs when using this microscope. This latter limitation may have lead to some discrepancies in the numbers as cells move in 3D space within the constructs as opposed to the 2D cross-section, where the depth through the constructs most probably varied between time points. The resulting numbers were plotted as a percentage of total cell number seen in the image in order to normalise for any variation in the area of scaffold viewed as well as any variation in cell proliferation. Plotting and statistical analysis were carried out using GraphPad Prism.

2.11 Computing and statistical analysis

All assays were performed in at least triplicate sets of samples for each time point and condition, sample numbers for each assay are given with the relevant results. Data were compared with baseline values where possible; this was either a day 0 value or a corresponding untreated sample from the same time point. Raw data handling was carried out in Microsoft Excel 2011 (Microsoft Redmond, WA, US). Scale bars were placed on images using the 'set scale' and 'add scale bar' functions in Image J64 (National Institutes of Health, Bethesda, US). Collagen construct area calculations, and Bio-Oss measurements were carried out in ImageJ64 as detailed in the appendix.

The two different channels for confocal microscopy images were merged in ImageJ64 using the 'merge channels' tools. Z-stacks and 3D image stacks were also created in ImageJ64. Fluorescent microscopy images (from the Leica DM IRB) were false coloured in ImageJ64 using the 'image', 'colors' and 'channels tool' functions and merged with the other channels to produce multicoloured images. Other microscopy and macroscopic images were edited using 'iPhoto' and 'Photos' software (Apple Inc, Cupertino, CA, US). Graphs were plotted and statistical analysis was carried out with GraphPad Prism 6 (GraphPad Software Inc. La Jolla, CA, US). Error bars were plotted on graphs using the 95% confidence interval (CI) as standard, or using the standard deviation (SD). Both of these were automatically calculated by GraphPad Prism. Use of either the CI or SD is specified on all graphs. One- and two-way ANalysis of VAriance (ANOVA) with multiple comparisons (Dunnett's and Tukey's multiple comparisons tests), Student's T-test and column analyses (depending on the study design) for statistical significances were also carried out in GraphPad Prism. The software indicated significance levels as the following: * = $p \leq 0.05$, ** = $p \leq 0.01$, *** = $p \leq 0.001$ and **** = $p \leq 0.0001$. Differences were considered statistically significant at $p \leq 0.05$.

Standard curves were plotted from data which had been normalised for background fluorescence / luminescence values. Plots were made in MS Excel 2011, the intersect at the y axis was set at 0 and the R^2 value and line equation were calculated by Excel. Example standard curves can be found in appendix C. These were then used to calculate corresponding values from experimental readings.

Where cell proliferation is expressed as a percentage, percentage survival was calculated based on readings obtained on either day 0 or day 1 of co-culture, where the earlier value was designated as '100%'.

Chapter 3

Development of a bone-like in vitro model

In this chapter, the development of the bone-like model to form the basis of the jaw bone mimicking, bone-like co-culture construct is described. The aims of this chapter were to first compare different methods for making bone-like scaffolds *in vitro*, and to ascertain that the developed bone-like scaffolds were able to support cell growth. The development involved the inclusion of bone cells to compressed collagen scaffolds together with Bio-Oss bovine bone particles.

Cells from the HOS cell line were used to initially develop, optimise and standardise the process for making the bone-like organotypic scaffolds. This cell line was chosen due to the fact that it proliferates quickly, which enabled manufacture of several scaffolds at one time, as well as its mostly osteoblastic morphology, which enabled the cells to mineralise the scaffold and model the behaviour of bone cells within the scaffolds. However, as the HOS cell line is cancerous, this was not the ideal model to use for co-culture. Once the HOS-incorporating model was optimised for ameloblastoma co-culture, primary osteoblast (HOB) cells were used instead. Due to their primary nature, the HOB cell-incorporating models were more organotypic and representative of the ameloblastoma tumour microenvironment.

The scaffolds were assayed for mineralisation using both qualitative histological staining as well as quantitative methods to assay alkaline phosphatase (ALP) production, as well as ALP and BMP-2 bone biomarker gene expression. Furthermore, cell behaviour in the scaffolds and the ease of scaffold manipulation were considered. An important consideration was the possibility to manufacture scaffolds consistently.

3.0.1 Factors considered in bone-like scaffold development

For the purposes of creating a scaffold which could easily be used for AM-1 incorporation or co-culture, the following parameters were considered when initially developing the bone-like scaffold:

- Cell survival and proliferation in the scaffold.
- Production of alkaline phosphatase (ALP) and bone morphogenic protein (BMP-2) by the cells in the scaffolds. These are commonly accepted as standard proteins to assess the level of mineralisation taking place.
- Cell-induced mineralisation of the scaffold which was visible using histology and increasing throughout culture time.
- Mechanical properties of the scaffold which were close to those of native mandibular or maxillar bone.

Initially, different scaffold options were explored in the form of a collagen-only matrix, and different collagen and Bio-Oss scaffold compositions considered in the form of Bio-Oss + collagen blocks and Bio-Oss granules. The resulting mineralised, bone-like scaffold was then used for the co-culture models as described in the following chapter.

3.1 Summary of methods

Collagen gels seeded with cells from the HOS cell line were plastic compressed (stabilised) and used as the starting point for model development. 300,000 cells/ml collagen were used and the final compressed collagen scaffolds were cut in 6-24 equal pieces, resulting in a cell number of approximately 3,125-12,500 cells per gel. The number of bone cells used was based on similar scaffolds made elsewhere (Bitar et al., 2008).
Bio-Oss-collagen blocks with 300,000 HOS cells per block were used as an initial alternative to collagen-only scaffolds to assess which scaffold provided the optimal basis for the bone-like scaffold.
Ultimately, Bio-Oss particles and rat-tail collagen solution were mixed together to achieve a suitable scaffold. Mineralisation was assayed using a quantitative alkaline phosphatase assay and expression of the alkaline phosphatase gene. Cell survival was analysed qualitatively using Live/Dead staining and quantitatively using the Alamar Blue and Cell Titre Glo 3D ATP assays. The latter measures cell metabolic activity by quantifying ATP levels, rather than proliferation, but there is a generally accepted correlation between the two (Crouch et al., 1993). Histology (Von Kossa and H&E) staining and scanning electron microscopy were used to visualise the scaffold structure and ultrastructure, respectively. Finally, HOS cells were substituted for primary osteoblast (HOB) cells to validate the results obtained and to provide a more *in vivo*-like model.

3.2 Collagen-only scaffold mineralisation

As bone is a mineralised construct, mineralisation of the cellularised collagen scaffolds was one of the main parameters investigated during the development of the initial bone-like organotypic scaffold. Mineralisation was assayed both qualitatively and quantitatively.

Initially, Von Kossa staining of the gels showed no mineral (brown staining) present in the scaffolds with HOS cells alone on days 1, 7 or 14 of culture in osteogenic media as seen in fig. 3.1A-C. Cells in these scaffolds (counterstained red), were sparsely distributed. However, in longer term culture for up to 36 days, Von Kossa staining showed a completely mineralised scaffold. Mineral staining in the collagen-only scaffolds appeared from day 16 fig. (3.1D), with the entire construct mineralised by day 36 (fig. 3.1E).

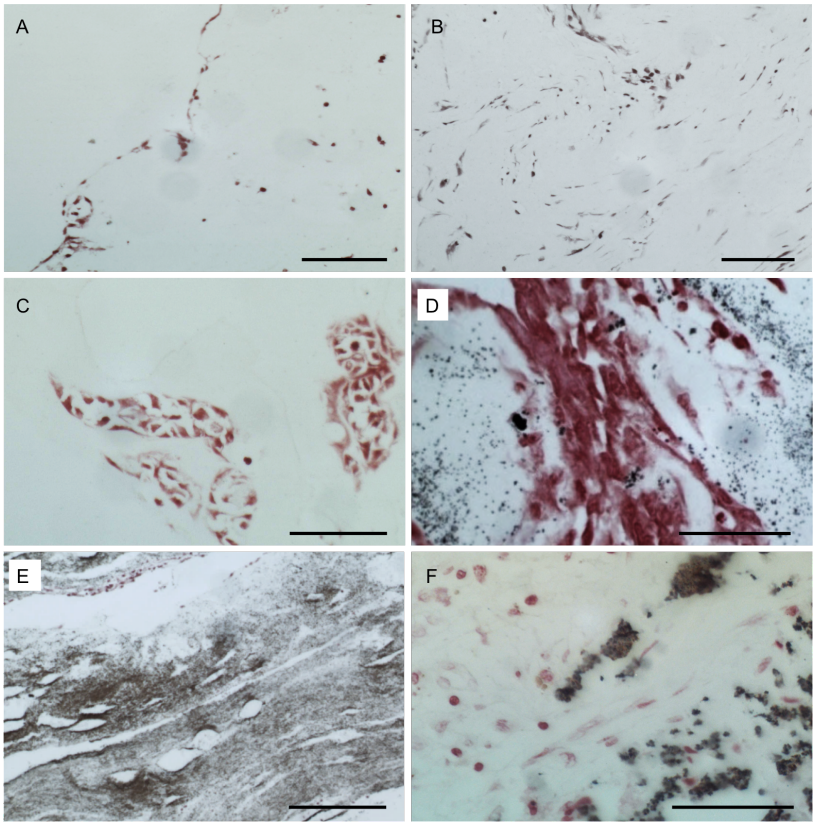

Figure 3.1: Light microscope images of von Kossa-stained (VK) cellularised collagen-only scaffolds. Collagen scaffolds on day 1 (A), day 9 (B), day 14 (C) did not stain for mineral when using the von Kossa histological stain. Collagen gels on day 16 (D) showed some VK staining (dark brown / black), with staining increasing until the whole structure appeared stained on day 36 of culture. F) A section of human trabecular bone used as a control. The cells in the scaffolds are counterstained red. Scale bars = 100μm.

This showed that the compressed cellularised collagen-only scaffolds provided a suitable environment for mineralisation by HOS cells. However, the time taken by the cells to mineralise the scaffolds was, at 36 days, considered to be prohibitively extensive.

3.3 Cell survival in collagen-only scaffolds

The bone-like scaffolds were also required to support cell proliferation. HOS cell survival within the scaffolds was assessed by Live/Dead staining. As shown in fig. 3.2, the cells appeared alive on days 7, 14 and 21 of culture. However, as seen in fig. 3.2D, cell death in the scaffolds had increased by 28 days in culture. 28 days was therefore deemed the maximum time HOS cells could be kept in collagen 3D culture. However, this time limit was 12 days less than the time necessary for mineralisation of the collagen-only scaffold to occur as seen in fig. 3.1.

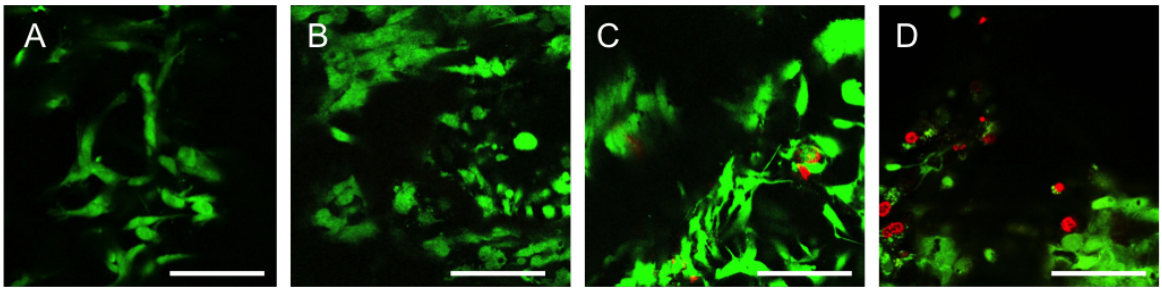

Figure 3.2: Confocal micrographs of Live/Dead stained HOS cells in the collagen scaffolds. A) A sample on day 7, when some cell proliferation was visible and HOS cells were all stained with the live (green) stain. B) On day 14, the cells within the scaffolds exhibited a characteristic, slightly elongated morphology. Cells remained mostly alive. C) By day 21, the scaffold had become largely confluent, which caused some cells to die (red staining). Here, mostly alive cells were seen, but these were irregularly shaped. D) A sample on day 28, where some cells were still alive within the collagen-only scaffolds. Extensive cell death was also seen. Representative images of n = 3. Scale bars = 50μm.

In addition, bearing in mind that the scaffold was required to be as mineralised as possible prior to co-culture with AM-1 cells, a further shortening of the initial HOS cell culture time within the scaffolds was required. Based on these results, it was decided that addition of mineral to these scaffolds would be necessary in order to make the constructs more bone-like and aid the mineralisation process and therefore the co-culture scaffold manufacture.

3.4 Addition of mineral: Bio-Oss granules and Bio-Oss blocks

A commercially available, bone-mimicking and mineralised construct was sought to provide the scaffolds with additional mineral at an early culture time point. Ideally, these minerals would be added at a ratio mimicking native bone composition both in mineral and collagen content.

Initially, hydroxyapatite (HA) was considered, as it is widely used for synthesis of bone-like scaffolds. However, work on similar collagen scaffolds found that during long-term culture, the HA had a tendency to be released into the surrounding media, as the spaces between the collagen fibre network were larger than the HA crystals. This rendered the amount of HA within the scaffolds variable and decreasing with increasing culture time (D. Thomas, *unpublished data*).

Bio-Oss is, as detailed in section 1.10.4, a commercially available, decellularised bovine bone substrate available both as granules and as pre-made blocks. The blocks are made up of 90% Bio-Oss held together with 10% porcine collagen, whereas the Bio-Oss granules are 100% decellularised bone substrate.

Both of these were added to cultures with HOS cells and kept in culture with osteogenic media to determine which scaffold would improve mineralisation time while allowing for cell proliferation and survival within the constructs.

Bio-Oss granules were used with a mixture of rat-tail collagen type II and Bio-Oss to create constructs seen in fig. 3.3. The amount of Bio-Oss granules in the constructs was roughly quantified using area measure-

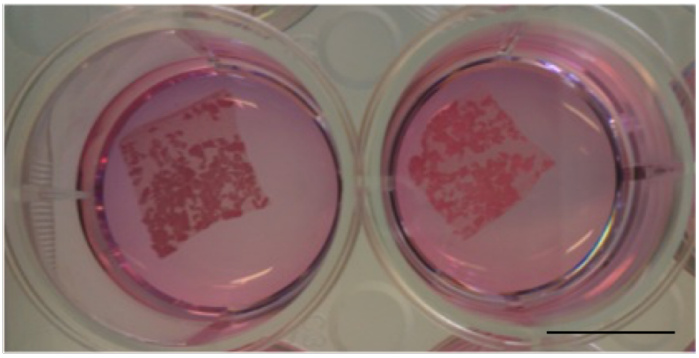

Figure 3.3: HOS cellularised collagen + Bio-Oss culture gels after compression in osteogenic media. The Bio-Oss granules were clearly visible when incorporated in the collagen constructs. The gels were cut after compression to 12 or 24 equal square pieces for culture and further analysis. Scale bar = 10mm.

ments in ImageJ (an example can be found in appendix C). In some parts of the scaffolds, the final amount of granules was varied due to uneven setting of the gels or clustering together of the granules. The results indicated that the total amount of Bio-Oss granules in the constructs was on average 30% of the total construct area, although this amount did vary somewhat. As this amount was lower than the mineral content in native bone, an alternative in the form of Bio-Oss blocks was considered.

Bio-Oss blocks, seen in fig. 3.4A, were made up of 90% Bio-Oss and 10% collagen. The latter were therefore more similar to native bone both in terms of protein (ECM) composition and mineral properties at the start of the study. However, the blocks began to disintegrate during culture, and by day 10 they had mostly dissolved in the culture media (fig. 3.4B), with abundant loose Bio-Oss granules present at the bottom of the well. Furthermore, these blocks also became compliant when handled and disintegrated further due to the slight disturbance caused by media changes.

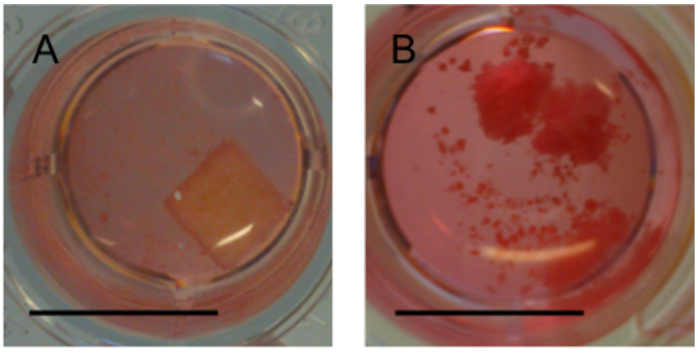

Figure 3.4: Bio-Oss blocks in culture with HOS cells. A) On day 1, the Bio-Oss block appeared intact. B) By day 10, the blocks had nearly disintegrated. The blocks became noticeably softer and more difficult to handle when degradation of the block structure was taking place. Little cell migration was observed when the bottom of the plate was examined microscopically. Scale bar = 10mm.

3.4.1 Cell survival on Bio-Oss blocks

HOS cells were incubated with Bio-Oss blocks for up to 14 days in osteogenic media and imaged using Live/Dead staining and confocal microscopy to assess cell survival. As the blocks were large in size (5mm

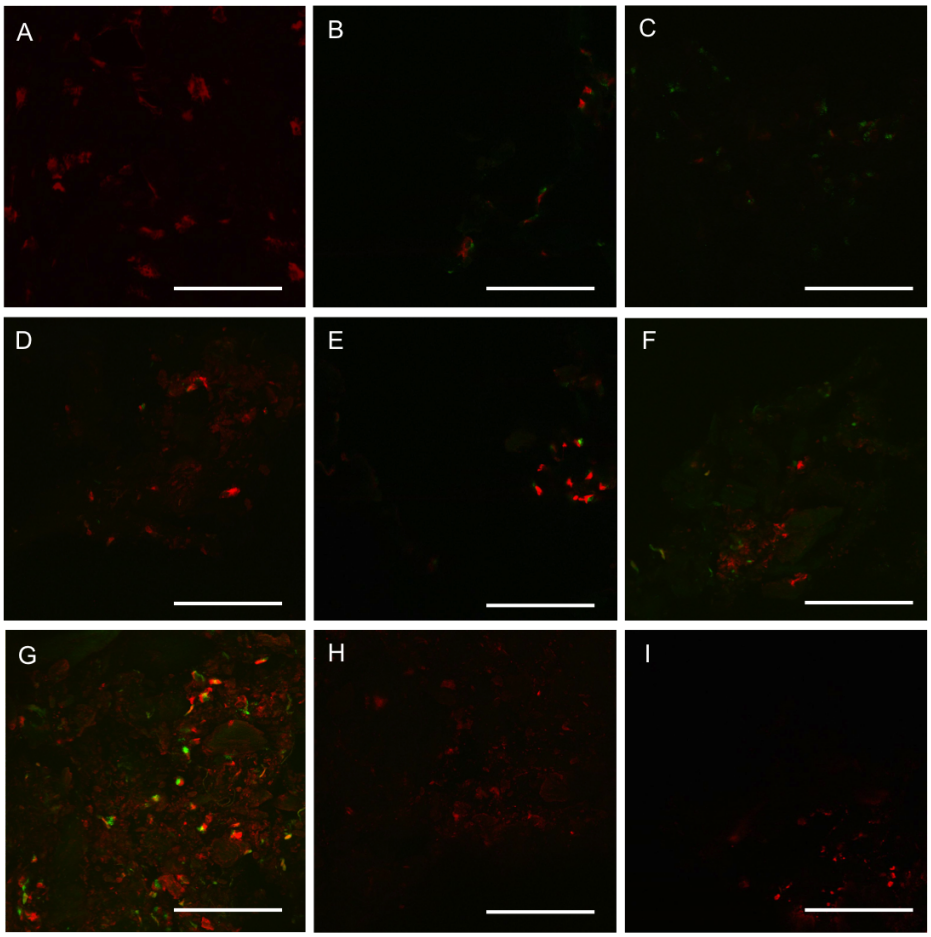

Figure 3.5: Live/Dead staining of HOS cells in 90% Bio-Oss + 10% collagen type I blocks. Red = dead cells, green = live cells. Some block samples were cut in half after staining to image the middle of the constructs. 'Surface' refers to one of two sides of the block onto which HOS cells were seeded.
Top row: Day 1 surface (A), surface (B) and middle (C) of 90% Bio-Oss + 10% collagen blocks. Mostly dead cells were seen at all points imaged on this early time point. Middle row: Day 7 surface (D), middle (E) and middle (F) of 90% Bio-Oss + 10% collagen blocks. The blocks became very soft and fell apart around day 10 of culture and as a result were difficult to handle and image. Mostly dead cells were seen in these samples. Bottom row: G, H and I are all arbitrary locations imaged in Bio-Oss collagen blocks on d14, where some alive but mostly dead cells were seen. Note also the abundant red staining of the scaffold present in G. Representative images of n = 3. Scale bars = 100μm.

on edge) and opaque, it was not possible to microscopically examine cells deep within the structures on a continuous basis.

Furthermore, due to the manner the cells were applied to the block (pipetting suspension on the surface of the block), the distribution of cells on the blocks was uneven. On day 1, some cells appeared dead (fig. 3.5A), whereas some were alive (fig. 3.5C). However, very few of the original 100,000 cells which were seeded onto the constructs were seen. Some cells were still alive on day 7 (fig. 3.5D-F), yet abundant cell death was seen in all samples at this time point. By day 14, very few live cells were seen in any of the samples examined (fig. 3.5G-I).

It is possible that the Live/Dead stain, in addition to staining HOS cells within the structures, also stained

some remnant nucleic acids and proteins on the surface of the Bio-Oss particles. If this was the case, then these nucleic acids and other remnant tissue components may have influenced the cells added to the blocks. This type of staining in decellularised tissues has been documented before, in one study up to 85% of decellularised samples examined stained for cytoskeletal proteins (Woods and Gratzer, 2005). Therefore, the extensive red staining seen in fig. 3.5 may be a combination of HOS cells and remnant nuclei acids. However, as can be seen, while numerous dead cells were observed, there were no extensive live cell populations present at either the surface or deeper within the constructs at any time point examined.

3.4.2 SEM on Bio-Oss blocks

Initially, the softening and thereby disintegration of the Bio-Oss blocks, as seen in fig. 3.4B, was thought to be due to the blocks absorbing the culture medium, but at later time points, when the blocks began disintegrating, this was thought to be due to cell-induced degradation of the collagen linkages holding the blocks together. Scanning electron microscopy was used to closely image the cells on the blocks, as well as the structure of the constructs themselves. On days 1 and 7, the Bio-Oss particles appeared randomly distributed, and the collagen fibres within the scaffolds were visible (fig. 3.6A and B).

Indeed, SEM imaging revealed that the most likely cause for the blocks softening, was the presumably cell-induced remodelling of the collagen fibres (fig. 3.6C), which were present in the structures to maintain them in their block conformation. Due to the difficulties in culturing the Bio-Oss blocks, as well as the decreased cell viability of HOS cells seeded on these blocks as seen in fig. 3.5, it was decided that the addition of Bio-Oss granules to the collagen gels was the more optimal solution and was explored further during the development of the bone-like model.

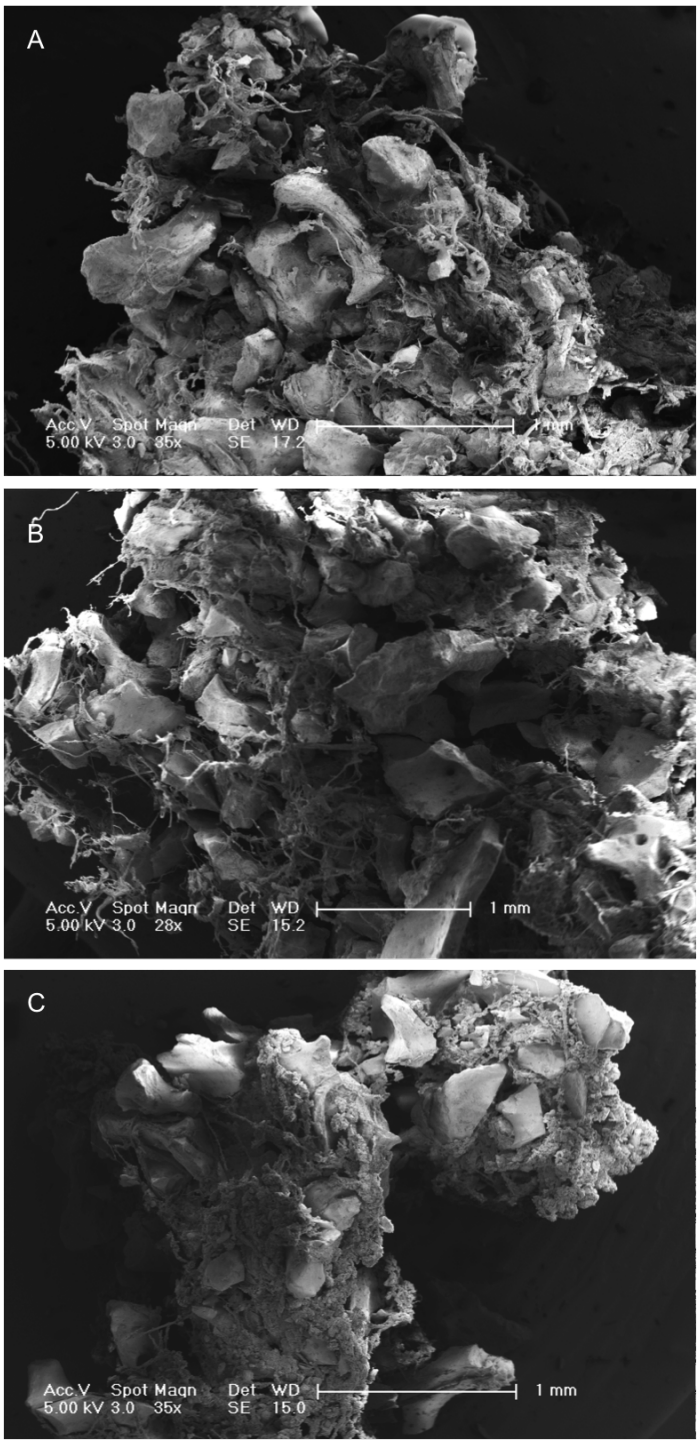

Figure 3.6: Scanning electron micrographs of Bio-Oss blocks with HOS cells. A) Bio-Oss block on day 1 after HOS seeding. The collagen fibres, which made up 10% of the scaffold, appeared disorganised. B) Day 7 of culture and C) Day 14 of culture, where the block structure has shrunk visibly, and the collagen strands previously incorporated in the scaffold seemed to have disappeared. Very few cells were seen at these time points. Representative images of n = 3. Scale bars = 1mm.

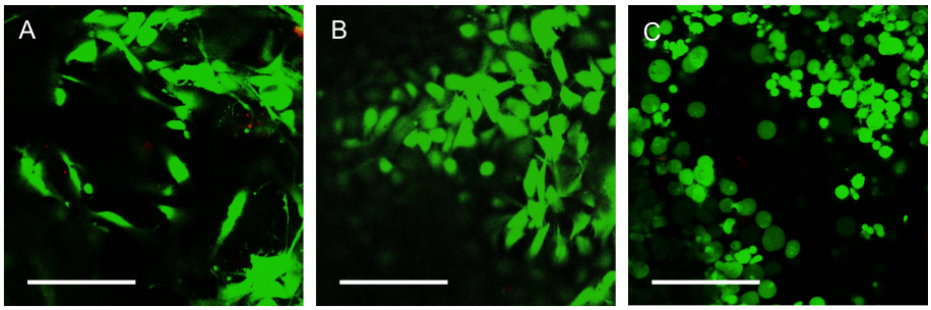

Figure 3.7: Confocal micrographs of HOS cells in collagen-Bio-Oss constructs stained with Live/Dead staining. A) Cells on day 6 of culture appeared alive (green) to a large extent, with only a few dead (red) cells seen throughout. Cells were elongated and well-dispersed within the scaffold. B) Cells on day 14 of culture. The constructs were becoming more confluent, and although the cells were therefore less elongated on this time point, they were all still alive. C) Cells on day 28 appeared very confluent. The majority of the cells were still alive, but there was a growing amount of cell death seen, especially in the deeper parts of the scaffolds. The live cells at this time point appeared more rounded than at the earlier time points, when the cell morphology was elongated. The Bio-Oss blocks obscured some parts of the constructs, as these were opaque (as seen here in the middle of A and C, where no cells were seen). Representative images of n = 3. Scale bars = 50μm.

3.4.3 Cell survival with Bio-Oss granules

The final amount of Bio-Oss granules to collagen was approximately 30% Bio-Oss and 70% collagen per scaffold area in all samples (an example measurement can be found in appendix fig. B.8). The total amount of collagen fibre in compressed constructs has been shown to be 10-20% of the total construct (Brown et al., 2005; Bitar et al., 2007; Brown, 2013).

Cells in the collagen-Bio-Oss constructs were examined using Live/Dead staining for 28 days of culture, with representative images seen in fig. 3.7. Cells in these scaffolds remained alive (stained green in fig. 3.7) and proliferated throughout the culture period. Cells in day 7 scaffolds were alive and appeared slightly elongated with multiple projections. Similarly, cells in day 14 scaffolds appeared to have an osteoblastic morphology and were largely alive; there were also noticeably more cells present on this longer time point. By day 28, some cell death was seen deeper in the constructs and close to the Bio-Oss particles. By the end of culture, the scaffolds appeared confluent and cells were evenly distributed throughout the scaffolds.

Initially, to quantify cell proliferation and survival in these constructs, the Alamar Blue metabolic assay was used. This assay seemed to give an indication of viable HOS cells within the scaffolds when used for the collagen-only constructs. As seen in fig. 3.8, HOS cells (white bars) appeared to increase in cell number throughout initial one-week culture. By day 10 however, the metabolic activity of these cells had decreased. In contrast, when Bio-Oss granules were added to the collagen constructs, the metabolic activity as measured by the Alamar Blue assay reduced significantly (fig. 3.8, filled bars), when the same amount of HOS cells was initially added to both scaffolds. This was thought to be due to a combination of factors: cell migration through the pores of the Bio-Oss granules, mineralisation of the scaffold by the cells, Alamar Blue reagent penetration issues through the Bio-Oss granules during incubation, remodelling of the scaffolds by the cells,

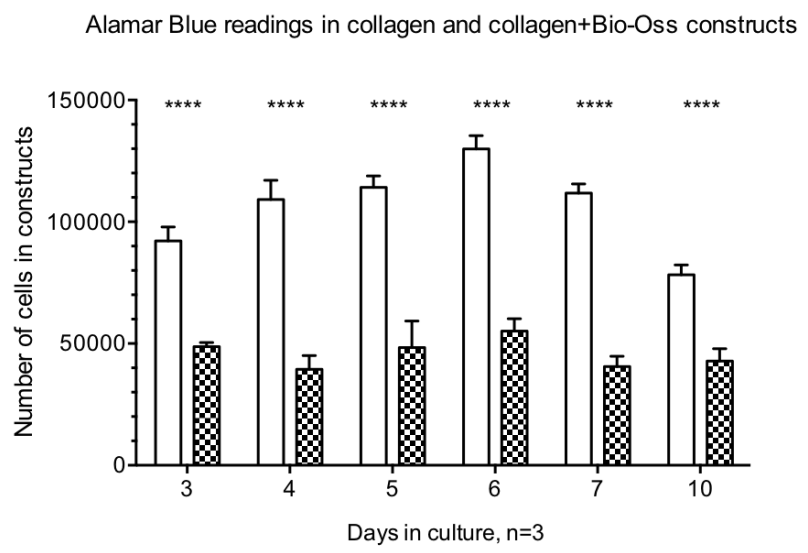

Figure 3.8: Cell proliferation as measured using the Alamar Blue cell metabolic assay on HOS cells in collagen-only scaffolds (unfilled bars) and in collagen + Bio-Oss scaffolds (filled bars). Significant differences were found on all time points ($p \leq 0.0001$), with more metabolically active cells present in the collagen-only scaffolds throughout culture time. In the collagen + Bio-Oss scaffolds, cell metabolic levels appeared constant throughout the culture time. **** indicates $p \leq 0.0001$, two-way ANOVA, error bars = 95% CI, n = 3 for both conditions.

and the Bio-Oss granules blocking the fluorescent reading upon measurement.

Additionally, as seen in fig. 3.7, the cells appeared to proliferate within the Bio-Oss scaffolds. A more reliable method for quantifying the number of cells within these constructs was therefore required.

3.5 Mineralisation of Bio-Oss granule constructs

Mineralisation of the scaffolds was also assessed after Bio-Oss incorporation. Von Kossa staining showed an instant increase in mineral in the scaffolds when Bio-Oss granules were incorporated (fig. 3.9A). The brown

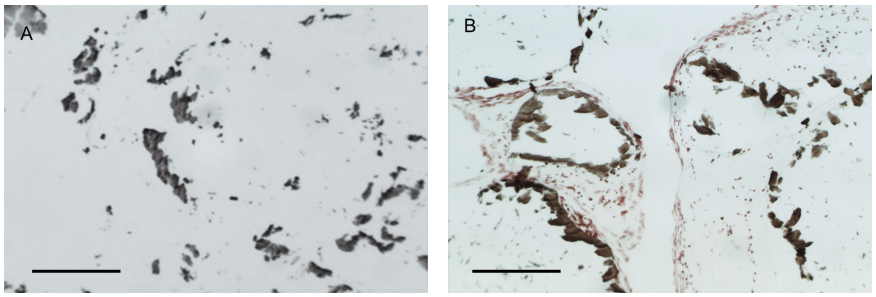

Figure 3.9: The addition of Bio-Oss granules to the collagen constructs provided the scaffolds with instant mineral. A) A day 1 sample, where the mineral (brown staining) is clearly seen. B) A day 7 sample, where mineralisation has increased while cells (stained red) have proliferated. The Von Kossa stain appeared both darker in colour as well as more abundantly distributed throughout the scaffold. Representative images of n = 3. Scale bars = 100μm.

mineral staining appeared similar to that seen in the trabecular bone controls in fig. 3.1. Additionally, as seen in fig. 3.9B, the staining appeared both stronger and more abundant with increasing culture time. This indicated increasing mineral produced by the cells in the constructs.

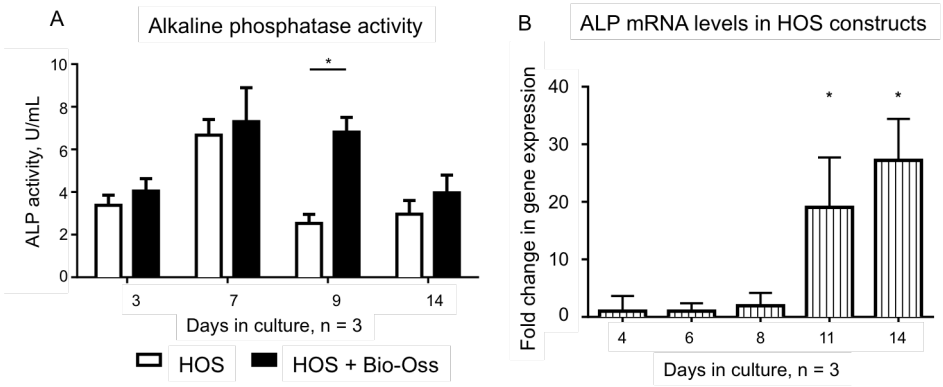

Figure 3.10: Alkaline phosphatase (ALP) levels in HOS cellularised collagen + Bio-Oss constructs. A) ALP activity was quantified in constructs with and without Bio-Oss. In both construct types, an increase in ALP was seen in the first week. After this, ALP activity reduced, although this reduction was more pronounced in the constructs without Bio-Oss. A significant difference in ALP activity was seen between the two construct types on day 9 of culture, with a more sustained level of activity seen in the constructs with added Bio-Oss (*). ALP activity in both constructs reduced to approximately equal levels after this time. B) ALP gene expression in HOS cells in collagen and Bio-Oss constructs as quantified by qRT-PCR analysis. There was a significant increase in ALP mRNA levels seen on days 8 and 11 (*) compared to the other time points. In both A and B, asterisks (*) indicate a $p \leq 0.05$. ALP levels in A are expressed as 'units per millilitre' (U/mL). Unpaired t tests, error bars = 95% CI.

3.6 Alkaline phosphatase levels increased in the bone-like constructs

Production of alkaline phosphatase as a marker of osteoblast activity was quantified in the scaffolds both using a colorimetric ALP assay as well as qRT-PCR gene expression.

Results from the protein-based ALP assay in fig. 3.10A indicated that ALP levels increased during the first week in culture. After the first week in the collagen-only cultures, ALP levels then quickly reduced to below day 3 levels for the remaining culture time. However, in cultures with added Bio-Oss, this decrease was more gradual, with ALP levels on day 9 remaining high and reducing to levels seen initially by day 14. This result correlated with the osteoblasts producing abundant ALP to induce the early stages of mineralisation, while the maturation and further mineralisation of the bone tissue proceeds by itself, as documented by other studies (Rattner et al., 2000).

Gene expression analysis (fig. 3.10B) revealed a significant increase in ALP levels in the constructs with increasing culture time. Initially, low levels of ALP mRNA were detected in all samples. A large increase was then seen during days 11 and 14 of constructs cultured in osteogenic media. Levels of ALP detected at these time points were approximately 30-fold compared to those detected in the calibrator (day 0) samples, indicating abundant active osteoblast-like cells within these cultures.

There was a discrepancy between the two graphs in fig. 3.10, as ALP gene expression (in fig. 3.10B) was seen to increase when ALP activity (fig. 3.10A) was already reducing. This could be due to the fact that the ALP activity assay was colorimetric, and therefore less sensitive than qRT-PCR, which measured mRNA levels. Additionally, all the cells in the constructs were carefully lysed for gene expression analysis, whereas the ALP activity assay was carried out on samples which were less well-lysed due to preparation methods.

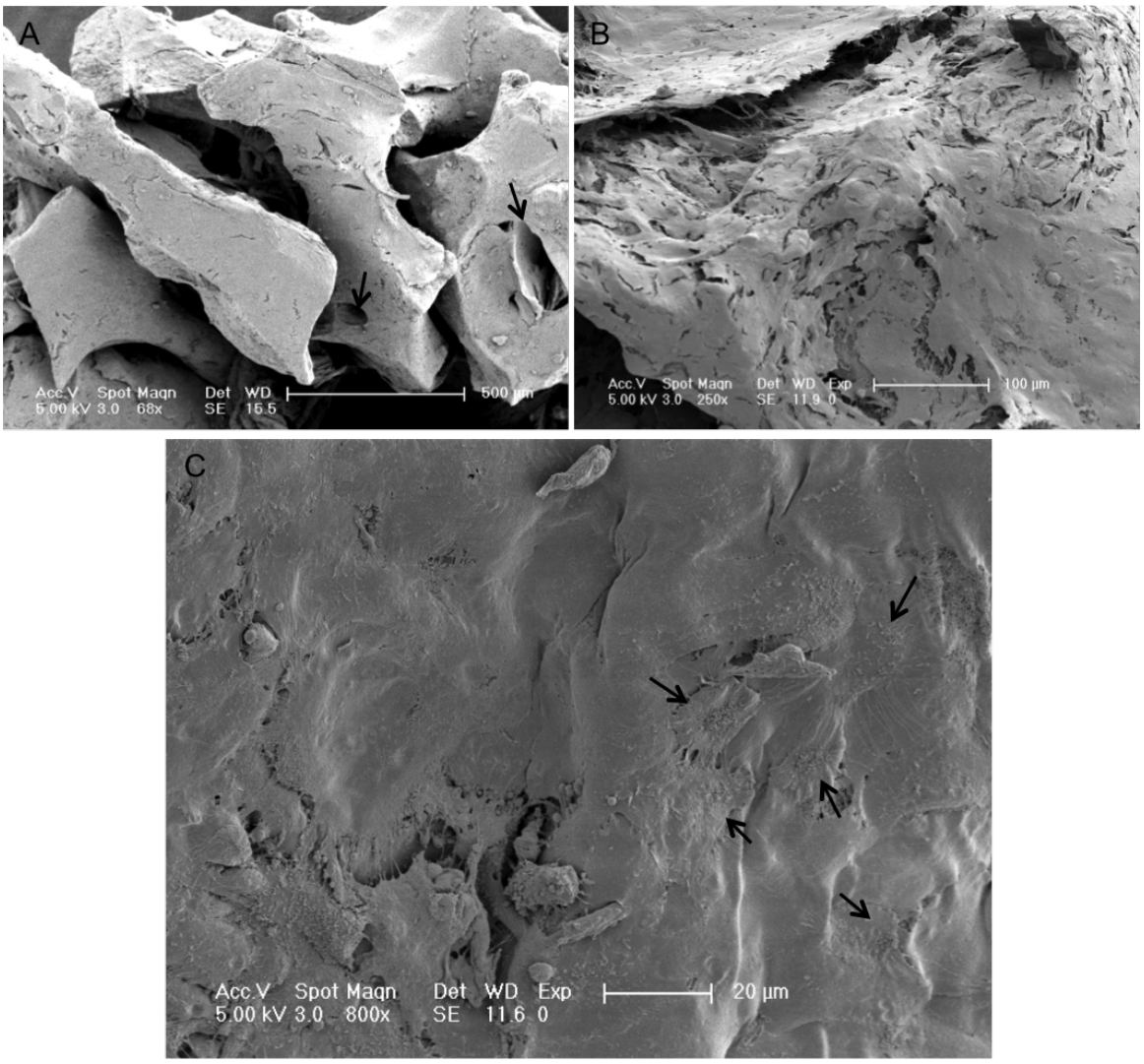

Figure 3.11: Scanning electron micrographs of collagen + Bio-Oss constructs. A) Bio-Oss granules were large and irregularly shaped. Some pores (indicated by black arrows) were visible on the surface of the granules. B) By day 14, the surfaces of samples seeded with HOS cells were seen entirely covered with a layer of flattened, elongated cells. C) Close-up of a surface, where cells with osteoblast-like morphologies were seen (indicated by black arrows). These cells had multiple projections and a ruffled nucleus.

Both these factors could have led to some, or even a large proportion, of the cells within the constructs and especially within the Bio-Oss particles, to not be included in the ALP activity analysis.

3.7 SEM on collagen-Bio-Oss scaffolds

Scanning electron microscopy was used to characterise the surface of the scaffolds, Bio-Oss granules and cell morphology more closely. The structure of the Bio-Oss particles was clearly seen when visualised using the SEM (fig. 3.11A). Pores on the surface of the Bio-Oss particles were also seen. No cells were seen in the vicinity of the Bio-Oss particles at this high magnification, although this could have been due to cell detachment during processing or cutting of the samples.

The Bio-Oss particles appeared for the most part coated with the collagen matrix (fig. 3.11B), although this coating had in some places become dislodged due to sample processing. The collagen coating provided a

cell-friendly environment and somewhere where the cells within the scaffolds could attach to - indeed, the surfaces examined were to a large extent coated with cells.

Cells which appeared morphologically osteoblastic were seen in the scaffolds on day 14 (indicated by arrows in fig. 3.11C). These cells were spread out on the collagen scaffolds, with abundant cytoplasmic processes and ruffled nuclei, both of which are osteoblast characteristics. The collagen fibres in these scaffolds appeared uniform with no major deformation due to degradation, and their distribution throughout the scaffolds was even, but random.

3.8 Mechanical analysis of collagen-Bio-Oss constructs

Dynamic mechanical analysis of the collagen-Bio-Oss constructs was carried out to determine how *in vivo*-like the mechanical properties of the scaffolds were. Even though the collagen-Bio-Oss constructs were noticeably stiffer when handled than collagen-only constructs, and could be in many ways thought to be bone-like, not least due to the inclusion of the bone particles, they were unable to withstand high frequencies when mechanical testing was performed. When tested at frequencies above 1 Hz, the scaffolds quickly failed.

The resulting stress-strain curves are shown in fig. 3.12, where differences in the stiffness between the different construct types can be seen. The addition of Bio-Oss increased the constructs' stiffness from approximately 15MPa in the acellular constructs to over 125MPa in the cellularised Bio-Oss scaffolds, irrespective which type of media the constructs were grown in (osteogenic media vs KSFM; results for this not shown). The box in fig. 3.12 shows the values used for calculating the elastic modulus of the constructs. This 0.5Hz frequency was chosen as this reading was taken twice over each DMA test (once at the start and a second time in the middle of the test). The dynamic amplitude for each test was 0.012mm.

The compression strength of the four different construct types were calculated at a frequency of 0.5Hz, and the results (mean $\pm$ standard deviation) are shown in table 3.1.

Table 3.1: Elastic modulus (E, in MPa) in the bone-like constructs as measured at 0.5Hz at an amplitude of 0.012mm using dynamic mechanical analysis (DMA). Collagen scaffolds with and without Bio-Oss granules were measured. Cell-dependent changes in scaffold mechanics were measured using cellularised and acellular samples. A significant difference was found in stiffness between the collagen-only and collagen + Bio-Oss samples. In the collagen-only samples, there was also a significant cell-mediated effect on stiffness, with the cellularised constructs exhibiting significantly reduced stiffness. Mean values $\pm$ standard deviation, n = 4.

Sample	**Elastic modulus (E) at 0.5Hz, MPa**
Cellularised collagen-only	5.26 ± 1.275
Acellular collagen-only	14.71 ± 1.348
Acellular collagen + Bio-Oss	137.3 ± 10.32
Cellularised collagen + Bio-Oss	155.3 ± 10.78

The addition of cells to the collagen-only cultures significantly reduced the scaffold stiffness compared to the acellular collagen-only constructs ($p \leq 0.05$).

The addition of Bio-Oss to the constructs was the factor which contributed the most to increasing the stiffness

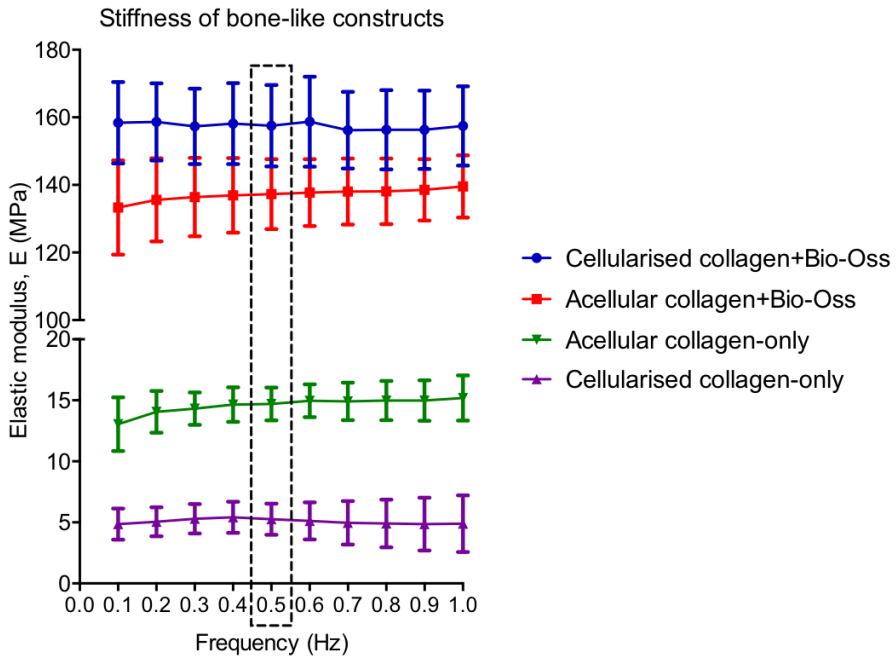

Figure 3.12: Graph showing the stiffness measurements obtained using DMA for the four conditions tested. The addition of Bio-Oss granules greatly increased the compression strength of the constructs (blue and red lines). The addition of cells in the collagen-only constructs decreased compression strength compared to the acellular collagen-only scaffolds. The superimposed box indicates the values (at 0.5Hz) used to calculate the average stiffness values as detailed in table 3.1. Overall, a 10-fold difference between the constructs with and without Bio-Oss was seen. A statistically significant difference in stiffness was found when comparing all groups; $p \leq 0.05$ (one-way ANOVA). Note the split y axis. Error bars = standard deviation, n = 4.

of the bone-like constructs ($p \leq 0.05$), with the elastic modulus (E) increasing from approximately 5MPa in cellularised collagen-only constructs to 150MPa in constructs with added Bio-Oss. Furthermore, it appeared that there was a slight increase in construct stiffness caused by the cells in the collagen + Bio-Oss constructs (and the increase in mineralisation as seen using the Von Kossa stain in fig. 3.9), when compared to the acellular collagen + Bio-Oss constructs. The E values for these were on average 155.3MPa and 137.3MPa respectively. However, this cell-mediated increase in stiffness was not found statistically significant.

3.9 Conclusions for this section

The main variables investigated in this initial HOS organotypic bone-like scaffold are summarised in table 3.2.

Table 3.2: An outline of the various parameters considered when developing the bone-like scaffolds and summarising the main findings of the research which concerned the variables, as well as the conclusion based on these results and the final composition of the bone-like model in subsequent experiments.

Variable investigated	**Range tested**	**Result**	**Outcome**
Collagen amount in scaffolds	10 - 100 %	Native bone is 30% collagen. Cell viability was found decreased on 10% collagen, whereas in 100% collagen scaffolds mineralisation was slow.	Per construct area, 60-70% collagen was used.
Bio-Oss amount in scaffolds	0 - 90 %	0% scaffolds showed slow mineralisation. Cells in 90% scaffolds died by day 14.	Used 30-40% of total area.
Number of days in culture	0 - 35 days	35 days in culture (in OM) allowed for visible mineralisation and significant ALP production in collagen-only scaffolds. Cells produced more ALP in constructs with added Bio-Oss; more sustained levels of ALP as a result. Cells proliferated in constructs, but begun to apoptose in long-term culture.	Scaffolds appeared confluent by day 14 of culture. By this time, mineralisation was also underway.
Mineralisation	HOS in collagen-only, collagen+Bio-Oss scaffolds and Bio-Oss blocks	Mineralisation of collagen-only scaffolds slow. Bio-Oss blocks and granules added instant mineral.	Bio-Oss granules beneficial for quick mineralisation times.
Mechanical properties (elastic modulus)	Collagen-only and collagen+Bio-Oss scaffolds	Collagen-only scaffolds were approximately 10 times softer than scaffolds with Bio-Oss. Scaffolds with Bio-Oss approaching stiffness of native bone.	Addition of Bio-Oss was deemed beneficial for achieving bone-like mechanical properties.

Based on the results presented in the first part of this chapter, it was decided that Bio-Oss granules provided the constructs with suitable mineral content and improved the mechanical properties of the constructs, while being cytocompatible and allowing the cells within the constructs to proliferate.
Subsequently, Bio-Oss granules were used to create the basis of the bone-like co-culture scaffolds. Furthermore, a 14 day initial culture period was decided on, as this allowed for both adequate cell expansion within the constructs, as well as further mineralisation of the constructs by the HOS cells.

3.10 Primary osteoblast culture further strengthens the model

In order to further strengthen the bone-like model and validate the results obtained with the subsequent co-culture scaffolds, the HOS cells in this scaffold were substituted with primary osteoblast cells (HOB). A selection of the above experiments, such as mineralisation and cell survival, were then carried out on this co-culture model.

3.10.1 HOB scaffold mineralisation

The collagen-Bio-Oss scaffolds with HOB cells were initially cultured as the HOS scaffolds for 14 days in mineralising media. Mineralisation of the HOB scaffolds was assessed using ALP and BMP2 gene expression using qRT-PCR during 14 days of single-cell culture. As is seen in fig. 3.13, there was a significant increase ($p \leq 0.001$) of ALP expression in the models on days 10 and 14. The difference in ALP expression between days 1 and 7 was deemed not significant.

BMP-2 mRNA levels (fig. 3.13) also significantly increased during culture in the HOB scaffolds ($p \leq 0.05$). The increase in BMP-2 levels was taken as another indication that the cells within the scaffolds were mineralising it and behaving like osteoblasts.

It should be noted that the ALP gene expression levels measured in the HOB scaffolds (fig. 3.13) appear approximately 10-fold less than those seen in the HOS scaffolds in fig. 3.10.

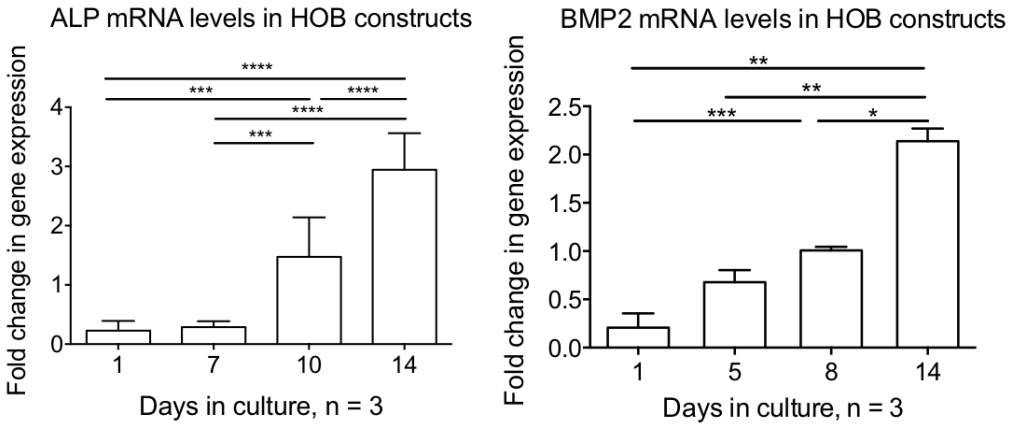

Figure 3.13: Alkaline phosphatase (ALP) gene expression plotted as fold change in cellularised HOB collagen + Bio-Oss constructs. ALP increased over time, with day 10 and day 14 expression statistically significant ($p \leq 0.001$) when compared to day 1 and day 7 expression. B) BMP-2 mRNA levels plotted as fold change in HOB-cellularised collagen + Bio-Oss constructs. Levels of BMP-2 in the constructs were also found to increase significantly over culture time ($p \leq 0.05$). One-way ANOVA, asterisks indicate significance levels as follows: * $p \leq 0.05$, ** $p \leq 0.01$, *** $p \leq 0.001$ and **** $p \leq 0.0001$. Error bars show the 91% CI, n = 3.

Mineralisation was also qualitatively assessed using Alizarin Red staining, as seen in fig. 3.14. On day 4, the Bio-Oss granules within the structures were stained strongly with Alizarin Red, whereas the collagen was only faintly stained. By day 7 (fig. 3.14B), the collagen structure was somewhat more stained, but the Bio-Oss granules still appeared more mineralised. By day 14 however, the entire construct appeared strongly stained (fig. 3.14C).

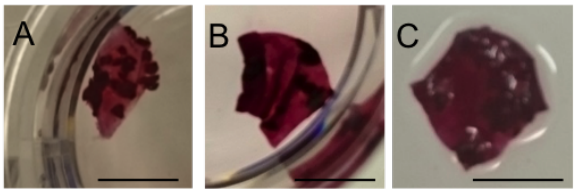

Figure 3.14: Alizarin Red staining of whole HOB constructs was used to indicate an increase in mineral present within the collagen + Bio-Oss constructs throughout culture time. A) A day 4 HOB cellularised construct, B) A day 7 construct and C) A HOB cellularised construct on day 14 of culture. Alizarin Red staining in the constructs appeared to increase over culture time, indicating increasing mineral in the scaffolds. Scale bar = 5mm.

3.10.2 Cell survival in HOB scaffolds

Cell proliferation in the HOB-only scaffolds was assessed using Cell Titre Glo ATP assays for 28 days. Approximately 12,000 cells were seeded per gel, which was measured accurately by the ATP assay as seen in fig. 3.15A. Cells within these scaffolds proliferated steadily throughout culture time. Cell proliferation in these constructs was slower than in AM-1 single-cell cultures and in the HOS scaffolds.

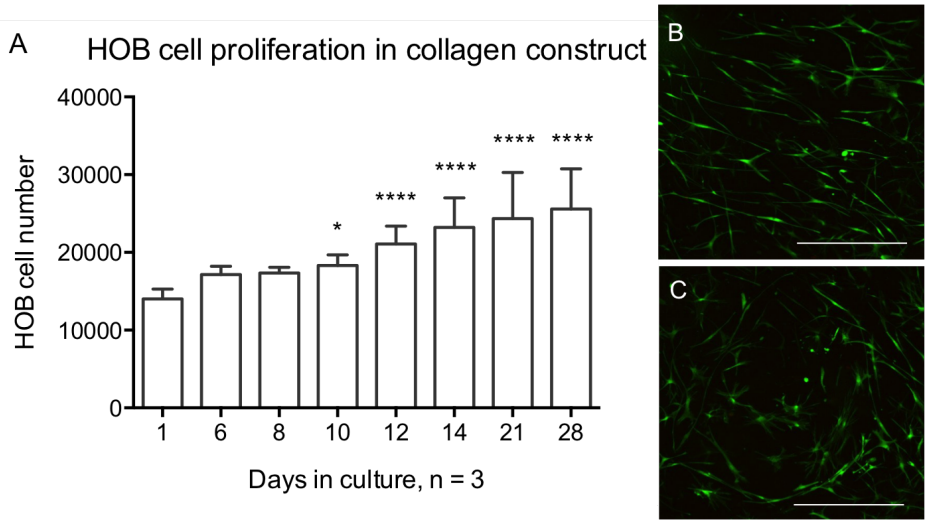

Figure 3.15: A) HOB cell proliferation in single-cell type collagen + Bio-Oss constructs as measured by the metabolic Cell Titre Glo ATP assay and normalised to values obtained from a standard curve. Cells proliferated significantly within the collagen + Bio-Oss constructs throughout the culture time. B) Live/Dead stained HOB cells on day 7 of culture. Cells appeared elongated and alive. C) Cells on day 14 of culture, with the majority of cells alive at this time point. Representative images of n = 3. One-way ANOVA (all time points compared to day 1), asterisks indicate significance levels as follows: * $p \leq 0.05$ and **** $p \leq 0.0001$. Scale bar = 100μm.

Live/Dead staining of the HOB cells in the collagen scaffolds revealed the cells to take on an elongated, fibroblast-like morphology (fig. 3.15B and C). The cells in the scaffolds formed an almost lattice-like structure. Both on days 7 and 14, a majority of the cells appeared to be alive within the scaffolds. Cell proliferation in the HOB cells was, as expected, noticeably slower than for HOS cells within the collagen scaffolds, and even by day 14, the scaffolds were not confluent.

The HOS and HOB cells within these constructs appeared mostly osteoblast-like in their morphology. HOS cells within the Bio-Oss-collagen scaffolds appeared small and rounded throughout - this is typical of the HOS

cell line and is also behaviour seen in 2D cultures. The cells were tightly clustered together in the scaffolds, with little migration evident. HOB cells on the other hand appeared initially elongated (preosteoblastic) and then mostly became stellate or more rounded with projections, indicating maturation into a potentially mineralising osteoblastic phenotype. This correlated with the mineralisation data obtained, where mineralisation of the scaffolds was indicated by a peak in ALP activity levels increased between days 7 and 10 of culture. Overall, these results indicated a suitable, bone-like environment for these cells.

3.11 Main findings and discussion

The development of the bone-like part of the co-culture scaffold involved several steps. The aims of this chapter were to first compare different methods for making bone-like scaffolds *in vitro*, and to ascertain that the developed bone-like scaffolds were able to support cell growth and mineralisation of the collagen matrix, to enable synthesis of reproducible, biomimetic scaffolds. Furthermore, cell behaviour in the scaffolds and the ease of scaffold manipulation were considered, as well as the consistent and reproducible manufacture of the bone-like constructs. In the initial collagen-only scaffolds, the following results were obtained:

- HOS cells within compressed collagen constructs in osteogenic media went on mineralise the construct in five weeks of *in vitro* culture. However, this culture time was deemed too long, as this was only the first step towards co-culture with ameloblastoma tumour cells.
- HOS cells remained mostly alive for 28 days within the constructs.

Different options for adding mineral more quickly to make the constructs more bone-like prior to AM-1 cell addition were therefore explored, and different bone particles to collagen ratios were considered: the 90% Bio-Oss blocks tested resulted in increased cell death and degradation of the block structure. Furthermore, the large size of the blocks potentially caused difficulties with nutrient diffusion through the constructs, oxygen gradients, hypoxia and waste products within the block constructs.
An approximate Bio-Oss content of 30-40% of the scaffold area was optimal for continued scaffold mineralisation, cell proliferation as well as scaffold visualisation and nutrient flow. In the bone-like Bio-Oss and collagen scaffolds developed in this chapter, the following results were observed:

- Bio-Oss bone particles were found a suitable addition due to their mineral content, cytocompatibilty and ease of incorporation to the compressed collagen constructs.
- The collagen and Bio-Oss models enabled the use of microscopes and a variety of different assays for analysis - this was convenient and did not significantly limit the analysis methods used in this project.
- The model was further optimised by substituting the HOS cells in the original bone model with primary human osteoblasts (HOB).
- HOB cells were shown to remain alive throughout culture time and were also found to mineralise the constructs.

- These results indicated that the collagen-Bio-Oss scaffolds were also able to support HOB cells and that these provided a suitable mineralised, bone-like growth environment for further co-culture with ameloblastoma tumour cells.

Previous studies have shown mineralising media to be an effective and relatively fast route to mineralisation of cellularised collagen-only scaffolds (Holy et al., 2000; Rattner et al., 2000; Pedraza et al., 2010). However, in this study, the addition of mineralising media to the collagen scaffolds resulted in a slow mineralisation rate. As expected, the addition of Bio-Oss to the collagen scaffolds quickly added mineral to these, and the resulting bone-like scaffold was found to promote the proliferation of osteoblastic cells. Mineralisation of the collagen-only scaffolds and Bio-Oss scaffolds was seen when these were examined using Von Kossa staining and Alizarin Red staining, where the scaffolds appeared increasingly mineralised during culture.
Furthermore, the cells within the scaffolds went on to further mineralise it, which was quantified by measuring ALP activity levels in the models as well as ALP and BMP-2 gene expression. An increase in ALP levels was seen in both the HOS- and HOB-cellularised scaffolds, and BMP-2 levels in the HOB-cellularised scaffolds also increased, indicating mineralisation of the scaffolds in culture.
BMP-2 has been shown to induce ALP activity and promote an osteoblast phenotype and maturation (Katagiri et al., 1994). Therefore, the results seen with HOB cultures with increases in both ALP and BMP-2 gene expression were to be expected and were indicative of bone synthesis within these scaffolds.
Levels of ALP activity seen in the Bio-Oss scaffolds in this study also closely followed those previously reported, where levels have been shown to initially increase and to then decrease; e.g. ALP activity has been found to increase in osteoblast-collagen cultures until day 16, and then decrease (Coyac et al., 2013). ALP is also not repeatedly required for continued mineralisation of the scaffolds (Rattner et al., 2000), which explains the decrease in ALP activity seen in the Bio-Oss scaffolds over time.

Retention of the smaller Bio-Oss particles within the collagen scaffolds was found difficult during this project. Some Bio-Oss particles (with cells migrated inside them) became dislodged and removed from the collagen constructs during handling, which may have contributed to decreases in some assay results on the later dates of analysis, e.g. ALP levels, cell proliferation and gene expression.
Further scaffold development could include ensuring the Bio-Oss particles were of a more uniform size distribution than in the models used here. In these models, the particle size was up to 200μm, ideally the particles would have been less than 100μm throughout the constructs. A more uniform size distribution could have been achieved by grinding the particles prior to incorporation; however this could have compromised the sterility of the Bio-Oss granules.
Additionally, from a practical point of view, the blocks were opaque, which lead to difficulties with cell visualisation once inside the blocks, as well as difficulties in attempting to extract cells from the blocks for further analysis.
Matrix stiffness is widely recognised as an important factor in cell proliferation, differentiation and behaviour

(Ghosh and Ingber, 2007; Hadjipanayi et al., 2008, 2009; Karamichos et al., 2007). Therefore, dynamic mechanical analysis was used to determine the elastic modulus of the bone-like scaffolds. This study was the first to carry out a mechanical study on Bio-Oss particles cultured *in vitro*. To date, only one study has examined the mechanical properties of Bio-Oss in rabbits (Orr et al., 2001), even though the decellularised bone substrate is used clinically for both human and canine bone defect augmentation (Carmagnola et al., 2000; Degidi et al., 2013; Piattelli et al., 1999).

A selection of bone tissue-engineered material stiffnesses used was outlined in table 1.6. The elastic modulus of the Bio-Oss + collagen scaffolds as measured during this study was found to be 155.3 $\pm$ 10.78MPa. This is stiffer than most other collagen-based scaffolds used for tissue engineering purposes, but still less stiff than other materials used for bone augmentation.

The properties outlined in table 3.2 were used to guide scaffold optimisation. The bone-like scaffolds were considered biomimetic due to the addition of *ex vivo* mineral to the scaffolds in the form of Bio-Oss, which contributed both mineral and increased the matrix density and scaffold stiffness as seen in fig. 3.12. Furthermore, the both the HOS and HOB cells in the scaffolds were seen to synthesise factors specific to osteoblasts, namely ALP, BMP-2 and to increase the mineral content of the scaffolds.

The 30-40% Bio-Oss particle to 60-70% collagen scaffolds additionally allowed for visualisation of the cells within the scaffolds, and they appeared alive and producing mineral throughout the culture time. Furthermore, the fact that the majority of the scaffold was collagen also allowed the models to be viewed in their 3D environments under various microscopes, stained *in situ*, and cells to be extracted for further analysis from them relatively easily. This bone-like scaffold was then used for development of a bone-like co-culture model together with ameloblastoma cells.

The final 14 day pre-culture (mineralisation) period was chosen based on the results presented here, where the optimum mineralisation and cellular proliferation within the scaffold was achieved between days 10 and 14 of culture. AM-1 cells were then added to the bone-like scaffolds developed in this chapter in order to develop ameloblastoma co-culture models, as described in chapter 4.

Chapter 4

Bone-like model and ameloblastoma co-culture

This chapter first details the results obtained when culturing AM-1 cells both on tissue culture plastic and in AM-1-only collagen gels. Then, the details of the basics of the co-culture models attempted during this project are described. Ultimately, the final co-culture model used in this project to make a novel organotypic bone-like model for the ameloblastoma tumour is described. This co-culture model developed initially for the bone-like scaffolds was then used as a basis for the soft tissue co-cultures described in chapter 5.

The aims of this chapter were firstly to maintain AM-1 cells alive within a collagen matrix and to characterise AM-1 cells in a three-dimensional model. Secondly, the aim was to develop a co-culture scaffold with the bone-like constructs and to sustain both cell types in a co-culture scaffold. Thirdly, using these co-culture scaffolds, the aim was to characterise cellular events, changes in gene expression and invasion caused by the co-culture of AM-1 cells with bone cells.

In this chapter, results obtained from these bone-like and AM-1 co-culture models are presented. HOS + AM-1 co-cultures were used initially, as these allowed for rapid construction of reproducible bone-like models to be co-cultured with the ameloblastoma cells. Throughout HOS + AM-1 co-culture however, it was recognised that any results obtained with this co-culture model was potentially due to the cancerous nature of the HOS cells. The results obtained with HOS + AM-1 co-culture scaffolds were therefore further validated by substituting the HOS cells in the models with HOB cells (HOB + AM-1). These experiments were carried out after the HOS experiments, but the results are presented here concurrently with the HOS results for ease of comparison of the two models.

4.1 Summary of methods

Cells from the AM-1 cell line were initially cultured in plastic compressed type I rat-tail collagen-only constructs for up to 28 days in order to ensure cell survival and to probe the behaviour of these cells in a 3D culture system.

For co-culture assembly, 5mm x 5mm bone-like HOS and HOB scaffolds, made with collagen and Bio-Oss particles, were pre-cultured for 14 days in osteogenic media for mineralisation and cell expansion. Mineralised bone-like scaffolds were then co-cultured with freshly made AM-1 cellularised scaffolds for up to 14 days in KSFM to construct the organotypic *in vitro* co-culture models. A single co-culture scaffold was 10mm x 5mm in size, and they were on average 400μm in thickness.

Cell metabolic levels, to give an indication of proliferation within the constructs, were analysed using the Cell Titre Glo ATP 3D reagent. Gene expression analysis in the co-cultures was carried out on Qiagen RNasy-extracted RNA (HOS + AM-1 co-cultures) and Trizol-extracted RNA (HOB + AM-1 co-cultures) and Taqman primers and polymerase.

Confocal microscopy was used for immunocytochemistry and Live/Dead assays in AM-1-only cultures as well as HOS + AM-1 and HOB + AM-1 co-cultures. Cell invasion in the HOB + AM-1 models was characterised using Cell Tracker fluorescent dyes and fluorescence microscopy for up to 14 days.

4.2 AM-1 cell culture in 2D and 3D

AM-1 was found to be a slow growing cell line on tissue culture plastic. The cells grew in islands (fig. 4.1A-B), which increased in size with increasing culture time. The cells were small in size with a varied morphology, mostly characterised by a cobblestone-like appearance and clustering behaviour. This characteristic morphology was especially prominent when the cells were approaching confluency.

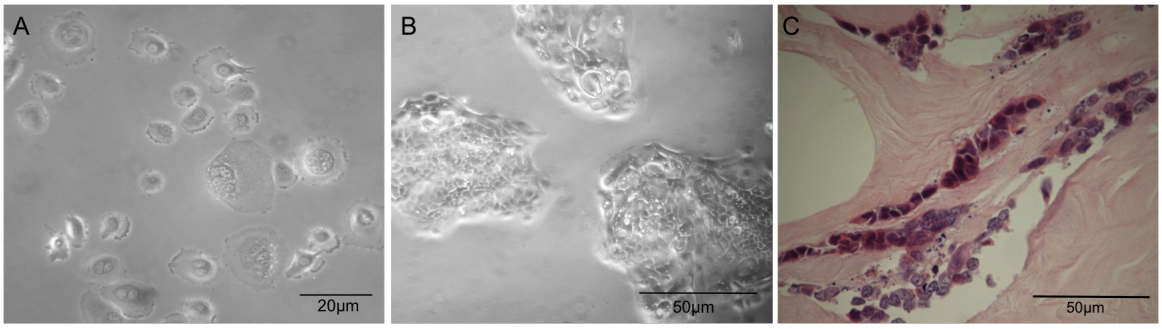

Figure 4.1: Light micrographs of AM-1 cells in culture. A) AM-1 cells cultured for 3 days on tissue culture plastic. Cell proliferation was slow initially due to the sparse seeding density. Single AM-1 cells (as the one in the middle of the image) appeared spread out over larger areas. AM-1 cells mostly appeared cobblestone-like, but cell morphology was not uniform. B) AM-1 cells cultured for 10 days on tissue culture plastic. Here, the characteristic clustering of AM-1 cells was seen as the cells grew more confluent. The middle of these clusters frequently had a larger density of cells, leading to crowded cluster centres and cells not growing in a monolayer. C) Histological staining of an AM-1 cellularised collagen gel. Cells (purple) within the collagen constructs (pink) also appeared clustered when stained using H&E staining on 14-day 3D collagen culture. Clustering behaviour is typical for ameloblastoma cells. Scale bar in A = 20μm, B and C = 50μm.

Clustering of AM-1 cells was also seen in 3D collagen cultures and was confirmed using histology as seen in fig. 4.1C. The clustering behaviour of the cells seen in the histological specimen is typical ameloblastoma tumour behaviour, indicating that the collagen matrix was a suitable growth environment for these cells. The compression technique rendered the collagen matrix striated, whereas the processing techniques used for histology caused folding of the collagen scaffolds and the apparent gaps in the scaffolds as seen in fig. 4.1C.

The cells in the clusters appeared mostly to be daughter cells of one original cell at that location, rather than caused by migration within the structures, although larger clusters were found to merge in longer term cultures. Immediately after seeding in collagen gels, when viewed under a fluorescent microscope, the AM-1 cells appeared as a monodispersion as can be seen in fig. 4.2B. This clustering effect was therefore not due to insufficient mixing after cell resuspension during passaging or at the seeding stage.

4.2.1 AM-1 cell viability in collagen scaffolds

Cell proliferation in AM-1-only 3D collagen constructs was assessed using the Cell Titre Glo ATP assay. Figure 4.2A shows the increase in cell proliferation in these constructs over 28 days in culture. Each construct, when cut immediately after compression, initially contained approximately 3,000 cells. AM-1 cells proliferated quickly and steadily in 3D collagen gels as seen in fig. 4.2A. By day 14 of culture, there were approximately ten times more cells in the scaffolds than when first seeded. By day 28, each cut construct contained approximately 100,000 cells, with the constructs appearing confluent.

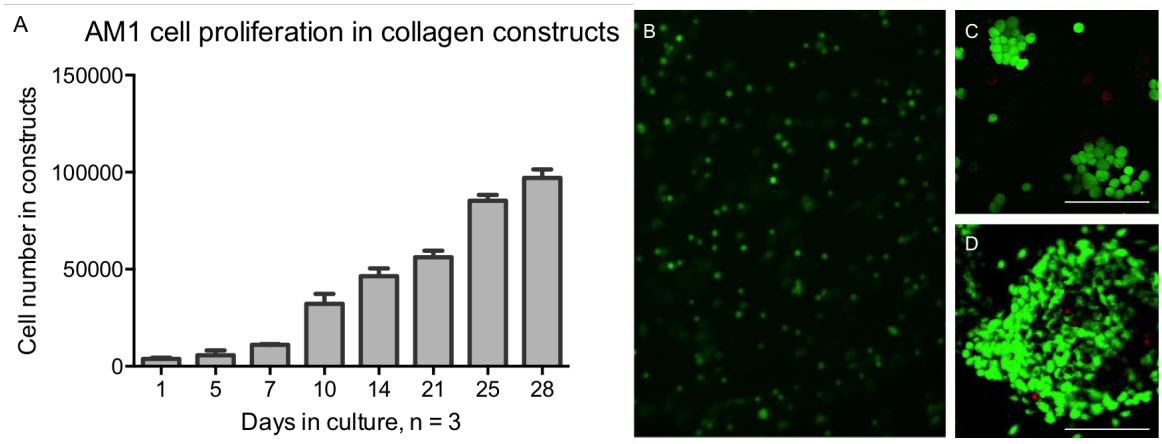

Figure 4.2: A) AM-1 cells proliferated when added to the collagen constructs. On day one, approximately 3,000 cells were present in each of the collagen constructs. Cell proliferation continued steadily within the constructs throughout the 28 day culture period. Luminescence readings were normalised to an AM-1 standard curve to obtain the corresponding cell numbers. Error bars = 95% CI. B) Live/Dead stained AM-1 cells (stained green) within the collagen constructs appeared monodispersed when first incorporated into the scaffold. No dead cells (stained red) were visible at this early time point (2h post seeding). The cells in the scaffolds also appeared rounded, as they did not yet have time to attach to the scaffolds after trypsinisation and seeding. This image is a 10X magnification. C) Live/Dead stained AM-1 collagen cultures on day 7 of culture. Cells appeared clustered in these constructs and remained alive. D) AM-1 cell clusters had increased in size by day 28, and the cells were still mostly alive after this long culture time. Some dead or dying cells were seen in the middle of these large clusters. Scale bars = 25μm.

AM-1 cell survival in the single-cell constructs was also assessed qualitatively using Live/Dead staining

(fig. 4.2B-D). Here, live AM-1 cells (green) and dead AM-1 cells (red) are seen at two hours after incorporation into the collagen gels (fig. 4.2B), and on days 7 (fig. 4.2C) and 28 (fig. 4.2D) of culture. The size of these clusters increased with increasing culture time. Initially, the clusters were less tightly packed (fig. 4.2C), with a rounded cell morphology. At the last time point (fig. 4.2D), the clusters were tightly packed, with the cells appearing slightly smaller and flattened as they became more crowded within the clusters. By the later time points, some AM-1 cells in the middle of the large clusters appeared dead (stained red), indicating that within the cluster core there was probably at least some level of hypoxia or a limited flow of nutrients, which caused the cells to die, although this would need to be confirmed with further assays. Hypoxia staining assays, such as the fluorescent Image-iT assay (Thermo Fisher), are available commerically and could be used here.

From one week in culture onwards, these clusters of AM-1 cells were prominent in the collagen models, and could be used to (by eye) distinguish the AM-1 cell type from the other cells in the models when examining the co-cultures microscopically. The AM-1 cells within these cultures were rounded and most often found in the aftermentioned clusters. HOS and HOB cells on the other hand were elongated, with HOB cells even displaying the occasional stellate morphology. AM-1 cells were also smaller in size (approx 10μm), and HOS and HOB cells were larger, although their size varied depending on the amount of individual cell elongation. Furthermore, HOS and HOB cells were found in the collagen + Bio-Oss parts of the co-cultures, where Bio-Oss granules were prominent, whereas in the AM-1 part of the constructs, no Bio-Oss granules were present.

4.3 Initial attempts at incorporating AM-1 cells in co-culture models

Once AM-1 cells were successfully maintained within the collagen constructs, several ways to incorporate AM-1 cells in the models were considered and are briefly discussed below. The main consideration for incorporation of AM-1 cells in co-cultures with the bone-like constructs was that the bone-like model was already mineralised once the co-culture phase of the experiments began. Based on the results detailed in chapter 4, it was decided day 14 of bone model culture was optimal for AM-1 addition.

4.3.1 Synthesis of AM-1 spheres for tumour models

Initially, it was thought the inclusion of AM-1 cells as pre-made spheres would be a suitable way of incorporating AM-1 cells to create co-culture models. Two methods commonly employed for sphericalisation of cell cultures were used to make AM-1 spheres:

First, a rotational culture was attempted. In this type of culture, due to the constant agitation of the culture media, the cells are inhibited from attaching to the flask and therefore attach to other cells in the culture. However, during attempted rotational culture, the AM-1 cells died and formed sheets of cell debris, rather than forming spheres with living, aggregated cells (results not shown).

Second, an ultra low-attachment (ULA) plate method was used. Similarly to the rotational culture method, the coating on the ULA plate prevents cell attachment. As an alternative, the cells attach to each other and thus form spherical aggregates during culture. HOS cells were used as a control and as a reference for the required culture time, as cancerous cell lines readily form spheres.

Figure 4.3 shows that HOS cells (indicated by arrows) were seen to start aggregating after a few hours in culture on the ULA plates (fig. 4.3A), and had formed very large aggregates by the end of culture (fig. 4.3B). AM-1 cells (indicated by arrows) were imaged as single cells after 4 hours in culture (fig. 4.3C). Even after 72 hours of culture, when HOS cell spheres were readily seen, AM-1 cells had not formed aggregates (fig. 4.3D). A large proportion of the AM-1 cells appeared dead after 72 hours of ULA culture when viewed under a light microscope.

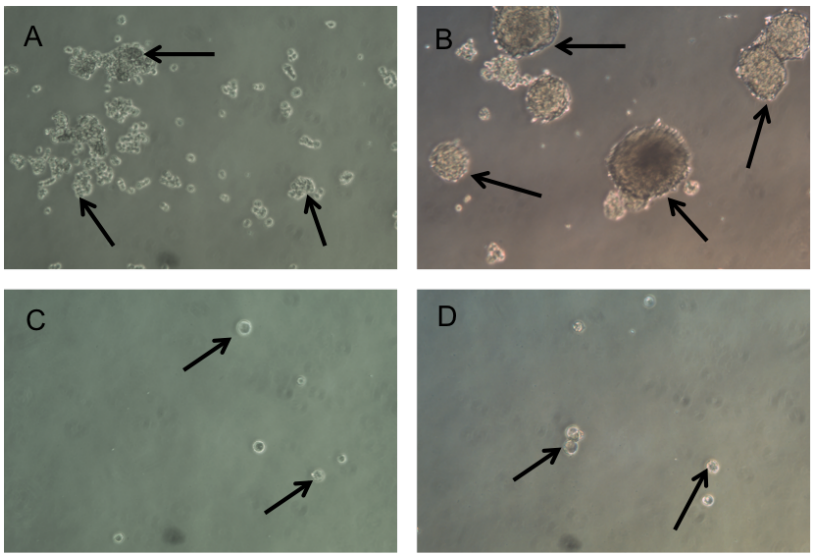

Figure 4.3: Light micrographs of attempted AM-1 sphere cultures on ultra-low attachment plates. HOS cells were used as a control. A) HOS cell culture after 4 hours on low-attachment plates. These cells were already beginning to cluster (arrows). B) HOS cells after 3 days in culture, where large spheres were seen (arrows). C) AM-1 cells at 4 hours in culture, with single AM-1 cells are indicated by arrows. D) AM-1 cells after 3 days in culture. Two or three-cell clusters were seen at most (arrows), but AM-1 cells were largely found in a monodispersion. Some AM-1 cells also appeared dead or dying by this point. Representative images of n = 3. All light micrographs are a 10X magnification of ULA plates using a light microscope.

These results indicated that AM-1 cells were contact dependent and that it would therefore be difficult to include these cells in the collagen constructs as pre-made tumour spheres. Consequently, a monodispersion of AM-1 cells was a more optimal way of incorporating these cells in the models for the subsequent experiments.

4.3.2 Further AM-1 incorporation attempts

During co-culture model development using collagen constructs with monodispersions of AM-1 cells, a range of scaffold assembly options were explored in order to obtain a co-culture model which was both easy and reproducible to assemble. Initially, a model where a punch biopsy of the bone-like matrix was removed from the centre of the construct (fig. 4.4) was considered. The removed section allowed incorporation of an un-

compressed, AM-1 cellularised collagen scaffold, which was then compressed for scaffold attachment. This allowed for assembly of a tumour construct with the organotypic tissue model on all sides, thereby better mimicking the *in vivo* situation of a tumour surrounded by ECM. Once the sections were removed, an AM-1 cellularised collagen gel was placed in the resulting perforation and the constructs were compressed to attach the two gels together.

Figure 4.4: Holes were made in the centre of collagen gels using Harris Unicore biopsy punchers in an attempt to assemble the co-cultures. AM-1 cellularised collagen gels were then included in the resulting holes and the constructs were compressed for co-culture assembly. Note that the samples shown in this image were not the final bone-like gels with Bio-Oss, but an acellular pilot set. Scale bar = 10mm.

In most of the co-culture constructs assembled using the biopsy punch technique, the AM-1 construct dissociated from the gel upon initial immersion in the culture media. The remaining constructs, which were successfully immersed in media and incubated, dissociated in culture overnight. This indicated that the two separate gels, despite the inherent stickiness of collagen and the tendency of the single-cell type models to fold and attach to themselves, would be difficult to maintain attached without some other attachment method. Therefore, this technique proved inefficient in manufacturing co-cultures for this project.

Attempts at injecting a concentrated suspension of AM-1 cells into the pre-cellularised and mineralised HOS constructs on day 14 were also made. This would have allowed omission of the non-mineralised collagen in which AM-1 cells were incorporated during AM-1-only culture, and thus provided a more organotypic AM-1 growth environment and model. However, with this method it was difficult to gauge when the needle was inside but not through the compressed collagen gel (of approximately 400μm in thickness), so that the AM-1 cells were added inside the construct.
Furthermore, it was difficult to know how many cells had been incorporated and whether they all remained inside the constructs, as the cell suspension was prone to leaking out of the constructs upon application of pressure to the syringe. Finally, it proved difficult to reliably replicate syringe positioning and thereby AM-1 cell location between constructs.

4.4 Final bone-like co-culture set-up

The final set-up for the bone-like co-cultures was as seen in fig. 4.5. By using this set-up, three distinct cell environments were created: a population of cells which was only made up of bone cells (initially HOS-

cellularised constructs, and to validate the results also HOB-cellularised constructs), and one which was only made up of AM-1 cells (AM-1 model). The third part consisted of a cell population in the middle (interface; IF) where the two cell types were interacting in a mixed population through both the physical proximity of the two gels, as well as any potential invasion occurring at the interface and any chemokines and growth factors exchanged by the two cell types. However, this method of constructing the co-culture models necessitated the addition of an approximately $50/mu$m acellular layer to combine the two cellularised gels, as initial and lasting attachment without it was difficult.

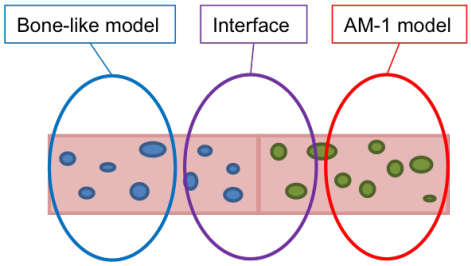

Figure 4.5: Schematic of the final bone-like co-culture model set up. The schematic also shows the three parts of the co-cultures, the AM-1 part, the bone-like part and the interface between the two construct types. The final co-cultures were split into these three parts in most analyses as indicated in this schematic. Note that this schematic does not include the acellular gel layer.

This method further enabled separation of the two cell types after culture prior to analysis, as well as viewing of the two cell types concurrently using microscopy techniques. Separation of the constructs was carried out by cutting the co-cultures into three parts using a scalpel prior to analysis. Additionally, in theory these co-culture constructs provided an internal, single cell type population, as controls at the non-interface edges of the constructs.

4.5 Cell proliferation in bone-like co-culture models

Cell proliferation in both types of bone-like co-cultures was measured over time using Cell Titre Glo. The results are shown here together with confocal micrographs of Live/Dead stained HOS, HOB and AM-1 cells in the co-culture models.

HOS + AM-1 models

Cell numbers for both cell types in the HOS + AM-1 co-cultures were found to increase with culture time as seen in fig. 4.6. AM-1 proliferation in the co-cultures was initially slow, but increased in the second week of co-culture. This was also reflected in the Live/Dead stained samples, where AM-1 cells as seen in fig. 4.6 remained alive in the co-cultures. The AM-1 cells clustered, and cluster size was seen to increase with culture time (fig. 4.6). Clustering was to be expected, as AM-1 is of follicular origin.

HOS cell proliferation was more gradual, which was due to the constructs having been cultured for 14 days prior to incorporation in co-cultures (fig. 4.6). HOS cells outnumbered the AM-1 cells, with approxi-

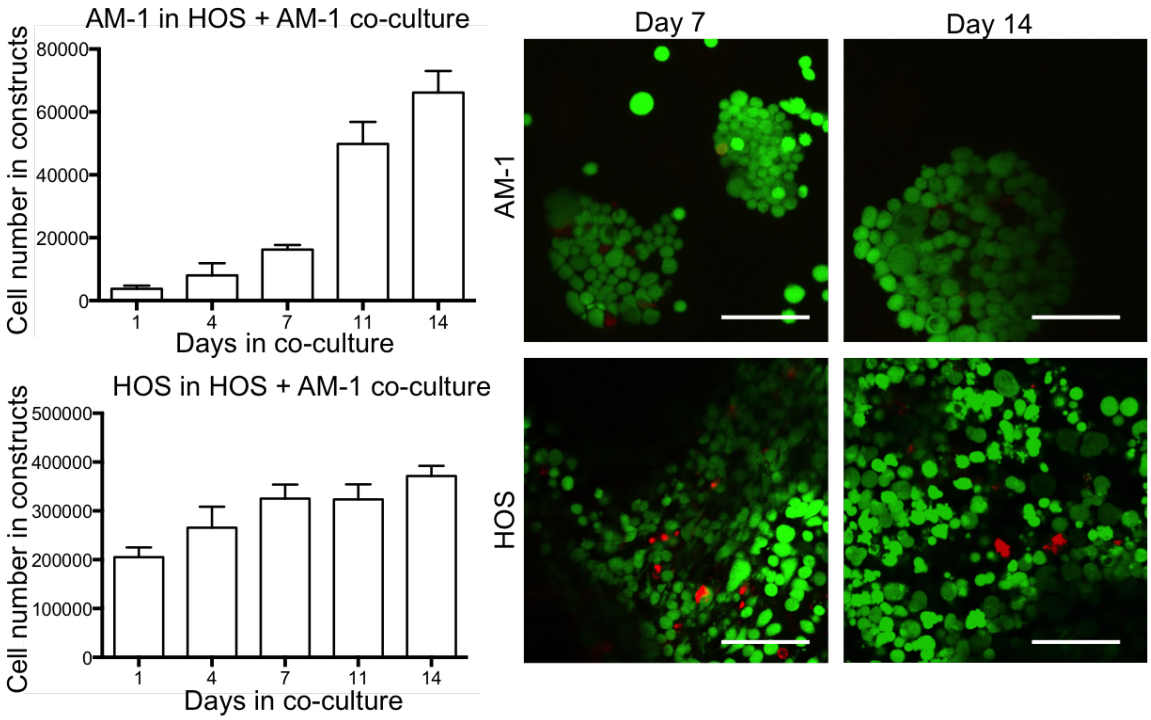

Figure 4.6: Cell proliferation for AM-1 cells and HOS cells in the co-cultures is shown in the two histograms. AM-1 cells proliferated at a relatively fast rate throughout the culture time. HOS cell proliferation was slower overall. Confocal micrographs of Live/Dead stained co-culture constructs showed that AM-1 cells remained alive (in green) within the scaffolds. The characteristic AM-1 clusters appeared to grow in size with increasing cell numbers through proliferation. HOS cells appeared mostly alive when Live/Dead stained, but increasing numbers of dead cells were seen. The HOS part of the constructs appeared confluent by day 14 of co-culture. Histograms: error bars = 95% CI, n = 3. Confocal micrographs: scale bars = 50μm, n = 3.

mately 350,000 cells measured within the constructs on day 14 of co-culture.

HOS cells, when Live/Dead stained, appeared mostly alive in these scaffolds as visualised in fig. 4.6. However, the HOS parts of the constructs were very confluent, and this had caused the cells to become smaller and more rounded as a result of a lack of space within the constructs. Due to the confluent constructs, as well as the long-term culture these cells were subjected to, there was also an increasing amount of cell death seen in the HOS parts of the co-cultures.

HOB + AM-1 models

HOB cells appeared larger and stellate with osteoblast-like cell morphology at both days 7 and 14 in co-culture (fig. 4.7). The HOB cellularised scaffolds, as seen previously in the single-cell constructs, were approaching confluency. Therefore, the number of HOB cells plateaued at the later time points measured as seen in fig. 4.7. HOB cells continued proliferating, and remained mostly stellate in their morphology but with some more elongated cells.

AM-1 cells were seen to proliferate in co-culture with HOB cells. AM-1 cells also appeared alive when Live/Dead stained on days 7 and 14 of co-culture. The cells, as seen in fig. 4.7, formed large clusters, characteristic of the cell type.

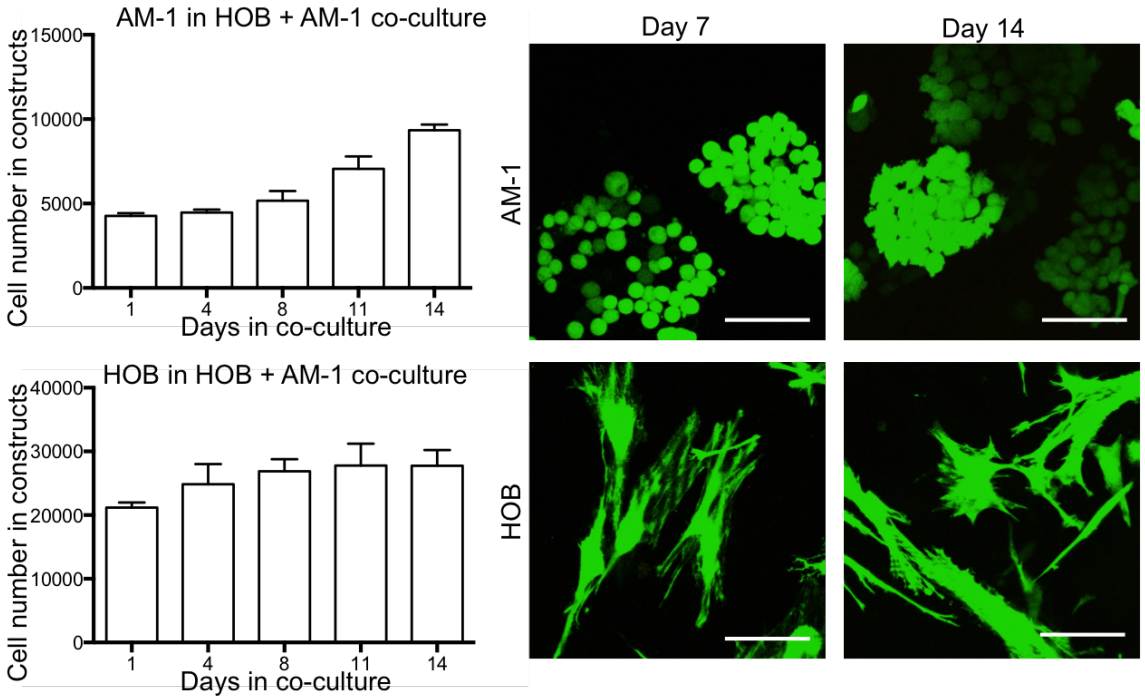

Figure 4.7: Cell proliferation for AM-1 cells and HOB cells in co-cultures is shown in the two histograms. AM-1 cells in co-culture appeared alive (in green) when stained using Live/Dead staining on days 7 and 14 of co-culture. AM-1 cells were characteristically rounded and clustered on both time points, with an increasing number of clusters seen with increasing culture time. HOB cells also remained alive within the co-culture scaffolds when Live/Dead stained on days 7 and 14. Striations in the HOB cells on day 7 were due to the sample moving when imaged in the Z-plane. Histograms: error bars = 95% CI, n = 3. Confocal micrographs: scale bar = 50μm, n = 3.

Interestingly, AM-1 cell proliferation appeared faster in the HOS co-cultures than in the HOB ones, with AM-1 cell numbers at the end of culture time in the HOS co-cultures approaching 80,000 cells per construct, whereas only 10,000 cells per construct were measured in the HOB co-cultures. In co-culture with HOB cells, AM-1 proliferation was slow throughout culture time (fig. 4.7). The AM-1 cell clusters also appeared smaller in co-culture with HOB cells than with HOS cells.

Cell-to-cell interactions were observed in both co-culture scaffolds. However, no migration was seen in the HOS + AM-1 scaffolds, even though the cells appeared in close contact with each other at the interface on day 14 of co-culture.

Contrastingly, in the HOB scaffolds, close co-localisation and potential cell-to-cell interactions at the co-culture interface were observed early on in co-culture (on day 7), as is seen in fig. 4.8A. In this figure, HOB cells are elongated in their morphology, whereas AM-1 cells are smaller, rounded and in clusters. Close cell-to-cell interactions were further observed in samples on days 10 and 14 (fig. 4.8B-C). In the image from day 14 in fig. 4.8C, the AM-1 cells had migrated to the HOB side of the scaffolds. Furthermore, potential AM-1 migration was seen relatively far inside the HOB scaffold - approximately 2mm towards the central parts of the HOB scaffold. That migration occurred in the HOB + AM-1 co-cultures but not in the HOS + AM-1 co-cultures was thought to be due to the non-cancerous nature of the HOB cells, as well as the locally

invasive capacity of the AM-1 cells.

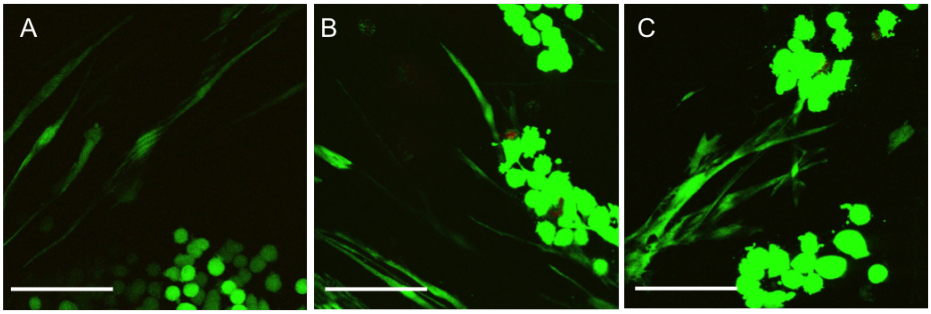

Figure 4.8: Cell-to-cell interactions in the HOB + AM-1 co-cultures. Live/Dead stained samples as seen using the confocal microscope. A) A day 7 co-culture sample, B) A co-culture sample on day 10 and C) A sample on day 14 of co-culture. At all time points, AM-1 cells appeared in clusters, with HOB cells more elongated. The two cell types were seen to interact in close proximity by day 7. The AM-1 cells took up more stain than the HOB cells, which resulted in stongly stained AM-1 cells and faintly stained HOB cells. Scale bar = 50μm.

It was also observed that HOB cells close to 'invading' AM-1 cells were more elongated (fig. 4.8) than cells towards the middle of the HOB constructs, which were not in contact with AM-1 cells (fig. 4.7). The most osteoblast-like cells seen in the co-culture scaffolds were found close to Bio-Oss granules in the scaffolds and not in the vicinity of AM-1 cells.

However, despite their distinct morphologies, the cells in fig. 4.8 were only stained with Live/Dead staining. Therefore, it was at this stage not possible to definitively determine that the cells with different morphologies were in fact cells from the distinct populations.

4.6 Gene expression in the bone-like co-cultures

Gene expression in the HOS co-culture models was examined using qRT-PCR on RNeasy-extracted RNA from three parts of the co-culture models: the HOS part, the interface (IF) and the AM-1 part. Gene expression in the HOB + AM-1 co-cultures was similarly analysed for the same construct areas, but using Trizol-extracted RNA. As RNA from these two different co-culture types was extracted using two different methods, caution should be taken when comparing these two sets of results.

For each gene analysed, the results for HOS + AM-1 co-cultures are presented first, followed by HOB + AM-1 results. For TRAIL gene expression, the results for both models are shown in one graph. Significant findings are indicated by asterisks. The asterisks are positioned on the bar which has a p value of ≤ 0.05 when compared to the corresponding single-cell type control.

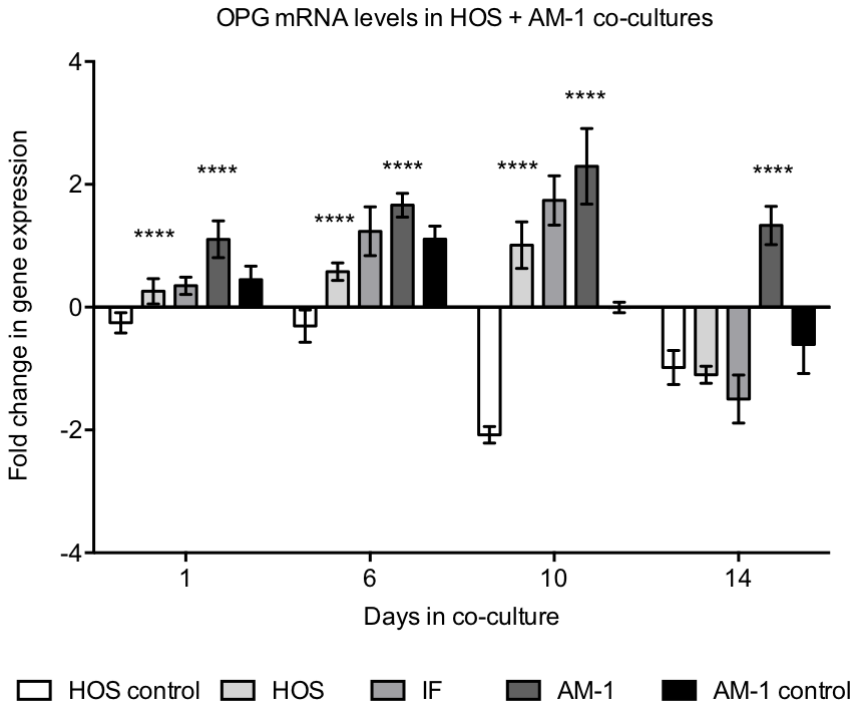

Figure 4.9: OPG expression in HOS + AM-1 co-cultures. OPG expression in the HOS controls remained low throughout culture and reduced in AM-1 controls. In HOS cells in co-culture, OPG expression was upregulated on days 1-10, but reduced on day 14. OPG gene expression in AM-1 cells in co-culture was found steadily upregulated throughout culture time. Two-way ANOVA, **** indicates $p \leq 0.0001$. Error bars = 95% CI, n = 6.

4.6.1 Osteoprotegerin gene expression

HOS co-cultures

Osteoprotegerin (OPG) is upregulated in bone synthesis *in vivo* and as it plays a role in bone turnover it was chosen as one of the genes examined during this study. Gene expression analysis in HOS co-cultures revealed a decrease in OPG in the models. Initially, expression in all parts of the models was slightly higher than the day 0 calibrator samples. OPG expression in the single-cell type bone model was lower throughout the culture time. However, OPG expression in the bone and interface parts of the co-cultures decreased significantly over the 14 day co-culture period.

As visualised in fig. 4.9, OPG expression levels in the HOS controls were significantly different when compared to the HOS co-cultures on days 1, 6 and 10 (all $p \leq 0.001$). OPG expression was also found significantly different in the AM-1 co-culture samples when compared to the AM-1 controls (all $p \leq 0.0001$). While OPG expression in the HOS controls had remained decreased throughout culture, and OPG expression in the HOS parts of the co-culture models had reduced over time, there was no reduction in OPG expression seen in the AM-1 parts of the co-culture constructs. The AM-1 part of the co-culture models was the only part of these models where OPG expression did not reduce over time, and it was maintained at an approximately 2-fold level compared to the calibrators throughout culture time.

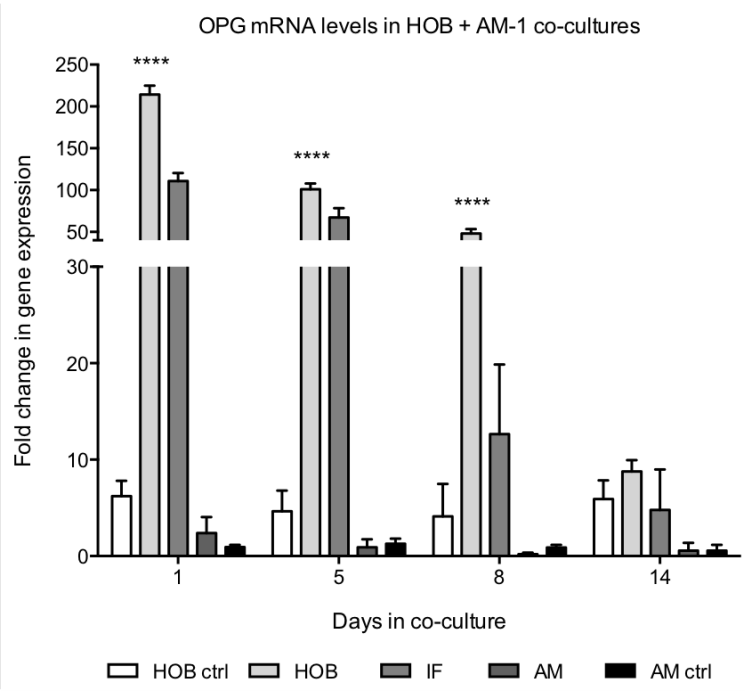

Figure 4.10: OPG expression in HOB + AM-1 co-cultures. OPG levels in the HOB and AM-1 control samples were found uniform and constant throughout culture time. HOB cells in co-culture initially displayed greatly upregulated HOB gene expression, which reduced over time. OPG expression in AM-1 cells in co-culture remained unchanged throughout culture time and was not found significantly different to OPG levels measured in the control AM-1 cells. Note the split y axis. Two-way ANOVA, **** indicates $p \leq 0.0001$. Error bars = 95% CI, n = 4.

HOB co-cultures

No significant difference was found in OPG expression levels in AM-1 cells grown in single-cell culture and in co-culture with HOB cells over time, with mRNA levels in both consistently appearing close to calibrator values.

HOB cells on the other hand exhibited a large increase in OPG expression when in co-culture with AM-1 cells. As can be seen in fig. 4.10, this increase was initially approximately 200-fold on day 1, prior to reducing to 50-fold on day 8 of co-culture. The levels of OPG mRNA when in co-culture with AM-1 cells compared to single-cell culture on their own was found statistically significant on days 1, 5 and 8 ($p \leq 0.0001$).

By day 14, OPG levels in the HOB parts co-culture constructs had reduced to a level similar to that in the control samples.

As can be seen when comparing fig. 4.9 and fig. 4.10, the HOB co-cultures showed a larger overall increase in OPG expression compared to the HOS co-cultures. Levels measured in the HOB co-cultures were increased 200-fold, whereas at most the increase seen in the HOS co-cultures was 2-fold. This may be due to the cancerous nature of the HOS cells, which in their native osteosarcoma environment increase bone resorption and therefore may downregulate OPG expression even in these co-cultures. The OPG levels seen in the HOS co-cultures were somewhat influenced by the presence of AM-1 cells, but this effect only lasted for the first ten days in culture.

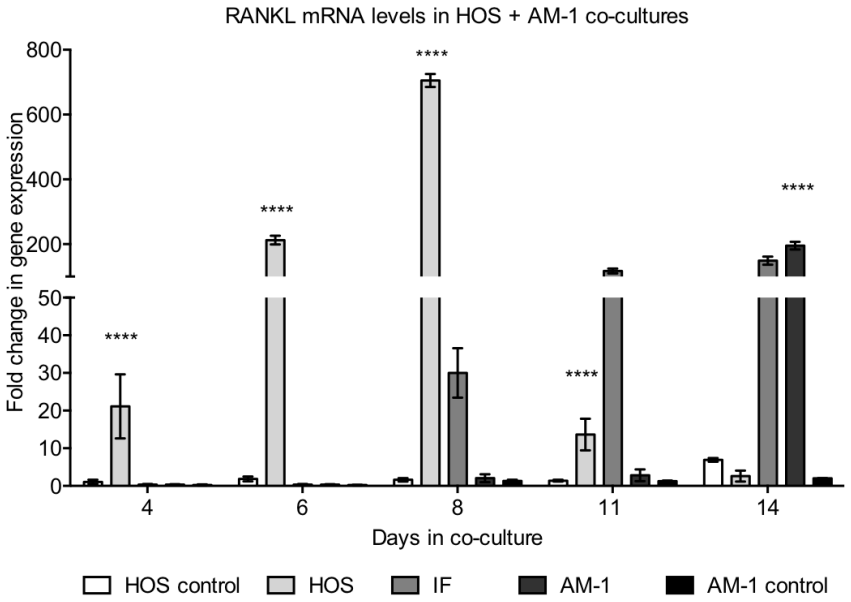

Figure 4.11: RANKL gene expression levels were quantified using qRT-PCR. RANKL expression in both the HOS and AM-1 controls remained low throughout culture time. There was a large increase in RANKL expression in HOS samples when cultured with AM-1 cells, which peaked on day 8 of co-culture. An increase was also seen in the AM-1 cells in co-culture, however this occurred later, on day 14 of co-culture. Note the split y axis. Two-way ANOVA, **** indicates $p \leq 0.0001$. Error bars = 95% CI, n = 6.

The upregulation of OPG in the HOB parts of the HOB + AM-1 co-cultures appeared to be a rapid response to the co-culture environment and the presence of AM-1 cells. However, gradually OPG levels reduced in these co-cultures. This could again be due to the HOB cells themselves downregulating OPG expression over culture time, or as a result of the co-culture environment.

4.6.2 RANKL gene expression

RANKL is an indicator for the potential activation of osteoclasts and bone resorption and was as such another gene examined using qRT-PCR. Based on previous increases in expression seen in ameloblastoma samples by Qian and Huang (2010), RANKL expression was analysed in these models for potential increased ameloblastoma cell invasion and putative bone resorption. The results for RANKL expression in HOS + AM-1 co-cultures are seen in fig. 4.11, and for HOB + AM-1 co-cultures in fig. 4.12.

HOS co-cultures

For HOS + AM-1 co-cultures, gene expression analysis revealed a 700-fold increase in RANKL expression in the HOS part of the bone-like co-culture model on day 8 of HOS + AM-1 co-culture as seen in fig. 4.11. There was also a 200-fold increase in RANKL expression in the AM-1 part on the day 14 time point when AM-1 cells were in co-culture. No such increases were seen in the other parts of the models or the single-cell type controls. In the single cell type control cultures, RANKL expression levels were up to 2-fold different in the AM-1 controls than the calibrator samples, and at most 7-fold increased in the HOS controls.

A statistically significant increase in RANKL levels was found in AM-1 cells in co-culture with HOS

cells when compared to the AM-1 control samples on day 14 of co-culture ($p \leq 0.0001$). RANKL expression in the HOS part of the co-cultures increased over time and was significantly upregulated compared to HOS controls on days 4, 6 and 8 in co-culture (all $p \leq 0.0001$). On day 11, RANKL levels in the HOS co-cultures had reduced to day 4 levels, but were still significantly upregulated compared to the control samples ($p \leq 0.0001$).

The increase in most parts of the co-culture models was in the region of 1-2-fold that of the single-cell type untreated controls. A gradual increase in RANKL expression was seen in the interface part, which reflected the increase seen in the other co-culture parts. This gradual increase in the IF part indicated that expression was upregulated in the HOS co-culture samples due to the presence of AM-1 cells, which then caused the expression levels to increase in the IF part, as well as the AM-1 part.

These results indicated that both AM-1 and HOS cells were trying to upregulate bone resorption in these *in vitro* models by secreting osteoclast activating factors, although the upregulation of RANKL in the AM-1 parts was more gradual and may have carried on past the 14 days of co-culture examined here. In HOS, this increase was only seen during the first week; expression decreased by day 11.

However, this increase could either be due to the presence of HOS cells or AM-1 cells in the co-culture models. HOB + AM-1 co-cultures were therefore used to further probe RANKL expression and to confirm what this increase in expression was due to.

HOB co-cultures

In HOB + AM-1 co-cultures, RANKL was found elevated at most time points, with the greatest increase in expression on days 5 and 8 as visualised in fig. 4.12.

When the HOB control samples were compared with the HOB co-culture samples and AM-1 control samples were compared with AM-1 in co-culture, RANKL gene expression was found significantly increased at days 1, 5 and 8 ($p \leq 0.0001$ for all). RANKL expression in the HOB co-culture samples was reduced on day 14 compared to the HOB-only control samples ($p \leq 0.0001$), whereas AM-1 sample RANKL expression remained upregulated ($p \leq 0.0001$), but decreased compared to the earlier time points.

A gradual increase in RANKL expression was seen in the HOB control samples over culture time, with the final measurement showing a 3-fold upregulation in these samples.

RANKL expression in the AM-1 controls remained at low levels throughout the culture time with expression around 0.01-0.1-fold increased over the calibrator day 0 samples, and with only a marginal increase over time by day 14.

Expression in the co-cultures increased early on in culture, especially in the HOB parts of the constructs. The highest RANKL expression levels as seen in fig. 4.12 were found in the HOB part of the constructs on day 5 (9-fold), after which it decreased, and in the interface on day 8 with an approximate 11-fold increase.

In the AM-1 parts of the constructs, RANKL mRNA levels also increased between days 1 and 5, peaking on

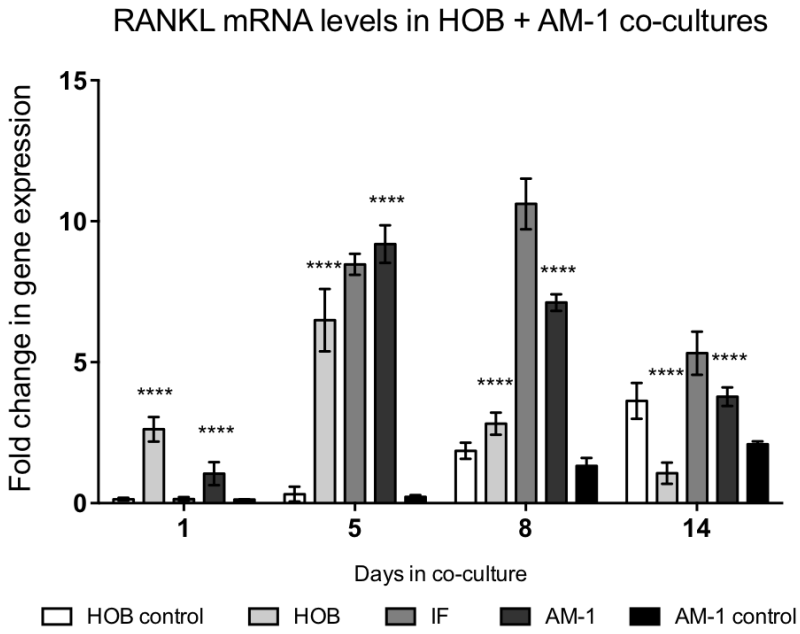

Figure 4.12: RANKL mRNA levels were quantified using qRT-PCR. RANKL expression in the HOB and AM-1 control samples increased slightly over culture time. An increase in RANKL levels was seen in the HOB samples in co-culture. A simultaneous increase was also seen in the AM-1 part of the samples. The largest (approximately 10-fold) increase was seen in the interface, where the two cell types were interacting. Two-way ANOVA, **** indicates $p \leq 0.0001$. Error bars = 95% CI, n = 4

day 5 of co-culture. The decrease in the AM-1 parts was more gradual however, which in part also appeared to contribute to the high RANKL levels found at the interface of the two gels.

The high RANKL expression at the interface where AM-1 cells interacted with the bone cells and the mineralised culture construct, supported the theory that AM-1 cells may use RANKL to increase bone turnover in the constructs in order to invade the bone-like tissue. Overall, a larger expression of RANKL was seen in the interface than in the HOB or AM-1 parts alone ($p \leq 0.0001$), and the expression at the interface was more sustained. This is in line with previous results showing that RANKL in *ex vivo* ameloblastoma samples have an increased staining of RANKL present on the region of the tumour in contact with its microenvironment (Qian and Huang, 2010).

The RANKL expression pattern in the co-cultures was similar overall when the two bone-like co-culture models were compared, with both HOS and HOB cells showing an initial increase, with a more sustained expression seen in the interface region of both types of organotypic model. There was an increase in RANKL expression seen at the interface in the HOS + AM-1 constructs, which may indicate an increase in AM-1-mediated bone resorption at the construct interface. However, this occurred once RANKL expression had already increased, and therefore this increase was probably due to a HOS-mediated effect; although this does not rule out that the HOS cells increased expression due to signalling from AM-1 cells.

There was also an increase in RANKL expression seen at the HOB + AM-1 interface. By the time this increase was seen, there was also a similar increase seen in both the HOB and the AM-1 parts of the scaffolds. This increase may have been due to increasing AM-1 invasion towards the bone-like scaffold and an increased

potential for bone resorption at this point in the constructs. However, it was not possible to determine whether this was the case at this stage.

While the RANKL expression levels in the HOS + AM-1 co-culture models reached over 700-times the level of expression seen in the control samples, RANKL expression in HOB + AM-1 co-cultures was only approximately 10-fold that of the control samples. The larger increase seen in the HOS scaffolds was thought to be due to the cancerous nature of the HOS cells.
Notably, a similar gradual increase in RANKL expression at the interface of the co-cultures was seen in both models. However, this increase requires further study, as it could be a response either to the presence of Bio-Oss mineral in both models, or an indication that the AM-1 cells upregulate RANKL to increase bone resorption close to the bone-like scaffolds in order to be able to invade the surrounding bone. A control without Bio-Oss could be used in the first instance to eliminate this possibility.

4.6.3 NFκB gene expression

NFκB is a downstream factor of RANKL in the OPG/RANKL bone turnover-regulating pathway, and its expression is therefore considered a useful indicator of aberrant bone turnover regulation. The results for HOS + AM-1 co-cultures are shown in fig. 4.13 and for HOB + AM-1 co-cultures in fig. 4.14.

HOS co-cultures

NFκB gene expression was found constant throughout culture time in both AM-1 and HOS control samples as seen in fig. 4.13. In the HOS controls, there was a slight 0.3-fold upregulation compared to the calibrator samples, whereas in the AM-1 control samples a 0.3-fold decrease was seen. NFκB expression in the co-culture models remained constant in the AM-1 part of the model, but downregulated compared to the calibrators.

Statistically significant differences in NFκB expression were found between HOS co-culture samples and the HOS control samples at all time points in the co-cultures (all $p \leq 0.0001$). Expression of NFκB in the HOS part of the co-cultures was slightly increased during the first ten days of co-culture, but decreased significantly to a 2-fold decrease compared to the calibrator sample by day 14.
When NFκB expression was compared in the AM-1 co-culture samples and the AM-1 controls, there was found to be a significant decrease in expression at all time points (all $p \leq 0.0001$). Expression in these two sample sets remained level throughout culture time, with a 0.3-fold decrease in the control samples and an approximate 2-fold decrease in the co-culture samples.
Therefore, AM-1 cells appeared to downregulate NFκB expression as a result of co-culture with HOS cells.

HOB co-cultures

A statistically significant increase in NFκB expression in the HOB part of these co-cultures was found on days 5 to 14 (all $p \leq 0.0001$). Expression of NFκB in the AM-1 parts of the co-cultures, when compared to

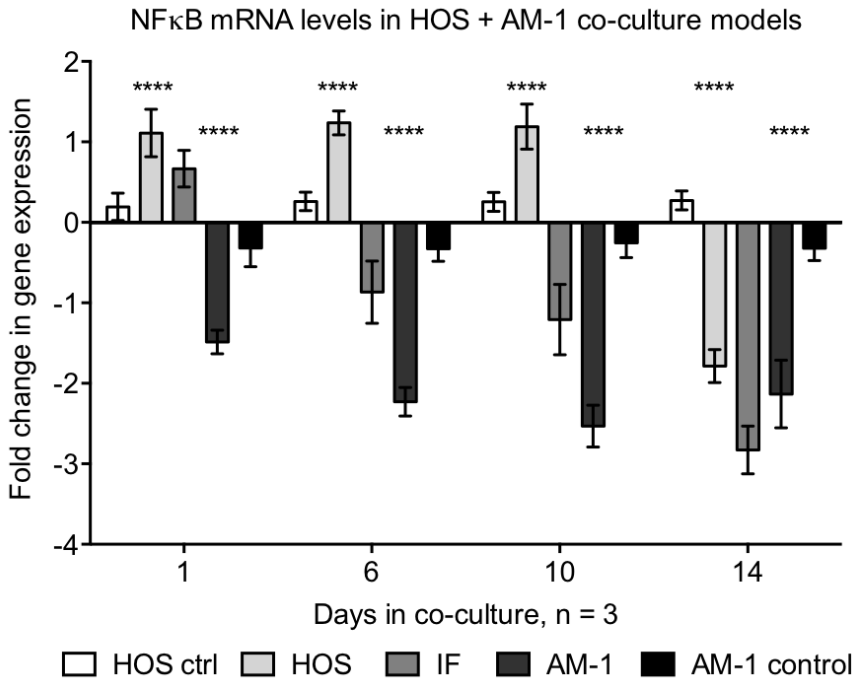

Figure 4.13: NFκB expression results in HOS+ AM-1 co-cultures. NFκB expression remained at a constantly low level in both control sets. Levels of NFκB were found underexpressed and decreasing with time in the AM-1 parts of the co-cultures. NFκB in the HOS parts of the co-cultures was intially upregulated, but there was a large drop from 1-fold upregulation on day 10 to a 3-fold downregulation on day 14. Two-way ANOVA, **** indicates $p \leq 0.0001$. Error bars = 95% CI, n = 3.

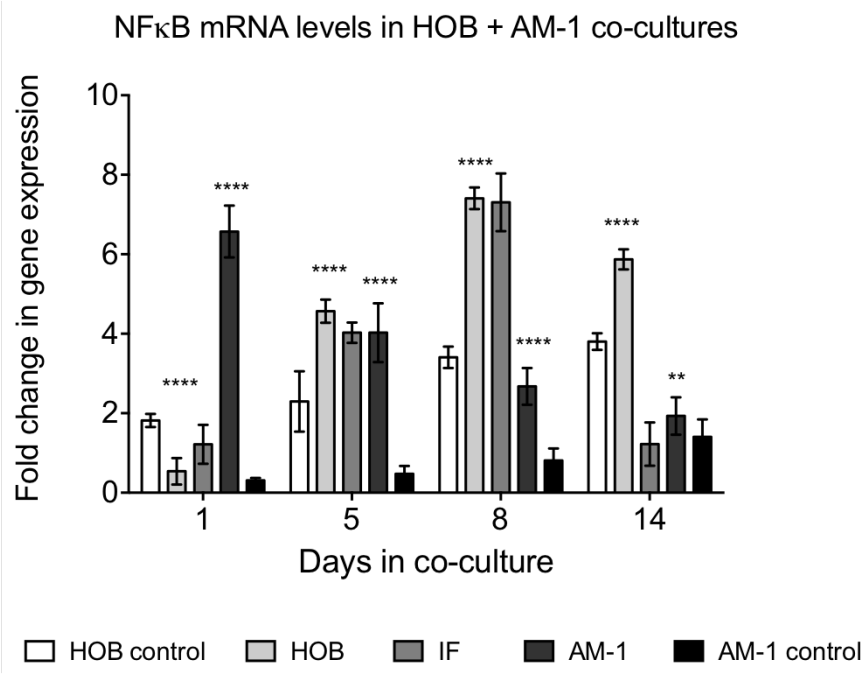

Figure 4.14: NFκB expression in HOB+ AM-1 co-cultures. NFκB levels slightly increased over time in both the AM-1 and HOB control samples. NFκB expression levels were greatly elevated initially in AM-1 cells in co-culture, but reduced over time. In the HOB cells, NFκB expression was initially below control levels, but gradually increased over co-culture time. Levels in the interface region broadly followed those seen in the HOS cells, apart from on day 14, when NFκB expression was reduced to day 1 levels. Two-way ANOVA, ** indicates $p \leq 0.01$ and **** indicates $p \leq 0.0001$. Error bars = 95% CI, n = 4.

AM-1 controls, was also found significantly increased on days 1, 5 and 8 (all $p \leq 0.0001$) and on day 14 ($p \leq 0.01$).

At the interface, NFκB expression was found similar to expression levels in the HOB parts of the constructs between days 1 and 10. However, expression reduced on day 14 to approximately AM-1-like levels.

Expression of NFκB was different in the HOS and HOB co-cultures. In both, expression levels in the controls were relatively stable over time. However, in the HOB co-cultures expression of NFκB increased with increasing culture time, whereas in the HOS co-cultures it decreased.

The decrease seen in HOS was markedly smaller than the corresponding increase seen in HOB co-cultures - a 2-fold decrease compared to an approximate 6-fold increase in HOB co-cultures.

The difference in AM-1 and HOB control gene expression compared to the HOS co-culture levels is explained by the use of a different calibrator sample pool as experiments were carried out at different times. Calibrators were freshly made (day 0) control constructs samples of both AM-1 and HOS or HOB.

However, as NFκB is a downstream factor of the RANKL pathway, the NFκB expression levels in the HOB + AM-1 co-culture correlate with the RANKL levels found in the graph shown in fig. 4.12, whereas the NFκB levels seen in the HOS + AM-1 co-cultures do not correspond to RANKL levels seen in these co-culture models.

4.6.4 SMO gene expression

Smoothened (SMO) gene expression was only analysed in the HOS + AM-1 co-culture samples, with the results visualised in fig. 4.15.

There was no difference in SMO expression seen in AM-1 controls and co-cultures between the different time points analysed. However, when compared to HOS single-cell type control constructs, there was a statistically significant difference between the HOS constructs at all time points ($p \leq 0.0001$ for all).

4.6.5 PTCH-1 gene expression

PTCH-1 gene expression was only assayed in the HOB + AM-1 co-culture models. The results are seen in fig. 4.16.

There was an increase in PTCH-1 gene expression levels seen in all parts of the co-culture constructs within the first week of co-culture (fig. 4.16). PTCH-1 expression was found 6-8-fold increased on day 8 in the whole co-culture construct. Subsequently, PTCH-1 expression reduced in all parts of the co-cultures.

PTCH-1 expression in the HOB controls was found to be slightly upregulated. HOB in the co-cultures were found to significantly upregulate PTCH-1 expression compared to the controls ($p \leq 0.0001$). There was no difference found in the AM-1 controls and AM-1 co-culture samples at any of the time points examined.

Both SMO and PTCH-1 have been shown to be dysregulated in ameloblastoma tumours, which is why

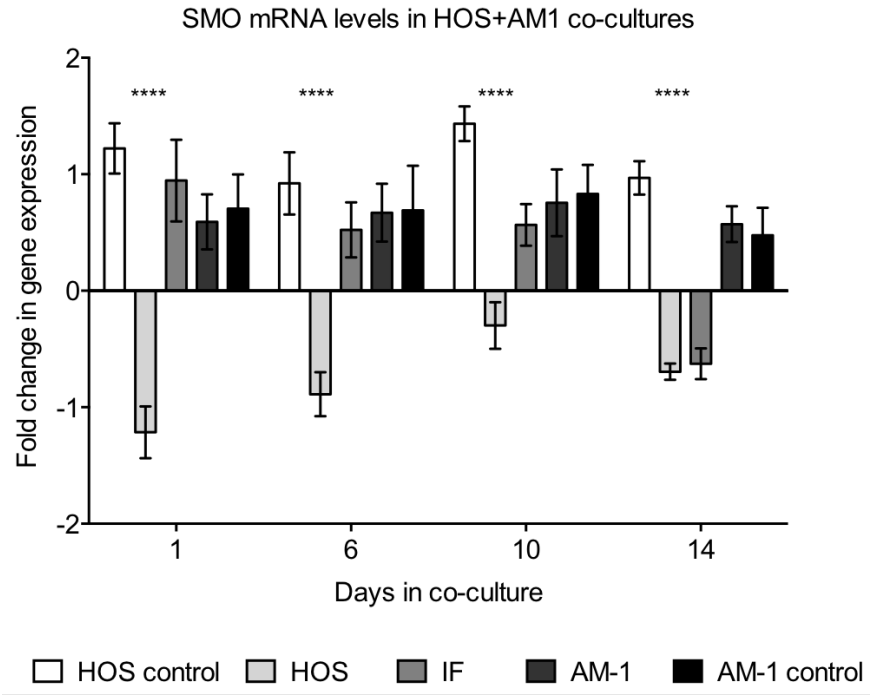

Figure 4.15: SMO expression in HOS + AM-1 co-cultures. SMO expression in both HOS and AM-1 control samples appeared relatively constant over culture time. In the AM-1 parts of the co-cultures, SMO expression was also constant but slightly increased compared to the calibrators. In the HOS co-culture parts, SMO expression was seen to decrease. The largest change in SMO expression over time was found in the interface region, where expression appeared to reduce over time. Two-way ANOVA, **** indicates $p \leq 0.0001$. Error bars = 95% CI, n = 3.

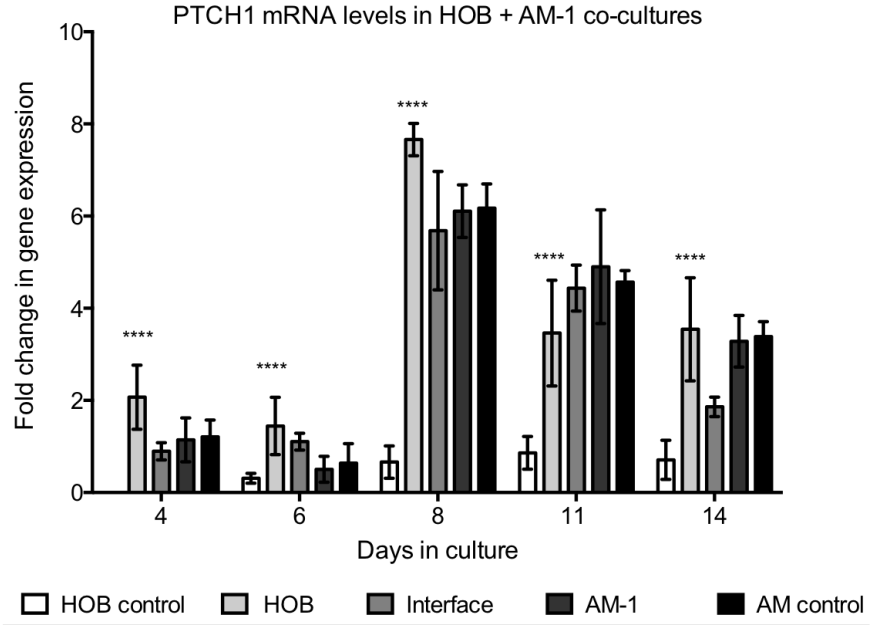

Figure 4.16: PTCH-1 gene expression in HOB + AM-1 co-cultures and controls. PTCH-1 expression increased in all parts of the models during the first week in culture. Expression then reduced in all co-culture parts. PTCH-1 expression was also high in the AM-1 controls throughout culture, whereas it was significantly increased in the HOB cells in co-culture compared to the controls. Two-way ANOVA, **** indicates $p \leq 0.0001$. Error bars = 95% CI, n = 3.

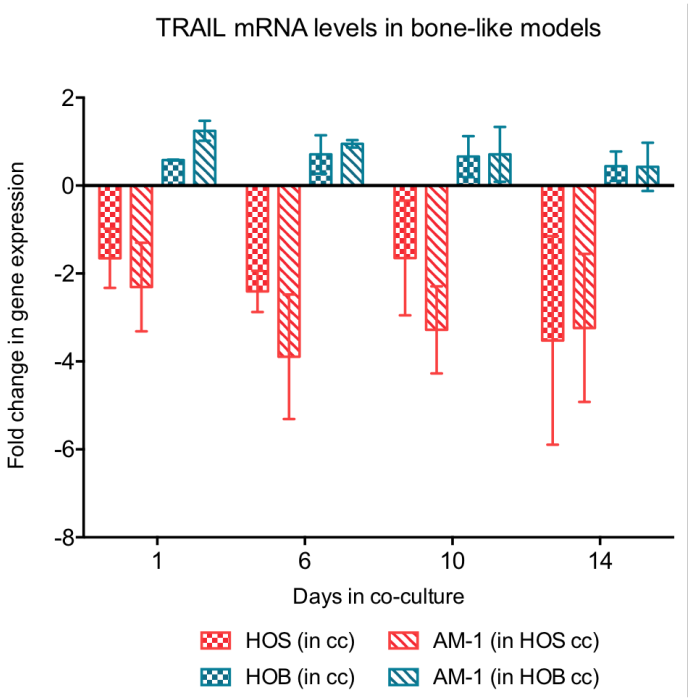

Figure 4.17: The effect of the two bone-like co-cultures on TRAIL expression. In HOB co-cultures, TRAIL was upregulated compared to the day 0 single-cell type calibrator samples in both HOB and AM-1 samples. Contrastingly, in HOS co-cultures, there was a marked downregulation of TRAIL expression in both HOS samples as well as AM-1 samples. Error bars = 95% CI, HOS + AM-1 n = 3, HOB + AM-1 n = 4.

the expression of these was probed in these co-culture constructs. Expression of these two genes was only analysed in one of the two co-culture models. However, no significant differences were seen in the AM-1 samples for either SMO or PTCH-1. This may be due to the cancerous properties of the HOS cell line in the case of SMO, or due to the fact that mutations for both already exist in AM-1 cells and may be predisposing for ameloblastomas in general. Therefore, the calibrators as well as the co-culture controls and samples would already express SMO as well as PTCH-1 at abnormal levels prior to incorporation in these models.

4.6.6 TRAIL gene expression

TRAIL acts as an apoptosis inducer in odontogenic tumours, and has been found expressed in the cytoplasms of ameloblastoma cells. TRAIL expression was therefore probed in both HOS + AM-1 and HOB + AM-1 co-cultures during this study.

No significant differences were found between TRAIL expression in HOS co-cultured and HOB co-cultured AM-1 cells or HOS and HOB cells respectively (fig. 4.17).

However, there were significant differences between the HOS and HOB co-cultures as seen in fig. 4.17, where the expression of TRAIL in the HOS co-cultures was greatly downregulated, whereas it was slightly upregulated in the HOB co-cultures ($p \leq 0.05$ on days 6, 10 and 14 of co-culture). This discrepancy in TRAIL gene expression levels illustrated the effect different culture environments can have on cells, especially in cultures with cancerous HOS cells and non-cancerous HOB cells.

Furthermore, this indicates that in the HOS co-cultures, AM-1 cells are not undergoing TRAIL-induced apop-

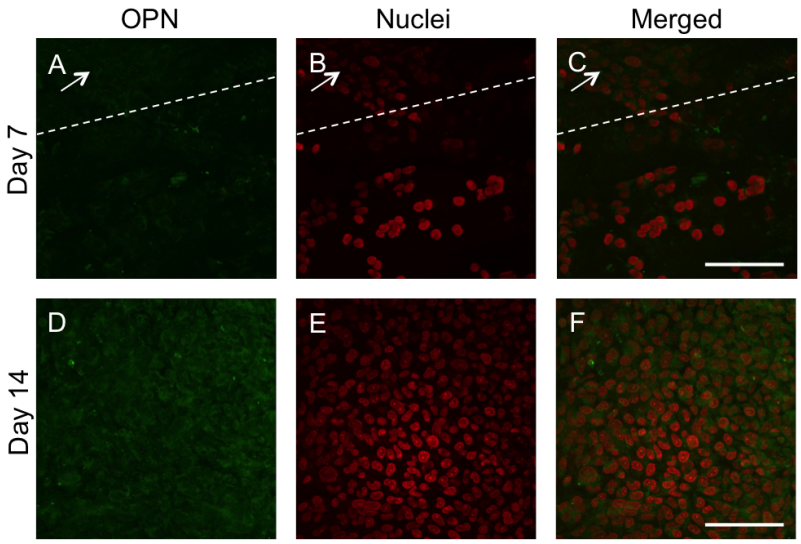

Figure 4.18: Confocal micrographs of immunocytochemically stained HOS + AM-1 co-cultures. A-C: The co-culture on day 7. HOS cells were stained for OPN (green) and nuclei (red), AM-1 cells were stained red only. OPN stained HOS cells on day 14 of co-culture. The white arrow indicates the AM-1 cell cluster close to the interface and the white dotted line indicates the construct interface. As can be seen in D-F, the culture scaffold appeared confluent by day 14. Representative images of n = 3. Scale bars = 100μm.

tosis. Conversely, in the HOB co-cultures, there is a greater potential for TRAIL to cause AM-1 cells to apoptose in these models. As TRAIL is found in the cytoplasms of ameloblastoma cells, this was an expected result. This expression pattern, in addition to the other gene expression results presented, indicated that the HOB + AM-1 co-cultures were an overall better organotypic ameloblastoma model than the HOS + AM-1 co-cultures.

4.7 Immunocytochemistry on co-cultures

In order to better distinguish the two cell types in both the HOS + AM-1 and HOB + AM-1 co-cultures from each other, immunocytochemical staining of cell type-specific epitopes was used to probe the co-culture scaffolds. It was also used to qualitatively assess the expression of some proteins in the co-cultures.

4.7.1 Osteopontin

HOS + AM-1 co-cultures

HOS cells were stained for the bone marker osteopontin (OPN) in the co-cultures (fig. 4.18). No AM-1 cells stained with this bone cell-specific marker.

Again, relatively close interaction between the AM-1 cells and HOS cells in these co-cultures can be seen in fig. 4.18A-C, where the OPN-stained HOS cells (green) appear close to the AM-1 cells (clustered, indicated by the white arrow) and close to the interface (white dotted line) between the two constructs. However, although close contact was observed, no actual migration was seen between the HOS and AM-1 constructs by either cell type.

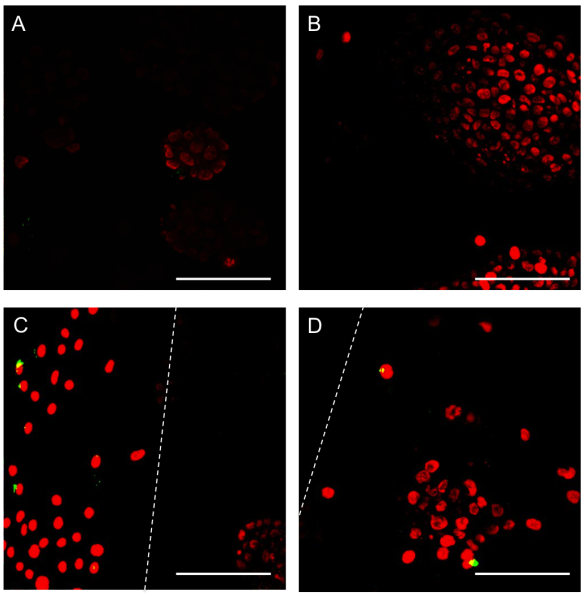

Figure 4.19: Immunocytochemistry on HOB + AM-1 samples on days 7 and 14. Osteopontin (green) was used to differentiate the two cell types in the co-cultures from each other. AM-1 cells are stained with the red nuclear stain only. A) Day 7 AM-1 cells in co-culture. B) Co-cultured AM-1 cells on day 14. C) Interface of the co-cultures on day 14, where no invasion was apparent. The white dotted line indicates the construct interface. A cluster of AM-1 cells on the right, with HOB cells stained red and green on the left. D) Image of a HOB part of the gel (AM-1 part of the construct to the left of the white dotted line) on day 14, where single HOB cells (red and green) were seen to surround a cluster of AM-1 cells (stained red only). Here, the AM-1 cells appeared to have migrated across the interface to the HOB part of the scaffold. Representative images of n = 3. Scale bars = 100μm.

Here, the fast proliferation rate of the HOS cells can also be seen, with the scaffolds not yet confluent on day 7, but as seen in fig. 4.18D-F, the cells have quickly proliferated to achieve confluency by day 14 of co-culture.

HOB + AM-1 co-cultures

Some HOB cells in co-cultures stained for OPN (green), which allowed distinction between the two cell types, as AM-1 cells were only stained with red nuclei. AM-1 clusters on day 7 are visible in fig. 4.19A, and increased in size by day 14 (fig. 4.19B).

In fig. 4.19C and D (co-culture interface on day 14), some AM-1 clusters with red nuclei were seen in the vicinity of some HOB cells stained with both OPN and the nuclear counterstain EthD-1. This co-localisation of the red and green staining of HOB cells and the red-only AM-1 cells in the samples on day 14 of co-culture indicated a potential invasion by one of the cell types to the other part of the co-cultures, as seen previously in fig. 4.8. This potential invasion was investigated further.

4.7.2 Ameloblastin

Ameloblastin (AMBN) is labelled as an AM-1 marker in the literature, and frequently used to differentiate cells from ameloblastomas with other cell types in biopsies and histological studies. However, it was found that AM-1 cells co-cultured with HOS and HOB cells during this project did not stain for AMBN at all (fig.

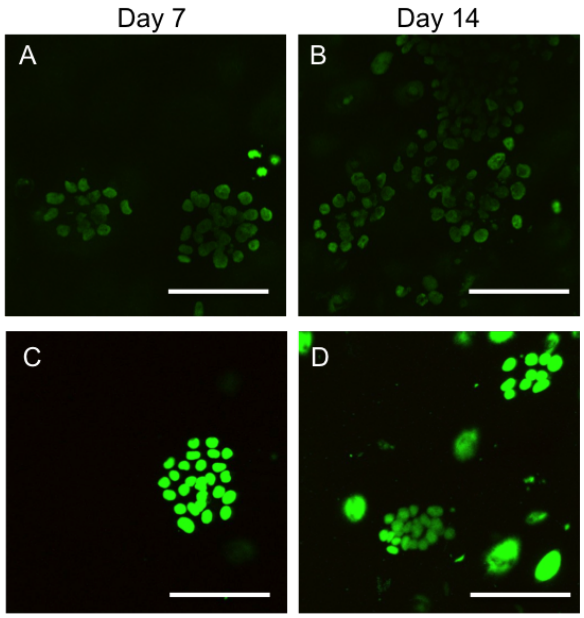

Figure 4.20: Immunofluorescent staining for expression of AMBN in bone-like co-cultures. Cell nuclei were stained green with Sytox green, and any AMBN expressed was stained red. No AMBN expression seen in at either time point in either co-culture construct. A) AM-1 cells in co-culture with HOB on day 7. B) AM-1 cells in co-culture with HOB on day 14. C) AM-1 cells co-cultured with HOS cells on day 7. D) AM-1 cells co-cultured with HOS cells on day 14. Representative images of n = 3. Scale bar = 100μm.

4.20).

Some AM-1 cells in co-culture with GF cells in the soft tissue models were seen to express a limited amount of AMBN, as seen in experiments detailed in chapter 5.

4.8 AM-1 invasion in bone-like scaffolds

Cell invasion and motility were assayed using the Cell Tracker fluorescent stains in the co-culture models and quantified using ImageJ. As mentioned, no invasion was seen in the HOS + AM-1 cells at any time point during any other assay. The high proliferation rate of the HOS cells was also a limiting factor when considering the use of Cell Tracker assays for assaying cell migration. Therefore, invasion was not assessed further in these scaffolds.

Invasion in HOB scaffolds was first visualised during confocal microscopy, where potential migration of AM-1 cell clusters was seen in the HOB part of the construct in early co-cultures (fig. 4.19).
To ensure that the invasion seen in this study was indeed AM-1 cells invading the HOB scaffold, rather than HOB cells becoming more AM-1-like in morphology, invasion in these co-cultures was studied using the Cell Tracker assay. The results of this assay are visualised in fig. 4.21. This was a long-time Cell Tracker culture, as both cell types in the co-cultures were slow-dividing and therefore retained the fluorescent stain for a longer time. It was therefore possible to carry out this assay over 14 days of co-culture.

On day 0, there was a small number of AM-1 cells (in green) visible in the HOB part of the co-culture scaffolds (fig. 4.21A). This was thought to be due to the expulsion of liquid from the AM-1 gel during compression and co-culture assembly. Throughout culture, there was only a small number of fluorescently stained HOB cells seen (faintly stained red), although using a light microscope, abundant cells were seen in the collagen + Bio-Oss constructs at all time points.
When AM-1 migration towards HOB scaffolds was quantified, a significant amount of migration was seen. The total amount of invasion in a construct on a given day is visualised as bars of increasing size in fig. 4.21C. An arbitrary measure of distance is then given as the different parts of the bar, with the different zones indicated in fig. 4.21B. Initially, as expected, AM-1 cells migrated close to the interface (zone 1; white bars at all time points in fig. 4.21C). From day 3 onwards, the migrated cells continued further into the HOB scaffolds, with the proportion of AM-1 cells migrating into ‘zone 2’ increasing 4.21C. Towards the end of the co-culture, most of the migrating cells had travelled to the furthest zone 4.21C, indicating that both distance of migration and cell number migrating increased with increasing culture time.

In scaffolds not analysed with Cell Tracker stains, the entire AM-1 part of the construct would be confluent by the end of the co-cultures. AM-1 cells were also normally found in large (20+ cell) clusters. This was not found to be the case in the CT stained samples; the largest cluster seen in any of the samples was six cells by day 14. This change in behaviour was thought to be a side-effect of the CT stain.
Furthermore, a large amount of autofluorescence from the Bio-Oss granules within the constructs was seen (e.g. on day 7 in fig. 4.21). This obscured the view of the cells within the constructs at times.

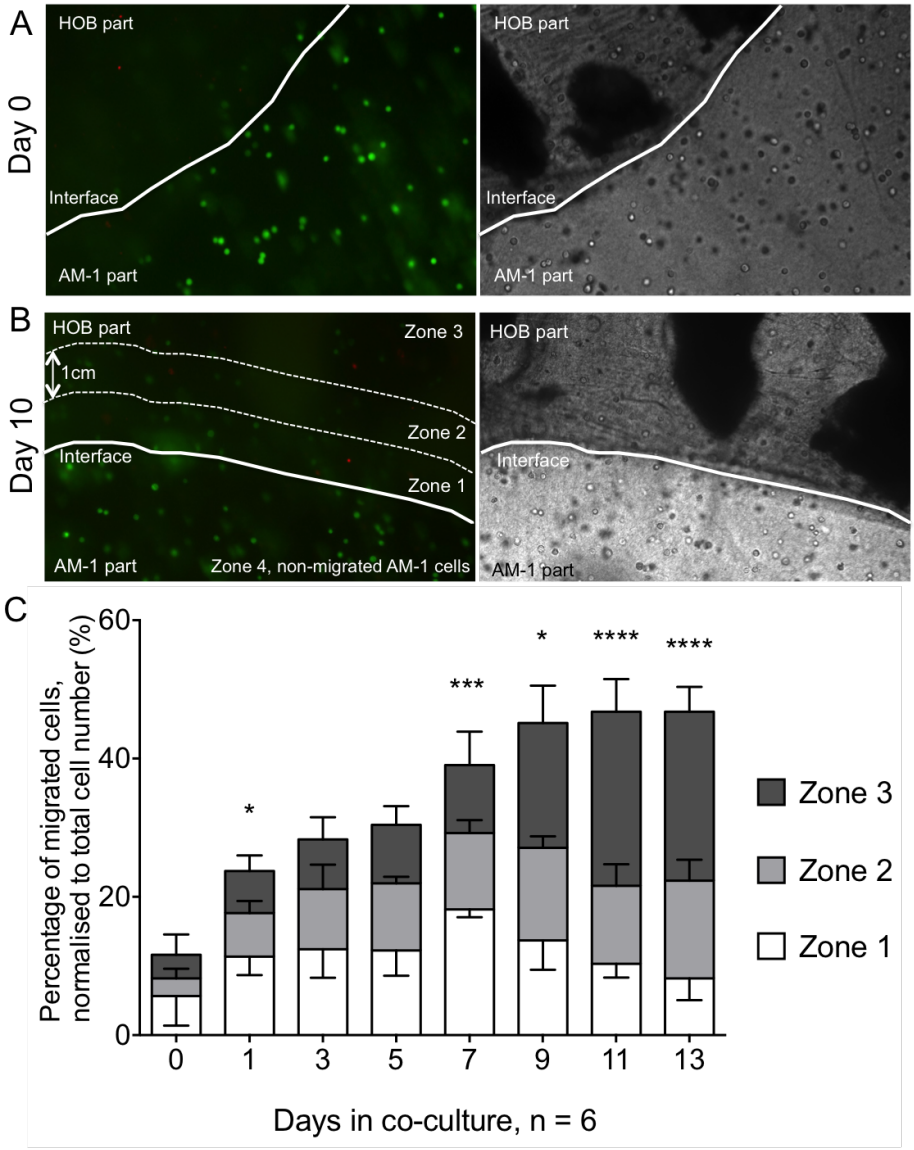

Figure 4.21: Invasion of the AM-1 cells towards the HOB scaffolds in the co-cultures was measured using Cell Tracker stained populations. HOB cells were labelled red and AM-1 cells green. In A and B, the interface between the two gels is indicated by the white line in both the fluorescent micrographs as well as the light micrographs. Only a few HOB cells appeared labelled with the red Cell Tracker stain, however distinction of the two parts was possible, as Bio-Oss particles were visible in the HOB parts of the constructs (on the top of each image). The AM-1 parts are seen the below the line. In A, the two populations of cells are seen in their distinct compartments on day 0 of co-culture. In B) Some migration of AM-1 cells (green) into the HOB part of the scaffold was visible by day 10. The invasion, which was quantified in C, was measured based on how far the cells had migrated. 3 zones, as seen in B, were used for this, where zone 1 is the region immediately adjacent to the interface, zone 2 is further away into the HOB construct and zone 3 is the furthest away (indeed the remainder of the HOB construct). The histogram in C shows AM-1 cell migration initially close to the interface, and further into the HOB construct by day 3, with an increasing distance migrated with increasing co-culture time. Cell numbers shown are the percentage of migrated cells counted of the total cell number seen in the micrograph per sample, i.e. not of the total cell number present in the construct. I.e. 50% of the total number of cells on day 11 did not migrate, rather the graph shows that 50% of cells seen close to the interface in the part of the construct which was captured migrated. Two-way ANOVA, * indicates $p \leq 0.05$, *** indicates $p \leq 0.001$ and **** indicates $p \leq 0.0001$. Representative images of n = 6. 10X magnification using the DMIRB fluorescent microscope.

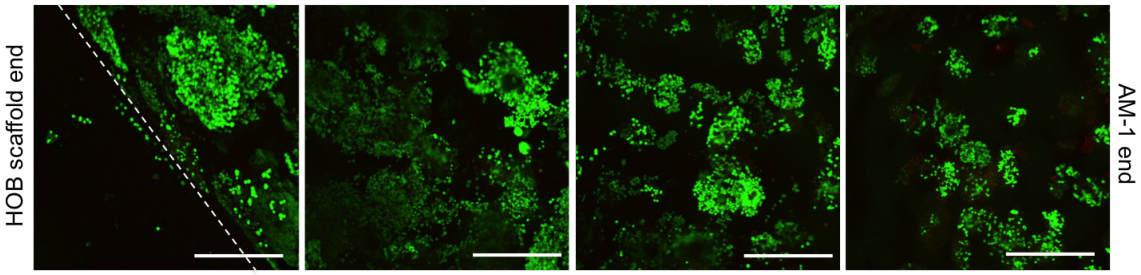

Figure 4.22: Live/Dead stained AM-1 cells in HOB + AM-1 co-cultures. There was an apparent increase of cell number and AM-1 cell cluster size towards the interface and the HOB part of the constructs. The approximate location of the interface is indicated by the white dotted line. Also note the three AM-1 cell clusters to the left of this line within the HOB construct. No HOB cells are visible. Scale bar = 100μm.

4.8.1 AM-1 directionality in HOB + AM-1 co-cultures

There was an apparent directional increase in AM-1 cell cluster size in the HOB co-cultures. When viewed in the confocal microscope, it appeared that AM-1 cells either migrated towards or increased proliferation when proximal to the HOB scaffold (fig. 4.22), creating a gradient of cells increasing towards the interface region of the co-culture models.

The AM-1 clusters at the end of the scaffold furthest away from the bone-like scaffold also appeared smaller in size as seen in fig. 4.22, indicating that AM-1 proliferation was increased in the vicinity of HOB cells. Furthermore, there was an increase in dead AM-1 cells seen at the end furthest away from the HOB scaffold. This is a similar phenomenon to an observation by Pinheiro *et al*, where AM-1 cells were reported to increase their proliferation rate in the part of the tumour proximal to the bone *in vivo* (Pinheiro et al., 2004). Some clusters of AM-1 cells were also seen in the HOB part of the scaffold. No HOB cells were visible in fig. 4.22 due to the reduced uptake of the Live stain by these cells. This type of invasion and clustering may go on to form a recurrence *in vivo* or invade the surrounding soft tissues, as it may remain in the bone tissue after surgical tumour excision.

4.9 Practical issues with the models

4.9.1 Diffusion of oxygen and nutrients

Both HOS + AM-1 and HOB + AM-1 co-cultures were measured to be no more than 400μm in thickness. As these were floating cultures, and the maximum distance for oxygen and nutrient diffusion is approximately 200μm, there should not have been an issue with diffusion within the models for the duration of culture time. In fig. 4.23, two day 14 Live/Dead stained co-cultures are visualised as side-on stacks. The increasing cell death seen with increasing depth of co-culture construct in fig. 4.23 indicated a problem with diffusion of oxygen, nutrients and removal of waste products in the deeper parts of the constructs. This may have caused increased cell death in some of the models, especially at the later time points in the co-cultures. However,

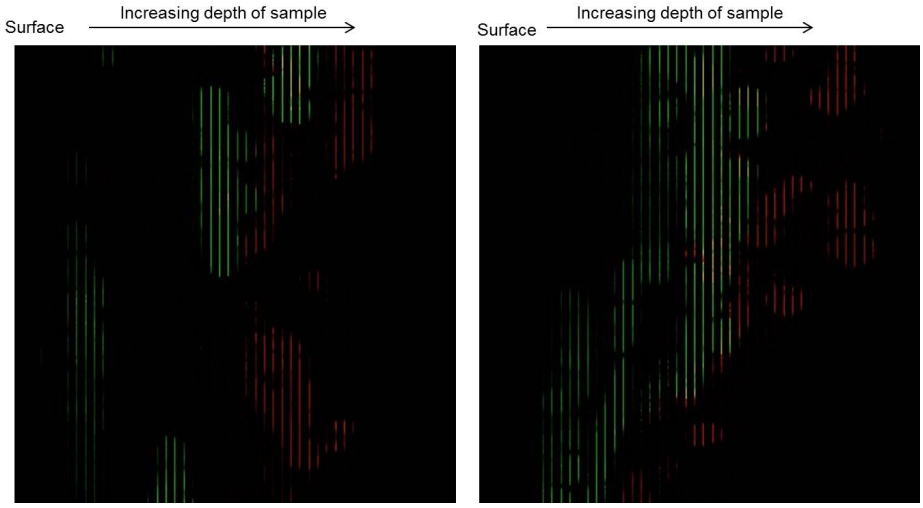

Figure 4.23: Side-on view of 3D 'stacks' assembled from d14 Live/Dead HOB+AM-1 co-culture model confocal images. The direction of the arrows indicates increasing depth of the constructs. Due to the stacking of the images, the cells are visualised here as coloured lines. Green indicated live cells and red staining corresponded to dead cells. The two images show an increase of cell death with increasing depth of construct. The space between the slices in the stack was 5μm. Both images were a 40X magnification.

results presented previously in this chapter, cell proliferation was ongoing in all scaffolds throughout the co-culture time and the cells appeared viable throughout. As this study did not assess this cell death or the potential presence of hypoxia in these scaffolds further, it is possible that the high proliferation numbers masked a smaller population of dying cells within the constructs.

4.9.2 Staining of the deeper construct parts

Constructs which were fluorescently labelled displayed some staining issues. The image in fig. 4.24 is a side-on view (angled at 45°) of an image stack of a construct, and shows the Sytox nuclear counterstain used. This stain has not distributed equally throughout the construct. The surface cells in these constructs were brightly stained and clearly visualised, whereas cells deeper within the constructs were not.

Furthermore, not all cells were stained, and all of the stained cells were not seen using the microscope due to obstruction of the fluorescent signal by the collagen fibres or other physical factors such as the construct thickness. This may have caused problems with correctly identifying protein expression and invasion within the co-cultures, as not all cells within the models were necessarily stained due to this effect.

4.9.3 Autofluorescence in models

As seen in fig. 4.21, the Bio-Oss granules exhibited autofluorescence within the constructs when viewed under a fluorescent microscope. In some cases, especially when using the confocal microscope, some of the collagen fibres were also autofluorescent. This made reliable imaging of the constructs more difficult. Non-fluorescent assay methods, such as immunohistochemistry could be used to overcome this issue.

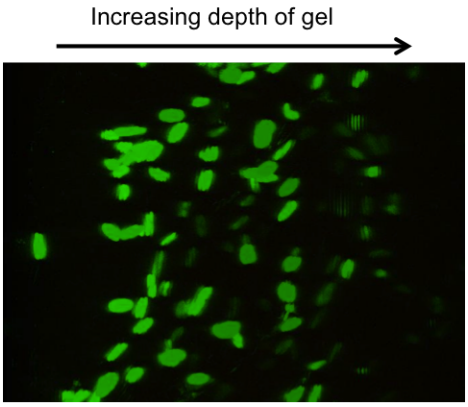

Figure 4.24: A 3D stack assembled from Sytox green stained nuclei viewed at a 45° angle. The nuclei closer to the construct surface are stained brighter, with staining decreasing with increasing depth of construct. The space between the slices in the stack was 5μm. 40X magnification.

4.10 Main findings and discussion

The initial objective of this chapter was to maintain AM-1 cells alive within a compressed collagen matrix and to characterise these. AM-1 cells were found to proliferate inside the collagen constructs, and were found in cell clusters, which is characteristic for the ameloblastoma tumour. Previously, AM-1 cells have been incorporated in hydrated collagen gels, which they were reported to degrade (Harada et al., 1998). As no degradation was seen here, and the cells were found to cluster within the constructs, the compressed collagen scaffolds were deemed more suitable for AM-1 culture than uncompressed collagen constructs by providing the cells with more tissue-like protein networks, scaffold mechanical properties and cell-to-cell interactions.

Subsequently, the aim of the experiments described in this chapter was to successfully develop a method with which a co-culture could be assembled using the pre-mineralised bone-like scaffolds to track changes in gene expression, cellular events and invasion in the models over time.
Several different methods to achieve this were attempted. AM-1 cells were found to be contact dependent, which caused them to die during attempted tumour sphere synthesis. This was later confirmed by another study (Kibe et al., 2013).

The co-culture models finally developed made use of a monodispersed AM-1 collagen gel placed next to (and in physical contact with) the pre-mineralised HOS and HOB gels as detailed in chapter 3. This method was the most reproducible out of all the ones attempted, and allowed for quick manufacture of several co-culture models at any one time. However, it is recognised that as the AM-1 cells were added as a separate collagen-only construct, some of the organotypic properties of the bone-like scaffold were no doubt lost as a majority of the AM-1 cells were experiencing a soft, collagen-only, monoculture.
The advantages of the bone-like scaffolds developed, and the subsequent AM-1 co-culture scaffolds used, were considered to be biomimetic due to the bone-like mechanical properties, mineral content provided by the Bio-Oss granules and the collagen + Bio-Oss mixture providing a microenvironment mimicking that

found in native bone. Additionally, the addition of osteoblasts in the form of HOB cells made the models more *in vivo*-like. Furthermore, the oxygen tensions and nutrient diffusion in the approximately 400μm thick constructs were thought to closely mimic the bioavailability of oxygen and nutrients in small tumours located between capillaries in tissues.

Using the co-culture models developed, with the two cellularised constructs placed proximal to each other on an acellular support gel, the following results were obtained:

- Cells in both HOS + AM-1 and HOB + AM-1 co-culture models appeared alive throughout culture.
- A large upregulation of the osteoclast-activating factor RANKL was seen in co-cultures of AM-1 cells with HOS scaffolds. This may have been due to the AM-1 cells within these models upregulating their production of RANKL, or that the presence of AM-1 cells within the co-cultures caused the HOS cells to upregulate RANKL production.
- AM-1 cells upregulated RANKL production when in co-culture with HOB cells, where the expression was found to be increased during the entire co-culture time. RANKL expression in the HOB cells was initially increased in co-culture but then reduced, indicating that these cells were not greatly promoting bone resorption. The increase in AM-1 RANKL expression also led to a greater amount of RANKL found in the interface throughout co-culture.
- OPG gene expression was also increased in the AM-1 cells in HOS co-cultures, whereas it was reduced over time in the HOS parts of the constructs, indicating a reduction in osteoblast activity in these scaffolds.
- OPG levels in the HOB + AM-1 models were found upregulated in the HOB parts of the constructs, and in the interface at the earlier time points. This indicated that the HOB cells in these constructs were still actively attempting to synthesise bone. OPG expression in the AM-1 parts of the constructs was low throughout, which was expected.
- The large increase overall in OPG levels seen in the HOB co-cultures was thought to be due to the osteoblastic, non-cancerous nature of the HOB cell line.
- Bone synthesis in the HOB models was clearly underway when AM-1 cells were included in the co-cultures (as seen in chapter 3), and based on this and the co-culture gene expression results, HOB co-cultures were deemed a better overall organotypic model.
- NFκB, which is a downstream factor of RANKL in the bone resorption pathway was downregulated in the HOS co-culture models. This decrease was thought to be an effect of the cancerous properties of the HOS cell line.
- NFκB was found upregulated in the HOB co-culture models, which was thought to reflect a potential increased osteoclast-activating potential in these, more organotypic models.

- The closer to the HOB + AM-1 interface AM-1 cells were found, the larger and more tightly packed the AM-1 clusters appeared. This indicated either a recruitment process of AM-1 cells by the HOB cells to the bone-like scaffold, or AM-1 cell migration towards the bone-like scaffold.
- In HOS + AM-1 scaffolds, close interactions between the two cell types were observed during confocal microscopy. However, no invasion was seen as the two cell types remained in their distinct gels.
- In HOB + AM-1 scaffolds, large numbers of AM-1 cells were seen to migrate from the AM-1 scaffold to the HOB scaffold. This migration was directional, as AM-1 migration to the acellular support gel surrounding the other sides of the constructs was limited.

A large proportion of the results obtained using the HOS + AM-1 co-cultures were undoubtedly influenced by the cancerous properties of the HOS cell line. While osteosarcoma cell lines appropriately respond to bone activating factors, they do not accurately mimic the bone mineralisation process *in vitro*, and events such as osteoclastogenesis cannot be reliably investigated in this model system; not least due to the lack of osteoclastic cells in these. Especially the large increase in RANKL gene expression in HOS co-cultures seen in this study was thought to be due the HOS cells' potential to invade and resorb bone as an osteosarcoma. However, the location and cause for RANKL expression in this co-culture system should be confirmed, as at present it is not known whether the cause for the increased RANKL levels was AM-1 cells increasing their RANKL production, or AM-1 cell interactions with HOS cells increasing RANKL production by the HOS cells. Additionally, it is also possible that the increase in RANKL signalling could be due to the presence of the Bio-Oss granules within the co-culture system, which could cause AM-1 to increase RANKL levels. Eliminating Bio-Oss from the cultures would control for this possibility, although it would also make the bone-like cultures less organotypic. Immunohistochemistry could be used to localise RANKL expression in the co-cultures.

In the HOS + AM-1 cultures, a large increase was seen in RANKL, combined with a relatively small increase in OPG levels over culture time. Therefore, there is probably a capacity for HOS + AM-1 co-cultures to activate osteoclasts. Increased RANKL expression has previously been found in both the epithelial cells of ameloblastomas as well as the surrounding stroma of 24 tumour biopsies by Qian and Huang (2010), and the results presented here appeared to agree with these findings.

However, in the more organotypic HOB co-culture models, the high OPG levels could lead to minimal RANKL-mediated osteoclast activation. In the HOB + AM-1 co-cultures, a large increase in the OPG levels was seen, with little RANKL expression over culture time. The initial high levels of OPG in these cultures may explain the longer time required to upregulate RANKL expression.

According to Boyce and Xing (2006), osteoclastogenesis is usually favoured out of the two outcomes of the RANKL / OPG pathway. Therefore, cells in HOB + AM-1 cultures could be able to induce RANKL-mediated bone resorption once the initially high OPG levels seen in these co-cultures had reduced to below RANKL levels.

Expression of TRAIL in the co-culture models (fig. 4.17) was found dependent on the co-culture cell type. The decrease in HOS + AM-1 co-cultures could allow for increased HOS and AM-1 cell survival in the co-cultures. This could also translate to the *in vivo* tumour setting, where the decrease in TRAIL could increase tumour cell survival, although further experiments on *ex vivo* tumours would be needed to confirm this.
TRAIL expression in the HOB + AM-1 co-cultures was found increased, which may cause some OPG to bind to it allowing for more RANKL to activate osteoclasts. The preferential binding of OPG to TRAIL rather than to RANKL could also lead to increased apoptosis in the AM-1 cells, as shown previously by Sandra et al. (2006a).

The decreasing expression of NFκB, a downstream factor of RANKL in bone resorption, seen in the HOB + AM-1 co-cultures was found to correlate with the decrease in RANKL levels seen in these scaffolds.
Osteoblasts, and other cell types e.g. endothelial cells, fibroblasts and chondrocytes, also express RANKL, with which they can activate osteoclasts (Kearns et al., 2008). OPG is also found expressed on endothelial cells, smooth muscle cells and fibroblasts (Kearns et al., 2008). Therefore, gene expression levels of these two molecules does not necessarily correlate with function. This means direct deductions of the level of potential bone turnover cannot be made based on gene expression data alone, and more tests on RANKL and OPG activity levels need to be carried out, ideally in the presence of osteoclasts. Immunocytochemical staining for OPG and RANKL could initially be used to confirm the presence and localisation of these two proteins in the co-culture models, followed by osteoclast activation (resorption pit) studies.

SMO expression in HOB + AM-1 co-cultures was not found significantly different in the single cell-type cultures and the co-cultures. This finding correlates with previous studies of ameloblastoma-predisposing SMO mutations in AM-1 cells and therefore the gene is already aberrantly expressed prior to the cells being incorporated in the co-cultures (Sweeney et al., 2014).
PTCH-1 in the bone-like co-culture models was found to increase with culture time in the HOB cells, whereas in the AM-1 cells expression increased in both the co-cultures and single cell controls. This may be due to a pre-existing PTCH-1 mutation in the AM-1 cells (Kanda et al., 2013). The presence of PTCH-1 in the SHH pathway has been shown to inhibit SMO expression (Jaaskelainen et al., 2002; Sweeney et al., 2014) and this may also partly explain why SMO was found expressed at low levels in these co-culture models.

Cell invasion in the HOB + AM-1 models was analysed using the Cell Tracker assay, where some AM-1 cells were seen to migrate from the AM-1 scaffold to the HOB scaffold. This migration was thought to be directional, as AM-1 migration to the acellular support gel surrounding the other sides of the constructs was limited. There was a small amount of AM-1 cells seen in the bone part of the model immediately after

construct assembly (2 hrs). This displacement of the AM-1 cells from the original construct could be due to the flow of liquid from the construct during compression. At the point of co-culture construction, only the AM-1 gel was compressed, which resulted in a uni-directional flow of liquid from the AM-1 construct to its surroundings. This flow of liquid was assumed to be even around the gel, so it could be expected that some peripheral AM-1 cells would be lodged in the nylon mesh used for compressing the constructs, as well as the other part of the construct.

Not all HOB cells stained with Cell Tracker, and there could therefore be undetected HOB migration to the AM-1 part of the constructs. The reason for this selective HOB staining is not known, but the red Cell Tracker stain was found fainter overall and more difficult to visualise under the microscope.
Furthermore, AM-1 cells in the stained samples were found not to cluster. The large amount of CT dye added to the cells during this study may have affected their proliferation capacity, as well as their invasion. As can be seen in fig. 4.21, there was not a marked reduction in AM-1 cell fluorescent signal even after 14 days of HOB co-culture.

This is the first organotypic co-culture scaffold developed for an odontogenic tumour. In this chapter, these co-culture scaffolds have been used to investigate specific pathways which the ameloblastoma tumour may use to both locally invade the tissue, and to regulate bone turnover. Furthermore, these scaffolds, and specifically the osteoblast-incorporating HOB + AM-1 co-culture scaffolds, allow monitoring of ameloblastoma tumour invasion. This organotypic co-culture scaffold further allows *in vitro* testing for potential therapeutic agents and any effects these might have on the AM-1 cells, which is further investigated in chapter 6.

Chapter 5

Development of an in vitro soft tissue ameloblastoma model

This chapter describes the development of a soft tissue organotypic model used in this project to form the basis of the soft tissue co-cultures, as well as the subsequent ameloblastoma and soft tissue co-culture models.

The initial aims of the experiments shown in this chapter were to maintain gingival fibroblast cells in collagen scaffolds, and to develop an organotypic soft tissue scaffold by using these cellularised scaffolds. Subsequently, the aim of the soft tissue-like construct was to model the growth of ameloblastoma tumours when they recur within the soft facial tissues, and due to the cells used in the organotypic model, specifically the gingivae.

Soft tissue invasion of ameloblastoma is a pertinent problem in recurrent tumours. The gingivae are one of the more common ameloblastoma recurrence sites due to their proximity to the initial tumour site within the jaw bones (Gardner, 1984; Jaaskelainen et al., 2002).
Furthermore, peripheral ameloblastoma is a tumour variant entirely involving the soft tissues (Philipsen et al., 2001a). By modelling this soft tissue growth *in vitro*, and discerning potential pathways the tumour uses to grow and invade in the soft tissue model, invasion within the soft facial tissues *in vivo* could be contained.

First, the methods used for soft tissue scaffold synthesis are briefly described. Then, basic findings of growing gingival fibroblasts within the collagen scaffolds in preparation for constructing a co-culture soft tissue model are described.
In the second part of this chapter, the soft tissue scaffold is made into a co-culture together with cells from the AM-1 cell line. This co-culture model firstly focussed on quantifying genes with which ameloblastoma could invade the soft tissue and secondly on attempting to assess this invasion in the *in vitro* model. Finally, experiments described in chapter 6 focussed on inhibiting AM-1 cells in the models by applying therapeutic agents.

5.1 Summary of methods

Rat tail collagen type I solution was initially cellularised using human gingival fibroblast (GF) cells. The basement membrane substrate Matrigel was added to the models to reduce fibroblast-induced contraction, as well as to provide a basement membrane and more ECM factors for an improved organotypic scaffold. The optimal cell number for this soft-tissue mimicking scaffold was determined using a collagen contraction assay, after it was found that the matrix contracted during culture. Collagen contraction was also quantified. The GF-cellularised constructs were analysed for cell proliferation, viability, protein production and scaffold structure using the Cell Titre Glo ATP assay, Live/Dead staining, histology, qRT-PCR, SEM and TEM. Then, these soft tissue scaffolds were co-cultured with AM-1 cellularised scaffolds as for the bone-like co-cultures in the previous chapter. This was done by placing the two scaffolds next to each other and compressing with an acellular collagen layer to attach the scaffolds. Soft tissue co-cultures were analysed for gene expression, AM-1 invasion and protein expression.

5.2 Fibroblasts in the soft tissue model

Initially, 300,000 fibroblast cells/ml collagen solution were used to cellularise the compressed collagen scaffolds, which was the same cell number as for the bone-like scaffolds. The constructs were examined using H&E staining to visualise the scaffold architecture and the cells within the collagen constructs. In fig. 5.1A, a collagen-only construct is seen stained faintly pink, with purple cells visible. Most of the cells seen in this scaffold were present on the surface of the scaffold. In fig. 5.1B, a collagen-Matrigel scaffold is seen, with cells evenly populating the scaffold.

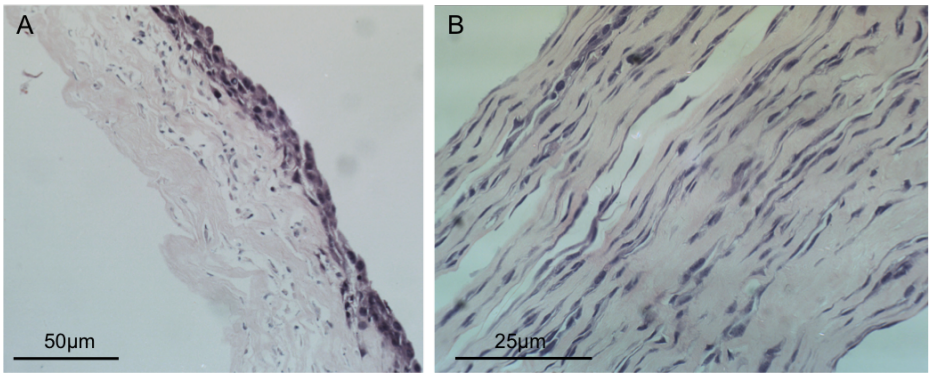

Figure 5.1: A) H&E stained gingival fibroblasts in collagen-only scaffolds on day 14 of culture. The cells (dark purple) had mostly migrated to one surface of the construct (pink), with very few cells remaining in the middle of the construct. B) Collagen constructs with added Matrigel on day 14, where cells were evenly spread out over the entire structure, with little migration to the surface seen. Both scaffolds were seeded with 300,000 cells/ml collagen mixture. Scale bars A = 50μm, B = 25 μm.

Two problems were therefore found with the initial collagen-only scaffold which was seeded with 300,000 cells/ml collagen:

Firstly, when the scaffolds were histologically examined using H&E staining, a large amount of cell migration

to the surface through the model was seen by day 14 of culture (fig.5.1A). This was an issue, as the cells were required to remain in the scaffold for a longer time period for the co-culture scaffolds, and to remain evenly spread out throughout the scaffold to create a suitable organotypic environment.

Secondly, macroscopic examination of the collagen constructs showed a 82% gel contraction, compared to the original construct area on day 1, as seen in fig. 5.2. The construct area was measured using the 'area' tool in ImageJ (see appendix fig. B.10). In fig. 5.2, the fibroblast scaffold (the edge of the construct is indicated by the white dotted line) is seen on day 7 in fig. 5.2A (in culture media), and on day 14 in fig. 5.2B (culture media removed).

The contraction of the scaffolds indicated the cells were actively excerting forces on the collagen fibres within the scaffold to remodel it and were mobile within the constructs. The cells were deemed viable during culture, but that the initial seeding density was too high, as it quickly resulted in a reduction in scaffold size.

Remodelling of the organotypic scaffold by the cells was desired, however this large reduction in scaffold size would have necessitated a large starting size for the collagen gel, which was unfeasible due to the large cell number required and therefore also associated large cost of materials. The amount of contraction of the scaffolds observed was also relatively uneven, making predictions of final size difficult.

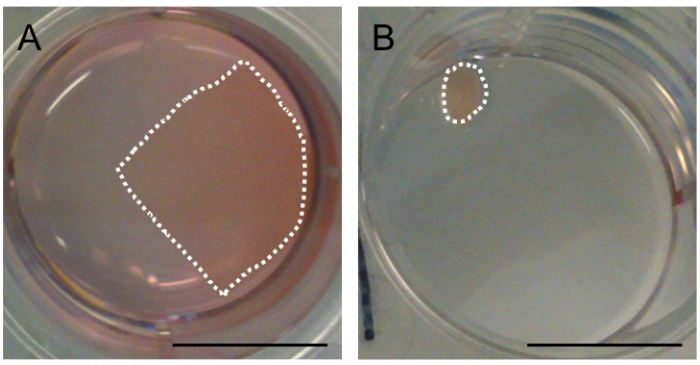

Figure 5.2: Compressed, cellularised collagen-only gels visibly contracted over time in the initial cultures. A) The white dotted line indicates the initial area of a representative collagen-only gel seeded with 300,000/ml fibroblasts on day 7 of culture. Note the gel is folded in the right-hand corner. B) The white dotted line indicates the same fibroblast collagen-only gel on day 14 of culture. Scale bar = 10mm.

5.3 Soft tissue model optimisation

Due to these initial challenges, the soft tissue scaffold was developed further. A two-pronged approach was decided on, whereby Matrigel was added to the scaffold to provide cells with more ECM factors to exert mechanical forces on. Additionally, the cell number in the scaffolds was optimised for minimal contraction using a collagen contraction assay.

5.3.1 Addition of Matrigel

Matrigel was added to the constructs prior to cellularisation to provide the scaffolds with ground substance, other ECM factors as well as collagens. Furthermore, Matrigel was added to reduce matrix contraction by the cells when these are added to the scaffolds. The cells in the collagen-Matrigel scaffolds did not migrate to the surface of the scaffolds, but appeared evenly distributed throughout the constructs (fig. 5.1B), where the addition of Matrigel was seen to limit the movement of the fibroblast cells to the construct surface on day 14. Cells in these samples appeared elongated, and aligned in the direction of the compressed collagen fibres (peripendicular to liquid flow under compression).

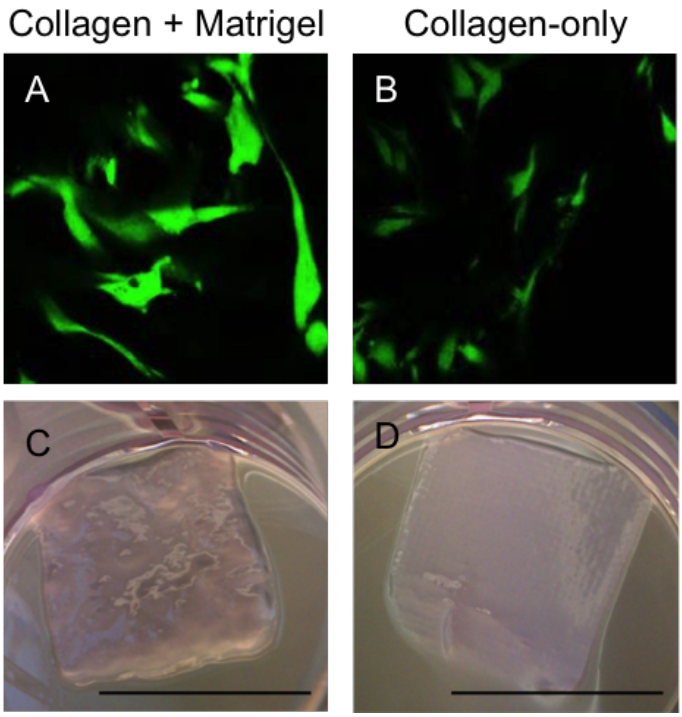

Figure 5.3: Live/Dead staining of fibroblasts in the organotypic scaffolds. Cells appeared alive in both the collagen-Matrigel scaffolds (A) and the collagen-only scaffolds (B) on day 7 of culture. Cells in the Matrigel-containing scaffolds appeared more elongated. The macroscopic appearance of the two construct types was discernibly different even after 7 days of culture. The collagen-only scaffolds (D) appeared smoother than the ones with added Matrigel (C), which set quicker once in the mould. A and B = 40X magnification, scale bar in C and D = 10mm.

When visualised using Live/Dead staining (in fig. 5.3), the cells in the Matrigel scaffolds appeared larger and more elongated than in collagen-only scaffolds. Cell viability, as observed visually using this stain, was approximately equal in both scaffold types. Cell proliferation in the collagen-only scaffolds was not further quantified at this time due to the above contraction issue.

5.3.2 Collagen contraction assay

Once Matrigel was added to the scaffolds, there was still some contraction observed when 300,000 cells/ml gel mixture were used. However, this was to a lesser extent than before, with an approximate 50% reduction in

gel area when comparing day 14 samples with day 0 samples. In order to minimise the amount of contraction occurring in the models throughout culture time, the optimal cell number in these constructs was determined by using a collagen contraction assay.

For this, the bottom-up compression method to create stabilised, cellularised collagen gels was used (section 2.4). The cell-induced collagen gel contraction over time is visualised as a percentage of the original construct area in fig. 5.4. An increasing amount of contraction was seen with increasing initial cell seeding density. A rapid, approximately 5% shrinkage was seen in most samples within the first three days in culture. A further accelerated contraction was seen between days 11 and 13 of culture, when especially the highest cell density gels contracted rapidly. In the samples with highest cell seeding density (120,000 cells, dark blue line in fig. 5.4), the final gel on day 14 was approximately 55% of the initial size measured on day 1. However, in the gel with the lowest cell seeding density (25,000 cells, blue line in fig. 5.4), the final samples as measured on day 14 remained at approximately 85% of the original gel size. The decrease in construct size between the different cell concentrations was deemed statistically significant at day 14 (significantly different standard deviations between the three 'groups' on day 14 as seen in fig. 5.4, $p \leq 0.05$).

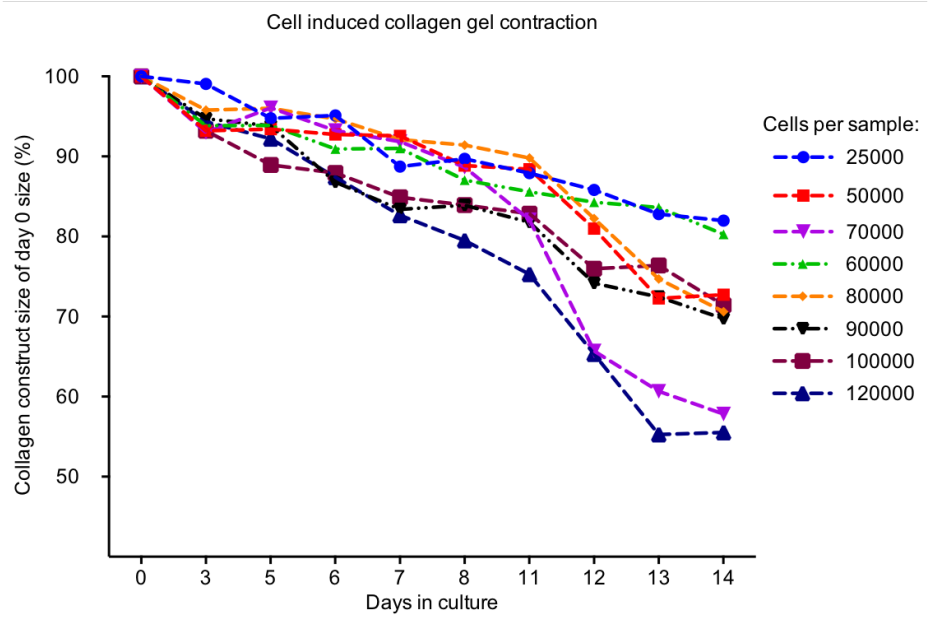

Figure 5.4: All fibroblast-seeded scaffolds contracted during a contraction assay carried out on fibroblast-seeded collagen-Matrigel scaffolds. Scaffolds were compressed using the bottom-up compression technique. Different cell densities (25,000 - 120,000 cells) were seeded onto the gels, in order to optimise the number of cells in the final constructs. Day 0 gel size (i.e. the size of the well) was designated as 100% of size. Cell densities shown are the number of cells seeded per ml of collagen gel; where each collagen gel volume prior to compression was 1ml. Even in the lowest seeding density constructs, some cell-induced contraction was seen. However, the highest seeding density resulted in a contraction of close to 50% over the two week culture time. For clarity of graph, averages were plotted without error bars. N = 3. Note the y-axis does not start from 0. A significant difference between standard deviations of samples on day 14 was found ($p \leq 0.05$; Bartlett's multiple comparisons test).

Interestingly, there was a higher amount of contraction seen in the samples initially seeded with 70,000

cells than in any higher seeding density samples (apart from the samples with 120,000 cells). Further, the 50,000 cell samples also decreased in size more than the 60,000 cell samples, to a size closer to that measured in the 100,000 cell samples.

It should be noted that the measurements from the images obtained were done over several days, rather than in one sitting, which explains the apparent levelling or even increase of area seen in some samples. The slight increases in area over culture time may also have been due to changes of media leading to increased hydration and media (water) entrapment within the samples. The samples measured were also free-floating and therefore moved around inside the wells upon handling. However, any increase was never more than a few percent of the original area, and any increase in size did not have an effect on the overall average size measurements for the scaffolds.

By decreasing the cell number from 300,000 to 120,000 per ml collagen, the contraction seen in these scaffolds was reduced from 82% to 45% of their original sizes. The slight 15% decrease in gel area over the 14 days of culture even in the lowest cell density (25,000 cells) samples in fig. 5.4 was indicative of scaffold remodelling still taking place.

Scaffold remodelling in all samples was confirmed by histological H&E staining, as seen in figures 5.5 and 5.6. None of the scaffolds, when examined with H&E staining on day 14, appeared confluent with cells (figs. 5.5 and 5.6). However, the cells did remain evenly distributed throughout the scaffolds in all seeding densities, with more even spread in the samples with fewer seeded cells. This finding further supported the benefit of adding Matrigel to the scaffolds. It should also be noted that the amount of cells which had potentially migrated out of the scaffolds to the tissue culture plate was not quantified.

The representative macroscopic images of the collagen-Matrigel gels in fig. 5.5 and fig. 5.6 show the contraction which took place in all scaffolds between days 7 and 14 of culture. To confirm that scaffold remodelling was still taking place despite the decrease in cell seeding density, as well as to check for any cell migration towards the surface of the construct as seen earlier in the collagen-only constructs, the scaffolds were examined using H&E staining. Histological staining of the contracted samples revealed a limited amount of ECM remodelling (light pink staining) in the lowest density gels as seen in fig. 5.5. There was clear ECM remodelling observed (pink staining) in the two highest density gels, with stronger cytoplasmic staining in these samples in fig. 5.6. In the samples with 25,000 cells, the cells (dark purple) were still evenly dispersed throughout the scaffold on day 14 (fig. 5.5). In some other samples, such as the ones seeded with 60,000 cells, some of the cells appeared to have migrated towards one of the surfaces of the gel.

In the samples seeded with 100,000 cells (seen in fig. 5.6), the contraction seen in the macroscopic images appeared similar to the 80,000 cell samples. Furthermore, the H&E stained sample for 100,000 cells was very contracted and thinner than the other samples. The other samples seemed to gain some thickness over time due to the scaffold remodelling and potential trapping of water from the culture media between the collagen

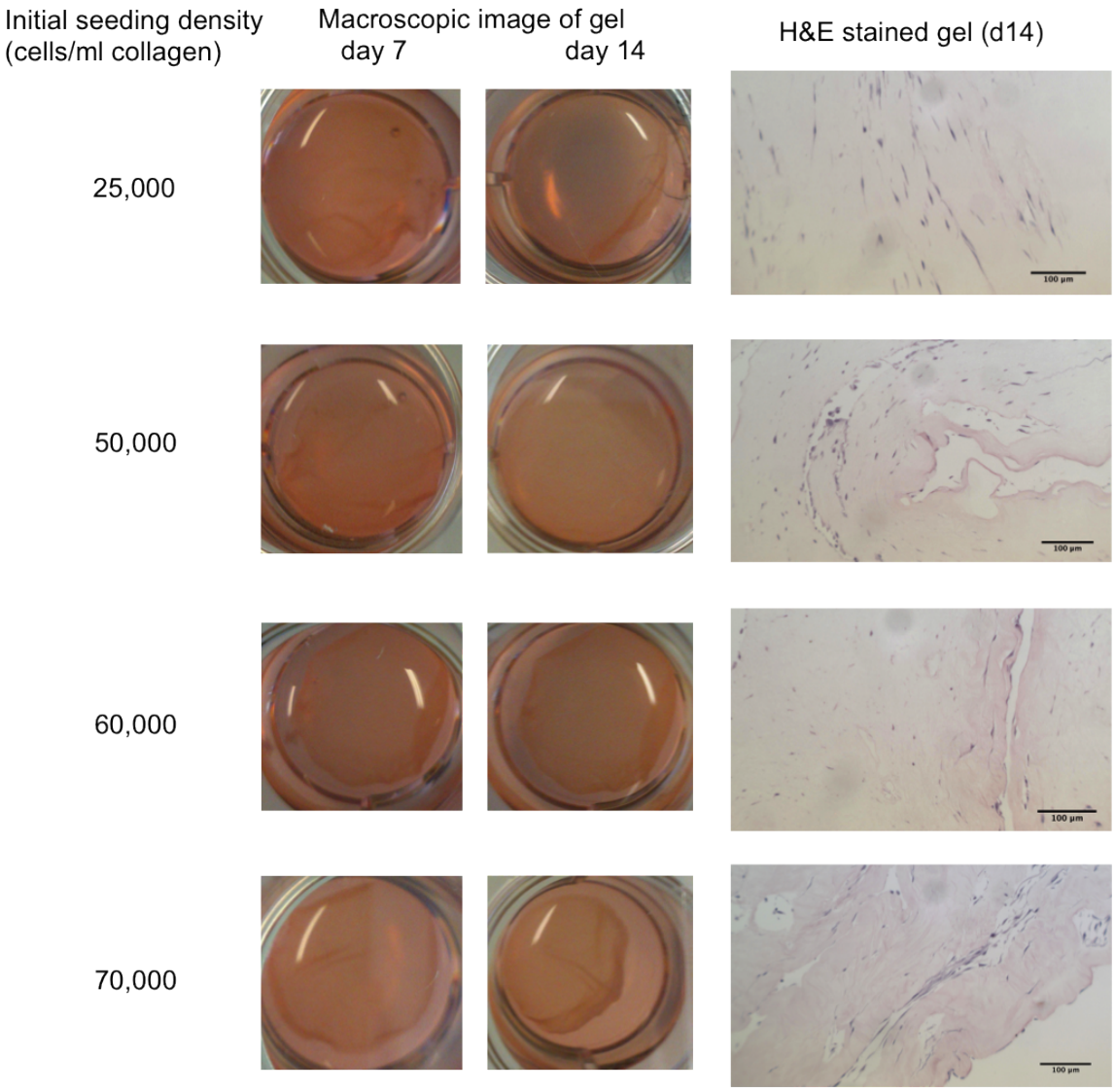

Figure 5.5: Macroscopic images of the collagen gels on day 7 (left column) and day 14 (middle column), with the contracting gels seen in media. H&E staining was used on the samples to view general tissue architecture and remodelling (right column). Here, cell seeding densities of 25,000-70,000 are seen. Plate diameter = 16mm.
In samples examined using histology, the cells (stained purple) appeared evenly spread throughout the scaffolds. A slight increase in the pink staining of the ECM indicated a slight increase in matrix remodelling with increasing cell number and an increase in collagen and ECM density. None of these scaffolds appeared confluent on day 14. Representative images of n = 3. Scale bars = 100μm.

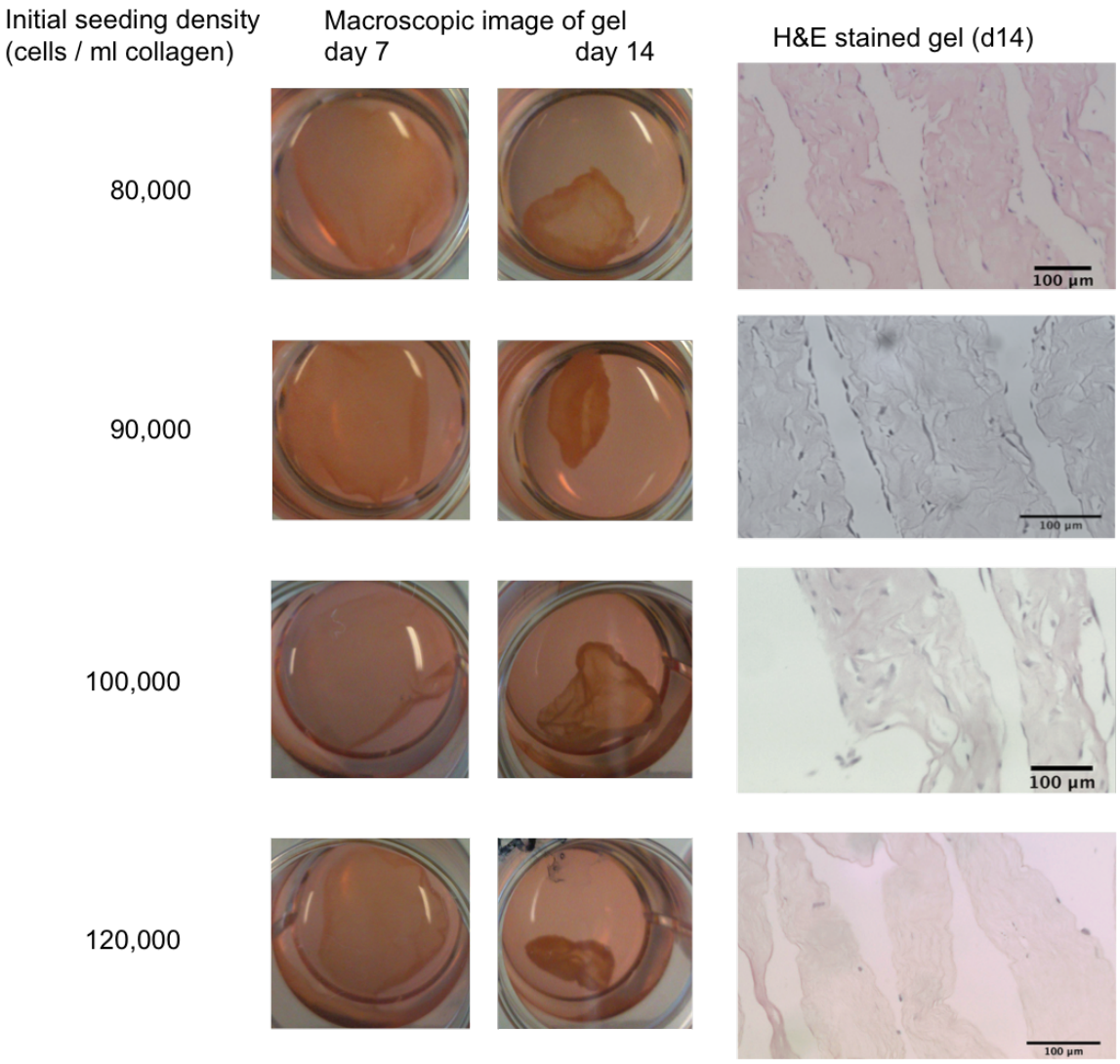

Figure 5.6: Macroscopic images of the collagen gels on day 7 (left column) and day 14 (middle column), with the contracting gels seen in media. H&E stained samples to view general tissue architecture and remodelling (right column). Here, cell seeding densities of 80,000-120,000 are seen. Plate diameter = 16mm. Increasing pink staining indicated an increase in ECM and collagen remodelling over time with increasing cell seeding density. Cells (purple) in the two lower density samples (80,000 and 90,000) appeared relatively evenly distributed throughout the scaffolds, whereas in the two highest density scaffolds (100,000 and 120,000 cells), few cells were seen throughout the samples. The scaffolds did not appear confluent even in the more densely seeded samples on day 14. Representative images of n = 3. Scale bars = 100μm.

fibres. As can be seen in all the macroscopic images, most of the contraction took place in the second week of culture; the contraction was therefore highly dependent on a higher number of cells present within the constructs. The gels appeared folded in the H&E images due the to the fixing and processing techniques used.

5.4 SEM on cells in scaffold

Scanning electron microscopy (SEM) was used to further examine both the cells and the collagen-only and collagen-Matrigel scaffolds more closely. The scaffolds with added Matrigel appeared creased (fig. 5.7A and C), whereas the collagen-only scaffolds appeared smoother overall (fig. 5.7B and D). Cells (white arrows) in all samples appeared elongated with projections, and especially in 5.7D, clustered together. Cells in the day 14 samples appeared more numerous, but a direct comparison of cell number based on the scaffold surface alone was not possible. The addition of Matrigel to these scaffolds was deemed beneficial to the cells both due to the reduction in gel contraction and enabling cell proliferation within the constructs, yet still allowing remodelling of the scaffolds to take place.

All subsequent experiments and co-cultures were carried out with soft tissue models made with collagen-Matrigel scaffolds and 25,000 gingival fibroblast cells per ml collagen-Matrigel solution, apart from the viability assay comparison presented in fig. 5.9, where a collagen-only scaffold was used. A 1:2 ratio of Matrigel:collagen was decided on. This was based on similar previous organotypic scaffold studies (Chaudhry et al., 2013), although the high cost of Matrigel and the difficulty of maintaining it at ice-cold temperatures before incorporating it to the collagen gels were also considered. In addition, the following practical aspects were considered: the collagen solution, which started at 4°C was warmed up during neutralisation, due to the addition of NaOH and handling at RT (21°C). This warming up was beneficial for cell survival upon incorporation in the gels, whereas to prevent gelling Matrigel needed to be kept ice-cold. Furthermore, a lower collagen gel temperature (as potentially caused by a higher volume of ice-cold Matrigel) could have negatively impacted the cells in the gel, as the cells were added immediately after neutralising the collagen, prior to it setting, which in practical terms left a very short window for Matrigel addition and sufficient mixing.

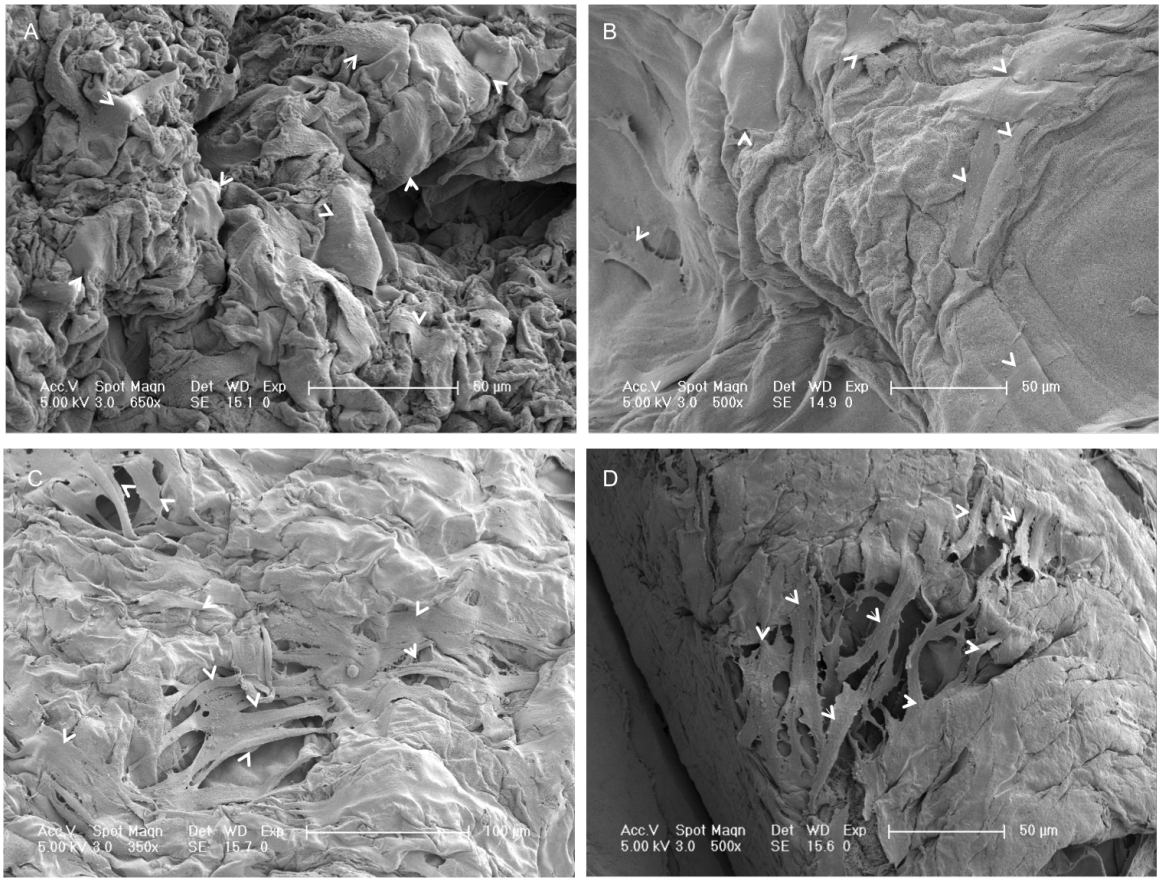

Figure 5.7: Scanning electron micrographs of fibroblast-seeded constructs on days 10 and 14. The fibroblasts in the scaffolds appeared flattened, elongated and spread out in all samples. Some of the cells in the scaffold are indicated by the white arrowheads. A) The collagen-Matrigel scaffold on day 10. B) A collagen-only scaffold on day 10. C) A collagen-Matrigel sample on day 14. D) A collagen-only scaffold on day 14. Fibroblasts in all samples appeared elongated and samples from the 14-day time points appeared more confluent. On day 14, the cells had formed networks on the scaffolds, as seen in the middle of C and D. Note all images are taken from the surface of the samples. Scale bars A, B and D = 50μm, C = 100μm.

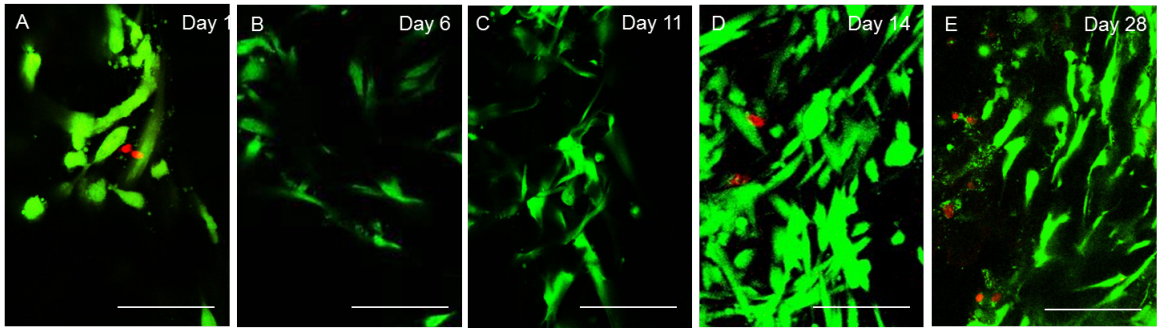

Figure 5.8: Confocal micrographs of gingival fibroblasts stained for live (green) and dead (red) cells on days 1 (A), 6 (B), 11 (C), 14 (D) and 28 (E). The cells in the collagen-Matrigel constructs appeared alive, with very few dead cells seen on the first four time points. Fibroblasts exhibited a characteristic elongated morphology within the collagen gels. Cell numbers appeared to be increasing over time to reach confluency around day 14. On day 28 (E), several dead or dying cells were observed within all scaffolds. Representative images of n = 3. Scale bars = 50μm.

5.5 Cell survival in soft tissue models

Fibroblast survival in the collagen-Matrigel scaffolds was qualitatively analysed using Live/Dead staining and confocal microscopy. The gingival fibroblasts appeared to survive inside the collagen gels for up to 28 days as seen in fig. 5.8. Fibroblasts appeared alive (stained green) and slightly rounded on day 1 of culture (fig.5.8A). On day 1 (fig. 5.8A), there were also a few dead cells (red) visible, which was thought to be due to the gel making process, where the cells were incorporated in a relatively cold collagen-Matrigel solution and left to set in it for approximately 20min prior to incubation, as well as the compression process itself, which may have had a negative effect on the cells. The more rounded cell morphology seen here on day 1 was also partly thought to be due to the chemical cell detachment process using trypsin, but most cells were still viable. No rounded cells were seen on any other time point, apart from when a cell was dying. Day 6 samples showed a limited amount of cell proliferation (fig. 5.8B), but most cells at this time stained green, indicating that the scaffold was able to support them.

By day 11, the cells had proliferated within the scaffolds (fig. 5.8C). At this time point, the cells (green) appeared elongated and displayed multiple projections. Fibroblasts at this time point also appeared clustered together. This was thought to be due to proliferation of the monodispersion of the cells seeded in the scaffolds and limited movement of the cells within the scaffolds. No dead cells (red) were seen at this time point. On day 14 (fig. 5.8D), a few dead cells were seen within the scaffolds. Live fibroblasts appeared elongated, spindle-like and occasionally stellate in their morphology. Most of the scaffolds at this time point appeared to approach confluency. On the last time point on day 28 (fig. 5.8E), the majority of the cells were still alive and their morphology was similar to the previous time points. However, there was some extensive cell death seen in parts of the constructs, with dead as well as dying cells (granular cytoplasms stained green) present in all samples. This was thought to partly be due to the confluent scaffolds at this late time point, but also due to nutrient and oxygen diffusion limitations in this long term culture. 28 days of fibroblast culture was therefore, as for the bone-like scaffolds, taken to be the last time point for analysis of the AM-1 co-culture scaffolds.

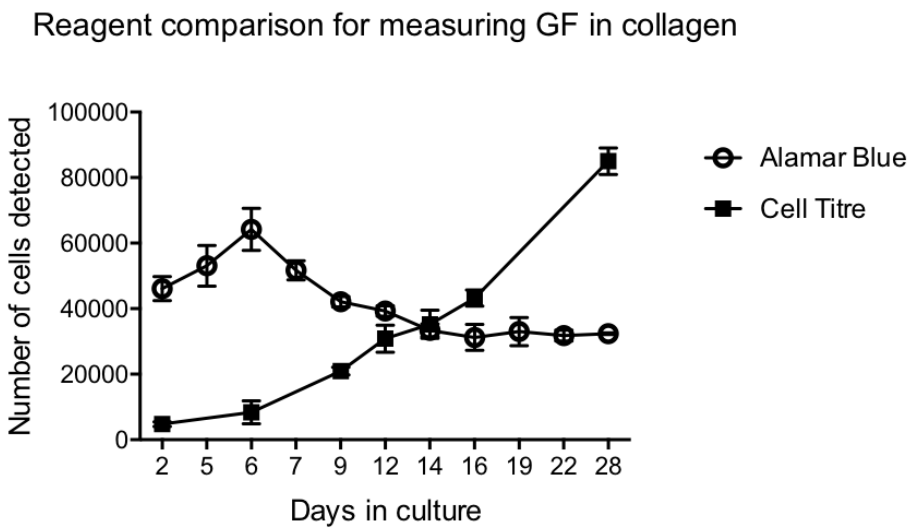

Figure 5.9: Comparison of cell number obtained in GF collagen-only scaffolds using Alamar Blue and Cell Titre Glo. Readings from both assays were normalised against background values and converted to cell number using standard curve values. The Alamar Blue metabolic measurement showed an increase in cell number during the first week, after which the reading reached a plateau. The Cell Titre Glo 3D metabolic assay gave a constant increase in cell ATP activity throughout culture. It should also be noted that while the Cell Titre assay picked up approximately the correct number of cells (approximately 3,125 seeded per scaffold on day 0), the Alamar Blue reading obtained correlated to approximately 50,000 cells (maximum on day 6), although 150,000 cells were seeded initially per scaffold.

5.6 Cell proliferation in soft tissue models

Initially, cell numbers within the soft tissue models were measured using the Alamar Blue metabolic colorimetric assay as for the bone-like co-cultures in chapter 3. However, as with the bone-like scaffolds, this was found to be unreliable and inconsistent. This was probably due to issues with reagent penetration in the scaffolds during the incubation time, especially in the more dense, contracted later time points examined. Measurements for cell number obtained using the Alamar Blue assay were compared with cell numbers obtained using the Cell Titre Glo 3D ATP luminescent assay. In fig. 5.9, the two methods are compared to show the discrepancy between the number of metabolically active/viable cells in the scaffolds.

Readings from the Alamar Blue assay indicated an initial increase in cell viability in these scaffolds in the first week of culture, with a peak in cell number on day 6 of culture. Subsequently, the cell metabolic activity declined to levels similar to those measured at the start of culture, with the cell number measured reaching a plateau between weeks 3 and 4 of culture.

In contrast, measuring cell number using the ATP-based Cell Titre Glo assay, GF cells in the scaffolds increased consistently in number throughout the 28-day culture time. The expected cell number per cut collagen scaffold on day 0 was approximately 3,100 cells (75,000 cells per 3ml collagen-only scaffold, compressed and cut into 24 equal pieces). Figure 5.9 shows an increase in fibroblast cell viability in the collagen scaffolds from initial seeding to day 28 in culture. Cell numbers in the scaffolds increased over culture time. By day

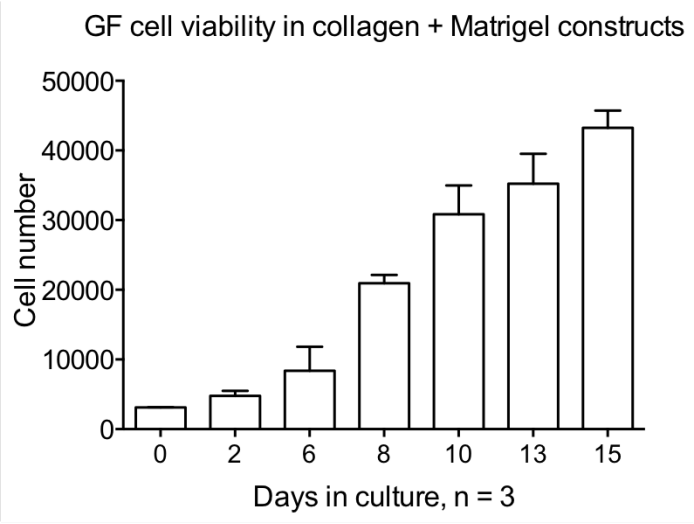

Figure 5.10: Gingival fibroblast cell viability in the collagen-Matrigel scaffolds as measured by the Cell Titre Glo ATP assay. Fibroblasts in the constructs proliferated steadily throughout the 15 day assay period. A tripling of cell number was seen within the first week of culture (on day 6), and by day 10, the cell number was ten-fold to that seeded. During this study time, no decrease in proliferation was seen, indicating that the scaffolds were not yet confluent by day 15. Error bars = 95% CI. N = 3.

6, an approximate tripling of cell number was observed (8,500 cells per scaffold). By day 9, cell number appeared 10-fold to the initial cell seeding number (approximately 30,000 cells). By day 14, when the AM-1 cells were incorporated to form the co-cultures, there were approximately 45,000 cells per construct.
The Alamar Blue assay picked up approximately 50,000 cells in a construct with of a seeded 150,000 initial cell number. Meanwhile, the Cell Titre Glo assay measured approximately 3,000 cells in the scaffolds of an approximate 3,125 cells per scaffold with an initial 25,000 cells per ml collagen seeded in the scaffolds.

Based on this finding, GF cell survival inside the collagen-Matrigel constructs was subsequently assessed by measuring cellular ATP using the Cell Titre Glo Assay and the results are visualised in fig. 5.10. On the day of seeding, day 0, the cells were in a monodispersion throughout the scaffolds. Cell number within these constructs increased steadily with increasing time in culture. Cell proliferation did not appear to plateau or decrease during the assay time, which indicated that the cells had not reached confluency within the constructs during the assay time. Indeed, this was consistent with the H&E staining seen previously in fig. 5.5.

These findings were also mainly consistent with the increasing cell number and confluency of the scaffolds seen using Live/Dead staining (fig. 5.8), up to the last 28-day time point. The increase in cell viability seen using Cell Titre Glo between days 21 and 28 was not seen when using the Live/Dead stain for day 28 samples. Instead, a lot of the cells at this last time point appeared to be dying when examined under the microscope. This indicates that the Cell Titre Glo assay may not be able differentiate between dying and living cells, which both contain ATP. This may affect the cell viability results obtained with this assay.

However, despite this potential over-estimation of cell viability when using the Cell Titre Glo assay, it was deemed more suitable for measuring cell viability within compressed and dense collagen-Matrigel scaffolds.

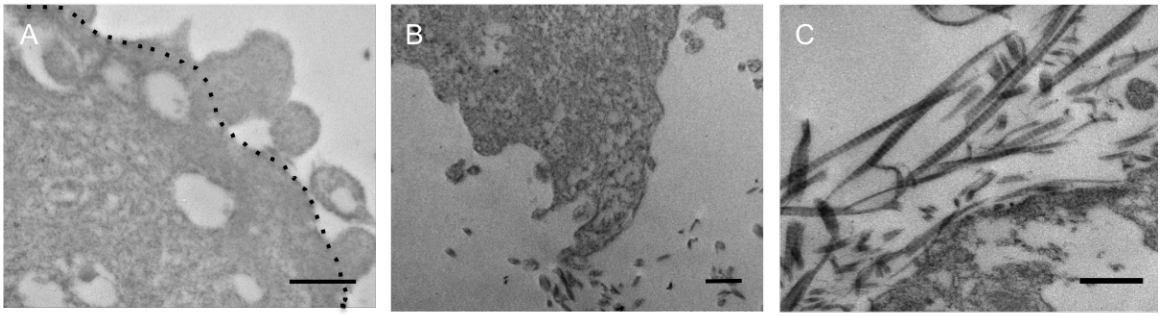

Figure 5.11: Transmission electron micrographs of gingival fibroblasts in collagen-Matrigel constructs on day 14. A) The approximate cell membrane of a part of a single fibroblast is indicated by the black dotted line. Abundant vesicles were seen along the cell membrane, indicating production and transport of various extracellular proteins. Vesicles were also seen inside the cell cytoplasm. B) Potential collagen fibre extrusion was also seen in these scaffolds, as seen here on the apex of the cell. C) Characteristic collagen fibre banding was seen in the scaffolds. Collagen fibres appeared randomly oriented throughout the scaffolds, although some in the vicinity of cells were aligned with the cell membranes. No difference in collagen or ECM appearance was found between collagen-only and collagen-Matrigel scaffolds when these were examined using the TEM. Scale bars = 500nm.

5.7 Transmission electron microscopy of scaffolds

Transmission electron microscopy was used to examine the cell ultrastructures more closely. Abundant vesicles were seen in the cell cytoplasms as seen in fig. 5.11A. Many of the vesicles seen appeared to be filled. Non-filled, rounded vesicles (or vacuoles) were taken to be either lipid droplets within the cells or a sign of ongoing apoptosis, although vesicles could also be an artefact created by sample processing. As the vesicles in fig. 5.11A were mostly filled, they were thought to indicate protein and ECM factor synthesis in the cells and protein transport out of the cell. Cells were seen to potentially extrude collagen fibres, as seen at the apex of the cell in fig 5.11B.

TEM analysis also allowed a closer look at the collagen fibres in the constructs, which are seen in fig. 5.11C. Collagen fibres, with their characteristic banding clearly visible, appeared somewhat disorganised, although some fibres, especially around the cells within the scaffolds, seemed more organised and aligned along the cell membrane (fig. 5.11C). Collagen fibres were evenly distributed across the scaffolds.

5.8 Conclusions for developing a soft tissue-like model

The first part of this chapter has described the development of a soft tissue organotypic scaffold to be incorporated with cellularised AM-1 tumour model constructs to form co-cultures.

The main parameters explored and conclusions for the development of the organotypic soft tissue part of the co-culture scaffold are summarised in table 5.1. The results obtained in the first part of this chapter informed the development of the subsequent soft tissue co-culture construct.

Table 5.1: Summary of variables considered when developing the soft tissue models. This table details the various parameters tested when developing the soft tissue scaffolds. The final parameters used are also outlined in the 'Outcome' column.

Variable investigated	**Range tested**	**Result**	**Outcome**
Collagen amount in scaffolds	67- 100 %	100% collagen constructs contracted excessively and the cells migrated to the surface. Contraction was reduced with the addition of Matrigel, which also provided the tissue models with a more native-like ECM protein composition.	67% collagen was decided on, with a 2:1 collagen: Matrigel ratio in the final scaffolds.
Matrigel amount in scaffolds	0 - 33 %	Matrigel was deemed beneficial for cell remodelling and for a more organotypic scaffold due to the addition of other ECM factors. No change in cell viability or proliferation was seen. Constructs with Matrigel contracted less.	Matrigel was added to all subsequent cultures.
Cell number	25,000 - 300,000 cells / ml	25,000 cells contracted the least (by approximately 15%). Up to 82% contraction seen in 300,000 cells/ml models and 45% in the 120,000 cells/ml models.	As a long term culture of the scaffolds was needed, the with 25,000 cells/ml were chosen.
Number of days in culture	0 - 28 days	A 28 day culture allowed for remodelling of the GF scaffold. By 28 days, there was extensive cell death seen in the single cell type GF scaffolds, therefore this was decided to keep as the end point for all cultures	28 days including AM-1 co-culture. This also allowed work on both scaffolds types in parallel.

The gingival fibroblast cells in the constructs initially caused a large amount of contraction due to scaffold remodelling. However, this was overcome by the addition of Matrigel basement membrane and by reducing the cell seeding density. Fibroblasts survival was assayed for 28 days within the scaffolds, during which time they proliferated to confluency. The cells in these scaffolds remained alive throughout culture time, appeared to proliferate and to remodel the matrix.

A day 14 culture time point was decided on for constructing the co-culture models, as this was found to be when the fibroblasts had expanded to most of the scaffold and a minimal amount of contraction was seen. This also allowed for experimentation on both the soft tissue model and the bone-like model in parallel.

5.9 Ameloblastoma and soft tissue model co-culture

In this part of the chapter, the synthesis of the soft tissue ameloblastoma co-culture model is described. As with the bone model, ameloblastoma cells from the AM-1 cell line were added to the soft tissue-like scaffold to form a co-culture, and these two cellularised constructs were cultured together for two weeks to produce an organotypic soft tissue model. It should be noted that for the GF + AM-1 co-culture scaffolds, any mention of 'collagen scaffold' refers to the collagen-Matrigel scaffolds.

This model was assembled in the same way as the bone-like model described in chapter 4, with the bone-like scaffold being substituted for a soft tissue mimicking fibroblast scaffold in addition to AM-1 cells. As with the bone-like models, there was also a layer of acellular collagen gel added to the co-cultures to ensure the model remained attached for the whole culture time and withstood manipulation. The set-up of the co-culture model is shown in fig. 5.12: the two separate cellularised gels were placed next to each other on top of an acellular gel. In the schematic in fig. 5.12, blue indicates the fibroblast-cellularised, soft tissue model

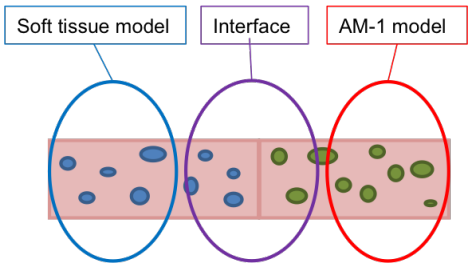

Figure 5.12: Schematic of the soft tissue co-culture model set-up. The soft tissue organotypic scaffold is denoted in blue and the AM-1 part of the model in red. The interface region, where the two different cellularised gels meet and where cells potentially closely interact with each other, is shown in purple. Note that this schematic does not include the acellular gel on the bottom.

part, the red is the AM-1 part and the purple indicates the interface between the two gels, where the two cell types come into physical contact, and where in theory, as in the bone-like co-cultures, there may be a mixed population of cells present. As the two constructs were in close contact, paracrine effects would also have been present.

The approximate size of the final co-culture model was 10mm x 5mm, and the constructs were approximately 250μm in thickness. The co-culture models were incubated in 24-well plates in 1ml KSFM, with media changed every 2 days. Co-cultures were analysed for gene expression using qRT-PCR, a selection of proteins were stained for and the cells in the scaffolds viewed using immunocytochemistry and confocal microscopy. Cell invasion was visualised using the Cell Tracker assay.

5.10 Cell survival in co-cultures

Cell viability in both the GF and AM-1 parts of the co-culture models was measured using Cell Titre Glo. The viability data for GF cells in the co-cultures is seen in fig. 5.13A. These cells had, as seen previously, already

been pre-cultured for 14 days to remodel the matrix and provide a more organotypic culture environment. Therefore, the proliferation rate of the GF cells had slowed down by the time these were incorporated in the co-cultures. As can be seen in figure 5.13A, there were approximately 40,000 fibroblast cells in the constructs at all time points during the two week co-culture. No significant difference between the time points was found.

In fact, the overall increase in cell number seen in GF-only constructs in fig. 5.9 was not seen here; although the cell numbers seen at the start of the co-culture here corresponded with those in the GF-only culture cell numbers in fig. 5.10. The addition of AM-1 cells appeared to have reduced or slowed down GF cell proliferation.

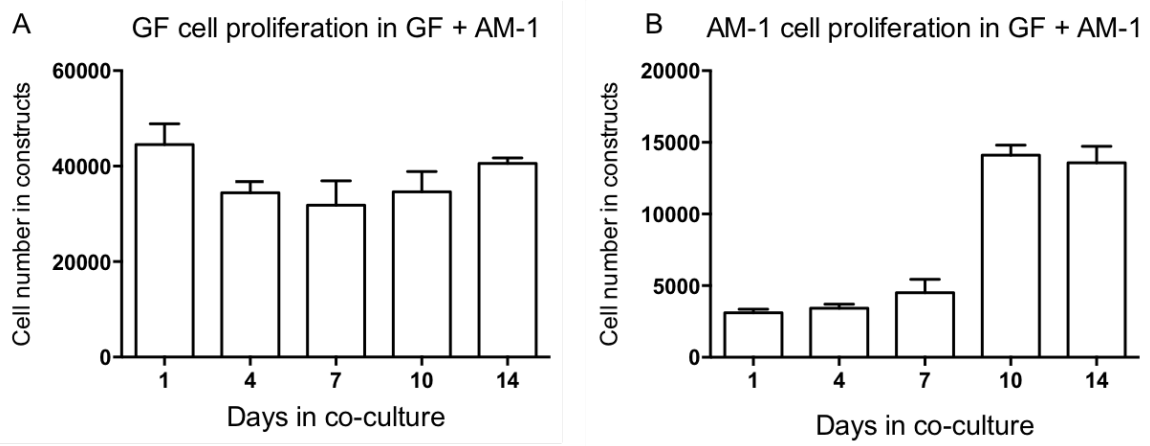

Figure 5.13: Cell Titre Glo measured cell viability in GF + AM-1 co-culture constructs. Cells in both parts of the constructs were viable. Cells in the GF part (A) of the construct had been pre-cultured in the collagen-Matrigel scaffolds for 14 days, so this longer culture period explains the reduced cell proliferation rate seen in these constructs. AM-1 cells (B), which had been freshly seeded to form the co-cultures, were seen to proliferate throughout the 14 day culture time. AM-1 cells increased from their initial 3,000 cells per construct to approximately 15,000 cells per construct after 10 days in co-culture. Error bars show the 95% CI, n = 3.

The results of AM-1 cell viability in the co-cultures as measured using the Cell Titre Glo assay are plotted in fig. 5.13B. These cells increased in cell number during the 14 day culture time. On days 1 and 4, approximately 4,000 cells were detected in the models. By day 14, there were 15,000 cells present in all models. There was a significant increase in cell number when comparing the early (days 1, 4 and 7) time points with the late ones (days 10 and 14, $p \leq 0.001$). There was no significant difference between the cell number seen between days 10 and 14, although as seen in fig. 5.13B, it appeared to decrease slightly. This could be due to inter-experimental variation in separating the two co-culture parts from each other in preparation for this assay.

AM-1 proliferation in GF + AM-1 co-cultures appeared similar, although was found slightly increased when compared to the proliferation levels seen in the HOB co-cultures (10,000 AM-1 cells were measured in HOB co-cultures), compared to the 15,000 cells by day 14 of co-culture measured in these models. In contrast, 70,000 cells were measured for the AM-1 part of the HOS + AM-1 scaffolds by day 14, again indicating that the cancerous HOS cell line had a major effect on the behaviour on the AM-1 cells.

5.11 Gene expression in co-culture models

In order to determine what effect co-culturing AM-1 cells together with the fibroblast scaffolds had on the gene expression in co-cultures, qRT-PCR was carried out. Changes in gene expression were analysed in the three different parts of the co-cultures as seen in fig. 5.12: AM-1, IF and GF. 'GF control' and 'AM-1 control' samples indicate single-cell type scaffolds cultured for the same time as the co-cultures. Asterisks have been placed on top of the bar where gene expression was found significantly different when compared to the corresponding control sample.

Firstly, MMP-2 and MMP-9 levels were examined (figures 5.14 and 5.15, respectively), as these are involved in matrix remodelling, collagen and ECM breakdown, as well as cell motility within tissues. Both have also been shown to increase in expression in ameloblastoma tumours, and it was therefore thought these could provide clues to AM-1 soft tissue invasion.

Matrix metalloproteinase-2 (MMP-2)

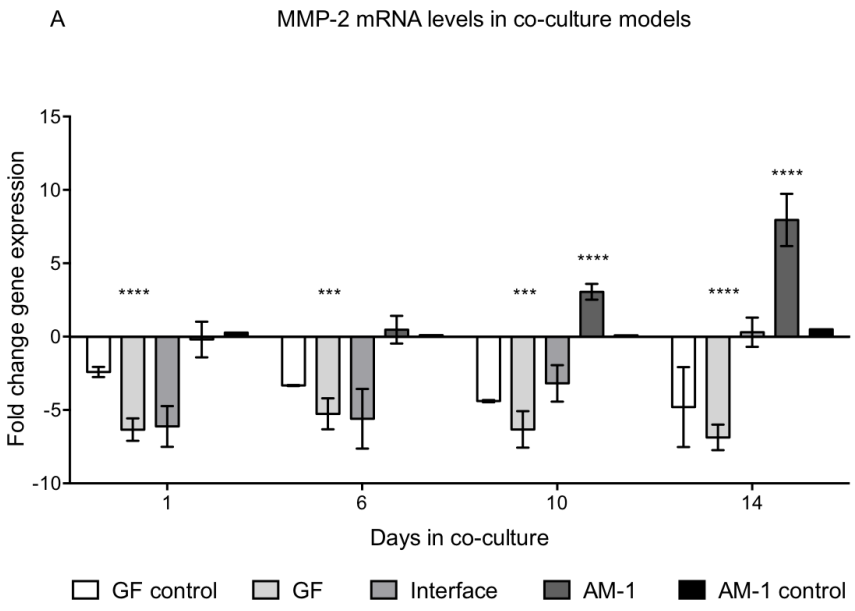

Figure 5.14: MMP2 mRNA levels in GF + AM-1 co-cultures. Gene expression levels of MMP-2 in the GF controls were around 5-fold less than in the calibrator samples, whereas in the AM-1 controls MMP-2 expression remained level with the calibrator. In the co-cultures, MMP-2 expression in the GF part was similar to the GF controls throughout. However, in the AM-1 part, MMP-2 expression steadily increased throughout culture time. MMP-2 levels in the interface also increased five-fold in the 14 days of culture. Two-way ANOVA, *** indicates $p \leq 0.001$, **** $p \leq 0.0001$. Error bars show the 95% CI, n = 4.

MMP-2 gene expression, as seen in fig. 5.14, increased significantly over time between the AM-1 control samples and AM-1 in the co-cultures on days 10 and 14 ($p \leq 0.0001$). No significant difference was found between the AM-1 samples and AM-1 controls on days 1 and 6. Note the minimal expression throughout culture time in the AM-1 control samples, indicating little MMP-2 expression present. This indicated that the increased expression of MMP-2 in the AM-1 part of the constructs later on in culture was due to the co-culture with GF cells.

Significant differences were also found between the GF control samples and the GF part of the co-cultures on day 1 ($p \leq 0.0001$), day 6 ($p \leq 0.001$), day 10 ($p \leq 0.001$) and day 14 ($p \leq 0.0001$). MMP-2 levels between GF and IF as well as IF and AM-1 were found significantly different on days 1, 6 and 10 ($p \leq 0.01$), but this difference disappeared between the AM-1 parts by day 14, with the observed increase in MMP-2 levels in the interface of the co-cultures.

Matrix metalloproteinase-9 (MMP-9)

MMP-9 expression levels throughout the GF + AM-1 co-culture scaffolds is plotted in fig. 5.15. On days 1 and 6, there was a significant increase (both $p \leq 0.01$) in MMP-9 levels observed in GF co-culture samples compared to the GF controls. However, on days 10 and 14 there was a significant decrease in MMP-9 expression between GF samples and GF controls (both $p \leq 0.0001$). As MMP-9 expression levels remained high in the GF control samples throughout culture time, this indicated that the decrease in MMP-9 in the co-culture samples was due to co-culture with AM-1 cells.

The difference in MMP-9 expression between AM-1 control and AM-1 co-culture samples was significant from day 6 of culture onwards (all $p \leq 0.0001$), with AM-1 in co-cultures exhibiting an approximate 5-fold increase in MMP-9 expression than their control equivalents. A significant difference was also found between IF and AM-1 in co-culture on day 1, however by day 6 this difference between the AM-1 part and the interface disappeared, with increased MMP-9 expression also in the interface. There was very little MMP-9 seen in the AM-1 controls throughout culture, indicating that the increase in MMP-9 expression was also due to the co-culture with GF cells.

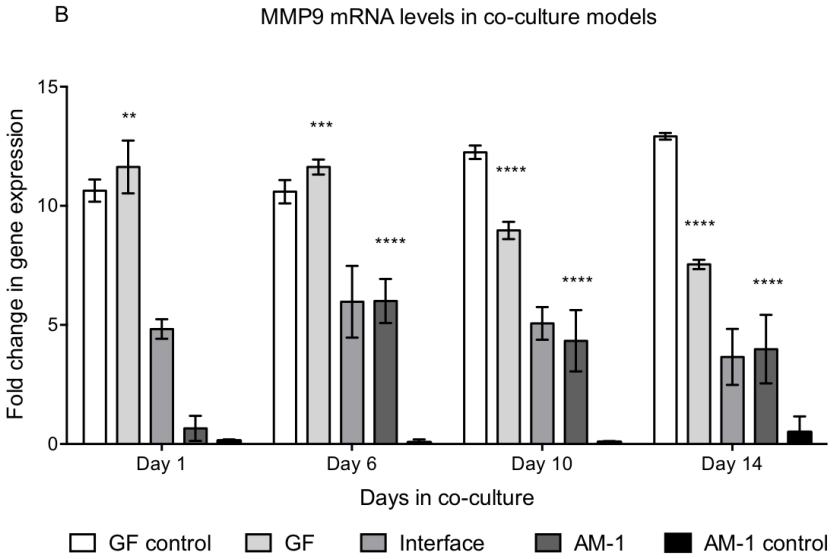

Figure 5.15: MMP-9 mRNA levels in the GF + AM-1 co-culture models. MMP-9 expression appeared to increase over time in the AM-1 part of the co-cultures. MMP-9 expression was high (10-fold compared to the calibrator) throughout culture time in the GF control samples, and relatively high but decreasing in the GF co-culture samples. Two-way ANOVA, ** indicates $p \leq 0.01$, *** $p \leq 0.001$ and **** $p \leq 0.0001$. Error bars show the 95% CI, n = 4.

The increase in MMP-9 in the AM-1 part of the co-cultures was not found as large as that for MMP-2;

with a 5-fold increase in MMP-9 compared to an 8-fold increase for MMP-2 by day 14. MMP-9 levels were higher in all other parts of the co-culture models and controls than in the AM-1 part (fig. 5.15), which indicated that the increase in MMP-9 in the AM-1 part was due to the high levels elsewhere, or due to a slower response by the AM-1 cells to the co-culture environment.

Unlike MMP-2 (fig. 5.14), where the levels were found to increase at the interface of the co-cultures, presumably due to the increasing MMP-2 expression seen in the AM-1 part, MMP-9 in the IF part remained at approximately 5-fold compared to the calibrator samples throughout co-culture.
Whereas for the MMP-2 gene expression data, it appeared that the increase in MMP-2 in the AM-1 samples caused a slow increase in MMP-2 expression in the IF part of the co-cultures, the opposite seemed to be the case for MMP-9 expression. An initially high MMP-9 expression level in the GF part of the constructs, but a low MMP-9 expression in the AM-1 part, translated to a relatively high level of MMP-9 expression in the IF part throughout co-culture. These increases in MMP levels for both cell types may aid potential cell invasion within the co-cultures. This was subsequently explored further.

Smoothened (SMO)

Finally, gene expression of SMO was examined and the results are plotted in fig. 5.16. Previous studies have shown SMO to be abundantly over-expressed in ameloblastoma tumours, and potentially indicated as causative in some ameloblastomas, which is why SMO expression was also examined during this study.

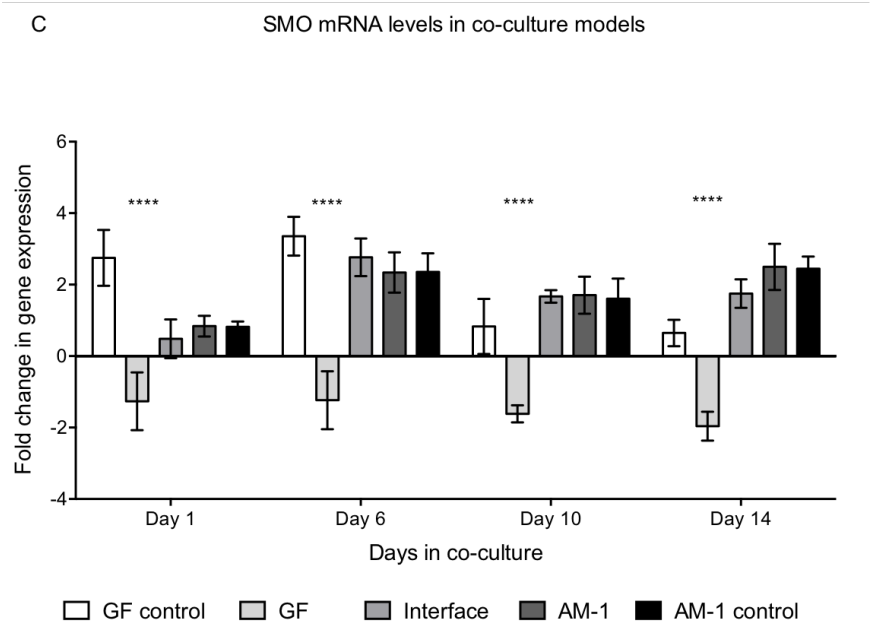

Figure 5.16: SMO mRNA levels in the GF + AM-1 co-culture models. SMO expression was found initially high and gradually decreasing in the GF control samples, whereas in the AM-1 controls expression was initially low and then increased. SMO expression in the GF parts of the co-cultures was found significantly lower compared to the controls. No change in SMO levels in the AM-1 co-cultures were seen compared to that seen in the AM-1 control samples. Two-way ANOVA, **** indicates $p \leq 0.0001$. Error bars show the 95% CI, n = 3.

In the AM-1 co-cultures, AM-1 controls and the interface, a slight increase in SMO expression was seen between days 1 and 6 of culture (fig. 5.16). SMO expression in the IF region was similar to the expression in the AM-1 parts, with no significant differences at seen any time point (fig. 5.16). SMO expression remained approximately 2-fold increased compared to the calibrator samples in both the AM-1 controls and co-culture samples throughout culture time.

SMO expression in the GF cells appeared to be influenced by whether they were cultured alone or with AM-1 cells (fig. 5.16). In the GF co-cultures, SMO was consistently underexpressed, whereas in the GF controls, there was a significant over-expression at all time points (all $p \leq 0.0001$).

When the SMO levels seen in AM-1 cells grown with GF cells were compared to the results obtained when AM-1 cells were grown in the bone-like co-cultures as seen in fig. 4.15, the results were similar overall. In both the bone-like and the soft tissue co-cultures, AM-1 SMO gene expression remained constant over culture time, at approximately 1-2-fold that of the calibrators. AM-1 cells cultured alone and in co-cultures showed no significant change in gene expression in either experimental set-up. The only change seen in both was in SMO expression by the other cell type AM-1 cells were cultured with, as both HOS cells and GF cells showed a significant reduction ($p \leq 0.0001$) in SMO expression when in co-culture with AM-1 cells compared to their respective controls.

5.12 Assessing invasion in the co-culture models

5.12.1 Confocal microscopy

The interface between the two gels was examined using confocal microscopy to visualise any close cell-to-cell interactions in the part of the co-cultures were the two constructs were proximal. Furthermore, any potential invasion was also visualised.

In fig. 5.17, confocal micrographs of the interface between the two gels are seen. The point at which the two constructs join is indicated by the white dotted line.

No invasion was seen in the co-culture constructs on either day 7 (fig. 5.17A) or day 14 (fig. 5.17B), but the two cell types were found closely interacting at the border of the two constructs in co-culture (denoted by the white dotted line). AM-1 cell clusters are indicated by the white arrows, whereas blue arrows denote fibroblast cells. The fibroblasts on both days shown here appeared peripendicular to the edge of the GF scaffold. Fibroblast nuclei appeared elongated, whereas the AM-1 cell nuclei were rounded. AM-1 cells appeared to have proliferated in the vicinity of the GF cells and were clustered together.

However, it was not possible to definitively determine which cells were which type using only the cell morphologies as a distinction.

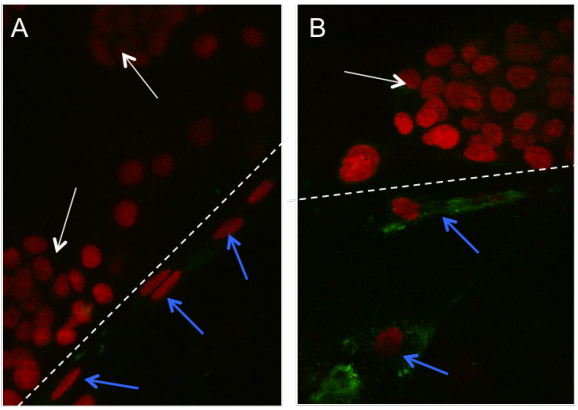

Figure 5.17: The co-culture interface between the GF and AM-1 cellularised constructs. A) Day 7 and B) Day 14. The white dotted line indicates the interface of the two construct parts. White arrows denote AM-1 cell clusters, blue arrows GF cells. No invasion was seen at any time point in the GF + AM-1 cultures, although the cells were in close proximity to each other at both days 7 and 14. Samples stained for fibroblast surface protein (green) and the EthD-1 nuclear stain (red). Both images are a 40X magnification. Confocal micrographs of immunocytochemically stained samples. Representative images of n = 3.

5.12.2 Cell Tracker

To more closely assess any potential invasion taking place between the two distinct cellularised gels, they were examined using the Cell Tracker assay. As the cells were stained prior to incorporation in the gels, the two populations were labelled with non-transferable fluorescent dyes as seen in fig. 5.18. The time for this assay was limited to four days due to the relatively fast proliferation rate of the GF cells. On day 0 (2 hours after co-culture assembly), the cells were in their distinct populations within the scaffolds (fig. 5.18A, B), with AM-1 cells stained red and GF cells in green (nuclei were counterstained blue).

By day 2, AM cells were beginning to form larger clusters (fig. 5.18C, D; insert: a cluster of AM-1 cells from another part of the construct) as expected. Staining in the GF cells had started to fade due to cell proliferation. The cell populations were still in their distinct parts of the co-culture models on this time point. By day 4, a limited amount of invasion was seen (fig. 5.18E), where the GF cells appeared to have invaded the AM-1 part of the model (the interface between the two parts is indicated by the dotted line). However, in another sample seen in fig. 5.18F, the cells remained in their distinct constructs; a lack of invasion was also found in the other samples examined. The dye in the fibroblast population had largely faded by this time point, and the AM-1 cells appeared to have lost the majority of their fluorescent signal. Arrows specific to the staining colour (AM-1 = red, GF = green) were therefore employed in fig. 5.18E and F to indicate the faint colouring of the cells seen in the day 4 samples.

Despite the increase in MMP-2 levels seen taking place using gene expression analysis, the AM-1 cells were not using MMP-2 to invade the GF part of the co-culture models. The AM-1 cells in these models must therefore require MMP-2 for some other function; this was investigated further.

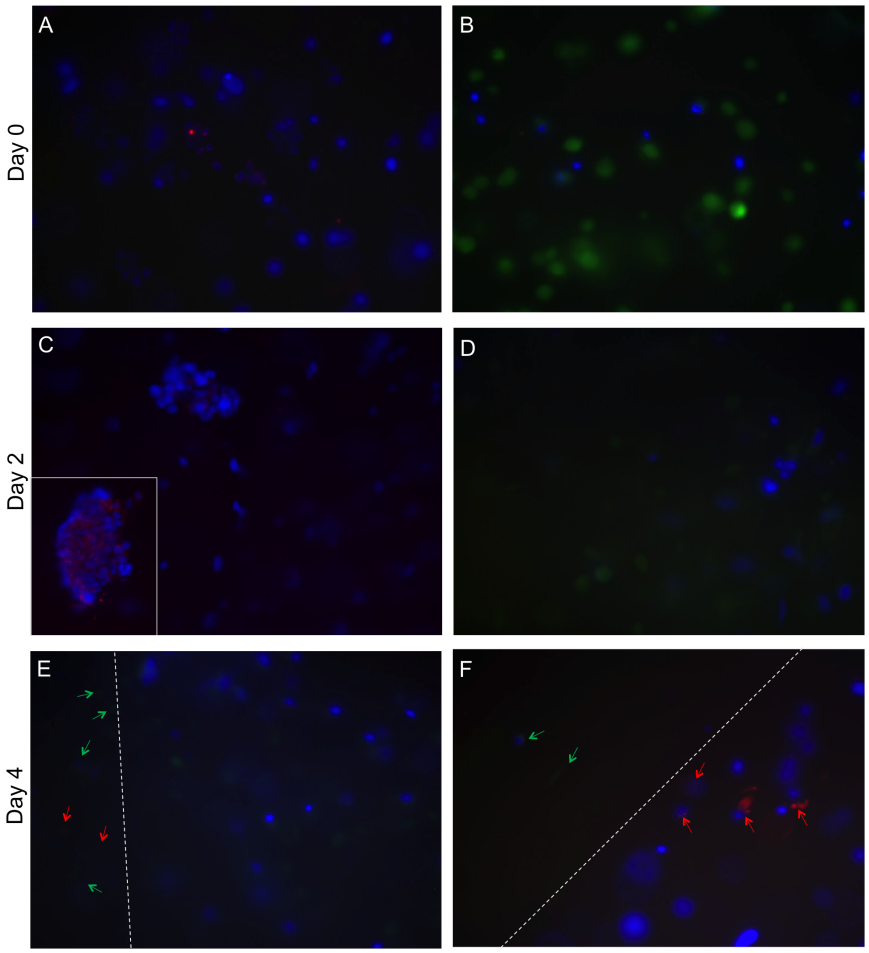

Figure 5.18: Cell Tracker dyes were used to distinguish the two cell populations from each other in the co-cultures. Here, nuclei are counterstained blue. Cells stained blue + green = fibroblasts, cells stained blue + red = AM-1 cells. Not all cells stained blue, and not all cells from one population were stained with the Cell Tracker dye. Top row: constructs two hours after assembly: A) AM-1 and B) GF parts of the samples. Middle row: constructs on day 2: C) AM-1 and D) GF parts of the samples. Bottom row: constructs on day 4: E and F two separate constructs, with the white dotted line indicating the interface of the two construct parts. Very little invasion was seen, with two AM-1 cells seen to invade the GF part of the construct in one scaffold on day 4 (E). The Cell Tracker dyes became much fainter in four days of culture due to cell proliferation, which is why in E and F, the cells stained green (GF) are indicated with green arrows, and the cells stained red (AM-1) are indicated with red arrows. Representative images, n = 6. 10X magnification.

5.13 Immunostaining of GF + AM-1 co-cultures

Invasion and cell movement within the scaffolds was analysed using immunocytochemistry (ICC) and viewed under a confocal microscope. ICC allowed for a longer co-culture time of these scaffolds than the Cell Tracker assay, as well as labelling of the distinct cell populations within the co-culture models, thereby allowing visualisation of any cell-to-cell interactions and invasion.

Cells were stained for fibroblast surface protein (FSP) and fibroblast activation protein (FAP). Both of these are used as fibroblast cell markers, and FAP is also used as a marker of activated (tumour associated) fibroblasts. GF cells did not, as expected, express AMBN, which was used as an AM-1 cell marker.

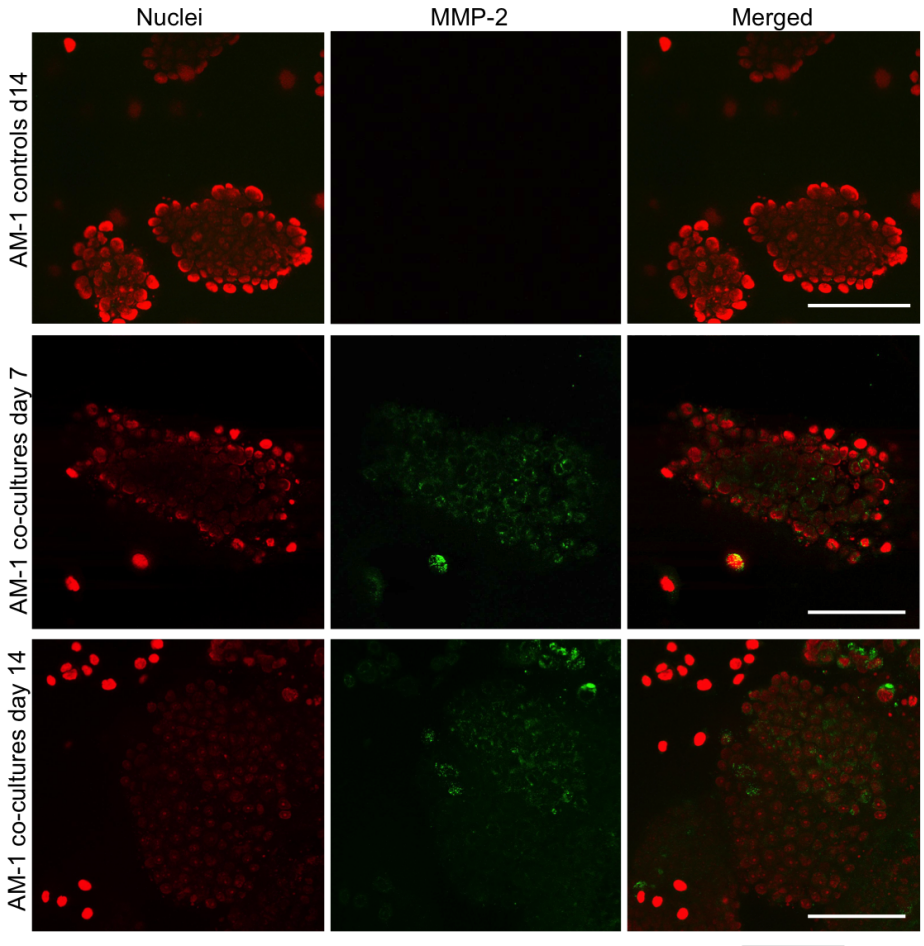

Figure 5.19: MMP-2 staining (green) in AM-1 cells in AM-1 single-cell control samples on day 14 and in the GF + AM-1 co-cultures on days 7 and 14. Nuclei were counterstained with EthD-1 and appeared red. AM-1 cells were rounded and in clusters. MMP-2 staining was seen in some parts of the AM-1 clusters when these were co-cultured with GF cells. MMP-2 staining appeared increased with culture time. Confocal micrographs of immunocytochemically stained samples. Representative images of n = 3. Scale bars = 50μm.

5.13.1 Matrix metalloproteinase-2

The previous gene expression data indicated that the expression of MMP-2 increased over time in the AM-1 parts of the co-culture models, but was not found expressed by the GF cells in the constructs. However, as MMPs are initially expressed as enzymatically inactive molecules, and require activation by a cysteine switch to cleave the pro-domain from the molecule (Kessenbrock et al., 2010), gene expression alone could not be used to reliably quantify active MMPs in the models.

MMP-2 staining revealed that AM-1 cells in co-cultures (seen in fig. 5.19) but not those in single-cell type controls expressed MMP-2. This indicated that MMP-2 was secreted by the AM-1 cells in response to being cultured together with GF cells, similar to expression found using gene expression analysis.

MMP-2 expression in the co-cultures appeared stronger on day 14 in culture than on day 7, although this was probably due to the cells proliferating and the increased AM-1 cluster size on the latter time point, causing a slight increase in MMP-2 staining. The intensity of ICC staining was not quantified further. However, correspondingly, qPCR results had also indicated an increase in MMP-2 expression between days 7 and 14.

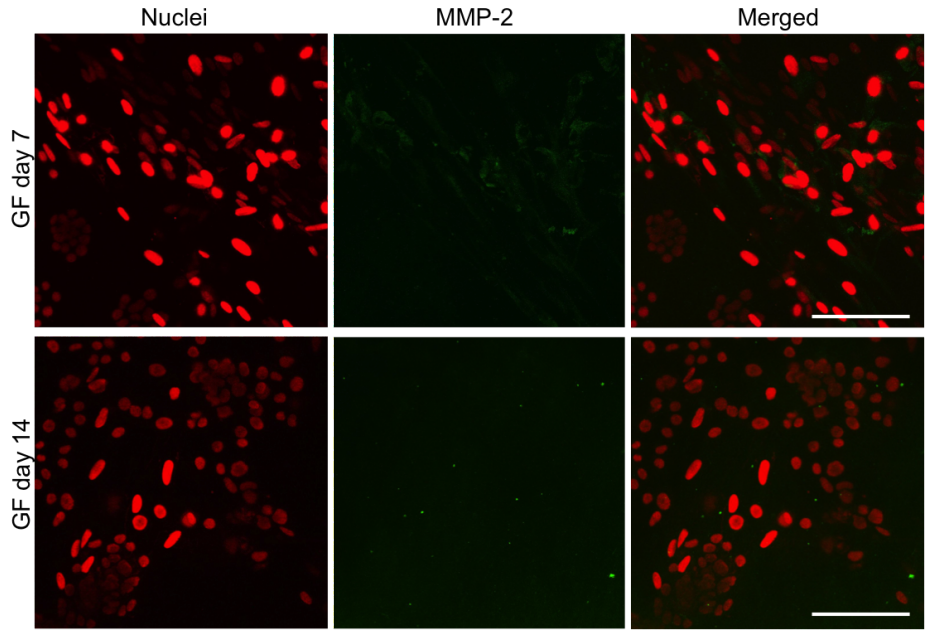

Figure 5.20: MMP-2 staining (green) in GF cells in the GF + AM-1 co-cultures on days 7 and 14. Nuclei were counterstained with EthD-1 and appeared red. GF nuclei appeared mostly elongated with some rounded morphologies. Small amounts of MMP-2 staining were seen in day 7 co-culture samples. MMP-2 staining in the GF cells decreased with culture time. Confocal micrographs of immunocytochemically stained samples. Representative images of n = 3. Scale bars = 50μm.

In the AM-1 clusters in fig. 5.19, staining was mostly visible on the edges of the tumour clusters. This could be due to the cells on the surface of the clusters using MMP-2 to break down the ECM surrounding the clusters in order to be able to expand, or it could be due to issues with decreased MMP-2 staining deep in the AM-1 clusters. However, AM-1 cells on the interface between the two cell populations did not express noticeably more MMP-2 than those elsewhere in the constructs. This indicated no MMP-mediated increase in invasion potential in the cells on the edge, which were close to the fibroblasts and interacted with these cells both through cell-to-cell interactions and paracrine factors, when compared to those in the single-cell populations at the other edge of the gels, and in single-cell control constructs.

A very limited amount of MMP-2 expression was also seen in the GF parts of the co-culture constructs on day 7 (fig. 5.20). MMP-2 levels went on to reduce to next to non-existent by day 14 of co-culture, as can be seen in fig. 5.20, with only a few cells staining green. No increase in MMP-2 staining was seen in the cells closer to the AM-1 population at the interface of the co-cultures.

Close interactions between the two different cell types within these co-culture models were seen, but no invasion was observed.

5.13.2 Fibroblast surface protein

Cells were initially stained with fibroblast surface protein in order to differentiate GF cells and AM-1 cells in the co-cultures. Fibroblast cells were therefore, as expected, stained green, with nuclei counterstained red on both days 7 and 14 of co-culture as seen in fig. 5.21. Both cell numbers as well as FSP staining appeared to increase with increasing culture time (fig. 5.21). The GF cells had by day 14 formed a confluent network of

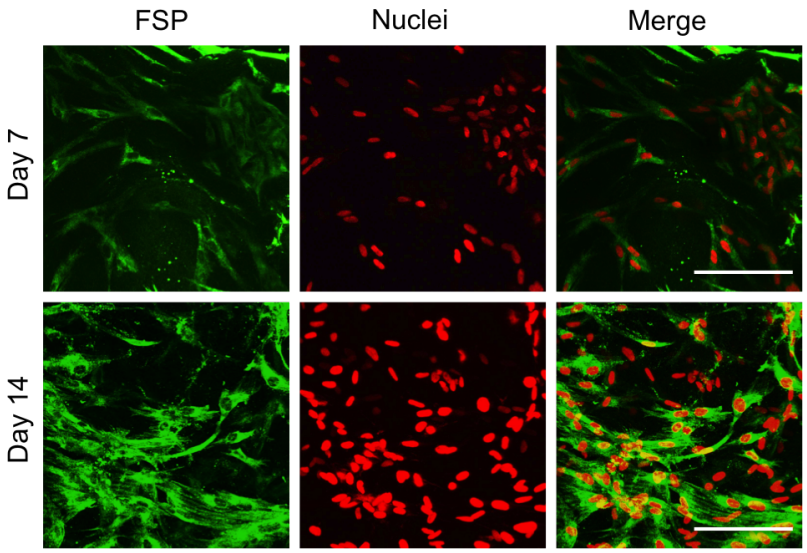

Figure 5.21: Confocal micrographs of GF cells in GF + AM-1 constructs stained for fibroblast surface protein (FSP) staining using immunocytochemistry. GF cells were stained with both red (nuclei) and green (FSP). The top row is a sample on day 7 of co-culture and the bottom row is a day 14 sample. Most fibroblast cells stained for FSP, with both cell number and FSP staining appearing to increase with increasing co-culture time. Representative images of n = 3. Scale bars = 50μm.

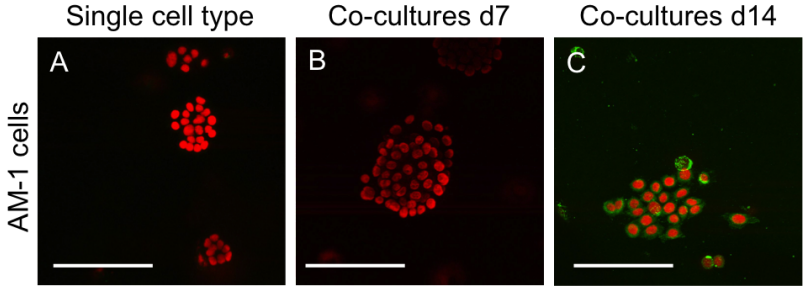

Figure 5.22: Confocal micrographs of immunocytochemically stained samples. AM-1 cells stained for fibroblast surface protein (FSP; green) with nuclei counterstained red. A) AM-1 cells did not stain for FSP on day 14 of single-cell type culture. Nuclei were counterstained red. B) AM-1 co-cultures did also not stain for FSP on day 7. C) AM-1 cells in GF + AM-1 co-cultures on day 14 stained for FSP. The AM-1 clusters also appeared less tightly packed in these late time-point samples. Representative images of n = 3. Scale bars = 50μm.

cells within the GF parts of the co-culture constructs.

No fibroblast surface protein staining was seen in AM-1 cells in single cell type controls (5.22A), or on day 7 of co-culture (5.22B). Interestingly however, by day 14 of co-culture, FSP appeared also to be expressed by AM-1 cells as seen in fig. 5.22C. As this effect was not seen in the single cell type control samples, it can be assumed that some AM-1 cells began to express FSP due to the co-culture environment.

The AM-1 cells which stained for FSP appeared to be less tightly clustered (fig. 5.22C), than the corresponding AM-1 cells which did not stain for FSP (fig. 5.22A). This change in FSP expression could be due to the AM-1 cells in co-culture becoming phenotypically more fibroblast-like, either through endothelial-mesenchymal transition or a tumour-induced invasion process requiring a more fibroblast-like AM-1 phenotype.

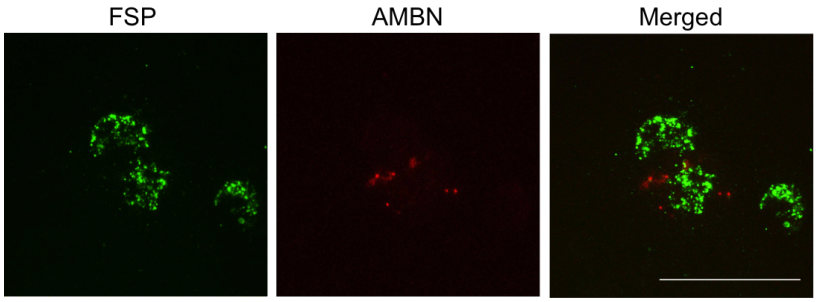

Figure 5.23: Ameloblastin (AMBN; red) and fibroblast surface protein (FSP; green) staining as seen on AM-1 cells on day 14 of co-culture. Confocal micrograph of immunocytochemically stained samples. FSP and AMBN staining appeared to co-localise to some AM-1 cells in the GF + AM-1 co-culture models. Representative images of n = 3. Scale bar 25μm.

Furthermore, AM-1 cells which stained for FSP remained morphologically AM-1-like (rounded), whereas all fibroblasts stained with FSP were fibroblast-like with an elongated morphology.

In order to confirm that the AM-1 cells which stained for FSP indeed were AM-1 cells, and not in fact fibroblasts, the cells were stained for both the AM-1-specific AMBN and FSP. A close-up of a representative sample is seen in fig. 5.23.

For samples which were stained with a double FSP and AMBN stain, the two stains co-localised to the cells, as seen in fig. 5.23, indicating that these were indeed AM-1 cells rather than migrated GF cells.

5.13.3 Fibroblast activation protein

As AM-1 cells appeared to take on a more fibroblast-like phenotype in co-cultures as seen in fig. 5.22C, the constructs were also stained for the tumour-associated fibroblast marker fibroblast-activation protein (FAP), which indicates an increased likelihood for tumour-associated fibroblasts, and correlates with an increased aggressiveness of tumours.

This was done primarily in order to assess whether this stain was appropriate to distinguish GF and AM-1 from each other in the co-cultures (as this was not possible with the FSP stain above), and additionally to assess whether the co-cultures induced a ‘malignant’ transformation in the AM-1 cells in the co-cultures.

AM-1 cells in the single cell type control samples and in the GF + AM-1 co-cultures on day 7 were not, as expected, stained for FAP (fig. 5.24A and B), although it should be noted that the AM-1 cells in fig. 5.24B stained for FSP on day 7 of co-culture.

However, AM-1 cells on day 14 of co-culture were stained for both FSP and FAP as seen in fig. 5.24C. AM-1 cells normally grew in a characteristic cluster formation both on tissue culture plastic, as well as inside the collagen scaffolds. However, AM-1 cells in co-cultures which stained for both FSP and FAP were found not to remain in clusters throughout the 14-day co-culture time. These cells also appeared larger in size with larger nuclei and cytoplasms than ‘normal’ AM-1 cells throughout culture time. Not all AM-1 cells in these samples were stained for FAP.

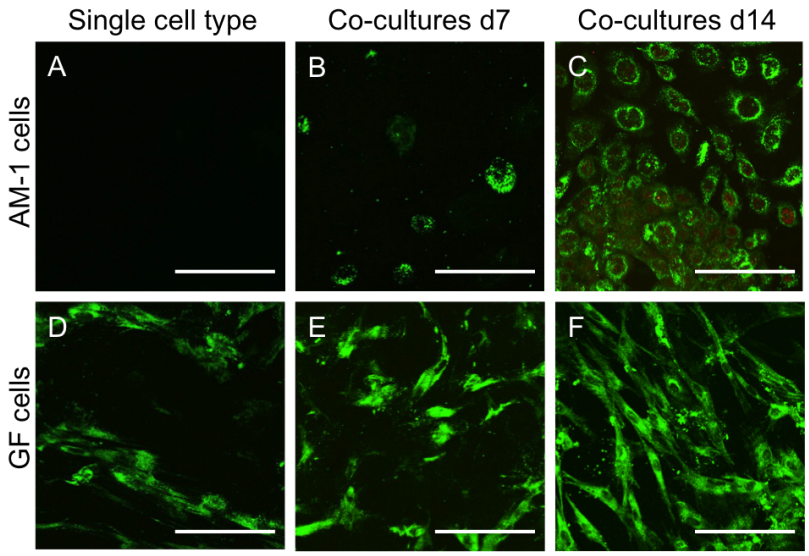

Figure 5.24: Confocal micrographs of immunocytochemically stained samples. Green staining = fibroblast surface protein (FSP), red staining = fibroblast activation protein (FAP). A) AM-1 cells in single cell type control cultures on day 14 did not stain for either FSP or FAP. B) AM-1 co-cultures did not stain for FAP (red) on day 7, but some FSP staining was seen. C) AM-1 cells in GF + AM-1 co-cultures on day 14 stained for both FSP and FAP. D) GF control samples only stained for FSP on day 14, no FAP staining was seen. E) GF cells in co-culture did not stain for FAP on day 7. F) GF co-cultures on day 14 stained for FSP but not FAP. Representative images of n = 3. Scale bars = 50μm.

As no FAP staining was seen in the single-cell type controls, or at the day 7 time-point, this effect was probably due to prolonged co-culture with fibroblasts.

It is not known why the day 7 co-cultured AM-1 samples seen in fig. 5.22B did not stain for FSP, whereas the AM-1 cells on day 7 in fig. 5.24B did stain for FSP. One possible explanation could be the that the AM-1 cells in the latter samples had been kept in culture for cell expansion for one week longer. This may have caused the cells to accumulate a mutation which enabled FSP expression in the latter samples.

As seen in fig. 5.24, there was no FAP staining (red) present in the fibroblast part of the models at any time point analysed, as these only stained green with FSP in the control samples (fig. 5.24D), as well as on both day 7 (fig. 5.24E) and day 14 (fig. 5.24F) of co-culture.

5.14 Main findings and discussion

The initial aims of this chapter were to incorporate and maintain gingival fibroblasts within the compressed collagen scaffolds. The main findings from this part of the experimental process were:

- The remodelling and contraction of the scaffolds caused by the fibroblasts necessitated further development of the fibroblasts scaffolds, which was achieved by carrying out a contraction assay to determine the suitable cell number as well as by adding Matrigel to the scaffolds.

- The culture of gingival fibroblast cells in the 3D collagen constructs showed that the cells experienced a complex environment, which supported their growth and proliferation but which they were also able to remodel over culture time.

The soft tissue collagen-Matrigel scaffolds developed were considered biomimetic due to the scaffold composition, which was mainly collagen but also other ECM factors such as laminin, which was added to the scaffolds in the form of Matrigel. The compression process made the scaffolds more biomimetic by making them stiffer, and mechanical testing indicated that the scaffolds were mechanically similar to native gingivae. The choice of cell type within these models, i.e. gingival fibroblasts, further made the scaffolds gingiva-like. Once the GF scaffolds were added to co-culture with AM-1 cellularised gels, the soft tissue co-culture constructs were analysed. The following results were obtained using these novel organotypic scaffolds:

- Gene expression analysis revealed that AM-1 cells in co-culture upregulated the expression of MMP-2 in the models.
- MMP-2 expression was also confirmed using immunocytochemistry, where MMP-2 staining increased in the AM-1 clusters and some single AM-1 cells over co-culture time.
- AM-1 did not significantly increase expression of MMP-9 when in co-culture, and in fact the majority of the MMP-9 expression found in the co-cultures was in the GF part of the constructs.
- These results indicated that MMP-2 activity seen in the AM-1 part of the scaffolds is essential for the tumour cells and their proliferation.
- Invasion was assayed using the Cell Tracker stain. However, due to the short time allowed for this assay using these cells, very little invasion was seen in any of the models.
- Furthermore, the results shown here indicated that AM-1 cells in this model took on a more fibroblast-like phenotype and expressed fibroblast-associated factors (FSP and FAP) after 7 days in co-culture.

Hydrated collagen gels have been shown to undergo contraction during culture due to the forces exerted on the collagen fibres by cells within the scaffolds (Szot et al., 2011; Brown, 2013). Keratinocytes in collagen matrices have been shown to generate forces (Wall et al., 2009), and fibroblasts in non-compressed collagen scaffolds have been reported to contract (Brown and Phillips, 2007; Brown, 2013; Chaudhry et al., 2013). Free-floating, hydrated collagen scaffolds seeded with 2 x 10^6 chondrocytes have been shown to contract up to 55% over 12 days of culture (Galois et al., 2006). Additionally, cell induced contraction is often seen in soft, non-compressed hydrogels, and only small changes in the construct shape have been seen by others (Brown, 2013). Fibroblasts in compressed (stabilised) collagen constructs have not previously been documented to cause significant contraction of the collagen matrix.

The largest cell-induced contraction during contraction studies commonly occurs early (within 72h of seeding) in the construct culture time (Brown, 2013). However, as presented here, the largest decrease in construct size was seen between days 11 and 13 of culture in the samples with 50,000, 70,000 and 120,000 cells. As different fibroblasts appear phenotypically different depending on their *in vivo* growth environment, it can be assumed that different fibroblast types may also behave differently when contracting collagen gels, with

gingival fibroblasts appearing to be a particularly contractile fibroblast type.

Both the spatial localisation of the two cell types as seen in Live/Dead stained samples (fig. 5.17) and the increase in MMP-2 levels seen in the AM-1 and the interface parts of the models (fig. 5.14) indicated that the AM-1 cells were interacting with the GF cells in these co-cultures. The MMP-2 data seen here is in line with recent histological data, where MMP-2 was reported to be over-expressed on the edges of ameloblastoma tumours (Ribeiro et al., 2009). The authors postulated that this may have been due to invasion to the surrounding tissue by the ameloblastoma tumour (Ribeiro et al., 2009).
AM-1 cells secreted MMP-2 to the scaffolds in the presence of gingival fibroblasts, while no staining was seen in AM-1 cells in collagen scaffolds on their own. The results from the Cell Tracker study indicated that the ameloblastoma tumour cells did not invade the surrounding tissue-engineered gingival model; at least not during the short time frame allowed by the assay. Further experiments with acellular gels for the AM-1 cells to invade to could be used to further study their invasion in the soft-tissue models, and to ascertain whether the lack of invasion as seen here was due to the presence of fibroblasts in the other part of the model or due to the non-invasive behaviour of the ameloblastoma cells. As no extensive invasion was seen in any part of the co-culture models, although some cell-to-cell contact was visible, the increase in MMP-2 indicated that AM-1 cells appeared to use MMP-2 locally to break down the ECM to enable proliferation and a larger cluster size. The use of MMP-2 to aid local invasion has been postulated by other groups investigating ameloblastoma (Gomes et al., 2010), and the results presented here appear to confirm this.
MMP secretion from tissue-engineered scaffolds has been found to be mechanosensitive, i.e. the scaffold stiffness changes the amount of MMP secreted by the cells in it (Karamichos et al., 2007). The stiffness of gingivae has been measured as 19.75 $\pm$ 6.20MPa (Goktas et al., 2011), whereas the average acellular, non-mineralised collagen scaffold stiffness in this study was measured as 14.71 $\pm$ 1.348MPa. This relatively similar scaffold stiffness indicates that these organotypic models were a mechanically suitable gingival environment for ameloblastoma modelling.

In ameloblastomas, increased levels of MMP-9 have previously been detected using immunohistochemistry and gene expression techniques (Qian and Huang, 2010), which the MMP-9 data presented here agrees with, as a large amount of MMP-9 expression was found in the AM-1 part of the soft tissue co-culture models at the later time points in co-culture.

AM-1 cells appeared to become more fibroblast-like and 'aggressive' with increasing culture time in co-culture with GF cells and expressed both FSP and FAP. Specifically, some AM-1 cells in co-culture were seen to express FSP by day 7 in culture, with FSP expression also seen on some AM-1 clusters by day 14. As the Cell Tracker study indicated, no migration from the fibroblast part of the co-culture models to the AM-1 part was seen in 5 out of 6 samples examined, which in turn indicated that the FAP stained cells were AM-1 cells,

not fibroblasts. Instead, the increase over time in FSP staining as well as FAP staining in some AM-1 cells indicated a potential for a more malignant transformation (endothelial-mesenchymal transition, EMT) within these co-culture models.

As for the bone-like co-culture models, this soft tissue co-culture model developed during this project could also be used for high-throughput characterisation of different ameloblastoma tumour types. Additionally, the soft tissue model presented here could be used for screening of potential therapeutic compounds to be used clinically in cases where the ameloblastoma tumour has invaded the surrounding soft tissues. Based on results presented here, the effectiveness of Doxycycline in reducing AM-1 cell growth was assessed in chapter 6.

Chapter 6

Application of potential therapeutic agents to the organotypic models

This chapter considers one of the practical applications of organotypic tumour models. In addition to analysing the behaviour of the incorporated tumour cells within their *in vitro* organotypic constructs, and measuring factors such as changes in gene expression, invasion and cell-cell interactions, as described in the previous chapters, organotypic models are also more representative than 2D cell cultures when it comes to *in vitro* testing and screening of potential therapeutic agents. Therefore, in the last part of this study, a therapeutic agent was applied to each of the models in an attempt to reduce the growth of AM-1 cells within the co-cultures. Ideally, in order to preserve as much as possible of the surrounding, healthy tissue architecture in the vicinity of the tumour tissue, the other cell type in the co-cultures should be minimally affected by the addition of the therapeutic agent.

Based on the bone turnover data obtained in chapter 4, and specifically the increase in bone-resorbing and osteoclast-activating factor RANKL in the models, the therapeutic agent alendronate (ALN) was applied to the bone-like co-culture models. The increase in RANKL indicated an attempt by the AM-1 cells to upregulate bone resorption. ALN is currently used clinically for osteoporosis treatment and for other diseases, where there is an upregulation of bone resorption.

The therapeutic use of developing the soft tissue co-culture models lies in that ameloblastoma invasion into the soft tissues surrounding the original tumour site also requires excision of these tissues.
Based on the data presented in chapter 5, where MMP-2 was found upregulated in the AM-1 parts of the scaffolds and potentially used by the AM-1 cells for local invasion and cell growth, Doxycycline (Dox) was added to the soft tissue models. Dox is a clinically available therapeutic agent of the tetracycline family, and a known MMP-inhibitor at low concentrations. Tetracyclines have been widely used in treatment of diseases with matrix destruction, and their efficacy is related to local MMP inhibition (Liu et al., 2003). A study carried

out by Liu *et al* found that in aortic smooth muscle cells, a 5μg/ml dose of Dox resulted in a 37% decrease in MMP-2 secretion, whereas a 97% decrease in MMP-2 levels was achieved with 20μg/ml (Liu et al., 2003).

6.1 Summary of methods

Alendronate (ALN) was applied to both HOS + AM-1 and HOB + AM-1 co-culture models. The results of a brief cytotoxicity study on AM-1 and HOS cells, which guided the concentration of ALN used, can be found in appendix B (fig. B.11). A cytotoxicity study was also carried out here by applying Dox on GF and AM-1 cells, and the results can be found in appendix B (fig. B.12); this guided the amount of Dox used.

ALN was applied to the HOS + AM-1 and HOB + AM-1 co-cultures every 1-2 days for a total of six times through the 14 day culture period. The concentrations tested were 10nM and 100nM.

Dox was applied to the GF + AM-1 co-cultures every 1-2 days throughout the 14 day culture period. The concentrations used were 10 and 20μg/ml.

Additionally, ALN on HOB + AM-1 and Dox on GF + AM-1 was tested on more established tumour models. For these established models, constructs were co-cultured for 7 days in a repeat experiment to allow AM-1 cells to proliferate - and, importantly, to form the characteristic clusters in the collagen scaffolds for an improved tumour model. After 7 days in culture, ALN and Dox were applied to the models every 1-2 days for the remaining 7 days of co-culture. Based on earlier results, 10nM and 100nM of ALN and 10μg/ml of Dox was used for the established models.

For all bone-like co-cultures, cell viability was measured using the Cell Titre Glo assay and constructs were stained using Live/Dead staining. Gene expression after ALN application was measured in HOB + AM-1 co-cultures. Cell viability in the soft tissue models was measured using Cell Titre Glo, and immunocytochemistry was carried out on all scaffolds to detect changes in MMP2, FSP, FAP, AMBN and OPN expression.

6.2 Application of Alendronate to the bone-like co-culture models

6.2.1 Cell survival in HOS co-cultures after ALN application

Cell survival in control samples and ALN-treated samples as measured using Cell Titre Glo is visualised in fig. 6.1. The results for all treated samples and conditions are shown as a percentage of day 1 values to better illustrate changes in cell viability over culture time.

Significant differences in cell viability were found in some of the samples when comparing the treated co-cultures with the corresponding control samples in fig. 6.1. A statistically significant increase in cell number was seen in the AM-1 + 10nM ALN samples compared to the AM-1 co-culture controls on day 4 ($p \leq 0.0001$) and day 14 ($p \leq 0.01$).

Indeed, the cell numbers in the 10nM ALN-treated co-culture models appeared to increase, with a statistically significant increase seen in both the AM-1 and IF parts of the co-cultures. An increase in cell viability on day

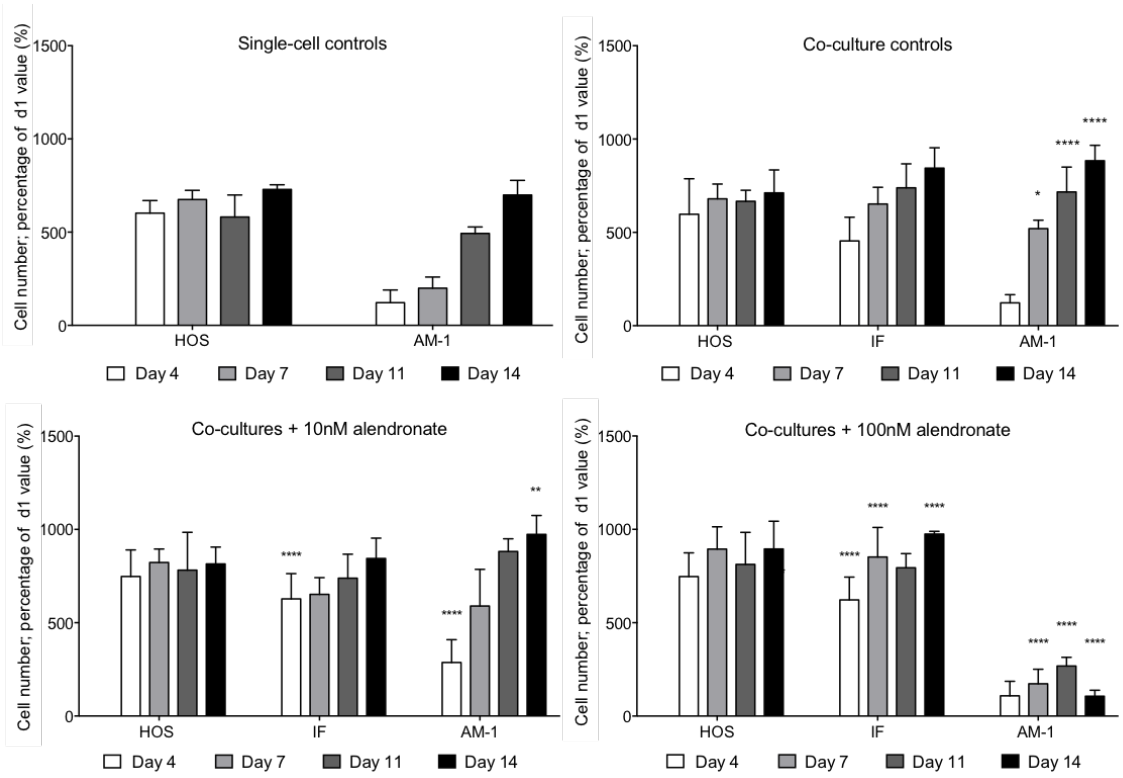

Figure 6.1: Cell viability as measured using the Cell Titre Glo assay in constructs on days 4 to 14 with Alendronate added at a concentration of either 10nM or 100nM every 1-2 days. Cell viability is seen here as a percentage of total cell number measured in the constructs on day 1 of culture. In the co-cultures treated with 10nM ALN, cell viability appeared to increase in the AM-1 co-culture parts on days 4 and 14 ($p \leq 0.01$), and the IF part on day 4. However, in the 100nM Alendronate-treated condition, there was a statistically significant decrease in cell number seen in the AM-1 part of the constructs on days 7, 11 and 14 ($p \leq 0.0001$). HOS cell viability appeared unaffected. Cell numbers were normalised to day 1 values and are expressed here as a percentage to visualise the change in viability. Error bars = 95% CI, n = 6, 2-way ANOVA, significance levels as indicated by asterisks are: * = $p \leq 0.05$, ** = $p \leq 0.01$, **** = $p \leq 0.0001$.

4 in IF + 10nM ALN was seen when compared to the IF control ($p \leq 0.0001$). Overall, the results in fig. 6.1 indicated that in the co-cultures treated with 10nM ALN, cell viability was increased and proliferation was in parts even faster in the ALN-treated samples than in the controls. HOS cell proliferation in this treatment group appeared similar to the co-culture controls. The plateauing of HOS cell number within these constructs was thought to be due to the longer time these cells had already been kept in collagen culture for.

No such increase in AM-1 cell viability was seen in samples treated with 100nM ALN. Cell viability in the HOS + AM-1 co-cultures was found to significantly decrease in the 100nM ALN-treated AM-1 model parts on days 7, 11 and 14 of co-culture as seen in fig. 6.1 ($p \leq 0.0001$), when compared to the co-culture controls. Overall, HOS cell viability did not appear to be affected by ALN application.
However, an increase in cell viability was seen in the IF region on days 4, 7 and 14 in the 100nM ALN-treated samples when compared to the control samples ($p \leq 0.0001$).

Overall, cell viability in both the single-cell type controls, co-culture controls and the 10nM ALN-treated samples appeared broadly similar. It should be noted that the cells in the co-culture control samples prolifer-

ated much faster than in the single-cell controls in the AM-1 cultures ($p \leq 0.01$).
However, even though a reduction in AM-1 cell viability was seen, cell numbers measured in the samples with 100nM ALN were still approximately 150% of cell numbers measured in day 1 constructs (which the readings were normalised to), indicating the presence of abundant viable cells.

Live/Dead staining of the co-culture models after ALN application was carried out only on models with 100nM ALN added based on the significant results in the previous experiment. As seen in fig. 6.2, a large increase in dead (red staining) and dying cells (green staining with granular cytoplasms) in the AM-1 part of the samples treated with 100nM ALN was observed. An increase in cell death was seen in samples examined on both days 7 (fig. 6.2C) and 14 (fig. 6.2G) of co-culture, with increased numbers of dying cells particularly seen at the edge of the tumour clusters (fig. 6.2H). AM-1 clusters on day 7 appeared larger but more dispersed in the ALN-treated samples than in the control samples (fig. 6.2E). This reflected the still viable AM-1 cells in these constructs seen in the Cell Titre study in fig. 6.1.

HOS cells appeared to proliferate throughout culture time as visualised in fig. 6.2. However, although mostly alive, the cells in the day 7 samples appeared rounded (fig. 6.2L), indicating a potential reduction in cell viability. Cell death also appeared increased in the HOS parts of the scaffolds, with abundant dead or dying cells seen on both time points. No increase in HOS cell death was seen in the ATP study in fig. 6.1. Dying cells were especially abundant in the day 14 HOS samples, where many stained green, but with granular cytoplasms, indicating apoptosis (fig. 6.2P).
HOS cells in the controls appeared mostly alive, with rounded cells seen on day 7 and slightly elongated cells on day 14. None of the control samples appeared confluent by day 14. Indeed, both HOS and AM-1 cells in the samples treated with ALN appeared to have proliferated more in co-culture than the untreated control samples.

6.2.2 Cell survival in the HOB co-cultures after ALN application

Alendronate was subsequently also added to the HOB + AM-1 co-culture models to validate the results obtained with the HOS + AM-1 co-cultures. The experiment was carried out both in co-cultures to which ALN was added on day 0 of co-culture, i.e. immediately after co-culture assembly, as well as to co-cultures which had been incubated for 7 days prior to ALN addition, in order to create a more established tumour model.

The results for HOB + AM-1 viability when ALN was added to the co-cultures for 14 days from day 0 of co-culture are visualised in fig. 6.3. When comparing the HOB control samples with HOB cells in co-culture with added ALN, there was a significant decrease in HOB viability in the HOB + 10nM ALN and the HOB + 100nM ALN samples on day 5 ($p \leq 0.001$) and on day 14 ($p \leq 0.01$), as seen in fig. 6.3.
AM-1 cell viability in the 10nM ALN-treated samples was not significantly different compared to the co-

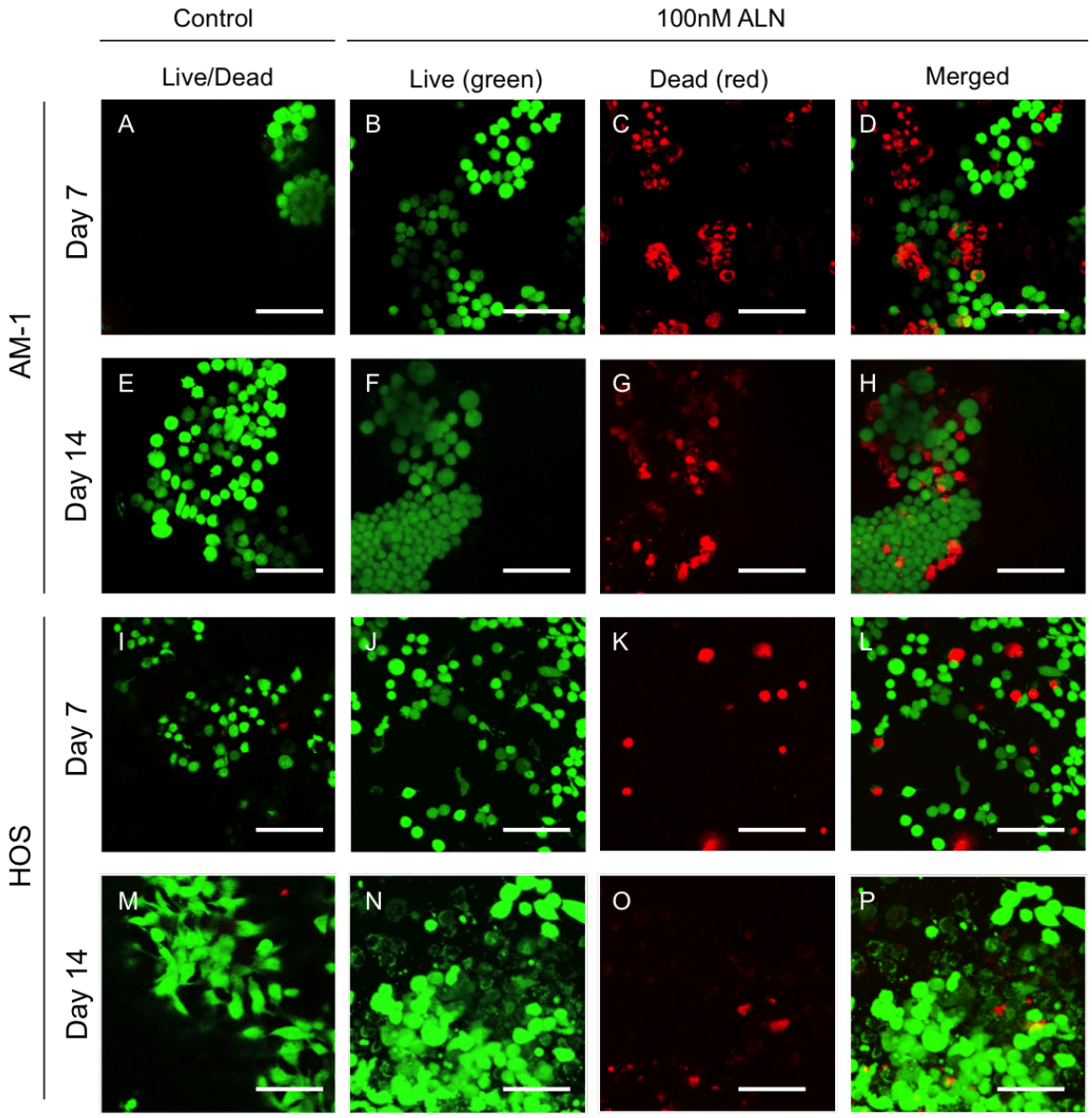

Figure 6.2: Live/Dead confocal micrographs of HOS + AM-1 co-culture models after Alendronate addition. Here, models without ALN and with 100nM ALN are shown. The samples with added ALN are shown in three separate columns (Live / Dead / Merged) to better distinguish dead and live cells at the two time points. Live cells were stained green and dead cells were stained red. Very few cells were seen to be dead or dying in the untreated control samples at either time point. An increased number of dead cells were visible in the AM-1 parts of the scaffolds treated with ALN. Representative images of n = 3. Scale bar = 50μm.

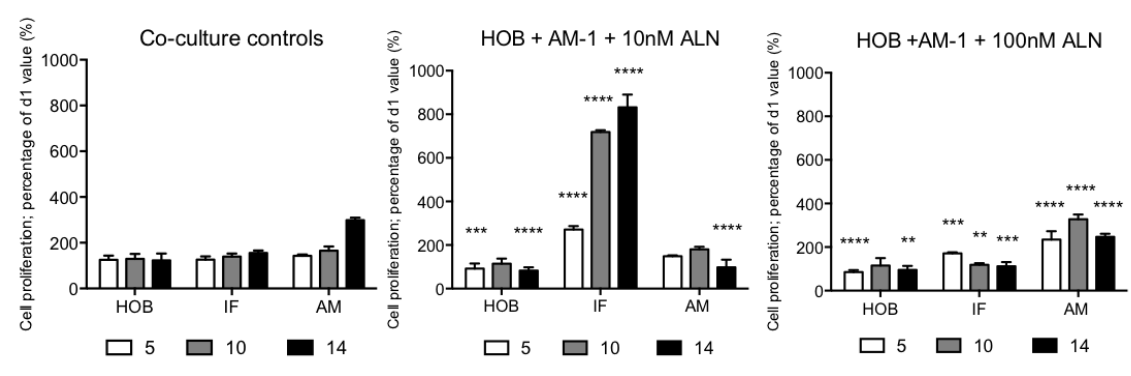

Figure 6.3: Cell viability in HOB + AM-1 co-culture controls and constructs treated with 10nM and 100nM ALN as measured using the Cell Titre Glo assay. Cell viability in the AM-1 part of the control samples increased over time. Statistically significant decreases in AM-1 cell viability were seen in both ALN-treated conditions by day 14. In the samples treated with 100nM ALN, there was an initial increase in cell viability, with AM-1 cell numbers increasing on days 10 and 14. A large increase in cell viability was also seen in the interface region in the 10nM ALN-treated sample compared to the co-culture controls. HOB viability in all samples with and without ALN was relatively equal. Cell viability values are shown here as a percentage of day 1 cell number. N = 3, 2-way ANOVA, where ** = $p \leq 0.01$, *** = $p \leq 0.001$, **** = $p \leq 0.0001$. Error bars = 95% CI.

culture controls on days 5 or 10, but a significant decrease in cell viability was seen on day 14 ($p \leq 0.0001$). There was a significant increase in AM-1 cell viability in the 100nM ALN-treated samples on days 4 and 10 (both $p \leq 0.0001$). However, on day 14, there was found to be a significant decrease in AM-1 viability in the 100nM ALN-treated samples when compared to the control samples ($p \leq 0.0001$).

Interestingly, a large and statistically significant increase in cell viability was seen in the interface part of the models treated with 10nM ALN at all time points ($p \leq 0.0001$). A similar increase was not seen in the samples treated with 100nM ALN, with cell viability significantly reduced in the IF part of the 100nM ALN-treated co-cultures on days 10 and 14 ($p \leq 0.01$).

These constructs were also viewed using Live/Dead staining to visualise the effect addition of ALN had on the cell viability in the samples. Control samples from the HOB part of the cultures (fig. 6.4A, C) and the AM-1 part (fig. 6.4B, D) were mostly alive (green) and appeared to have proliferated on both days 7 and 14 of co-culture. HOB cells appeared elongated and evenly spread out throughout the constructs. AM-1 cells appeared in their characteristic clusters.

When alendronate was added to the co-cultures, HOB cell viability was reduced in the 10nM ALN samples (fig. 6.4E, G), and the cells appeared less elongated on day 7 (fig. 6.4E). There was an increased number of dead (red) cells seen on day 14 (fig. 6.4G).

AM-1 cells treated with 10nM ALN appeared slightly more confluent than in the control on day 7 (fig. 6.4F), with a notable increase in both cell number and cluster size by day 14 (fig. 6.4H). There was cell death seen in the HOB parts of the constructs by day 14, and the live cells had become rounded (fig. 6.4G), indicating reduced cell viability in these treated constructs.

In the samples with the higher concentration of ALN added, HOB cells on day 7 (fig. 6.4I) appeared more

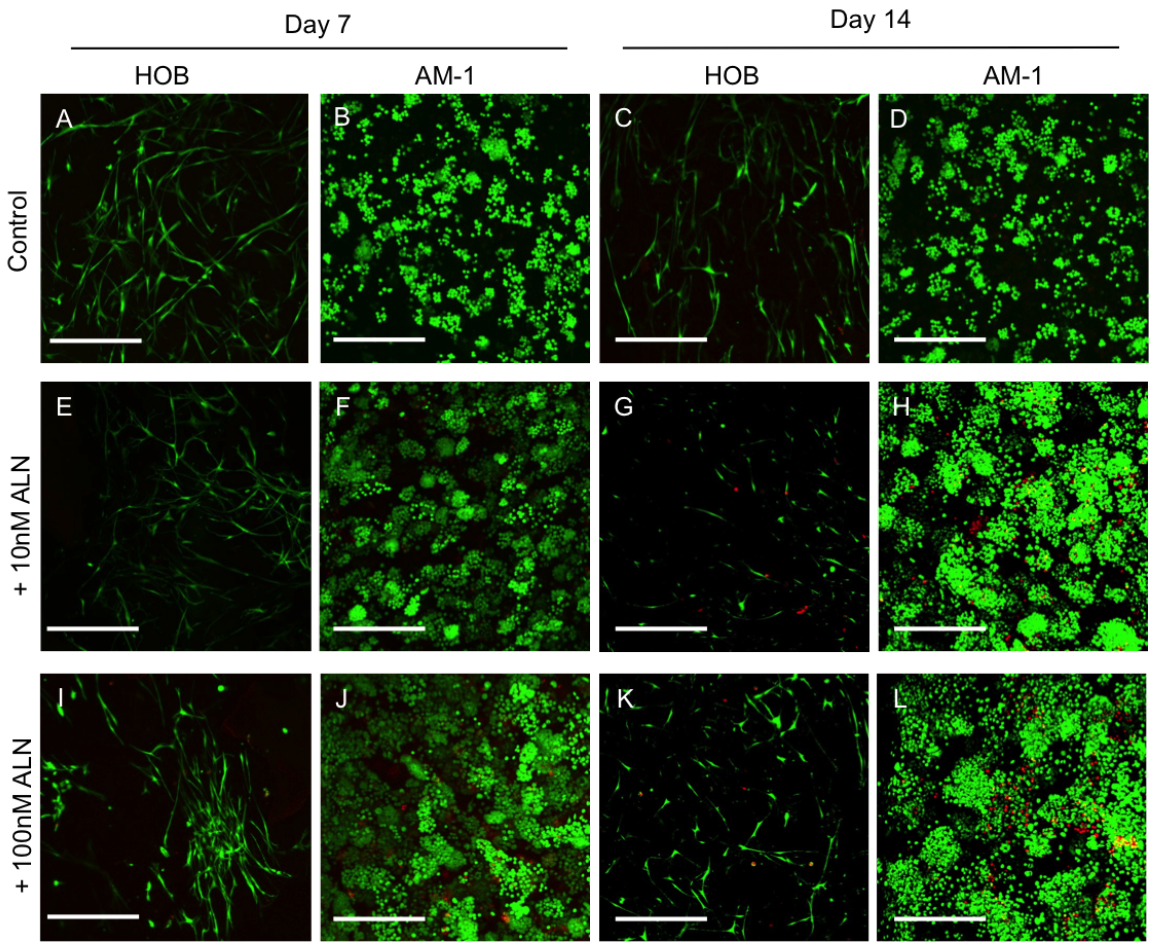

Figure 6.4: Live/Dead staining of cells in HOB + AM-1 co-cultures on days 7 and 14 with added Alendronate (ALN). A-D) Control samples where both HOB cells (A, C) and AM-1 cells (B, D) were mostly alive (green) and proliferating. E-H) Co-cultures with 10nM added ALN. Here, HOB cell viability was reduced, and the cells appeared less elongated on day 7 (E). There was some cell death (red) seen by day 14, and the live cells had become rounded (G). On day 7 (F), AM-1 cells in treated samples appeared slightly more confluent than in the control, but by day 14 (H), they have increased in number and cell cluster size. I-L) Co-cultures with 100nM ALN added. Here, HOB cells on day 7 (I) appeared to increase proliferation compared to the 10nM treatment group, and by day 14 (K), there were approximately the same number of cells seen as in the control (C), albeit with a few more dead cells. AM-1 cells in this experimental group appeared to have proliferated on day 7 (J) and reached confluency within the scaffold by day 14 (L). Representative images of n = 3. Scale bars = 100μm.

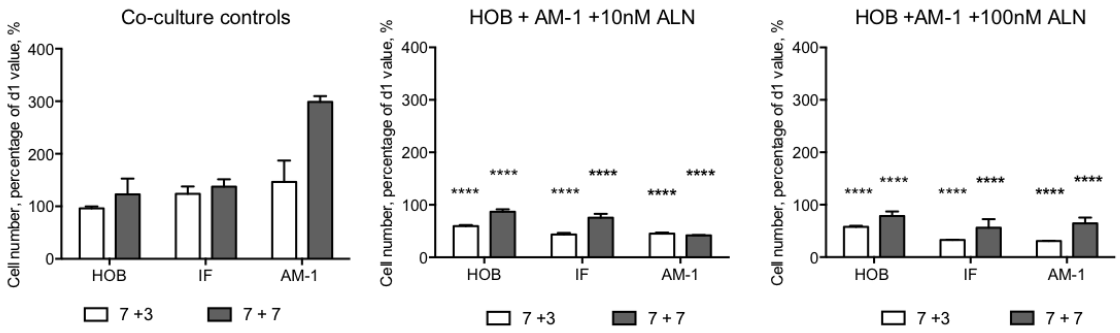

Figure 6.5: Cell viability in HOB + AM-1 controls and 'established' tumour models treated with 10nM and 100nM ALN. Cell viability increased over time in the co-culture samples, but there was a significant reduction in AM-1 cell viability seen in the samples treated with either 10nM or 100nM ALN ($p \leq 0.0001$). Cell numbers in both the IF and HOB parts of the co-culture constructs in both ALN-treated groups also appeared significantly reduced. N = 3, 2-way ANOVA, where **** = $p \leq 0.0001$ compared to the co-culture control values. Error bars show the 95% CI.

numerous than in the 10nM condition, and by day 14 (fig. 6.4K), there was approximately the same number of HOB cells seen as in the control (fig. 6.4C), albeit with a few more dead cells. AM-1 cells in this experimental group appeared to have proliferated on day 7 (fig. 6.4J) and reached confluency within the scaffold by day 14 (fig. 6.4L). In both sets of AM-1 samples with 100nM ALN (J and L), some cell death was seen, but this could be attributed to the confluent 3D culture and large cluster sizes, which may have led to cells in the middle lacking nutrients.

Finally, ALN was also added to established models throughout the last week of HOB + AM-1 co-culture. The results of a viability assay are shown in fig. 6.5. There was a significant decrease in cell viability seen in the HOB parts of the constructs in both 10nM and 100nM-treated samples compared to the control co-cultures (all $p \leq 0.0001$). There was also a significant decrease in cell number seen in the 10nM and 100nM ALN-treated AM-1 parts of the constructs when compared to the large cell numbers seen in the control co-cultures (all $p \leq 0.0001$).

Cell viability in the interface part of the co-culture constructs appeared similar in both the treated samples, and was reduced compared to the controls (all $p \leq 0.0001$).

However, despite the reduction in cell viability compared to the untreated control samples, there was still an overall increase seen in the AM-1 cells in the 100nM ALN-treated samples between the two time points, and the cell numbers in the 10nM ALN-treated samples appeared similar on both days. This indicated that there were viable cells still present within these constructs despite ALN treatment.

Indeed, when the treated samples were visualised using Live/Dead staining (fig. 6.6), most AM-1 and HOB cells were alive after ALN application on days 10 (d7 + 3) and 14 (d7 + 7) of culture. Overall, HOB cells appeared less healthy in the models with added ALN, and there was an increase in dead or dying cells in the treated scaffolds (fig. 6.6E, G, I and K). On day 14, in both sets of samples treated with ALN (fig. 6.6G, K), there were more HOB cells seen than in the untreated control samples.

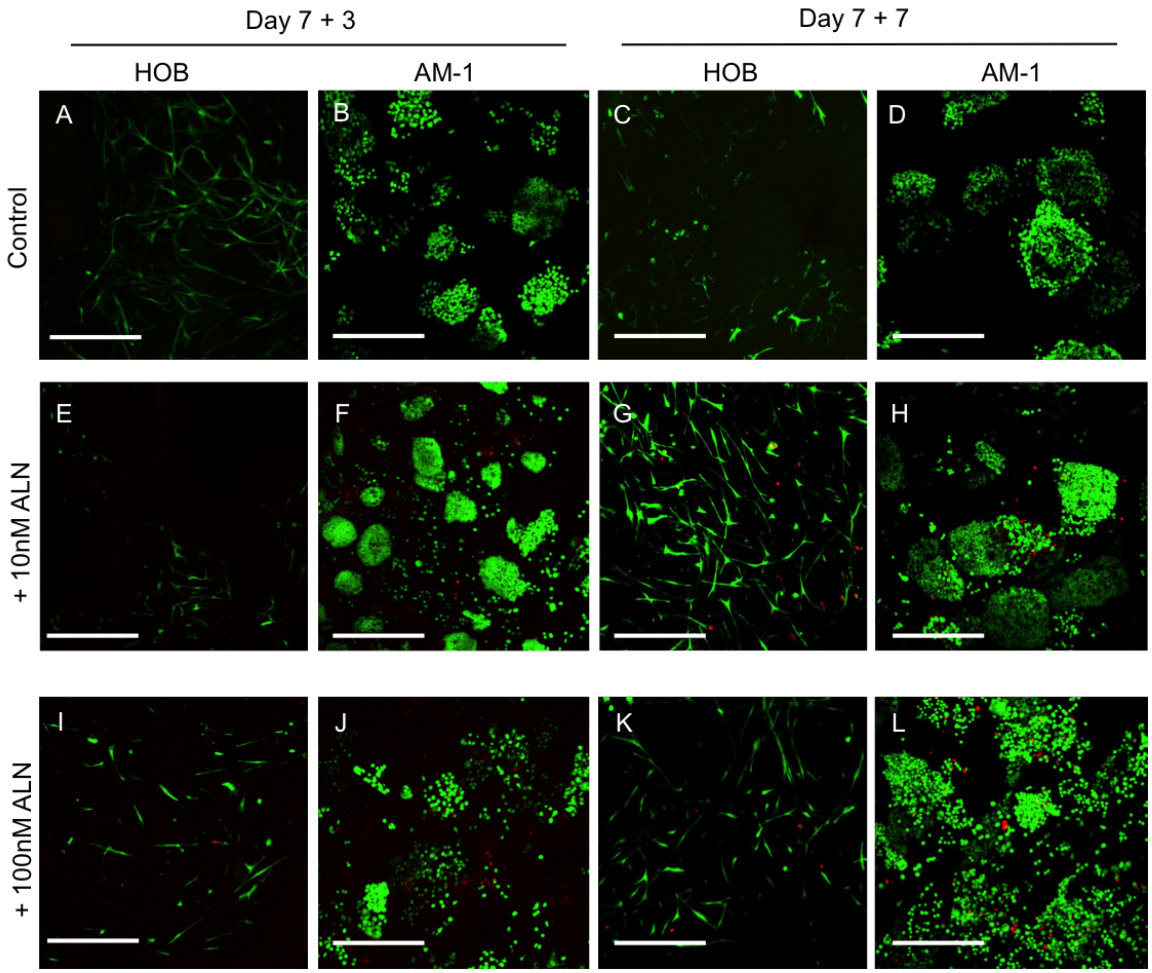

Figure 6.6: Live/Dead assay and confocal micrographs on HOB+AM-1 co-cultures on days 10 and 14 of co-culture. Alendronate was added to the HOBAM co-cultures when these were 'established', i.e. 7 days after co-culture assembly. ALN was added at two concentrations, 10nM and 100nM. Controls showed an increase cell numbers in the AM-1 (A, C) and a slight increase in HOB (B, D) populations of the co-cultures (live cells = green), with few dead cells (red). However, AM-1 cells appeared to have proliferated more in the samples with added ALN on both days 7 (F, J) and 14 (H, L), with the most viable AM-1 cells seen in the 100nM ALN-treated samples on day 14. Similarly, in the 10nM ALN samples, HOB cell number also appeared increased (G), whereas in the 100nM ALN-treated samples (K), HOB cell viability appeared similar to the control samples (C). Representative images of n = 3. Scale bars = 100μm.

Dead or dying cells were commonly seen in the middle of AM-1 cell clusters at the later time point (fig. 6.6H, L). However, the AM-1 cell population within the treated samples appeared largely alive. On day 14, AM-1 cells in the constructs treated with 100nM ALN (fig. 6.6L) appeared more confluent and less clustered together than the cells in either the control samples (fig. 6.6D) or the other treated samples (fig. 6.6H).

6.2.3 Immunocytochemistry on ALN-treated bone-like co-cultures

Fibroblast surface protein

When AM-1 cells were co-cultured with GF cells in the soft tissue models for 14 days, AM-1 cells were found to express the fibroblast markers FSP and FAP as detailed in sections 5.13.2 and 5.13.3. Based on this data FSP staining was carried out on HOS + AM-1 co-cultures. Initially, some single AM-1 cells in the co-cultures were found to express FSP as seen in fig. 6.7. However, when ALN was added to the HOS + AM-1 models, expression of FSP appeared to increase, initially especially in the unclustered AM-1 cells as seen in fig. 6.7. By day 14, AM-1 cell clusters were also found to express FSP, in addition to the already FSP expression seen on unclustered AM-1 cells (fig. 6.7). Overall, FSP expression by AM-1 cells grown in co-culture with HOS cells was observed to a lesser extent than in the fibroblast co-cultures.

When AM-1 cells in HOB + AM-1 co-cultures were examined for expression of FSP, no expression was seen on either day 7 or day 14 of co-culture as seen in fig. 6.8.

Fibroblast activation protein

Furthermore, AM-1 cells grown in co-culture with HOB cells did also not express FAP on either day 7 or day 14 of co-culture (fig. 6.8). Any FAP staining would have appeared in red on these cells, but no red staining was seen at either time point examined.
HOS + AM-1 co-cultures were not examined for FAP staining in this study.

The lack of FSP and FAP staining at both time points examined in the HOB + AM-1 co-cultures therefore indicated that the fibroblast-like staining of the AM-1 cells in both the HOS and the GF co-cultures was due to the co-culture environment and the presence of the other cell type.

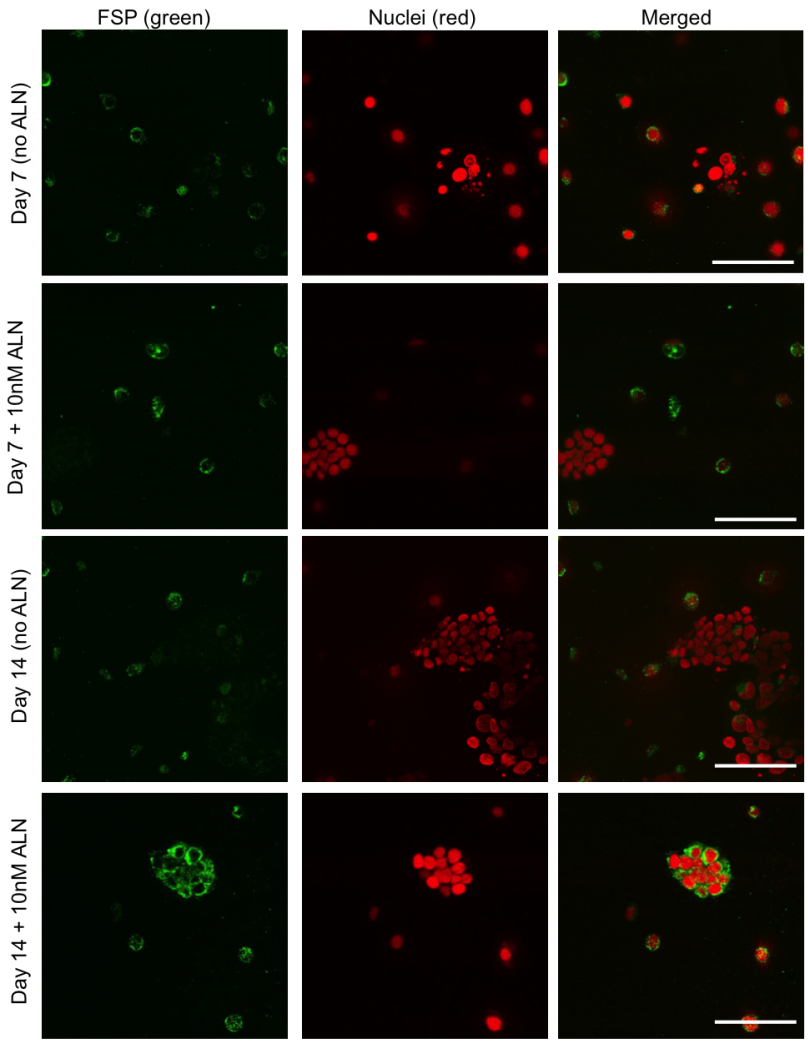

Figure 6.7: AM-1 cells in HOS + AM-1 co-culture models on days 7 and 14 with and without added ALN stained for fibroblast surface protein (FSP, green) and nuclei (red). AM-1 cells stained for FSP both with and without added ALN on both day 7 and 14 of co-culture. FSP staining appeared to increase with increasing co-culture time. Initially, single AM-1 cells were stained for FSP, but by day 14 even AM-1 clusters with added ALN were expressing FSP. Representative images of n = 3. Scale bars = 50μm.

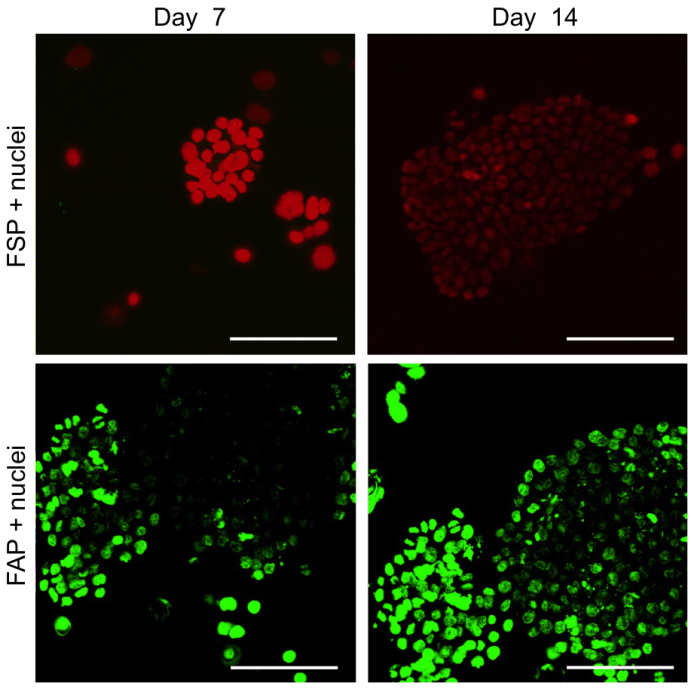

Figure 6.8: HOB + AM-1 co-cultures on days 7 and 14 stained for fibroblast surface protein and fibroblast activation protein. Nuclei were counterstained red when staining for FSP (top) and green when staining for FAP (bottom). Top row: No fibroblast surface protein staining (green) was visible AM-1 cells co-cultured with HOB cells at either time point examined. Bottom row: No fibroblast activation protein staining (red) was visible in AM-1 cells co-cultured with HOB cells on days 7 or day 14. Representative images of n = 3. Scale bars = 50μm.

6.2.4 Gene expression in HOB + AM-1 co-culture models after ALN application

Gene expression analysis was also carried out on the HOB + AM-1 co-cultures on constructs which had been treated with ALN to investigate whether any changes in gene expression took place due to the treatment.

RANKL

RANKL, which was previously shown upregulated in both HOS + AM-1 and HOB + AM-1 co-cultures, was examined in ALN-treated HOB co-culture samples. RANKL expression levels in the HOB part of the constructs were found not to be significantly different at either time point in the control compared to the treated samples. However, a significant decrease was found in the treated AM-1 cells within the constructs on both days 7 and 14 when compared to the co-culture controls ($p \leq 0.0001$).

OPG

OPG gene expression in the ALN-treated models was also measured. OPG expression after Alendronate treatment appeared decreased in all parts of the models tested. The only statistically significant difference found here was between AM-1 control samples and ALN-treated AM-1 samples: OPG in the treated samples was approximately 5-fold reduced compared to the controls ($p \leq 0.0001$).

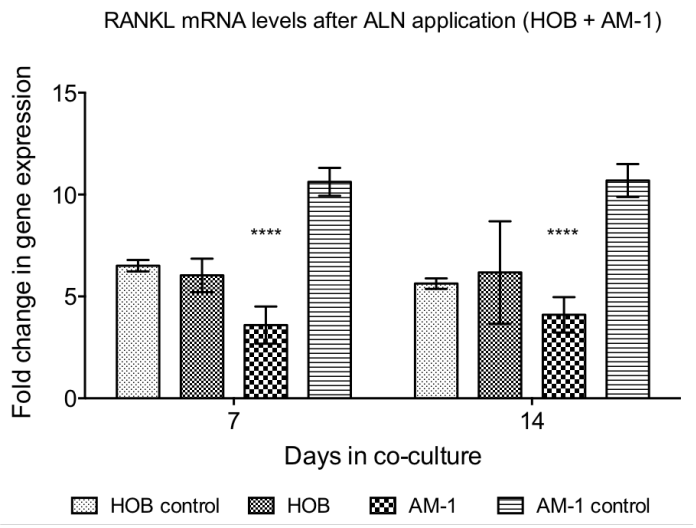

Figure 6.9: RANKL mRNA levels in HOB + AM-1 co-culture samples treated with 100nM ALN on days 7 and 14. RANKL levels in the HOB parts of the co-cultures appeared similar in the untreated and treated samples on both days. RANKL levels were significantly reduced in the AM-1 samples in the ALN-treated cultures compared to the untreated controls. Error bars = 95% CI, n = 3. 2-way ANOVA, **** = $p \leq 0.0001$.

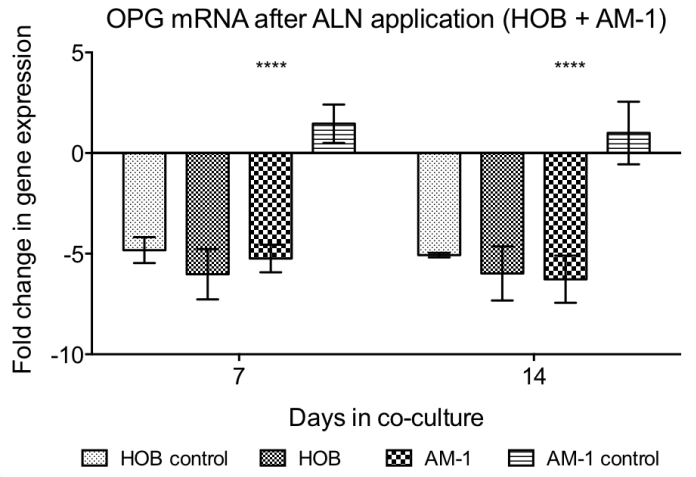

Figure 6.10: OPG expression levels as measured by qRT-PCR in HOB + AM-1 co-culture samples treated with 100nM ALN on days 7 and 14. OPG levels in AM-1 cells in ALN-treated co-culture samples were significantly reduced compared to the AM-1 controls. No difference was found in the HOB parts of the co-cultures. Error bars = 95% CI, n = 3. 2-way ANOVA, **** = $p \leq 0.0001$.

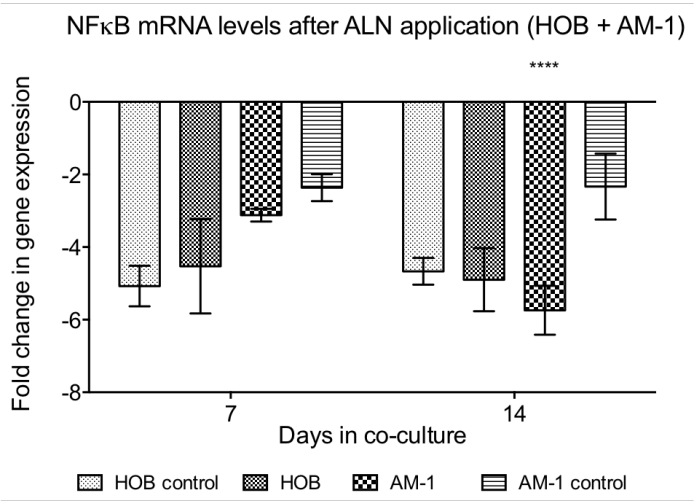

Figure 6.11: NFκB expression in HOB + AM-1 co-culture samples treated with 100nM on days 7 and 14. NFκB gene expression appeared unchanged with ALN-treatment in the HOB parts of the co-cultures on both time points. Expression in the AM-1 parts was significantly reduced with both time and ALN-treatment from a 3-fold downregulation on day 7 to a 6-fold downregulation on day 14. N = 3, 2-way ANOVA, **** = $p \leq 0.0001$. Error bars show the 95% CI.

NFκB

Expression of NFκB did not appear changed in the co-culture model parts after ALN application. NFκB gene expression was not found significantly different in the HOB control and the ALN-treated HOB samples. Expression was also not found significantly changed in the AM-1 control group when compared to the treated samples on day 7 of co-culture. However, there was a significant decrease in NFκB gene expression levels in ALN-treated AM-1 co-cultures compared to the AM-1 controls on day 14 of co-culture ($p \leq 0.0001$).

While it should be noted that the untreated HOB + AM-1 samples in chapter 4 and the ALN-treated HOB + AM-1 co-culture samples here did not have the same calibrators, and therefore cannot be directly compared, some broad conclusions can be made:
RANKL levels in the untreated and treated HOB + AM-1 co-cultures did not appear changed, with an approximate 10-fold upregulation of RANKL seen in both the untreated and treated samples.

OPG, which was seen to be up to 100-fold upregulated in the AM-1 part of the HOB + AM-1 co-cultures and up to 200-fold upregulated in the HOB parts in fig. 4.10, was seen around 5-fold downregulated in the ALN-treated samples. This change could be due to the age of the HOB cells used in the two experiments (passage number 6 in the models in chapter 4 and passage number 8 in the ALN experiments presented here), where the increase in time on a 2D culture plate may have caused a difference in OPG expression in these primary cells.
Similarly, NFκB levels were seen to be up to 7-fold upregulated in the AM-1 parts of the co-cultures in fig. 4.14, whereas here there was a large 5-fold decrease seen in the ALN-treated AM-1 parts of the model by day 14. However, overall, it was encouraging that gene expression of especially RANKL and its downstream

factor NFκB were seen to significantly reduce in the treated models, indicating a reduced potential for bone resorption.

6.3 Application of Doxycycline to soft-tissue co-culture models

6.3.1 Cell viability in GF + AM-1 after Dox application

In the soft tissue models, cell viability was first assessed on constructs where Doxycycline (Dox) was added immediately after co-culture set-up at two different concentrations, with the results shown in fig. 6.12.
Subsequently, cell viability was also measured on constructs where Dox was added after seven days of co-culture (fig. 6.13). This allowed for AM-1 cell proliferation in the co-culture models, a more organotypic environment and characteristic cluster formation.
AM-1 cell viability appeared slightly reduced in the co-culture control samples when compared to the single-cell type controls at all time points measured ($p \leq 0.0001$). In the single-cell type controls, GF cell viability was relatively even throughout culture time, or even reduced over time due to the long culture time, whereas in the co-culture controls, GF viability was found slightly increased.
Cell viability in the Dox-treated GF + AM-1 co-cultures was significantly reduced as seen in fig. 6.12. AM-1 cell viability was reduced in all of the 10μg/ml Dox-treated conditions on days 4, 7, 10 and 14 (all $p \leq 0.0001$). In the 20μg/ml Dox-treated sample set, viability was reduced at all times in the AM-1 part of the co-cultures (all $p \leq 0.0001$), apart from the AM-1 cells on day 4, where no significant difference was found.

Cell viability in the IF region of both the Dox-treated sample sets was also significantly reduced on days 4 and 14 compared to the co-culture controls ($p \leq 0.001$). Gingival fibroblast viability was not significantly different in any of the treated or control groups on days 4, 7 and 14. On day 10, the only difference in GF viability was a significant reduction in cell number in the 20μg/ml Dox group when compared to the co-culture controls ($p \leq 0.01$). This was thought to be due to the cells already being confluent by the time Dox was applied and the measurements were started.

A similar decrease in AM-1 cell numbers was seen when cell viability was measured in the established GF + AM-1 models, where Dox was applied between days 7 and 14 of co-culture. The results for this study are visualised in fig. 6.13.
Cell viability in the established GF + AM-1 tumour models was found significantly reduced in the AM-1 part of the models at all time points, when compared to the untreated co-culture models as seen in fig. 6.13 ($p \leq 0.0001$). Fibroblast viability was significantly decreased on day 7 + 3 in the Dox-treated models compared to the untreated controls ($p \leq 0.0001$), but no difference was found on days 7 + 5 or 7 + 7. There was also a slight increase in cell viability in the interface region on day 7 + 5 ($p \leq 0.001$), but otherwise cell viability in this part of the co-culture appeared similar to the untreated controls.

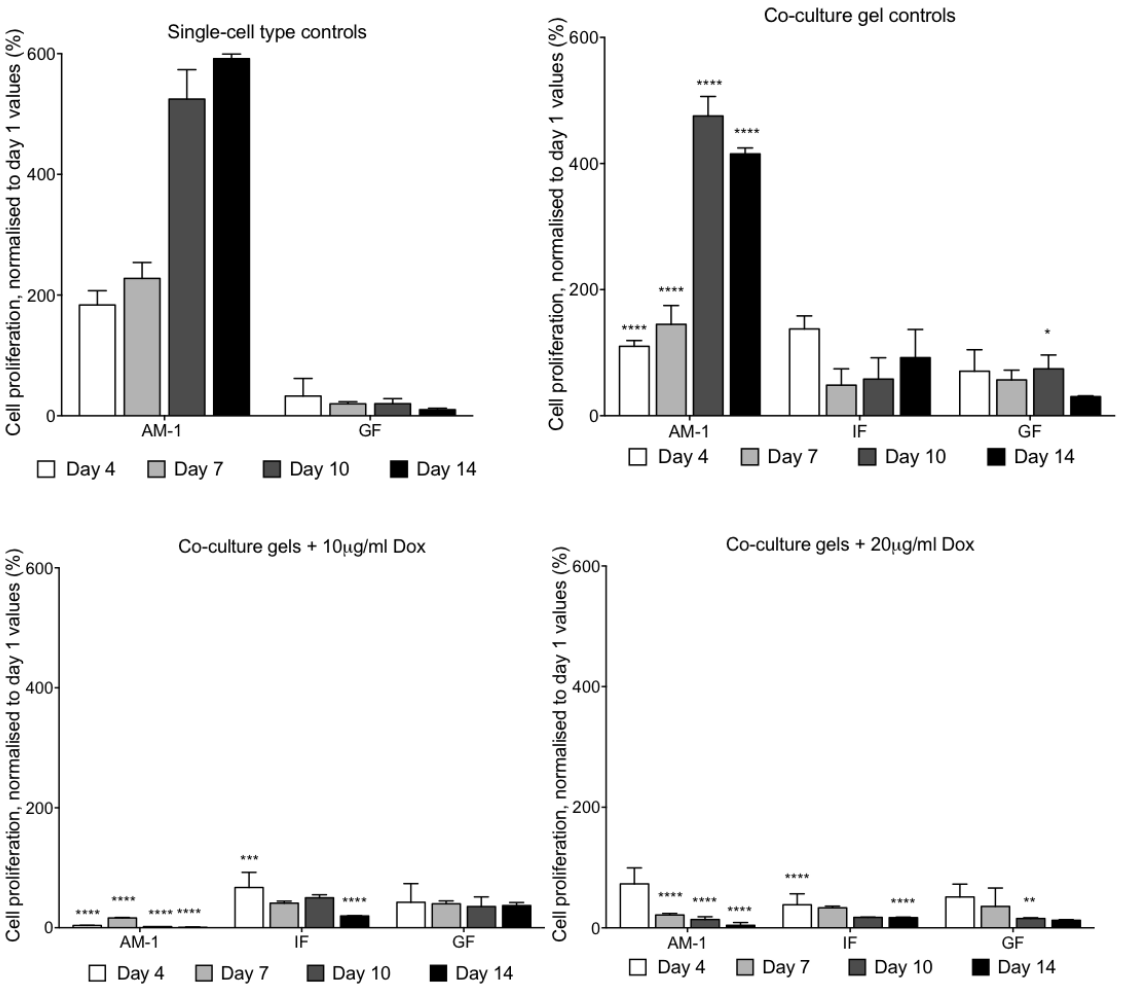

Figure 6.12: Cell Titre Glo cell viability measurements after Doxycycline application. Here, cell viability in single-cell type controls and co-culture controls with no Dox added are shown. 10μg/ml and 20μg/ml Dox were added to GF + AM-1 co-culture samples. AM-1 cell numbers were significantly reduced over time in all samples with added Dox when compared to both the co-culture controls. GF cell viability was mostly unaffected by Dox addition in the 10μg/ml treatment group, but appeared slightly reduced in the 20μg/ml Dox-treated samples. 2-way ANOVA, * = $p \leq 0.05$, ** = $p \leq 0.01$, **** = $p \leq 0.0001$. Error bars = 95% CI, n = 6.

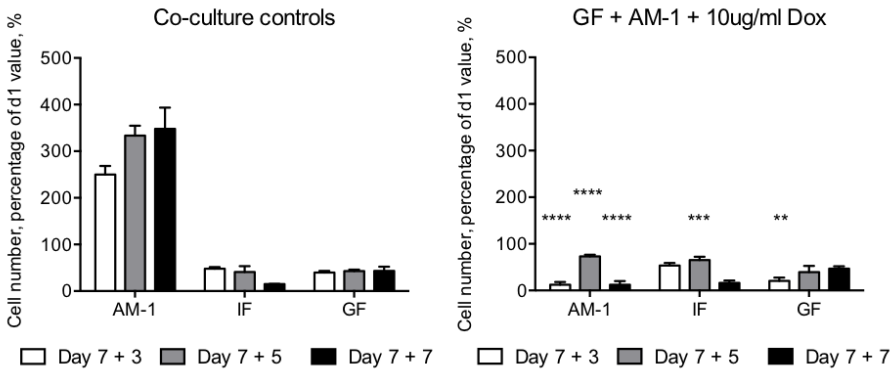

Figure 6.13: Cell Titre Glo cell viability measurements in constructs when 10μg/ml of Doxycycline was applied to 'established' AM-1 co-cultures, i.e. after 7 days of co-culture assembly. All results are shown as a percentage of cell number compared of day 1 values. There was a significant decrease in AM-1 cell viability in the Dox-treated samples even in the 'established' models. GF cell viability appeared unaffected by Dox addition in this experimental set-up, with only a slight decrease seen on the first time point (d7 + 3). 2-way ANOVA, ** = $p \leq 0.01$, *** = $p \leq 0.001$ and **** = $p \leq 0.0001$. Error bars = 95% CI, n = 3.

6.3.2 Immunocytochemistry of Dox-treated GF+AM-1 cultures

Cells in the Dox-treated co-culture scaffolds were visualised using immunocytochemical staining on the GF + AM-1 co-cultures over 14 days.

Fibroblast surface protein

A slight reduction in the number of FSP stained GF cells was seen in the models when staining the Dox-treated samples as seen in fig. 6.14. GF cells in both the control and treated samples appeared elongated with elongated nuclei and remained abundant throughout the scaffolds.

Doxycycline appeared to have more of an effect on the AM-1 cells, as seen in fig. 6.14: instead of forming the characteristic clusters as in the co-culture control samples, the cells were inhibited from doing this in the Dox-treated samples. The single AM-1 cells stained mostly green for FSP. Similarly, in samples examined on day 14 of co-culture, AM-1 cells stained green for FSP in all co-culture samples as seen in fig. 6.15. Again, doxycycline appeared to reduced AM-1 proliferation and the cells were found not to have grown in clusters. As previously noted in fig. 5.22, AM-1 cells were seen to express FSP by day 7 when in co-culture with fibroblast cells. This was also observed in these samples.

Ameloblastin

AMBN was used as an AM-1 specific marker during this study in an attempt to distinguish the two separate cell types from each other. There was a varying level of AMBN staining seen in the GF + AM-1 co-cultures, with some co-cultures on day 7 showing some AMBN expression (6.14), but with no expression seen in the day 14 samples (fig. 6.15). However, AM-1 cells in most co-cultures with GF cells appeared to not express any AMBN, so the AMBN staining was inconsistent and was therefore not the optimal AM-1 marker. GF

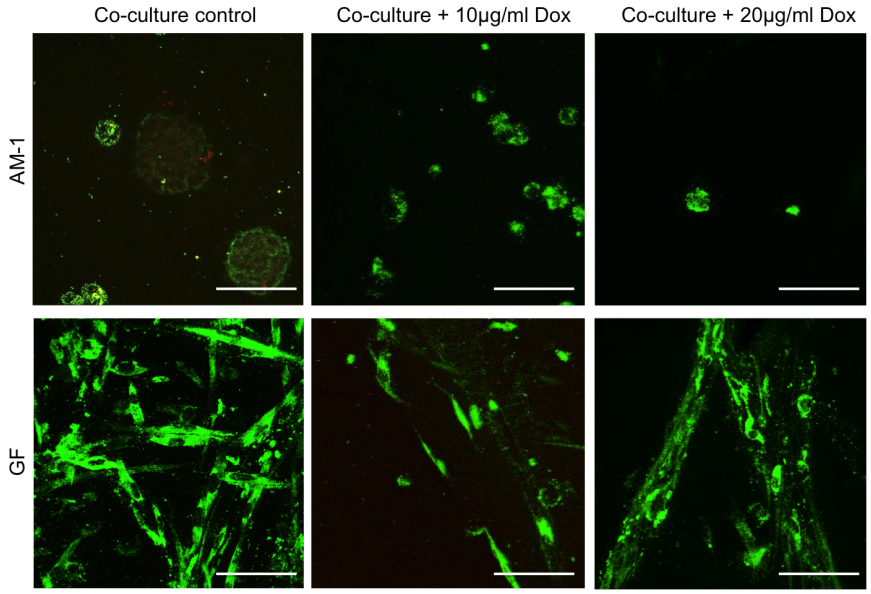

Figure 6.14: Confocal micrographs of immunostained GF + AM-1 co-cultures on day 7 of co-culture. Samples were stained with FSP (green) and AMBN (red). GF cells remained elongated and randomly oriented with added Dox. However, Dox appeared to inhibit AM-1 cell proliferation by inhibiting their characteristic clustering behaviour within the 3D collagen models. Representative images of n = 3. Scale bars = 50μm.

cells did also not express AMBN.

The Dox-treated AM-1 cells were not stained for AMBN as seen on days 7 and 14 in figures 6.14 and 6.15, respectively. However, it should be noted that the cells for all ICC assays were fixed and lysed, which made definite analysis difficult and may have had an effect on the proteins visible in these cells.

Fibroblast activation protein

In the previous chapter, AM-1 cells co-cultured with GF cells and found as single cells rather than clustered, were seen to express FAP. In the Dox-treated GF + AM-1 co-cultures, no FAP staining was seen in any AM-1 cells, nor on any GF cells (fig. 6.16).

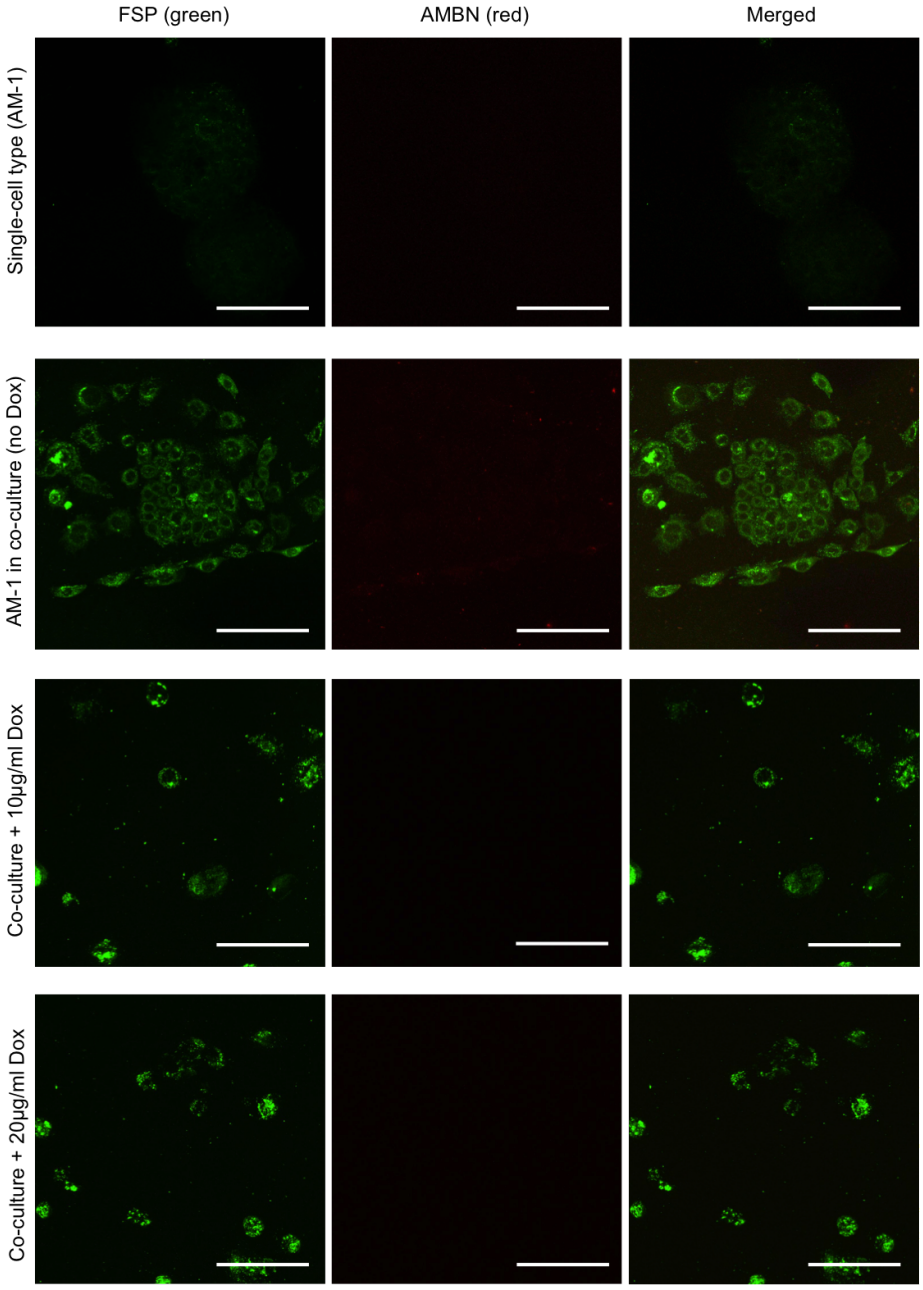

Figure 6.15: Confocal micrographs of immunocytochemically stained GF + AM-1 co-culture samples. A closer look at the AM-1 parts of GF + AM-1 co-culture constructs with and without Dox stained for FSP (green) and AMBN (red) on day 14. No AMBN staining was seen in the single-cell type AM-1 samples, and these cells did also not stain for FSP. AM-1 cells in co-culture stained for FSP, but only faint AMBN staining was visible in these samples. Dox seemed to also inhibit AM-1 cell proliferation in these day 14 samples by inhibiting their characteristic clustering behaviour. Representative images of n = 3. Scale bars = 50μm.

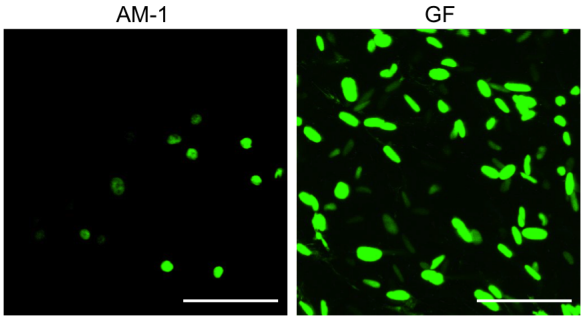

Figure 6.16: Confocal micrographs of GF + AM-1 co-cultures on day 14, where nuclei were stained green, and any potential expression of FAP in the cells was stained red. No expression was seen in either the AM-1 or the GF cells in these co-cultures. Representative images of n = 3. Scale bars = 50μm.

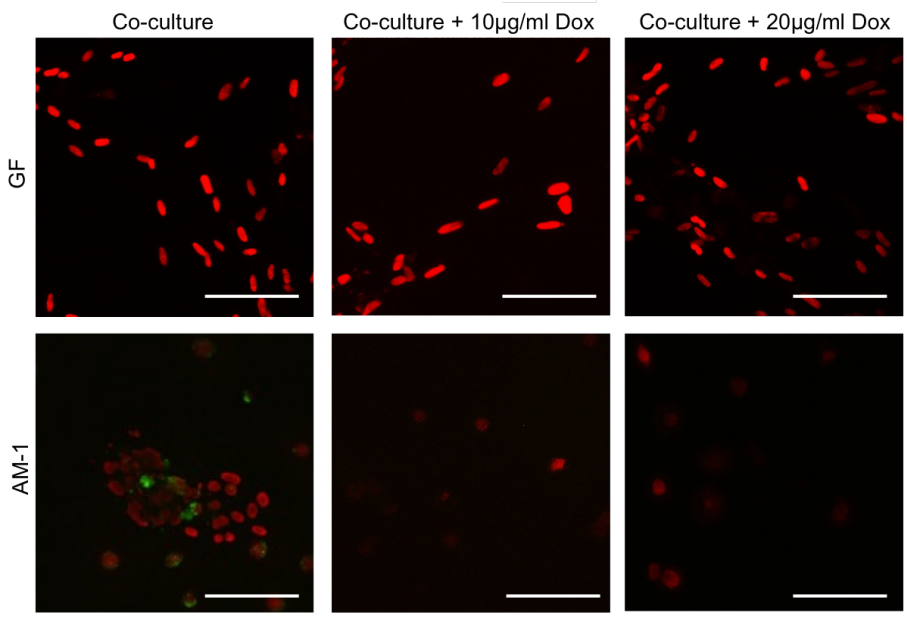

Figure 6.17: Confocal micrographs of GF + AM-1 co-cultures on day 7, where MMP-2 was stained green and EthD-1-stained cell nuclei are visualised in red. The AM-1 cells in co-cultures without Dox stain for MMP-2. As expected, addition of Dox to the co-cultures caused a reduction in MMP-2 expressed by the AM-1 cells in the co-cultures. Representative images of n = 3. Scale bars = 50μm.

MMP-2

MMP-2 staining was found only in the co-cultures with no Dox-treatment on day 7, as visualised by the green staining in fig. 6.17. The MMP-2 staining on day 14 (faint green in fig. 6.18) was localised to the AM-1 clusters in the co-culture control samples. In co-cultures treated with either 10 or 20μg/ml Dox, no MMP-2 staining was detected at either time point.

GF cells in the co-cultures did not stain for MMP-2 either before or after Doxycycline application (fig. 6.17). AM-1 cells appeared to stain more strongly for MMP-2 when in co-culture with GF cells, as very little green MMP-2 staining was seen in the single cell-type control cultures even after 14 days of culture (fig. 6.18). It is therefore possible, that the co-culture with GF cells caused an increase in MMP-2 production by AM-1 cells.

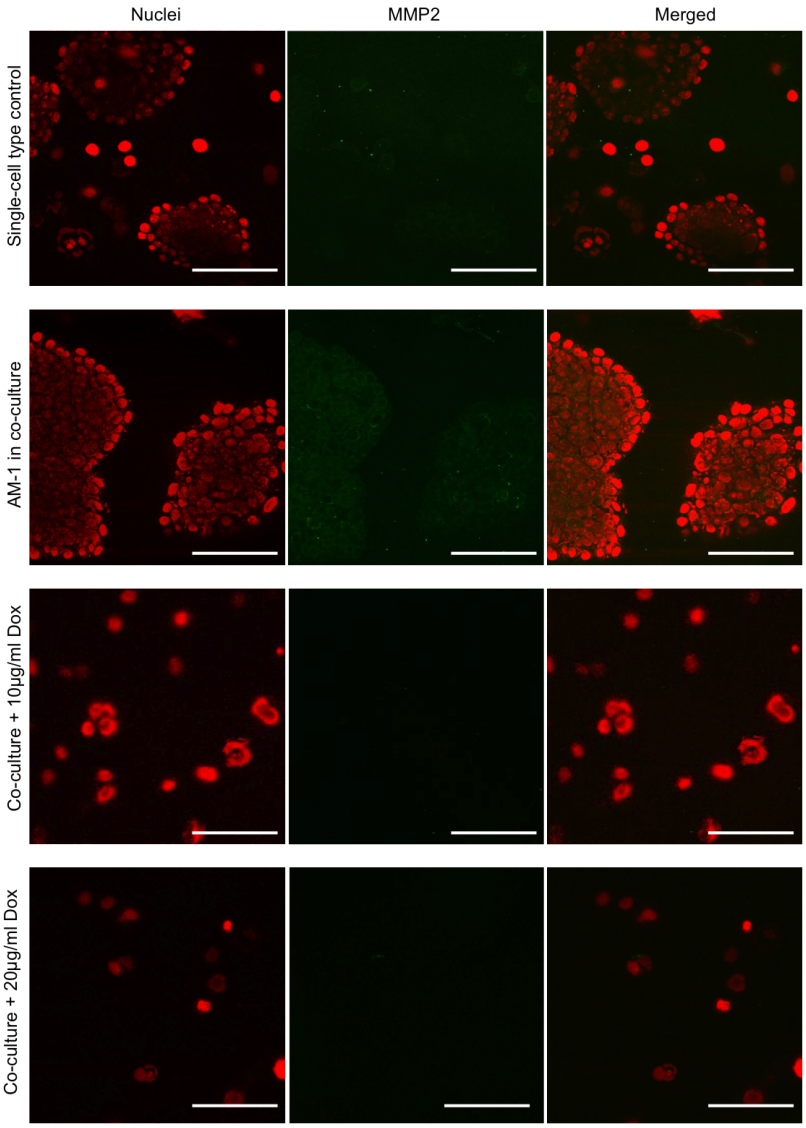

Figure 6.18: Confocal micrographs of GF + AM-1 co-cultures on day 14, where MMP-2 staining is seen in green, and the nuclear counterstain EthD-1 is in red. No MMP-2 staining was seen in the single-cell type control samples. Some MMP-2 staining was visualised on the AM-1 clusters when in co-culture with GF cells. As expected, AM-1 which had been treated with Dox showed no MMP-2 expression on day 14 of co-culture. Representative images of n = 3. Scale bars = 50μm.

Doxycycline appeared to, as expected, inhibit MMP-2 synthesis in the co-culture constructs when examined on day 7 (fig. 6.17), as well as on day 14 (fig. 6.18). Furthermore, there was a noticeable reduction in AM-1 cell clustering in the samples with Dox applied.

6.4 Main findings and discussion

3D organotypic culture models allow for improved, more *in vivo*-like testing of therapeutic agents. While the main focus of this project was not to test out therapeutic agents, based on the gene expression data obtained and the potential mechanisms and pathways involved, a therapeutic agent was applied to each model for a brief pilot study. It should be noted that as the HOS cells are both cancerous and a cell line, and the AM-1 cells are also a cell line, further experiments on primary cells should be carried out to confirm the findings of this chapter.

Anti-tumour agents typically passively diffuse through the tumour and the surrounding extracellular environment to target the tumour cells. Therefore, it is possible to distinguish tumour-specific killing agents from general cytotoxic agents by using the two-cell type 3D culture model to screen for potential therapeutic agents. Although both Alendronate and Doxycycline are widely used clinically, no data is available for their use for treatment of ameloblastoma. However, as Dox at low doses is an anti-MMP agent, and these have previously been shown to reduce ameloblastoma growth by inhibiting MMP production by the tumour cells (Kumamoto et al., 2003; Zhang et al., 2010c), the effect of Dox on AM-1 cell growth in these models was also tested.

The main findings of these experiments presented in this chapter were:

- AM-1 cell viability was significantly reduced in samples treated with 100nM ALN compared to both the single cell and co-culture controls ($p \leq 0.0001$).
- In samples with 10nM ALN, the number of AM-1 cells increased over time. Cell numbers in the IF region of these constructs remained similar to the untreated co-culture controls.
- Cell viability data for the HOB + AM-1 scaffolds indicated a statistically significant decrease in cell number in the AM-1 cells in both treatment groups.
- Both HOS and HOB cells appeared mostly viable after ALN treatment.
- Cell death in the ALN-treated samples was particularly abundant on the edges of the tumour clusters in the HOS + AM-1 co-cultures. This was due to a probable higher concentration of the drug at the edges of the models and thereby the cell clusters.
- No increase in dying or dead cells was seen in the established HOB + AM-1 tumour models using Live/Dead staining. However, a significant decrease in cell number was observed when cell viability was measured.

- A significant reduction in RANKL gene expression levels was seen in the ALN-treated HOB co-cultures, indicating a reduction in osteoclastic potential.
- OPG gene expression levels were also found to decrease significantly in the ALN-treated HOB co-cultures, indicating a reduction in osteoblast activity as a result of ALN treatment.
- NFκB gene expression levels were shown to decrease in the ALN-treated HOB co-culture models over time. NFκB is a factor in the osteoclast-activating pathway, but also involved in general cell survival.
- In the HOS + AM-1 co-cultures (but not in the HOB + AM-1 co-cultures), AM-1 cells stained for FSP. This indicated a more fibroblast-like AM-1 phenotype in the vicinity of the cancerous HOS cell line.
- Doxycycline was found to reduce cell viability in the GF + AM-1 cultures. This reduction was greater than in the co-cultures treated with Alendronate.
- Immunocytochemical staining indicated that AM-1 cells require MMP-2 activity to form clusters, as cluster formation appeared inhibited when Dox was added to the models.
- This clustering behaviour is essential for AM-1 survival, and with added Dox there was a decrease in surviving AM-1 cells in the models.

RANKL levels in samples with and without added ALN appeared similar overall, which was expected as ALN does not interfere with the OPG / RANKL pathway when regulating bone turnover as discussed in section 1.10. The large decrease in OPG levels in the co-culture models was to be expected, as ALN is also known to inhibit new bone formation by inhibiting osteoblast proliferation (Schott et al., 2015).
However, it is not known whether ALN is able to achieve such a marked downregulation of OPG gene expression in a relatively short time. Further studies would therefore be needed to look into more details effects the addition of ALN may have on ameloblastoma cells, and to further probe more detailed effects it may have on gene expression.
A reduction in AM-1 cell viability using Dox was seen in both freshly made and 'established' co-culture models. The addition of Dox reduced MMP-2 levels in these co-culture models, resulting in reduced AM-1 proliferation. This indicated that MMP-2 is necessary for AM-1 cell characteristic cluster behaviour and blocking MMP-2 with Doxycycline disabled the mechanism AM-1 cells utilise to form clusters. MMP-2 could be used by the cells to break down the surrounding ECM, after which they use the resulting space to proliferate.
Dox application did not appear to reduce fibroblast numbers significantly, which is encouraging from a therapeutic point of view.
However, the samples which were treated for Dox were not stained for Live/Dead after Dox application, so definite conclusions that Dox caused AM-1 cells to apoptose in greater quantities cannot be drawn; it may only have reduced their metabolic activity as shown by the Cell Titre Glo assay. Further experiments should be carried out with adding Dox to primary ameloblastoma cells or *ex vivo* tumours to assess the effectiveness

of this potential therapeutic agent in the reduction of ameloblastoma tumour cell growth, and to compare these findings with the results obtained here using the AM-1 cell line.

As both Alendronate and Doxycycline are clinically available and widely used therapeutic agents, these results indicated that they could be used prior to or in conjunction with surgery to reduce the size of the ameloblastoma tumour or prevent it from further spreading in the soft tissues.

Overall, as Alendronate has the potential to inhibit osteoblast function as well as osteoclast-mediated bone resorption, Doxycycline may be the better therapeutic candidate. Doxycycline was found to specifically target the AM-1 cells within the co-cultures, although further testing is required.

Chapter 7

Discussion and future directions

A limited amount of literature had at the start of this project been published on a suitable organotypic model as a starting point for the research presented here. Therefore, a significant amount of time had to be spent initially developing both a bone-like and a soft tissue scaffold, which would lend themselves to the manipulation and further analysis of the ameloblastoma tumour which was carried out during this project.

At the start of this project, much was still unknown about the molecular pathways and mutations which may lead to the development of ameloblastoma. During this project however, great leaps forward were made by other groups (Brown et al., 2014; Kurppa et al., 2014; Sweeney et al., 2014): high-throughput screening allowed extensive genetic mapping of large numbers of ameloblastoma tumours, providing far more accurate data regarding potential tumour formation, genetic causes as well as the clinical situation, than organotypic models are able to provide.

The models developed during this project improved on previous ameloblastoma *in vitro* studies as detailed in table 1.5 by being in 3D and by being co-cultures, although as AM-1 were found difficult to incorporate in the organotypic scaffolds, they were not uniform co-cultures. Furthermore, the models incorporated the correct proteins in the scaffolds, with collagen, laminin and other ECM factors in the soft tissue models, and the addition of Bio-Oss to mineralise the bone-like scaffolds. The scaffolds developed also allowed for a variety of *in vitro* techniques to be used on them to further set them apart from previous models. The models were validated against both older findings regarding ameloblastoma bone resorption and MMP-mediated matrix remodelling, as well as the more novel SMO and PTCH-1 mutations. The results obtained from the high-throughput studies by Sweeney *et al* and Brown *et al* also provided the ameloblastoma research community with valid drug targets, such as the BRAF pathway. Unfortunately, there was no time left during this project to test these targets, but instead the final part of the research focussed on inhibiting local ameloblastoma invasion.

7.1 Discoveries in the bone-like model

There are multiple factors to consider when mimicking bone in an *in vitro* environment, and many ways to achieve a bone-like scaffold in a laboratory setting. Ultimately, in order to accurately reflect the matrix composition, mineral content and cell actions in native bone, the bone-like scaffolds during this project were required to enable cell proliferation throughout culture time, to mineralise and to be mechanically similar to native bone scaffolds, while being reproducible to manufacture and relatively easy to manipulate.

The gene expression and mineralisation results obtained here suggested that the bone-like environment of the collagen + Bio-Oss scaffolds was capable of supporting mineralisation through hydroxyapatite growth and was considered to be similar to events observed *in vivo* (Bitar et al., 2008; Pedraza et al., 2010). Other osteoblast lineage factors, which could also have been used to assess mineralisation in the scaffolds include runx2, osterix, osteocalcin or collagen type I.

Osteopontin (OPN) was used as a marker for bone cells in the co-culture scaffolds during fluorescent examination of the scaffolds and was found abundantly expressed during culture time, has previously been found expressed early in bone-like collagen cultures (Coyac et al., 2013).

In addition to the cellular mineralisation processes, this increased mineralisation in the Bio-Oss supplemented scaffolds was potentially further aided by ionic release from the Bio-Oss granules, which enabled faster scaffold mineralisation and osteoblast function. The pores in the scaffold further provide the cells with access to environmental cues similar to those in native bone.

Furthermore, the addition of Bio-Oss to the scaffolds was also shown to increase the stiffness of the bone-like constructs by approximately 10-fold compared to scaffolds without Bio-Oss. The presence of cells within the Bio-Oss collagen constructs, which were seen using histology to have mineralised the scaffold further during culture, did not significantly affect the constructs' mechanical properties. However, there was still a very large difference between the Bio-Oss scaffolds and native bone in terms of mechanical properties and substrate stiffness. The reduced stiffness of the Bio-Oss particles measured here compared to native bone, as well as the failure of the Bio-Oss constructs observed at testing frequencies over 1Hz, could be due to one or several of the following:

The repeated force exerted on the particles during testing may have caused the Bio-Oss particles to disintegrate or break, ultimately reducing construct stiffness. Scaffolds, which were initially tested with a higher frequency, were indeed measured to have a stiffness approaching that of collagen-only scaffolds.

Bone is, like many others, an anisotropic, directional material, meaning that it has different mechanical properties depending on the direction of the force applied (Nomura et al., 2005). The bone in the Bio-Oss particles was most likely not in the correct orientation to withstand mechanical pressure; there was no way of knowing which way particles were oriented.

During production, Bio-Oss particles are sintered to decellularise and disinfect them. This, or another part

of the manufacturing process, may make the granules less stiff. Other studies have found heat treatment to change a material's mechanical properties (Wolfenden et al., 1996).
Taken together, this reduced mechanical stiffness of the Bio-Oss granules should be taken into account in future *in vitro* and *in vivo* studies.

The collagen scaffold enabled a cell-friendly environment which was easy to manipulate and the manufacturing process was repeatable. Overall, Bio-Oss particles were deemed a suitable addition for further scaffold development, as they appeared cytocompatible, mineralised the scaffold and proved easy to incorporate in the scaffolds, as well as to analyse.
AM-1 cell clustering, seen in biopsy samples, was used as an indicator that the AM-1 collagen cultures and co-cultures were organotypic and a suitable environment for growing these cells and modelling the ameloblastoma tumour.
The organotypic bone-like co-culture model developed in the first part of this study was used to examine differences in gene expression when AM-1 cells were cultured with cancerous HOS cells, and with osteoblastic HOB cells, as well as AM-1 behaviour and invasion within the models.

The results from this study, especially those obtained with the HOB + AM-1 co-culture models, appear to agree with previously published results on RANKL and OPG expression in the ameloblastoma tumours, indicating that the organotypic models developed here are suitable ameloblastoma models. The RANKL gene expression data was in agreement with previous publications, where 24 ameloblastoma tumour biopsies were subjected to histological examination and gene expression analysis, and where RANKL expression was found in all cases (Qian and Huang, 2010). Previous reports using immunohistochemical staining on histological samples have shown a strong OPG expression in ameloblastoma, along with some RANKL and TRAIL expression, which all appeared to correlate with the reported invasive behaviour of the particular tumour *in situ* (Iakovou et al., 2015).
Additionally, these findings support the theory that ameloblastoma tumour cells may use pressure absorption to invade their surrounding bone tissue as proposed by (Imamura et al., 1990). The potential increase in bone turnover, as seen here, could be due to the pressure by the tumour within the jaw bone leading to an increased activation of osteoclasts, combined with a reduction in osteoblast function. This could then lead to an increase in the level of local bone resorption, allowing the ameloblastoma tumour to increase in size and invade the bone tissue.

Ameloblastoma staining for ameloblastin (AMBN) appears varied in the literature: some studies have shown AMBN to be a marker for ameloblastoma cells, with positive staining of biopsies (Perdigao et al., 2004; Crivelini et al., 2012). Cases of peripheral ameloblastoma have also been found positive for AMBN (Kim and Lee, 2014). Other studies have not found any expression, including in the AM-1 cell line (Takata

et al., 2000; Gomes et al., 2010; Kiyoshima et al., 2013).
Mutations to the AMBN gene have also been found in solid ameloblastoma tumours (Perdigao et al., 2004). Indeed, the addition of full length AMBN to AM-1 cells has been found to prevent ameloblastoma growth, which suggests that AMBN prevents odontogenic tumour formation (Sonoda et al., 2009). These results indicate that AM-1 cells express little or no AM-1, and that this was again a downside of using a single cell line; whereas previous studies have found varied AMBN expression in their varied biopsies, the AM-1 cell line alone is not enough to study the ameloblastoma tumour.
The variability of AMBN staining in the co-culture models, with occasional AMBN staining seen in AM-1 cells co-cultured with GF cells, but no staining found in the bone-like cultures, indeed indicates a lack of AMBN expression in ameloblastomas and specifically AM-1 cells. This discrepancy also indicates that AMBN should not be used as a marker for ameloblastomas of similar molecular origin as the AM-1 cell line.

The invasion of the AM-1 cells towards the HOB part of the constructs was supported by the observation that in these co-culture scaffolds, AM-1 cells appeared to proliferate faster in the vicinity of the HOB scaffolds, which has been reported before in ameloblastoma tumour biopsies (Pinheiro et al., 2004). It is therefore possible that the HOB cells secreted a cytokine or other chemoattractant which enabled AM-1 cell migration. However, it was not possible to determine what this factor might have been during this study. If this increased growth is confirmed to be similar to that taking place in *in vivo* tumours, these models could be used to determine what the role of these invading AM-1 cells may be in tumour progression and prognosis, and what mechanisms and pathways are activated during invasion.

Movement of cells is caused both by intrinsic and extrinsic factors within the ECM, with cells in gels reacting to anything occurring within the gel environment, and many factors able to trigger movement (Brown and Phillips, 2007). Biname *et al* argue that cell movement should be thought of as the default, and the more appropriate question would be to ask why some cells remain stationary, and what mechanisms keep them from moving (Biname et al., 2010).
Durotaxis, or cell movement towards a stiffer substrate from a less stiff matrix area (Brown and Phillips, 2007), could in part explain the movement of AM-1 cells towards the bone-like part of the co-culture scaffolds. Furthermore, some of the movement seen towards the HOB cells in the scaffolds but not the HOS cells was probably due to less cells present in HOB scaffolds; HOS cells were confluent and could even have released factors to deter AM-1 movement, whereas in the HOB scaffolds cell proliferation was slower and there was therefore space in these scaffolds.

7.1.1 Limitations of the bone-ameloblastoma co-culture models

Even though the organotypic models were carefully constructed to mimic native mineralised tissue as closely as possible, whilst still lending themselves for manipulation, there were several limitations to the models and

thereby the bone-like ameloblastoma co-culture studies.
The main disadvantage of both the HOS and HOB co-culture models was the lack of osteoclasts, which could have been shown to degrade the bone-like scaffolds. Osteoclast incorporation in the models would also have allowed these organotypic models to more closely examine the changes in bone turnover caused by ameloblastoma cells. The increase seen in RANKL levels, originating from both cell types in the co-cultures, may despite having the potential to activate bone resorption not actually activate osteoclasts. Therefore, using this osteoblast-incorporating model alone, it was impossible to determine what the effect of AM-1 cells would be on bone turnover.

The HOS cells used initially in the co-culture models are cancerous, and AM-1 cells in the models may have been unduly influenced by this fact. For example, in addition to the very high RANKL expression levels seen in the HOS + AM-1 co-cultures, no invasion was seen in these co-cultures, whereas abundant invasion was seen in the HOB + AM-1 co-cultures on day 7 of culture. The fast proliferation rate of HOS cells could have influenced this as well by leaving little space for AM-1 cells to move into in the bone-like part of these co-cultures. Overall, the HOB co-culture results obtained were thought to be more representative of and relevant to the *in vivo* ameloblastoma tumour.

The final scaffold constructs did not have the same proportional composition as bone; as the scaffolds developed here were composed of significantly more collagen fibres, with a relatively homogeneous cell population and reduced amounts of mineral. However, the increased collagen content enabled use of confocal microscopy to study the cells and their interactions.
Scaffold analysis was made more difficult by cell migration to the Bio-Oss pores in the scaffolds, rendering these cells invisible to microscopic analysis as the Bio-Oss granules were opaque. Furthermore, both the collagen fibres as well as the Bio-Oss granules were autofluorescent (at 488nm) to a degree, especially when viewed under the fluorescent microscope, making imaging difficult. This has previously been cited as a problem in working with collagen structures and fluorescent imaging of these (Gareau et al., 2004).

It is possible that the cells within these scaffolds, due to the addition of Bio-Oss granules, effectively ended up in a pseudo-3D environment (Brown and Phillips, 2007), where due to the large size of the pores on the bone granule surface (up to 100μm), as well as the spaces between them, the cells were only able to attach to the one surface thus making the cells experience a 2D environment.

7.2 Discoveries in the soft tissue model

The cell-induced contraction by gingival fibroblasts in the collagen scaffolds seen here has not been documented in compressed collagen scaffolds elsewhere. Others have suggested that the fibroblast contraction of the matrix in free-floating collagen constructs (as used here) is in fact not due to remodelling of the scaffold,

but due to attempts by the cells to migrate out of the scaffolds as well as within the scaffolds as they become entangled with the collagen fibres (Grinnell, 2003; Rhee and Grinnell, 2007). However, histological examination of these scaffolds appeared to show matrix remodelling taking place, and microscopic examination of the scaffolds and wells they were kept in appeared not to show excessive numbers of migrated cells once Matrigel had been added to the scaffolds.

The only movement seen in these scaffolds was an increase in fibroblast directionality, as the GF cells over time appeared to align with each other, as well as the edge of the GF - AM interface.

Cell motility within matrices has been shown to be dependent on the ease with which the substrate can be remodelled, deformed and reorganised (Biname et al., 2010). Cell contraction expectedly produces some cell motility within the matrix (Brown and Phillips, 2007), and localised denser areas of substrate around the cells in question (Brown, 2013), as was also seen here using histology.

The Cell Tracker stain appeared to cause the GF cells to remain more rounded throughout culture time than they were during other assays. There may have been other ways the staining process impacted the cells as well, and if so, invasion may have been one of the behaviours impacted.

During this study, SMO gene expression levels were not found greatly different from the control and calibrator samples in either type of co-culture scaffold, nor was there a significant change over time in the co-culture scaffolds. However, it is probable that calibrator samples which included AM-1 cells were not the optimal ones to use for qRT-PCR analysis in this study, as these could already have had high or aberrant SMO expression. Changes in SMO expression appears to be one of the more defining features in ameloblastoma tumours (Zhang et al., 2010b; Sweeney et al., 2014; Diniz et al., 2015).

The mechanical stiffness of soft tissue-like compressed collagen scaffolds with fibroblast cells has previously been reported as 1-2MPa (1MPa on the soft end and 2MPa at the stiff end of a graded construct) (Hadjipanayi et al., 2009). The stiffness of soft tissue-like scaffolds as measured here was approximately 15MPa. Other collagen scaffolds have been reported to be between 1-40kPa, and with normal gingival stiffness being in the region of 20MPa (Goktas et al., 2011), the scaffold here was stiffer than other similar collagen (hydro)gels, but roughly the same stiffness as native gingival tissue, making these scaffolds more organotypic than other collagen-based scaffolds.

Fibroblasts form the basic cellular component of the ECM, and provide the ECM with a variety of proteins. However, in addition to the normal stroma, they have also been found to be a major component of the tumour stroma, where they are known as tumour-associated fibroblasts (TAFs), carcinoma associated fibroblasts (CAFs), tumour stroma fibroblasts, senescent fibroblasts or myofibroblasts (Xouri and Christian, 2010). Tumour associated fibroblasts are a heterogeneous, activated fibroblast population within the tumour microenvironment, which participate in tumour growth and invasion by remodelling the tumour microenvi-

ronment (Kalluri and Zeisberg, 2006). Activated fibroblasts are the most abundant stromal cellular component in tumours of epithelial origin (Veirman et al., 2014). Normal fibroblasts undergo conversion to a more activated type of fibroblast in the presence of tumour cells, but also change when stimulated by a tumour-altered microenvironment (Hakanson et al., 2014). They are also recruited by various types of tumours to their vicinity to assist with invasion and growth (Cirri and Chiarugi, 2011; Horie et al., 2012).

Ameloblastoma-associated fibroblasts (AAFs) have previously been explored in one *in vitro* study, which found that AAFs increased both the proliferation and invasion of the tumour cells they were co-cultured with (Chantravekin and Koontongkaew, 2014). If this kind of interaction is found to also occur *in vivo*, impeding it may also impede tumour growth. Incorporation of a population of activated fibroblasts into these co-culture scaffolds would be beneficial, as the ameloblastoma tumours are a heterogeneous population of cells, including fibroblasts. This improved co-culture model could then be used both as a model for ameloblastoma and the role of fibroblasts in expanding the tumour within the native tissue.

Markers for activated fibroblasts include FAP, FSP and vimentin (Veirman et al., 2014), and during this study, AM-1 cells were found to express two of these by the end of two weeks in co-culture with fibroblast cells. AM-1 cells have previously been reported to express vimentin, which is an epithelial and ameloblastoma cell marker (Harada et al., 1998; Sahai, 2005).

The expression of both FSP and FAP by AM-1 cells in co-culture with HOS and GF cells indicated the AM-1 cells had become more fibroblast-like and 'aggressive' with increasing culture time.

Human fibroblasts have been shown to be able to promote proliferation of malignant epithelial cells in culture (Bhowmick et al., 2004). Furthermore, the tumour stroma has been shown to be mechanically different, and also displays different fibrous components and growth factors when compared to healthy ECM (Jamshidi et al., 2008). Additionally, higher numbers of fibroblasts have been documented to be present in tumour ECM than in physiological ECM (Kalluri and Zeisberg, 2006). As this was also the case here as abundant GF cells were seen especially at the later co-culture time points, this could have promoted a more aggressive AM-1 phenotype.

Analysing the protein content of the collagen + Matrigel scaffolds at various time points of co-culture could be an avenue for further research to establish what ECM factors the two cell types in the co-culture secrete during culture, and how these might influence the other cells in the co-cultures.

FSP was also found expressed on the AM-1 cells when in co-culture with HOS cells, supporting the theory of AM-1 cells becoming 'activated' or more fibroblast-like in longer term cultures, and therefore potentially more invasive or aggressive.

Furthermore, the FSP and FAP staining seen on AM-1 cells in GF and HOS co-cultures could also indicate a potential of the ameloblastoma tumours to undergo some form of endothelial-mesenchymal transition (EMT), which is a process whereby cells of endothelial origin become more mesechymal in order to facilitate

processes such as tissue invasion (Chen et al., 2012). EMT is seen in other oral tumours and has recently been explored in ameloblastoma tumours with varied results, however as yet the potential role of EMT in ameloblastomas is unknown. Several authors have made cases for potential EMT in ameloblastomas (Chen et al., 2012; Andisheh-Tadbir et al., 2015), as well as cases against (Gonzalez-Alva et al., 2010). This phenomenon, if found to be present in *in vivo* tumours, could ultimately aid ameloblastoma invasion *in situ*.

MMPs have the ability to initiate epithelial cell transformation to a more cancerous cell type. Faulty signals from the ECM can promote cancer initiation, even in the context of normal cellular development (Comoglio and Trusolino, 2005). Therefore, the addition of Matrigel, even with reduced levels of growth factors, may have facilitated the increases observed in both fibroblast-like ameloblastoma cells and MMP levels, as Matrigel may in effect have been providing the cells with a 'faulty' set of signals.

Further examination of the co-cultures for various proteins involved with EMT or activation of fibroblasts should be carried out to confirm whether either of these play a role in local ameloblastoma invasion.
α-smooth muscle actin (SMA), vimentin, β-catenin and MMP-7 are frequently used together as markers for EMT, as confirmed EMT cases in other tumours express these molecules (Bello et al., 2009). A loss of E-cadherin expression, an important molecule in cell adhesion, is also an indicator of EMT (Bello et al., 2009). SMA and β-catenin expression has also been found in the stroma of ameloblastoma samples (Bello et al., 2009). MMP-7 has been shown to both act as a enhancer β-catenin expression, as well as aiding in the destruction of E-cadherin in the cells on the tumour surface (Radisky and Radisky, 2010).
However, the expression of α-SMA and vimentin are also recognised as artefacts seen in HPV-transfected cell lines, such as AME-1 (Pinheiro da Rosa et al., 2014), and as AM-1 was also transfected with this viral vector, expression of these molecules should not be unexpected.
Electron microscopy could also be carried out on suspected cases of TAFs, as activated fibroblast cells have a set of distinct morphological features, such as indented nuclei and prominent actin microfilaments, which can help to identify these from the normal fibroblast population (Xouri and Christian, 2010).

7.2.1 Limitations of the soft tissue-ameloblastoma co-culture models

As with the bone-like co-culture models, there were several limitations to the soft tissue models. The main limitation was that the Matrigel used in their development, although growth factor reduced, still originated from murine sarcomas. It is therefore, at least to an extent, a tumour stroma and even the growth factor reduced version may have provided the organotypic model with increased, non-ameloblastoma growth factors, which may have influenced the cells in the co-cultures. For instance, the FSP and FAP staining of the AM-1 cells in these co-cultures may have been an effect of the Matrigel in the co-cultures rather than an activated fibroblast or AM-1 cell transformation caused by the ameloblastoma tumour.

As only gingival fibroblast cells were used to develop this soft-tissue model, the model produced is in effect solely a gingival tissue model. However, as ameloblastoma tumours spread to other tissues in addition to the gingivae, so this study only modelled a small fraction of ameloblastoma recurrences. Additionally, the ameloblastoma tumour is not only composed of the tumour cells themselves, but a large number of stromal fibroblasts, as well as potentially tumour-associated fibroblasts recruited by the tumour cells themselves. Adding more fibroblasts into the models and into a physical co-culture with ameloblastoma cells could further improve the model developed here.

Additionally, fibroblasts *in vivo* are heterogenous in terms of cell size, proliferation rate and protein synthesis, in both healthy and diseased tissues (Hasseil and Stanek, 1983), whereas they were relatively homogeneous in these models, as only one type of fibroblasts was used.

Furthermore, fibroblast cells in culture have been documented to quickly change both in morphology and genetic make-up (Mariotti and Cochran, 1990). Here, inter-experimental variation and any effects on the cells caused by 2D culture were minimised by limiting their culture on TCP by using cells from similar passage numbers.

Additionally, a more organotypic, *in vivo*-like, model could be made by incorporating both fibroblasts as well as ameloblastoma tumour cells in collagen scaffolds at the same time. A similar study has previously been carried out by Chantravekin and Koontongkaew (2014), where ameloblastoma-associated fibroblasts and gingival fibroblasts were co-cultured to examine invasion.

As the tissue-like scaffold were required to be organotypic prior to the addition of tumour cells in this project, the AM-1 cells were added as a separate scaffold to the soft tissue scaffold after a pre-culture period. As with the bone-like model, it was difficult to incorporate the AM-1 cells to a pre-made soft tissue scaffold, e.g. by injecting the AM-1 cells into the scaffold. Therefore the approach with the two distinct scaffolds was used, although this consequently makes the models less *in vivo*-like.

7.3 Testing of potential therapeutic agents

A previous study suggested that treating cells with lower ALN concentrations induced osteogenic differentiation in stem cell cultures, whereas higher ALN levels were cytotoxic and inhibited osteogenesis (Alqhatani, 2014). Therefore, this study also used lower ALN concentrations so as to limit the damage on the bone cells within the models.

Alendronate significantly decreased AM-1 cell viability as seen both by using a cell viability assay in both HOS and HOB co-culture models as well as the ‘established’ HOB + AM-1 models. Some dead or dying cells were also seen in the bone-like part of the models, especially in the HOB scaffolds, but to a lesser extent than the AM-1 tumour cells.

Bisphosphonates have been shown to suppress endothelial cell growth *in vitro* and to induce endothelial cell apoptosis in *in vivo* studies (Kearns et al., 2008). Therefore it was not surprising that the AM-1 cells appeared to be affected by the addition of ALN to the co-culture models.

Doxycyclines have been extensively studied and used to treat a variety of diseases with high MMP activity (Stechmiller et al., 2010). Therapeutic agents from this group have also been used clinically for oral diseases such as periodontitis (Gorska and Nedzi-Gora, 2006) and oral squamous cell carcinoma (Shen et al., 2010). Doxycycline addition to the models resulted in a large reduction in AM-1 cell numbers in both the constructs where Dox was added immediately upon co-culture assembly, as well as in the 'established' tumour models, where cell viability was again reduced through the reduction of MMP levels in these co-culture models. Previous studies have used MMP inhibitors (MMPIs) as potential therapeutic agents (Zhang et al., 2010c). This could also have been attempted during this study. However, MMPIs are cytostatic rather than cytotoxic, which means that results such as a reduction in tumour size may not be achieved using these drugs (Curran and Murray, 2000). However, achieving dormancy of tumour cells or metastasis (quiescent phenotype) may be an acceptable therapeutic outcome (Curran and Murray, 2000).

Additionally, the cells in these models were only subject to treatment with the therapeutic agents for a maximum of 14 days. A 14-day treatment time for both the ALN and Dox-treated co-cultures was relatively short. Further scaffold development to allow for longer time-point studies would be required.

Drug distribution is a challenge with organotypic models, as 3D models display different drug kinetics and diffusion properties to drugs applied purely in 2D cultures, and it presents a major difficulty in translation from primary cell research to functioning therapeutics within pharmacology (Astashkina and Grainger, 2014). During the studies of this thesis, neither ALN nor Dox diffusion throughout the constructs was measured, so there may have been parts of the cultures where the drug concentration was low, which could have contributed to the increase in AM-1 number seen in some of the treated models. There was a noticeable increase in cell death at the edges of the ALN-treated AM-1 tumour clusters, which was thought to be due to a potentially higher ALN concentration at this location. This may be something to probe further, both to ensure uniform drug distribution, and that some therapeutic agent is left to treat tumour cells deeper inside the tumours.

Furthermore, cell-adhesion mediated drug resistance (CAM DR) (Hakanson et al., 2014) has been reported as an issue with 3D and *in vitro* pharmaceutical studies. CAM DR is a protective effect, which is mediated by integrins and protects tumour cells from therapeutic agents by their adhesion to other cells as well as ECM components at the treatment site (Hakanson et al., 2014).

In light of the newest experimental results published by other groups involving the BRAF V600E and SMO mutations, inhibitors of these two pathways should be explored in these organotypic models. However, stromal resistance to a RAF inhibitor used to treat other similar tumours has been reported, resulting in constitutive, low RAS activity (Hakanson et al., 2014). In addition, to further validate these models, Ve-

murafenib, which has been shown to clinically decrease ameloblastoma tumour size (Kaye et al., 2015), and other currently clinically tested therapeutic agents could be applied.

7.4 Differing ameloblastoma behaviour in the models

Overall, it is clear from the results presented here that the ameloblastoma tumour models exhibited different behaviour when cultured in the different models. This was partly due to the other cell type they were co-cultured with, but also due to the difference in the ECM composition in the two models.
The presence of the other cell type within the co-cultures would be sensed by AM-1 cells at least in immediate vicinity of the interface either by direct cell-to-cell contacts or paracrine effects, and would be perceived as an *in vivo*-like environment, causing *in vivo*-like responses, e.g. RANKL upregulation. The heterogeneous cell-to-cell interactions as mimicked in these models have been shown to be crucial for tumour invasion and progression (Hakanson et al., 2014).

AM-1 cell growth was most abundant when the cells were in co-culture with HOS cells, reaching numbers seven-fold greater than in both HOB and GF co-cultures. Meanwhile, AM-1 cells in co-culture with HOB and GF cells exhibited a similar and overall slower proliferation rate, which better mimicked the behaviour of an *in vivo*, slow-growing ameloblastoma tumour. The faster cell proliferation observed in the HOS co-cultures, as well as all the control co-culture samples compared to the single-cell type controls, may be due to paracrine effects with the cells in the cultures. Little MMP-2 expression was seen in single cell AM-1 cultures, indicating that AM-1 cells specifically in co-culture with GF cells upregulated MMP-2 expression.
Invasion was not observed in the HOS or GF co-culture models. In the GF co-cultures, cells from the two cell types were co-localised and potentially interacting at the interface of the two constructs, whereas in the HOB + AM-1 models, AM-1 invasion was apparent by day 7 of co-culture. The increase in cell number and AM-1 cluster size seen at the interface in the HOB + AM-1 co-cultures was not observed in the other co-culture models, and could be due to the AM-1 invasion seen in these models. This was indicative of bone-specific AM-1 invasion.

Gene expression analysis did not reveal large differences between the co-culture constructs in the genes analysed in the bone-like and the soft tissue models. In particular, SMO gene expression levels were similar in all constructs and control samples, which was thought to be due to a potential ameloblastoma causing mutation already present in the AM-1 cells, and levels in both co-cultures and control samples therefore remained similar throughout culture.
AM-1 cells were stained for FSP and FAP when in co-culture with GF cells, and for FSP when in co-culture with HOS cells, but staining for neither was observed in co-cultures with HOB cells. The FSP and FAP staining in co-culture with HOS cells could again be due to a paracrine, cancerous effect of the HOS cells. The increased FSP and FAP staining in both the HOS + AM-1 and the GF + AM-1 co-cultures indicated that the

AM-1 cells became more fibroblast-like as a result of the co-culture environment.

Collagen gel degradation by AM-1 cells has previously been reported elsewhere (Harada et al., 1998), but was not observed during this study. However, the Harada *et al* study placed AM-1 cells on top of hydrated collagen gels, which is a different cellular environment than in the models developed here.
The closest this study came to cell degradation of the collagen scaffolds was the initial, large contraction exhibited by the GF cells. No significant amount of contraction was observed in the bone-like scaffolds.

7.5 General limitations of the organotypic models developed

While 3D organotypic models are an improvement on the 2D tissue culture environment; they are not *in vivo* structures, and lack vasculature, immune cells and systems, as well as other cell populations normally present in tissues. Even though attempts were made to make the models used in this project as *in vivo*-like as possible, these models are not perfect. In addition, the results presented here are based on only one ameloblastoma cell line, and as such, these results may not reflect a true *in vivo* ameloblastoma tumour.

In order to incorporate cells from another ameloblastoma to further verify the results obtained with AM-1 cells, cells from the AM-3 cell line were obtained from the Japanese group which created them (Kibe et al., 2013). However, the cells did not survive the transit and could therefore not be used for further development of these co-culture models. These models should therefore be validated with other ameloblastoma cells, either using primary cells from tumours or other cell lines. Were the models to be validated and developed further using excised tumour cells, they could potentially also be used as personalised screens of potential therapeutic agents in conjunction with patient treatment.

The models developed here lacked any immune cells, which play an important role in tumour formation, as well as in bone turnover as cells from the macrophage lineage mature to form osteoclasts. An interesting model was developed by Linde *et al*, where macrophages were incorporated into collagen gels with human squamous cell carcinoma cells in order to add an immune system component to the models (Linde et al., 2012). A similar experimental system could be attempted with these ameloblastoma models.

Previous ameloblastoma models have focussed on incorporating AM-1 cells in fully hydrated collagen hydrogels (Yasuda et al., 1991a,b). However, this study did not consider fully hydrated scaffolds, as plastic compressed ones have been shown to be more tissue-like (Brown et al., 2005), and therefore a better in vitro mimic for both soft and hard tissue models. Nevertheless, a single-protein gel is not enough to successfully mimic the complexities of a native ECM, and collagen alone does not provide the cells within the scaffolds with all the required ECM molecules, adhesion molecules and ligands to full physiological extent, which can have an effect on cell-cell interactions, signalling and gene and protein expression (Astashkina and Grainger,

2014). This was to some extent rectified by the use of Bio-Oss and Matrigel in the scaffolds, but the resulting ECM compositions were not native, and especially the addition of Matrigel may have affected the fibroblasts and AM-1 cells as discussed above. Furthermore, AM-1 cells were incorporated into collagen-only scaffolds and were only proximal to these other ECM factors when in co-culture, which may have affected their behaviour.

With the large cell number in the confluent scaffolds by the end of the 'pre-culture' in both the bone-like and soft tissue models, more cell movement purely due to crowded constructs would have been expected. This was especially expected on the edges of the gel, and in particular towards the acellular support gels which were added to the co-cultures, as there were no other cells preventing the invasion of the confluent cell type. However, very limited amounts of cell movement towards the other cell type construct or the acellular layer were seen.

In fact, the only cell movement seen was the cell-to-cell interactions seen in the soft-tissue model between the two cell types, and the directional invasion of AM-1 cells towards the HOB cells in the bone-like scaffolds. Furthermore, some cell movement out of the constructs onto the plates was seen, amounting to some tens of cells. These cells were not accounted for in any analysis, as the constructs were always moved to a fresh plate for microscopy and other assays. This lack of movement was interesting, and indicates that the cells when incorporated in the models were in a suitable organotypic niche with little need to search for a more suitable environment.

A majority of available assays were originally developed for 2D cell cultures and not 3D, with adaptation of these into 3D collagen constructs unreliable and unpredictable, such as the results seen here with the Alamar Blue metabolic assay used on the different constructs.

Even though the Cell Titre Glo study, which is based on the amount of ATP present in cells, has been shown to be a relatively accurate measure of cell proliferation in 3D scaffolds both in this study and elsewhere (Crouch et al., 1993), the levels of ATP and the metabolic activity of a cell do not necessarily translate to viable cells within the scaffolds. Use of the Cell Titre Glo assay may have led to an overestimate of viable cells in the co-cultures, as 2 ATP molecules are found per anaerobic cell and 38 ATP per aerobic cell in the Krebs cycle (Malda et al., 2008). Furthermore, increasing cytosolic levels of ATP have been documented in cells undergoing apoptosis (Zamaraeva et al., 2005). It is therefore possible that dying or dead cells were counted by the Cell Titre assay. This may explain the increase in cell numbers seen in some parts of the models when these were treated with ALN or Dox.

Additionally, maturation of osteoblasts to a more osteocyte-like phenotype leads to a reduction in cell metabolic activity (Gartland et al., 2012a), which may again result in an unreliable Cell Titre Glo result. Other methods to quantify proliferation should therefore be employed to confirm cell viability levels seen in this study, especially after the application of ALN and Dox.

The construct thickness varied, with the bone co-cultures being approximately 400μm, while soft tissue ones were no thicker than 200μm - this was due to the inclusion of the Bio-Oss granules to the bone-like constructs. The granules prevented further compression of the bone-like constructs, making them thicker. Oxygen and nutrient diffusion was already limited due to the Bio-Oss particles, and may have been further affected by the construct thickness. Any potential differences in cell behaviour due to the difference in construct thickness were not explored.

In addition, the collagen in the bone-like constructs may have been less dense as a result of adding Bio-Oss to the constructs, than the 13-20% density previously reported in other compressed collagen constructs (Brown et al., 2005; Brown, 2013). The addition of Matrigel to the soft tissue models would also have affected the density of the collagen fibres in the constructs; both of these could be further studied in more detail.

For improved, more organotypic models, and improved testing of therapeutic agents, tumour models should incorporate a blood supply, other cells (stromal cells, fibroblasts in the bone-like model, macrophages, immune cells), as well as components of the immune system and other signalling systems. Therefore, several different aspects of the models developed during this study could be improved to further develop the organotypic ameloblastoma models.

7.6 Future work

As with all organotypic and tumour models, countless different aspects of tissue and tumour biology can be modelled using these constructs. In this report, a selection of experiments carried out on the bone-like and soft tissue *in vitro* ameloblastoma models has been presented; yet many other aspects of ameloblastoma tumour behaviour, growth and invasion remain unexplored.

7.6.1 Further scaffold development

In developing the scaffolds further, the following aspects could be explored: osteoclasts (or macrophages with the potential for becoming osteoclasts) should be incorporated into the models. In addition, substituting the fibroblasts in the soft-tissue scaffolds to primary fibroblast cells would further make these models more *in vivo*-like. Further scaffold development could include combining the bone-like and soft tissue models so that the ameloblastoma cells would receive signals from both fibroblasts and bone cells, making the tumour microenvironment even more varied and organotypic. By combining the two organotypic models, any preferential migration to either scaffold by the AM-1 cells could be mapped, and other cell behaviour dependent on scaffold type analysed.

Modelling the bone marrow cavity by using a softer, collagen-only scaffold could also allow for further characterisation of the ameloblastoma tumour. Additionally, further data could be obtained on how the various

ameloblastoma tumours invade this space, as it is often key for further soft tissue invasion.

The collagen in compressed scaffolds is more randomly distributed (less aligned) than in tissues in general (Cheema et al., 2007), and especially in the jaw bones the collagen fibres are very aligned to produce the characteristic lamellar bone structure. Reducing the randomness of the fibres to provide a more jaw bone-like construct would be something to probe further.

As shown in chapter 4, AM-1 cells are contact dependent and did therefore not form the spherical structures which were initially thought to be the most *in vivo* tumour-like for ameloblastoma modelling. To aid future synthesis of 3D sphere cultures, AM-1 and other ameloblastoma cells could be grown on (biodegradable) microspheres to enable sphericalisation prior to incorporation in the models. This would also allow for analysis of a single ameloblastoma tumoroid at a time, rather than an unquantified number of separate tumours as in this study.

7.6.2 Further ameloblastoma analysis

It would have been interesting to further probe the co-culture models for changes in the production of e.g. ALP, BMP2, collagens, and other proteins involved in bone synthesis, and to ascertain whether the presence of ameloblastoma cells changed the levels of these in the models. There would also be scope to determine levels of other factors considered in the recent studies on ameloblastoma, such as BRAF-V600E.
Recently, a study on using microarrays in ameloblastoma biopsies to look at protein expression was published (Neves-Silva et al., 2016), adding to the other microarray data existing on the ameloblastoma tumour (Heikinheimo et al., 2002; DeVilliers et al., 2011). There is potential to further develop the co-cultures developed here in a direction which would enable the use of microarrays or other high-throughput methods to characterise the organotypic models by further miniaturisation and streamlining of the co-culture manufacturing process.
More assays for protein expression should be carried out. For example, it would be interesting to quantify the increase in collagen in the scaffolds, if indeed cells are extruding collagen as seen in fig. 5.11. ELISAs, western blots and in-cell westerns (a combination of immunofluorescent staining and western blotting) could be used to probe the samples for expression of proteins such as MMPs, bone turnover proteins, SMO pathway factors and various other ameloblastoma-associated proteins.

Additionally, cell migration and cell-to-cell interactions could be further explored by applying therapeutic agents to the co-culture models and then carrying out a Cell Tracker study. Furthermore, it would be interesting to look more closely at apoptosis and any specific locations for increased cell proliferation in the models, especially after application of therapeutic agents using AnnexinV and Ki-67 assays for apoptosis and proliferation, respectively.

The models could be made more clinically relevant by substituting AM-1 cells for either explanted

ameloblastoma cells, obtained from tumours or from e.g. the ameloblastoma cell bank at the University of Birmingham Alabama (Dr Hope Amm, UBA, *personal communication*). Ideally, the models should incorporate patient-derived tumour cells, as these would be the most useful in determining drug responses and establishing relevant organotypic models. This cell substitution may then enable improved comparisons with this model system to clinical data.

It would have been interesting to probe the co-cultures, and in particular the cell-to-cell interactions seen in the HOB + AM-1 cells, for cell type-specific markers and indicators of cell-to-cell contacts (filopodia, invadopodia, actin, markers of cell movement) to determine whether or not the cell populations came in physical contact with each other. Assays could also be used to probe whether the putative contact was due to release of a growth factor of some sort, or whether it was an artefact of the compression process or due to durotaxis.

7.6.3 Further therapeutic agent testing

Finally, the relatively high-throughput models presented here and the high-throughput screening presented elsewhere (Brown et al., 2014; Kurppa et al., 2014; Sweeney et al., 2014) opens doors for various therapies and screenings. This could be personalised, as cells from excised tumours can easily be added to the scaffolds developed here prior to drug therapies and other tests.

In addition to applying Alendronate and Doxycycline to these models based on gene and protein expression results from this study, it would have been interesting to apply some of the BRAF V600E-targeting therapeutic agents, such as Vemurafenib, to the *in vitro* models to test the drugs' efficacy in this model system; as well as the handful of other potential therapeutic agents currently being, or about to be, tested clinically for their effectiveness on ameloblastoma tumours.

The effect of other therapeutic agents such as Denosumab, which is a human monoclonal anti-RANKL antibody, binding to and neutralising RANKL activity (essentially a synthetic OPG), could also be analysed. The long half-life of Denosumab further enables sustained suppression of bone resorption (Kearns et al., 2008). Denosumab is currently used for osteoporosis treatment, and has also been trialled for use in metastatic cancers with bone spread, but it has the potential to be used with other diseases involving aberrant bone turn-over (Body et al., 2006). This could include ameloblastomas, if further experiments indicate that increased osteoclast activation is the main mechanism with which the ameloblastoma tumour invades *in vivo* bone tissue.

For the soft tissue models, other MMP-inhibiting agents could be tested.

7.7 Conclusions

This thesis has described work undertaken to develop two separate organotypic models for the oral tumour ameloblastoma in order to model tumour invasion to and growth in bone tissues as well as soft tissues. Initially, the bone-like scaffolds were characterised, and it was found that the collagen and Bio-Oss composite

scaffold developed here was able to support both HOS and HOB cells, with the cells proliferating within the constructs and mineralising it.

In co-cultures, ameloblastoma cells were found to greatly upregulate RANKL, which is involved in osteoclast activation. Furthermore, some AM-1 cells became more fibroblast-like in prolonged culture with HOS cells. The HOB + AM-1 co-cultures were the only samples in which ameloblastoma invasion towards to bone-like constructs was seen over 14 days.

When AM-1 cells were co-cultured with the gingival soft tissue models developed, a large upregulation of MMP-2 expression was seen in the models. Subsequently, this MMP-2 synthesis was found necessary for AM-1 cells to locally break down their surrounding ECM in order to proliferate and form their characteristic clusters.

The addition of the potential therapeutic agents Alendronate and Doxycycline significantly reduced AM-1 cell proliferation in the co-culture models. This indicates that the co-culture models developed here may also be used to validate therapeutic targets in ameloblastoma tumours in an organotypic setting.

The results presented here are novel in the following aspects:

- Bio-Oss granules and compressed collagen scaffolds were used as a cellularised bone-like matrix.
- The addition of cells to the Bio-Oss granules and collagen scaffolds was found to increase in their mineral content.
- Bio-Oss + collagen *in vitro* constructs were tested for their mechanical properties. The constructs' compressive strength was found to increase with the addition of Bio-Oss.
- Documentation of gingival fibroblast-induced scaffold contraction even when in a compressed environment; previous reports on other fibroblast types do not detail this.
- Culture and maintenance of AM-1 cells in compressed collagen scaffolds for up to 28 days.
- Co-culture of AM-1 cells with another cell type in an organotypic collagen scaffold with either Matrigel or Bio-Oss granules.
- MMP-2 identified as a requirement for successful AM-1 ECM breakdown and tumour cluster growth.
- Successful staining of constructs with the Cell Tracker assay for 14 days, 11 days longer than the limit suggested by the manufacturer.
- Testing of potential therapeutic agents on ameloblastoma tumours using the organotypic cultures, thereby creating the first *in vitro* therapeutic agent testing models for ameloblastoma.
- Reduction of AM-1 cell viability in co-cultures treated with Alendronate and Doxycycline.

The results presented here show that it is possible to develop *in vitro* organotypic models for odontogenic tumours using tissue engineering techniques. If validated *in vivo*, the results presented here could translate

to the clinical setting, as some of the results have been shown to be in line with results obtained by others using ameloblastoma tumour samples. The models developed here have also been shown to enable testing of potential therapeutic targets in an organotypic setting. Furthermore, these models could easily be adapted for modelling other odontogenic tumours and oral cancers, and could also be used for more reliable, organotypic screening of potential therapeutic agents for these.

Bibliography

Abou Neel, E. A., Cheema, U., Knowles, J. C., Brown, R. A., and Nazhat, S. N. (2006). Use of multiple unconfined compression for control of collagen gel scaffold density and mechanical properties. *Soft Matter*, 2(11):986–992.

Aghaloo, T. L., Chaichanasakul, T., Bezouglaia, O., Kang, B., Franco, R., Dry, S. M., Atti, E., and Tetradis, S. (2010). Osteogenic potential of mandibular vs long-bone marrow stromal cells. *Journal of Dental Research*, 89:1293–1298.

Al-Bayaty, H. F., Murti, P. R., Thomson, E. R. E., and Niamat, J. (2002). Soft tissue recurrence of a mandibular ameloblastoma causing facial deformity in the temporal region: Case report. *Journal of Oral and Maxillofacial Surgery*, 60:204–207.

Albini, A. and Sporn, M. B. (2007). The tumour microenvironment as a target for chemoprevention. *Nature Reviews Cancer*, 7(2):139–147.

Alqhatani, N. (2014). The effect of bisphosphonates on hMSCs proliferation and osteogenic differentiation. *Journal of Dental Research*, 93(Special Issue Letter C).

Alves Pereira, K. M., do Amaral, B. A., Martins dos Santos, B. R., Galvao, H. C., Freitas, R. d. A., and de Souza, L. B. (2010). Immunohistochemical expression of e-cadherin and beta-catenin in ameloblastomas and tooth germs. *Oral Surgery Oral Medicine Oral Pathology Oral Radiology and Endodontology*, 109(3):425–431. Times Cited: 4.

Amini, A. R., Laurencin, C. T., and Nukavarapu, S. P. (2012). Bone tissue engineering: Recent advances and challenges. *Crit Rev Biomed Eng.*, 40(5):363–408.

Andisheh-Tadbir, A., Pardis, S., and Ranjbaran, P. (2015). Twist expression in dentigerous cyst, odontogenic keratocyst, and ameloblastoma. *Oral and maxillofacial surgery*, 19(1):103–7.

Arora, H., Setty, S., Pai, K., and Srilatha, P. (2009). Soft tissue recurrence of ameloblastoma. *International Journal Oral Medical Science*, 8(1):60–63.

Astashkina, A. and Grainger, D. W. (2014). Critical analysis of 3-D organoid in vitro cell culture models for high-throughput drug candidate toxicity assessments. *Advanced Drug Delivery Reviews*, 69-70:1–18.

Avelar, R. L., Primo, B. T., Pinheiro-Nogueira, C. B., Studart-Soares, E. C., de Oliveira, R. B., de Medeiros, J. R., and Gonzalez Hernandez, P. A. (2011). Worldwide incidence of odontogenic tumors. *Journal of Craniofacial Surgery*, 22(6):2118–2123.

Bachmann, A. M. and Linfesty, R. L. (2009). Ameloblastoma, solid/multicystic type. *Head and neck pathology*, 3(4):307–9.

Bedi, R. S., Chugh, A., and Pasricha, N. (2010). Ameloblastic carcinoma of maxilla. *National Journal of Maxillofacial Surgery*, 3(1):70–74.

Bello, I., Alanen, K., and Slootweg, P.J. Salo, T. (2009). Alpha-smooth muscle actinin within epithelial islands is predictive of ameloblastic carcinoma. *Oral Oncology*, 45:760–765.

Bhowmick, N. A., Neilson, E. G., and Moses, H. L. (2004). Stromal fibroblasts in cancer initiation and progression. *Nature*, 432(7015):332–337.

Biname, F., Pawlak, G., Roux, P., and Hibner, U. (2010). What makes cells move: requirements and obstacles for spontaneous cell motility. *Molecular Biosystems*, 6(4):648–661.

Bindra, R. S. and Glazer, P. M. (2005). Genetic instability and the tumor microenvironment: towards the concept of microenvironment-induced mutagenesis. *Mutation Research-Fundamental and Molecular Mechanisms of Mutagenesis*, 569(1-2):75–85.

Bitar, M., Brown, R. A., Salih, V., Kidane, A. G., Knowles, J. C., and Nazhat, S. N. (2008). Effect of cell density on osteoblastic differentiation and matrix degradation of biomimetic dense collagen scaffolds. *Biomacromolecules*, 9(1):129–135.

Bitar, M., Salih, V., Brown, R. A., and Nazhat, S. N. (2007). Effect of multiple unconfined compression on cellular dense collagen scaffolds for bone tissue engineering. *Journal of Materials Science-Materials in Medicine*, 18(2):237–244.

Body, J.-J., Facon, T., Coleman, R. E., Lipton, A., Geurs, F., Fan, M., Holloway, D., Peterson, M. C., and Bekker, P. J. (2006). A study of the biological receptor activator of nuclear factor-kappab ligand inhibitor, denosumab, in patients with multiple myeloma or bone metastases from breast cancer. *Clinical Cancer Research*, 12:1221–1228.

Bologna-Molina, R., Mosqueda-Taylor, A., and Molina-Frechero, N. (2015). Differential expression of glypican-1 in ameloblastoma variants. *Applied Immunohistochemistry & Molecular Morphology*, 23(2):153–160.

Bonzani, I. C., George, J. H., and Stevens, M. M. (2006). Novel materials for bone and cartilage regeneration. *Current Opinion in Chemical Biology*, 10(6):568–575.

Bose, S., Roy, M., and Bandyopadhyay, A. (2012). Recent advances in bone tissue engineering scaffolds. *Trends in Biotechnology*, 30:546–554.

Boyce, B. F. and Xing, L. (2006). Biology of RANK, RANKL, and osteoprotegerin. *Arthritis Research & Therapy*, 9.

Brazis, P. W., Miller, N. R., Lee, A. G., and Holliday, M. J. (1995). Neuro-ophthalmologic aspects of ameloblastoma. *Skull Base Surgery*, 5:233–244.

Brown, N. A. and Betz, B. L. (2015). Ameloblastoma: A review of recent molecular pathogenetic discoveries. *Biomarkers in cancer*, 7(Suppl 2):19–24.

Brown, N. A., Rolland, D., McHugh, J. B., Weigelin, H. C., Zhao, L., Lim, M. S., Elenitoba-Johnson, K. S. J., and Betz, B. L. (2014). Activating FGFR2-RAS-BRAF mutations in ameloblastoma. *Clinical Cancer Research*, 20(21):5517–5526.

Brown, R. A. (2013). In the beginning there were soft collagen-cell gels: towards better 3D connective tissue models? *Experimental Cell Research*, 319(16):2460–2469.

Brown, R. A. and Phillips, J. B. (2007). Cell responses to biomimetic protein scaffolds used in tissue repair and engineering. In *International Review of Cytology*, volume 262, pages 75–150. Academic Press.

Brown, R. A., Wiseman, M., Chuo, C. B., Cheema, U., and Nazhat, S. N. (2005). Ultrarapid engineering of biomimetic materials and tissues: Fabrication of nano- and microstructures by plastic compression. *Advanced Functional Materials*, 15(11):1762–1770.

Buchner, A., Merrell, P. W., and Carpenter, W. M. (2006). Revelative frequency of central odontogenic tumors: A study of 1,088 cases from northern california and comparison to studies from other parts of the world. *Journal of Oral and Maxillofacial Surgery*, 64(9):1343–1352.

Burdett, E., Kasper, F. K., Mikos, A. G., and Ludwig, J. A. (2010). Engineering tumors: A tissue engineering perspective in cancer biology. *Tissue Engineering Part B-Reviews*, 16(3):351–359.

Buxton, P. G., Bitar, M., Gellynck, K., Parkar, M., Brown, R. A., Young, A. M., Knowles, J. C., and Nazhat, S. N. (2008). Dense collagen matrix accelerates osteogenic differentiation and rescues the apoptotic response to MMP inhibition. *Bone*, 43(2):377–385.

Cargnello, M. and Roux, P. P. (2011). Activation and function of the MAPKs and their substrates, the MAPK-activated protein kinases. *Microbiology and Molecular Biology Reviews*, 75(1):50–83.

Carinci, F., Francioso, F., Piattelli, A., Rubini, C., Fioroni, M., Evangelisti, R., Arcelli, D., Tosi, L., Pezzetti, F., Carinci, P., and Volinia, S. (2003). Genetic expression profiling of six odontogenic tumors. *Journal of Dental Research*, 82(7):551–557. Times Cited: 17.

Carinci, F., Palmieri, A., Delaiti, G., Rubini, C., Fioroni, M., Martinelli, M., Pezzetti, F., Scapoli, L., and Piattelli, A. (2004). Expression profiling of ameloblastic carcinoma. *Journal of Craniofacial Surgery*, 15(2):264–269. Times Cited: 10.

Carmagnola, D., Berglundh, T., Araujo, M., Albrektsson, T., and Lindhe, J. (2000). Bone healing around implants placed in a jaw defect augmented with Bio-Oss - an experimental study in dogs. *Journal of Clinical Periodontology*, 27(11):799–805.

Carmeliet, P. and Jain, R. K. (2000). Angiogenesis in cancer and other diseases. *Nature*, 407(6801):249–257.

Caton, J., Mitsiadis, T. A., and Morgan, P. R. (2012). In vitro studies on odontogenic tumors. *Odontogenesis: Methods and Protocols, Methods in Molecular Biology, (ed. Chrissa Kioussi*, 887:167–177.

Cawson, R. A. and Odell, E. W., editors (2008). *Cawson's Essentials of oral pathology and oral medicine*, book section Odontogenic tumours and tumour-like lesions of the jaws, pages 136–140. Churchill Livingstone, London, 8th edition.

Cen, L., Liu, W., Cui, L., Zhang, W. J., and Cao, Y. L. (2008). Collagen tissue engineering: Development of novel biomaterials and applications. *Pediatric Research*, 63(5):492–496.

Chae, M. P., Smoll, N. R., Hunter-Smith, D. J., and Rozen, W. M. (2015). Establishing the natural history and growth rate of ameloblastoma with implications for management: Systematic review and meta-analysis. *PLoS ONE*, 10(2).

Chantravekin, Y. and Koontongkaew, S. (2014). Effects of ameloblastomaassociated broblasts on the proliferation and invasion of tumor cells. *Journal of Cancer Research and Therapeutics*, 10:1082–1087.

Chapelle, K., Stoelinga, P. J. W., de Wilde, P. C. M., Brouns, J. J. A., and Voorsmit, R. (2004). Rational approach to diagnosis and treatment of ameloblastomas and odontogenic keratocysts. *British Journal of Oral & Maxillofacial Surgery*, 42(5):381–390.

Chaudhry, S. I., Hooper, S., Nye, E., Williamson, P., Harrington, K., and Sahai, E. (2013). Autocrine IL-1 beta-TRAF6 signalling promotes squamous cell carcinoma invasion through paracrine INF alpha, signalling to carcinoma-associated fibroblasts. *Oncogene*, 32(6):747–758.

Che, Z. M., Jung, T. H., Choi, J. H., Yoon, D. J., Jeong, H. J., Lee, E. J., and Kim, J. (2006). Collagen-based co-culture for invasive study on cancer cells-fibroblasts interaction. *Biochemical and Biophysical Research Communications*, 346(1):268–275. Times Cited: 23 24.

Cheema, U., Chuo, C. B., Sarathchandra, P., Nazhat, S. N., and Brown, R. A. (2007). Engineering functional collagen scaffolds by mechanical loading. *Tissue Engineering*, 13(7):1688–1688.

Cheema, U., Yang, S. Y., Mudera, V., Goldspink, G. G., and Brown, R. A. (2003). 3-D in vitro model of early skeletal muscle development. *Cell Motility and the Cytoskeleton*, 54(3):226–236.

Chen, C. S., Tan, J., and Tien, J. (2004). Mechanotransduction at cell-matrix and cell-cell contacts. *Annual Review of Biomedical Engineering*, 6:275–302.

Chen, L., Xiao, Z., Meng, Y., Zhao, Y., Han, J., Su, G., Chen, B., and Dai, J. (2012). The enhancement of cancer stem cell properties of MCF-7 cells in 3D collagen scaffolds for modeling of cancer and anti-cancer drugs. *Biomaterials*, 33(5).

Chioni, A.-M. and Grose, R. (2008). Organotypic modelling as a means of investigating epithelial-stromal interactions during tumourigenesis. *Fibrogenesis & tissue repair*, 1(1):8–18.

Cirri, P. and Chiarugi, P. (2011). Cancer associated fibroblasts: the dark side of the coin. *American journal of cancer research*, 1(4):482–97.

Coleman, H., Altini, M., Ali, H., Doglioni, C., Favia, G., and Maiorano, E. (2001). Use of calretinin in the differential diagnosis of unicystic ameloblastomas. *Histopathology*, 38(4):312–317. Times Cited: 16.

Comoglio, P. M. and Trusolino, L. (2005). Cancer: the matrix is now in control. *Nature Medicine*, 11(11):1156–1159.

Coyac, B., Chicatun, F., Hoac, B., Nelea, V., Chaussain, C., Nazhat, S., and McKee, M. (2013). Mineralization of dense collagen hydrogel scaffolds by human pulp cells. *Journal of Dental Research*, 92:648–654.

Crivelini, M. M., Felipini, R. C., Miyahara, G. I., and Orsini Machado de Sousa, S. C. (2012). Expression of odontogenic ameloblast-associated protein, amelotin, ameloblastin, and amelogenin in odontogenic tumors: immunohistochemical analysis and pathogenetic considerations. *Journal of Oral Pathology & Medicine*, 41(3).

Crouch, S., Kozlowski, R., Slater, K., and Fletcher, J. (1993). The use of ATP bioluminescence as a measure of cell proliferation and cytotoxicity. *Journal of Immunological Methods*, 160:81–88.

Cully, M., You, H., Levine, A. J., and Mak, T. W. (2006). Beyond PTEN mutations: the PI3K pathway as an integrator of multiple inputs during tumorigenesis. *Nature Reviews Cancer*, 6:184–192.

Curran, S. and Murray, G. I. (2000). Matrix metalloproteinases: molecular aspects of their roles in tumour invasion and metastasis. *European Journal of Cancer*, 36(13):1621–1630.

Currey, J. D. (2002). *R. Huiskes: The Structure of Bone Tissue*. Bones: structure and mechanics. Second edition. Princeton University Press.

da Costa, N. M. M., Fialho, A. D. V., Proietti, C. C., da Silva Kataoka, M. S., Jaeger, R. G., de Alves-Junior, S. M., and de Jesus Viana Pinheiro, J. (2016). Role of hypoxia-related proteins in invasion of ameloblastoma cells: crosstalk between NOTCH1, hypoxia-inducible factor 1α, a disintegrin and metalloproteinase 12, and heparin-binding epidermal growth factor. *Histopathology*.

Dandriyal, R., Gupta, A., Pant, S., and Baweja, H. H. (2011). Surgical management of ameloblastoma: Conservative or radical approach. *National Journal of Maxillofacial Surgery*, 2:22–27.

Dashti, A., Ready, D., Salih, V., Knowles, J. C., Barralet, J. E., Wilson, M., Donos, N., and Nazhat, S. N. (2010). In vitro antibacterial efficacy of tetracycline hydrochloride adsorbed onto Bio-Oss bone graft. *Journal of Biomedical Materials Research Part B-Applied Biomaterials*, 93B(2):394–400.

de Souza Andrade, E. S., da Costa Miguel, M. C., Freitas, R. d. A., Pinto, L. P., and de Souza, L. B. (2008). Immunoexpression of integrins in ameloblastoma, adenomatoid odontogenic tumor, and human tooth germs. *International Journal of Surgical Pathology*, 16(3):277–285.

De Wever, O., Hendrix, A., De Boeck, A., Westbroek, W., Braems, G., Emami, S., Sabbah, M., Gespach, C., and Bracke, M. (2010). Modeling and quantification of cancer cell invasion through collagen type I matrices. *International Journal of Developmental Biology*, 54(5):887–896.

Deakin, A. S. (1975). Model for growth of a solid invitro tumor. *Growth*, 39(1):159–165.

Degidi, M., Daprile, G., Nardi, D., and Piattelli, A. (2013). Buccal bone plate in immediately placed and restored implant with Bio-Oss collagen graft: a 1-year follow-up study. *Clinical Oral Implants Research*, 24(11):1201–1205.

Dellinger, M. and Geze, M. (2001). Detection of mitochondrial DNA in living animal cells with fluorescence microscopy. *Journal of Microscopy-Oxford*, 204:196–202.

DeVilliers, P., Suggs, C., Simmons, D., Murrah, V., and Wright, J. T. (2011). Microgenomics of ameloblastoma. *Journal of Dental Research*, 90(4):463–469.

Diniz, M. G., Gomes, C. C., Antonini Guimaraes, B. V., Castro, W. H., Tanos Lacerda, J. C., Cardoso, S. V., de Faria, P. R., Dias, F. L., Amaral Eisenberg, A. L., Loyola, A. M., and Gomez, R. S. (2015). Assessment of BRAFV600E and SMOF412E mutations in epithelial odontogenic tumours. *Tumor Biology*, 36(7):5649–5653.

Discher, D. E., Janmey, P., and Wang, Y. L. (2005). Tissue cells feel and respond to the stiffness of their substrate. *Science*, 310(5751):1139–1143.

Domaschke, H., Gelinsky, M., Burmeister, B., Fleig, R., Hanke, T., Reinstorf, A., Pompe, W., and Rosen-Wolff, A. (2006). In vitro ossification and remodeling of mineralized collagen I scaffolds. *Tissue Engineering*, 12(4):949–958.

Egeblad, M. and Werb, Z. (2002). New functions for the matrix metalloproteinases in cancer progression. *Nature Reviews Cancer*, 2(3):161–174.

Fassett, J., Tobol, D., , and Hansen, L. K. (2006). Type I collagen structure regulates cell morphology and EGF signaling in primary rat hepatocytes through cAMP-dependent Protein Kinase A. *Molecular Biology of the Cell*, 17:345–356.

Ferretti, C., Polakow, R., and Coleman, H. (2000). Recurrent ameloblastoma: Report of 2 cases. *Journal of Oral and Maxillofacial Surgery*, 58(7):800–804.

Fisher, J. E., Rogers, M. J., Halasy, J. M., Luckman, S. P., Hughes, D. E., Masarachia, P. J., Wesolowski, G., Russell, R. G. G., Rodan, G. A., and Reszka, A. A. (1999). Alendronate mechanism of action: geranylgeraniol, an intermediate in the mevalonate pathway, prevents inhibition of osteoclast formation, bone resorption, and kinase activation in vitro. *Proceedings of the National Academy of Sciences of the United States of America*, 96(1):133–138.

Fisher, J. E., Rosenberg, E., Santora, A. C., and Reszka, A. A. (2013). In vitro and in vivo responses to high and low doses of nitrogen-containing bisphosphonates suggest engagement of different mechanisms for inhibition of osteoclastic bone resorption. *Calcified Tissue International*, 92(6):531–538.

Foroodi, F., Duivenvoorden, W. C., and Singh, G. (2009). Interactions of doxycycline with chemotherapeutic agents in human breast adenocarcinoma MDA-MB-231 cells. *Anti-Cancer Drugs*, 20(2):115–122.

Friedl, P. and Brocker, E. B. (2000). The biology of cell locomotion within three-dimensional extracellular matrix. *Cellular and Molecular Life Sciences*, 57(1):41–64.

Friedrich, J., Seidel, C., Ebner, R., and Kunz-Schughart, L. A. (2009). Spheroid-based drug screen: considerations and practical approach. *Nature Protocols*, 4(3):309–324.

Froehlich, M., Grayson, W. L., Wan, L. Q., Marolt, D., Drobnic, M., and Vunjak-Novakovic, G. (2008). Tissue engineered bone grafts: Biological requirements, tissue culture and clinical relevance. *Current Stem Cell Research & Therapy*, 3(4).

Fuchigami, T., Kibe, T., Koyama, H., Kishida, S., Iijima, M., Nishizawa, Y., Hijioka, H., Fujii, T., Ueda, M., Nakamura, N., Kiyono, T., and Kishida, M. (2014). Regulation of IL-6 and IL-8 production by reciprocal cell-to-cell interactions between tumor cells and stromal fibroblasts through IL-1-alpha in ameloblastoma. *Biochemical and Biophysical Research Communications*, 451(4):491–496.

Furuta, H., Osawa, K., Shin, M., Ishikawa, A., Matsuo, K., Khan, M., Aoki, K., Ohya, K., Okamoto, M., Tominaga, K., Takahashi, T., Nakanishi, O., and Jimi, E. (2012). Selective inhibition of NF-kappa B suppresses bone invasion by oral squamous cell carcinoma in vivo. *International Journal of Cancer*, 131(5):E625–E635.

Gadbail, A. R., Patil, R., and Chaudhary, M. (2012). Co-expression of Ki-67 and p53 protein in ameloblastoma and keratocystic odontogenic tumor. *Acta Odontologica Scandinavica*, 70(6).

Galois, L., Hutasse, S., Cortial, D., Rousseau, C. F., Grossin, L., Ronziere, M.-C., Herbage, D., and Freyria, A.-M. (2006). Bovine chondrocyte behaviour in three-dimensional type I collagen gel in terms of gel contraction, proliferation and gene expression. *Biomaterials*, 27:79–90.

Gardner, D. G. (1984). A pathologist's approach to the treatment of ameloblastoma. *Journal of Oral and Maxillofacial Surgery*, 42(42):161–166.

Gardner, D. G., Heikinheimo, K., Shear, M., Philipsen, H. P., Coleman, H., and Barnes, E. (2005). *Pathology & Genetics of Head and Neck Tumours; section Ameloblastomas*, volume 65 of *World Health Organisation publications*, pages 296–299. World Health Organization Press, Geneva Switzerland.

Gareau, D. S., Bargo, P. R., Horton, W. A., and Jacques, S. L. (2004). Confocal fluorescence spectroscopy of subcutaneous cartilage expressing green fluorescent protein versus cutaneous collagen autofluorescence. *Journal of Biomedical Optics*, 9(2):254–258.

Garnett, M. J. and Marais, R. (2004). Guilty as charged: B-RAF is a human oncogene. *Cancer Cell*, 6(4):313–319.

Gartland, A., Buckley, K. A., Dillon, J. P., Curran, J. M., Hunt, J. A., and Gallagher, J. A. (2005). Isolation and culture of human osteoblasts. *Methods in molecular medicine*, 107:29–54.

Gartland, A., Orriss, I. R., Rumney, R. M. H., Bond, A. P., Arnett, T., and Gallagher, J. A. (2012a). Purinergic signalling in osteoblasts. *Frontiers in Bioscience-Landmark*, 17:16–29.

Gartland, A., Rumney, R. M. H., Dillon, J. P., and Gallagher, J. A. (2012b). *Isolation and Culture of Human Osteoblasts*, volume 806 of *Methods in Molecular Biology*, pages 337–355. Springer Protocols, Humana Press.

Gertz, B., Holland, S., Kline, W., Matuszewski, B., and Porras, A. (1993). Clinical pharmacology of alendronate sodium. *Osteoporosis International*, 3(Suppl 3):13–16.

Ghajar, C. M. and Bissell, M. J. (2010). Tumor engineering: The other face of tissue engineering. *Tissue Engineering Part A*, 16:2153–2156.

Ghosh, K. and Ingber, D. E. (2007). Micromechanical control of cell and tissue development: Implications for tissue engineering. *Advanced Drug Delivery Reviews*, 59(13):1306–1318.

Ghosh, S. and Karin, M. (2002). Missing pieces in the NF-kappa B puzzle. *Cell*, 109:S81–S96.

Gill, B. J. and West, J. L. (2014). Modeling the tumor extracellular matrix: Tissue engineering tools repurposed towards new frontiers in cancer biology. *Journal of Biomechanics*, 47(9):1969–1978.

Goktas, S., Dmytryk, J., and McFetridge, P. S. (2011). Biomechanical behaviour of oral soft tissues. *Journal of Periodontology*, 82:1178–1186.

Gomes, C. C., Duarte, A. P., Diniz, M. G., and Gomez, R. S. (2010). Current concepts of ameloblastoma pathogenesis. *Journal of Oral Pathology & Medicine*, 39(8):585–591.

Gonzalez-Alva, P., Tanaka, A., Oku, Y., Miyazaki, Y., Okamoto, E., Fujinami, M., Yoshida, N., Kikuchi, K., Ide, F., Sakashita, H., and Kusama, K. (2010). Enhanced expression of podoplanin in ameloblastomas. *Journal of Oral Pathology & Medicine*, 39(1):103–109.

Gorska, R. and Nedzi-Gora, M. (2006). The effects of the initial treatment phase and of adjunctive low-dose doxycycline therapy on clinical parameters and MMP-8, MMP-9, and TIMP-1 levels in the saliva and peripheral blood of patients with chronic periodontitis. *Archivum Immunologiae Et Therapiae Experimentalis*, 54(6):419–426.

Griffith, L. G. and Swartz, M. A. (2006). Capturing complex 3D tissue physiology in vitro. *Nature Reviews Molecular Cell Biology*, 7(3):211–224.

Grinnell, F. (2003). Fibroblast biology in three-dimensional collagen matrices. *Trends in Cell Biology*, 13(5):264–269.

Gurgel, C. A. S., Ramos, E. A. G., Buim, M. E. C., Carvalho, K. C., Schlaep-der Sales, C. B., Souza, R. O., Soares, F. A., and Santos, J. N. (2010). Gene expression of sonic hedgehog molecules, D1 cyclin and BCL2 in keratocystic odontogenic tumor and ameloblastoma. *Histopathology*, 57.

Hadjipanayi, E., Mudera, V., and Brown, R. A. (2008). 3D durotaxis within a collagen matrix. *Tissue Engineering Part A*, 14(5):799.

Hadjipanayi, E., Mudera, V., and Brown, R. A. (2009). Guiding cell migration in 3D: A collagen matrix with graded directional stiffness. *Cell Motility and the Cytoskeleton*, 66(3):121–128.

Hakanson, M., Cukierman, E., and Charnley, M. (2014). Miniaturized pre-clinical cancer models as research and diagnostic tools. *Advanced Drug Delivery Reviews*, 69-70:52–66.

Hanemaaijer, R., Visser, H., Koolwijk, P., Sorsa, T., Salo, T., and Golub, L. (1998). Inhibition of MMP synthesis by doxycycline and chemically modified tetracyclines (CMTs) in human endothelial cells. *Advances in Dental Research*, 12:114–118.

Harada, H., Mitsuyasu, T., Nakamura, N., Higuchi, Y., Toyoshima, K., Taniguchi, A., and Yasumoto, S. (1998). Establishment of ameloblastoma cell line, AM-1. *Journal of Oral Pathology & Medicine*, 27(5).

Harjanto, D. and Zaman, M. H. (2009). Matrix mechanics and receptorligand interactions in cell adhesion. *Organic & Biomolecular Chemistry*, 8:299–304.

Hartman, G. A., Arnold, R. M., Mills, M. P., Cochran, D. L., and Mellonig, J. T. (2004). Clinical and histologic evaluation of anorganic bovine bone collagen with or without a collagen barrier. *The International journal of periodontics & restorative dentistry*, 24(2):127–35.

Hasseil, T. M. and Stanek, E. J. (1983). Evidence that healthy human gingiva contains functionally heterogeneous fibroblast subpopulations. *Archives of Oral Biology*, 28(617).

Hayes, A. J., Hughes, C. E., and Caterson, B. (2008). Antibodies and immunohistochemistry in extracellular matrix research. *Methods*, 45:10–21.

Heikinheimo, K., Jee, K. J., Niini, T., Aalto, Y., Happonen, R. P., Leivo, I., and Knuutila, S. (2002). Gene expression profiling of ameloblastoma and human tooth germ by means of a cDNA microarray. *Journal of Dental Research*, 81(8):525–530.

Heikinheimo, K., Kurppa, K. J., and Elenius, K. (2015). Novel targets for the treatment of ameloblastoma. *Journal of Dental Research*, 94(2):237–240.

Hendarmin, L., Kawano, S., Yoshiga, D., Sandra, F., Mitsuyasu, T., Nakao, Y., Higuchi, Y., Nakamura, N., and Nakamura, S. (2008). An anti-apoptotic role of NF-KB in TNFα-induced apoptosis in an ameloblastoma cell line. *Oral Science International*, pages 96–103.

Hendarmin, L., Sandra, F., Nakao, Y., Ohishi, M., and Nakamura, N. (2005). TNF alpha played a role in induction of Akt and MAPK signals in ameloblastoma. *Oral Oncology*, 41(4):375–382.

Hirschhaeuser, F., Menne, H., Dittfeld, C., West, J., Mueller-Klieser, W., and Kunz-Schughart, L. A. (2010). Multicellular tumor spheroids: An underestimated tool is catching up again. *Journal of Biotechnology*, 148(1):3–15.

Hirshberg, A. and Buchner, A. (1995). Metastatic tumours to the oral region. an overview. *Oral Oncology-European Journal of Cancer Part B*, 31B(6):355–360.

Hofbauer, L. C. and Heufelder, A. E. (2000). The role of receptor activator of nuclear factor-kappa B ligand and osteoprotegerin in the pathogenesis and treatment of metabolic bone diseases. *Journal of Clinical Endocrinology & Metabolism*, 85(7):2355–2363.

Holy, C. E., Stoichet, M. S., and Davies, J. E. (2000). Engineering three-dimensional bone tissue in vitro using biodegradable scaffolds: Investigating initial cell-seeding density and culture period. *Journal of Biomedical Materials Research*, 5:376–382.

Horie, M., Saito, A., Mikami, Y., Ohshima, M., Morishita, Y., Nakajima, J., Kohyama, T., and Nagase, T. (2012). Characterization of human lung cancer-associated fibroblasts in three-dimensional in vitro co-culture model. *Biochemical and Biophysical Research Communications*, 423(1).

Hubbell, J. A. (2003). Materials as morphogenetic guides in tissue engineering. *Current Opinion in Biotechnology*, 14(5):551–558.

Hughes, C. S., Postovit, L. M., and Lajoie, G. A. (2010). Matrigel: A complex protein mixture required for optimal growth of cell culture. *Proteomics*, 10:1886–1890.

Hutmacher, D. W. (2000). Scaffolds in tissue engineering bone and cartilage. *Biomaterials*, 21(24):2529–2543.

Hynes, R. O. (2009). The extracellular matrix: Not just pretty fibrils. *Science*, 326:1216–1219.

Iakovou, M., Chrysomali, E., Piperi, E., Fanourakis, G., Sklavounou, A., Vlachodimitropoulos, D., and Tseleni-Balafouta, S. (2015). A comparative study of bone remodeling molecules expression in different types of jaw ameloblastoma. *Journal of Oral Pathology and Medicine*, 44:543–551.

Iezzi, G., Piattelli, A., Rubini, C., Artese, L., Goteri, G., Perrotti, V., and Carinci, F. (2008). Expression of transforming growth factor beta-1 in ameloblastomas. *Journal of Craniofacial Surgery*, 19(6):1618–1621.

Imamura, K., Ozawa, H., Hiraide, T., Takahashi, N., Shibasaki, Y., Fukuhara, T., and Suda, T. (1990). Continuously applied compressive pressure induces bone-resorption by a mechanism involving prostaglandin-E2 synthesis. *Journal of Cellular Physiology*, 144(2):222–228.

Iyer, R. K., Chiu, L. L. Y., and Radisic, M. (2009). Microfabricated poly(ethylene glycol) templates enable rapid screening of triculture conditions for cardiac tissue engineering. *Journal of Biomedical Materials Research Part A*, 89A(3):616–631.

Jaaskelainen, K., Jee, K. J., Leivo, I., Saloniemi, I., Knuutila, S., and Heikinheimo, K. (2002). Cell proliferation and chromosomal changes in human ameloblastoma. *Cancer Genetics and Cytogenetics*, 136(1):31–37.

Jamshidi, F., Nielsen, T. O., and Huntsman, D. G. (2008). Can cancer be reversed by engineering the tumor microenvironment? *Seminars in Cancer Biology*, 18:356–364.

Jamshidi, F., Nielsen, T. O., and Huntsman, D. G. (2015). Cancer genomics: why rare is valuable. *Journal of Molecular Medicine*, 93:369–381.

Jayakumar, P. and Di Silvio, L. (2010). Osteoblasts in bone tissue engineering. *Proceedings of the Institution of Mechanical Engineers Part H-Journal of Engineering in Medicine*, 224(H12).

Jimi, E., Furuta, H., Matsuo, K., Tominaga, K., Takahashi, T., and Nakanishi, O. (2011). The cellular and molecular mechanisms of bone invasion by oral squamous cell carcinoma. *Oral Diseases*, 17(5):462–468.

Kalluri, R. and Zeisberg, M. (2006). Fibroblasts in cancer. *Nature Reviews Cancer*, 6(5):392–401.

Kanda, S., Mitsuyasu, T., Nakao, Y., Kawano, S., Goto, Y., Matsubara, R., and Nakamura, S. (2013). Anti-apoptotic role of the sonic hedgehog signaling pathway in the proliferation of ameloblastoma. *International Journal of Oncology*, 43(3):695–702.

Karamichos, D., Brown, R. A., and Mudera, V. (2007). Collagen stiffness regulates cellular contraction and matrix remodeling gene expression. *Journal of Biomedical Materials Research Part A*, 83A(3):887–894.

Karin, M. (2006). Nuclear factor-kappa B in cancer development and progression. *Nature*, 441(7092):431–436.

Katagiri, T., Yamaguchi, A., Komaki, M., Abe, E., Takahashi, N., Ikeda, T., Rosen, V., Wozney, J. M., Fujisawa-Sehara, A., and Suda, T. (1994). Bone morphogenic protein-2 converts the differentiation pathway of C2C12 myoblasts into the osteoblast lineage. *Journal of Cell Biology*, 127(6):1755–1766.

Kawabata, T., Takahashi, K., Sugai, M., Murashima-Suginami, A., Ando, S., Shimizu, A., Kosugi, S., Sato, T., Nishida, M., Murakami, K., and Iizuka, T. (2005). Polymorphisms in PTCH1 affect the risk of ameloblastoma. *Journal of Dental Research*, 84(9).

Kaye, F. J., Ivey, A. M., Drane, W. E., Mendenhall, W. M., and Allan, R. W. (2015). Clinical and radiographic response with combined BRAF-targeted therapy in stage 4 ameloblastoma. *Journal of the National Cancer Institute*, 107(1):378–378.

Kearns, A. E., Khosla, S., and Kostenuik, P. J. (2008). Receptor activator of nuclear factor kappa b ligand and osteoprotegerin regulation of bone remodeling in health and disease. *Endocrine Reviews*, 29(2):155–192.

Keller, R. K. and Fliesler, S. J. (1999). Mechanism of aminobisphosphonate action: Characterization of alendronate inhibition of the isoprenoid pathway. *Biochemical and Biophysical Research Communications*, 266(2):560–563.

Kerr, J. F. R., Wyllie, A. H., and Currie, A. R. (1972). Apoptosis - basic biological phenomenon with wide-ranging implications in tissue kinetics. *British Journal of Cancer*, 26(4):239.

Kessenbrock, K., Plaks, V., and Wer, Z. (2010). Matrix metalloproteinases: Regulators of the tumor microenvironment. *Cell*, 141:52–67.

Kibe, T., Fuchigami, T., Kishida, M., Iijima, M., Ishihata, K., Hijioka, H., Miyawaki, A., Semba, I., Nakamura, N., Kiyono, T., and Kishida, S. (2013). A novel ameloblastoma cell line (AM-3) secretes MMP-9 in response to Wnt-3a and induces osteoclastogenesis. *Oral Surgery Oral Medicine Oral Pathology Oral Radiology*, 115(6):780–788.

Kim, H. W., Kim, H. E., and Salih, V. (2005). Stimulation of osteoblast responses to biomimetic nanocomposites of gelatin-hydroxyapatite for tissue engineering scaffolds. *Biomaterials*, 26(25):5221–5230.

Kim, J. B., Stein, R., and OHare, M. J. (2004). Three-dimensional in vitro tissue culture models of breast cancer - a review. *Breast Cancer Research and Treatment*, 85:281–291.

Kim, Y. S. and Lee, S. K. (2014). Different protein expressions between peripheral ameloblastoma and oral basal cell carcinoma occurred at the same mandibular molar area. *Korean journal of pathology*, 48(2):151–8.

Kiyoshima, T., Nagata, K., Wada, H., Fujiwara, H., Shiotsuka, M., Kihara, M., Hasegawa, K., Someya, H., and Sakai, H. (2013). Immunohistochemical expression of thymosin beta 4 in ameloblastomas and odontomas. *Histology and Histopathology*, 28(6):775–786.

Klapsinou, E., Stavros, A., Smaragda, A., Despoina, P., and Dimitra, D. (2013). Fine-needle aspiration cytology of ameloblastoma and malignant ameloblastoma: A study of 12 cases. *Diagnostic Cytopathology*, 41(3):206–211.

Kleinman, H. K. and Martin, G. R. (2005). Matrigel: Basement membrane matrix with biological activity. *Seminars in Cancer Biology*, 15(5):378–386.

Koh, C. J. and Atala, A. (2004). Tissue engineering, stem cells, and cloning: Opportunities for regenerative medicine. *Journal of the American Society of Nephrology*, 15(5):1113–1125.

Koukourakis, G. V., Miliadou, A., and Sotiropoulou-Lontou, A. (2011). Ameloblastoma, a rare benign odontogenic tumour: an interesting tumour review targeting the role of radiation therapy. *Clinical & Translational Oncology*, 13(11).

Kranz, S. (2015). Metastatic ameloblastoma to a cervical lymph node: A case report and review of literature. *Pathology - Journal of the RCPA*, 47.

Kumamoto, H., Izutsu, T., Ohki, K., Takahashi, N., and Ooya, K. (2004a). p53 gene status and expression of p53, MDM2, and p14(ARF) proteins in ameloblastomas. *Journal of Oral Pathology & Medicine*, 33(5):292–299.

Kumamoto, H., Ohki, K., and Ooya, K. (2004b). Expression of sonic hedgehog (SHH) signaling molecules in ameloblastomas. *Journal of Oral Pathology & Medicine*, 33:185–190.

Kumamoto, H. and Ooya, K. (1999). Expression of E-cadherin and alpha-catenin in epithelial odontogenic tumors: an immunohistochemical study. *Journal of Oral Pathology & Medicine*, 28(4):152–157.

Kumamoto, H. and Ooya, K. (2004). Expression of parathyroid hormone-related protein (PTHrP), osteoclast differentiation factor (ODF)/receptor activator of nuclear factor-kappa b ligand (RANKL) and osteoclastogenesis inhibitory factor (OCIF)/osteoprotegerin (OPG) in ameloblastomas. *Journal of Oral Pathology & Medicine*, 33(1):46–52.

Kumamoto, H. and Ooya, K. (2005). Immunohistochemical detection of beta-catenin and adenomatous polyposis coli in ameloblastomas. *Journal of Oral Pathology & Medicine*, 34(7):401–406.

Kumamoto, H. and Ooya, K. (2007a). Immunohistochemical detection of phosphorylated Akt, PI3K, and PTEN in ameloblastic tumors. *Oral Diseases*, 13(5):461–467.

Kumamoto, H. and Ooya, K. (2007b). Immunohistochemical detection of phosphorylated JNK, p38, MAPK, and ERK5 in ameloblastic tumors. *Journal of Oral Pathology & Medicine*, 36(9):543–549.

Kumamoto, H., Yamauchi, K., Yoshida, M., and Ooya, K. (2003). Immunohistochemical detection of matrix metalloproteinases (MMPs) and tissue inhibitors of metalloproteinases (TIMPs) in ameloblastomas. *Journal of Oral Pathology & Medicine*, 32(2):114–120.

Kurppa, K. J., Caton, J., Morgan, P. R., Ristimaki, A., Ruhin, B., Kellokoski, J., Elenius, K., and Heikinheimo, K. (2014). High frequency of BRAF V600E mutations in ameloblastoma. *Journal of Pathology*, 232(5):492–498.

LaBarge, M. A., Parvin, B., and Lorens, J. B. (2014). Molecular deconstruction, detection, and computational prediction of microenvironment-modulated cellular responses to cancer therapeutics. *Advanced Drug Delivery Reviews*, 69-70:123–131.

Langer, R. and Vacanti, J. P. (1993). Tissue engineering. *Science*, 260(5110):920–926.

Langley, R. R. and Fidler, I. J. (2011). The seed and soil hypothesis revisited - the role of tumor-stroma interactions in metastasis to different organs. *International Journal of Cancer*, 128:2527–2535.

Levenberg, S., Rouwkema, J., Macdonald, M., Garfein, E. S., Kohane, D. S., Darland, D. C., Marini, R., van Blitterswijk, C. A., Mulligan, R. C., D'Amore, P. A., and Langer, R. (2005). Engineering vascularized skeletal muscle tissue. *Nature Biotechnology*, 23(7):879–884.

Liang, Q.-X., Liang, Y.-C., Xu, Z.-Y., Chen, W.-L., Xie, H.-L., and Zhang, B. (2014). RECK overexpression reduces invasive ability in ameloblastoma cells. *Journal of Oral Pathology & Medicine*, 43(8):613–618.

Lim, J., Ahn, H., Min, S., Hong, S. D., Lee, J. I., and Hong, S. P. (2006). Oligonucleotide microarray analysis of ameloblastoma compared with dentigerous cyst. *Journal of Oral Pathology & Medicine*, 35(5):278–285.

Lin, Y., He, J.-F., Li, Z.-Y., and Liu, J.-H. (2014). Ameloblastoma with varied sites of metastasis: Report of two cases and literature review. *Journal of Cranio-Maxillofacial Surgery*, 42(5):E301–E304.

Linde, N., Gutschalk, C. M., Hoffmann, C., Yilmaz, D., and Mueller, M. M. (2012). Integrating macrophages into organotypic co-cultures: A 3D in vitro model to study tumor-associated macrophages. *Plos One*, 7(7).

Linnes, M. P., Ratner, B. D., and Giachelli, C. M. (2007). A fibrinogen-based precision microporous scaffold for tissue engineering. *Biomaterials*, 28:5298–5307.

Lito, P., Rosen, N., and Solit, D. B. (2013). Tumor adaptation and resistance to RAF inhibitors. *Nature Medicine*, 19(11):1401–1409.

Liu, J., Xiong, W. F., Baca-Regen, L., Nagase, H., and Baxter, B. T. (2003). Mechanism of inhibition of matrix metalloproteinase-2 expression by doxycycline in human aortic smooth muscle cells. *Journal of Vascular Surgery*, 38(6):1376–1383.

Liu, Y., Lin, X.-P., Tan, L.-S., and Wei, W. (2006). Construction of tissue engineered bone by osteoblasts from canine bone marrow mesenchymal stem cells and bio-oss: an in vitro study. *Shanghai journal of stomatology*, 15(6):627–631.

Lovett, M., Lee, K., Edwards, A., and Kaplan, D. L. (2009). Vascularization strategies for tissue engineering. *Tissue Engineering Part B-Reviews*, 15(3):353–370.

Lutolf, M. P. and Hubbell, J. A. (2005). Synthetic biomaterials as instructive extracellular microenvironments for morphogenesis in tissue engineering. *Nature Biotechnology*, 23(1):47–55.

MacDonald, B. T., Tamai, K., and He, X. (2009). Wnt / β-catenin signaling: components, mechanisms, and diseases. *Developmental Cell*, 17(1):9–26.

Maehara, Y., Anai, H., Tamada, R., and Sugimachi, K. (1987). The ATP assay is more sensitive than the succinate-dehydrogenase inhibition test for predicting cell viability. *European Journal of Cancer & Clinical Oncology*, 23(3):273–276.

Malda, J., Radisic, M., Levenberg, S., Woodfield, T., Oomens, C., Baaijens, F., Svalander, P., and Vunjak-Novakovic, G. (2008). Cell nutrition. *Tissue Engineering*, pages 327–362.

Mariotti, A. and Cochran, D. L. (1990). Characterization of fibroblasts derived from human periodontal-ligament and gingiva. *Journal of Periodontology*, 61(2):103–111.

Martin, L. J. and Boyd, N. F. (2008). Mammographic density. Potential mechanisms of breast cancer risk associated with mammographic density: hypotheses based on epidemiological evidence. *Breast Cancer Research*, 201, 10(Suppl 1).

Mastrangelo, F., Quaresima, R., Grilli, A., Tettamanti, L., Vinci, R., Sammartino, G., Tete, S., and Gherlone, E. (2013). A comparison of bovine bone and hydroxyapatite scaffolds during initial bone regeneration: an in vitro evaluation. *Implant dentistry*, 22(6):613–22.

McClary, A. C., Sweeney, R. T., Biscocho, J., Meyers, B. R., Neahring, L., Kwei, K. A., Qu, K., Gong, X., Jones, C. D., Varma, S., Odegaard, J. I., Rubin, B., Ng, T., Troxell, M. L., Pelham, R. J., Zehnder, J. L., Beachy, P. A., Pollack, J. R., and West, R. B. (2014). Mutational profiling of ameloblastoma identifies common gain-of-function mutations. *Modern Pathology*, 27:324A.

McMahon, A. P. (2000). More surprises in the hedgehog signaling pathway. *Cell*, 100:185–188.

Meloan, S. N. and Puchtler, H. (1985). Chemical mechanisms of staining methods: Von Kossa's technique: What von Kossa really wrote and a modified reaction for selective demonstration of inorganic phosphates. *Journal of Histotechnology*, 8(1):11–13.

Mendenhall, W. (2011). Neoplasms of the oral cavity - ameloblastoma. In Wenig, B. M., editor, *Atlas of Head and Neck Pathology*, pages 298–308. Quintessence Publishing.

Mendenhall, W. M., Werning, J. W., Fernandes, R., Malyapa, R. S., and Mendenhall, N. P. (2007). Ameloblastoma. *American Journal of Clinical Oncology-Cancer Clinical Trials*, 30(6).

Mishra, P., Panda, A., Bandyopadhyay, A., Kumar, H., and Mohiddin, G. (2015). Sonic hedgehog signalling pathway and ameloblastoma - a review. *Journal of clinical and diagnostic research : JCDR*, 9(11):ZE10–3. 0.

Mistry, A. S. and Mikos, A. G. (2005). Tissue engineering strategies for bone regeneration. *Regenerative Medicine II: Clinical and Preclinical Applications*, 94.

Mitsuyasu, T., Harada, H., Higuchi, Y., Kimura, K., Nakamura, N., Katsuki, T., Kubota, E., Toyoshima, K., and Ohishi, M. (1997). Immunohistochemical demonstration of bcl-2 protein in ameloblastoma. *Journal of Oral Pathology & Medicine*, 26(8):345–348.

Mosqueda-Taylor, A. (2008). New findings and controversies in odontogenic tumors. *Medicina oral, patologia oral y cirugia bucal*, 13(9).

Neves-Silva, R., Fonseca, F. P., de Jesus, A. S., Pontes, H. A. R., Rocha, A. C., Brandao, T. B., Vargas, P. A., Lopes, M. A., de Almeida, O. P., and Santos-Silva, A. R. (2016). Tissue microarray use for immunohistochemical study of ameloblastoma. *Journal of Oral Pathology & Medicine*.

NICE (2008). Alendronate, etidronate, risedronate, raloxifene, strontium ranelate and teriparatide for the secondary prevention of osteoporotic fragility fractures in postmenopausal women. National Institute for Health and Care Excellence - technology appraisal guidance [TA161].

Nomura, T., Katz, J. L., Powers, M. P., and Saito, C. (2005). Evaluation of the micromechanical elastic properties of potential bone-grafting materials. *Journal of Biomedical Materials Research Part B-Applied Biomaterials*, 73B(1):29–34.

Nurmenniemi, S., Sinikumpu, T., Alahuhta, I., Salo, S., Sutinen, M., Santala, M., Risteli, J., Nyberg, P., and Salo, T. (2009). A novel organotypic model mimics the tumor microenvironment. *American Journal of Pathology*, 175(3):1281–1291.

Nyga, A., Cheema, U., and Loizidou, M. (2011). 3D tumour models: novel in vitro approaches to cancer studies. *Journal of cell communication and signaling*, 5(3):239–48.

O'Brien, F. J. (2011). Biomaterials & scaffolds tissue engineering. *Materials Today*, 14:88–95.

Orimo, A. and Weinberg, R. A. (2007). Heterogeneity of stromal fibroblasts in tumors. *Cancer Biology & Therapy*, 6(4):618–619.

Orr, T. E., Villars, P. A., Mitchell, S. L., Hsu, H. P., and Spector, M. (2001). Compressive properties of cancellous bone defects in a rabbit model treated with particles of natural bone mineral and synthetic hydroxyapatite. *Biomaterials*, 22(14):1953–1959.

Pedraza, C. E., Marelli, B., Chicatun, F., McKee, M. D., and Nazhat, S. N. (2010). An in vitro assessment of a cell-containing collagenous extracellular matrix-like scaffold for bone tissue engineering. *Tissue Engineering Part A*, 16(3):781–793.

Perdigao, P. F., Gomez, R. S., Pimenta, F., and De Marco, L. (2004). Ameloblastin gene (AMBN) mutations associated with epithelial odontogenic tumors. *Oral Oncology*, 40(8):841–846.

Philipsen, H. P. and Reichart, P. A. (1998). Unicystic ameloblastoma. a review of 193 cases from the literature. *Oral Oncology*, 34(5):317–325.

Philipsen, H. P. and Reichart, P. A. (2004). *Odontogenic tumours and allied lesions; Section II; Ameloblastomas*, pages 41–86. Quintessence Publishing, Hanover Park, IL, US.

Philipsen, H. P., Reichart, P. A., Nikai, H., Takata, T., and Kudo, Y. (2001a). Peripheral ameloblastoma: biological profile based on 160 cases from the literature. *Oral Oncology*, 37(1):17–27.

Philipsen, H. P., Reichart, P. A., and Takata, T. (2001b). Desmoplastic ameloblastoma (including "hybrid" lesion of ameloblastoma). Biological profile based on 100 cases from the literature and own files. *Oral Oncology*, 37(5):455–460.

Piattelli, M., Favero, G. A., Scarano, A., Orsini, G., and Piattelli, A. (1999). Bone reactions to anorganic bovine bone (Bio-Oss) used in sinus augmentation procedures: A histologic long-term report of 20 cases in humans. *International Journal of Oral & Maxillofacial Implants*, 14(6):835–840.

Pietras, K. and Ostman, A. (2010). Hallmarks of cancer: Interactions with the tumor stroma. *Experimental Cell Research*, 316(8):1324–1331.

Pinheiro, J. J. V., Freitas, V. M., Moretti, A. I. S., Jorge, A. G., and Jaeger, R. G. (2004). Local invasiveness of ameloblastoma. Role played by matrix metalloproteinases and proliferative activity. *Histopathology*, 45(1).

Pinheiro da Rosa, M. R., Carreira Falcao, A. S., Fuzii, H. T., da Silva Kataoka, M. S., Ribeiro, A. L. R., Boccardo, E., de Siqueira, A. S., Jaeger, R. G., Viana Pinheiro, J. d. J., and Alves Junior, S. d. M. (2014). EGFR signaling downstream of EGF regulates migration, invasion, and MMP secretion of immortalized cells derived from human ameloblastoma. *Tumor Biology*, 35(11):11107–11120.

Place, E. S., Evans, N. D., and Stevens, M. M. (2009). Complexity in biomaterials for tissue engineering. *Nature Materials*, 8(6).

Polyak, K., Haviv, I., and Campbell, I. G. (2009). Co-evolution of tumor cells and their microenvironment. *Trends in Genetics*, 25(1):30–38.

Qian, Y. and Huang, H.-Z. (2010). The role of RANKL and MMP-9 in the bone resorption caused by ameloblastoma. *Journal of Oral Pathology & Medicine*, 39(8).

Quan, J., Zhou, C., Johnson, N. W., Francis, G., Dahlstrom, J. E., and Gao, J. (2012). Molecular pathways involved in crosstalk between cancer cells, osteoblasts and osteoclasts in the invasion of bone by oral squamous cell carcinoma. *Pathology*, 44(3):221–227.

Radisic, M., Malda, J., Epping, E., Geng, W. L., Langer, R., and Vunjak-Novakovic, G. (2006). Oxygen gradients correlate with cell density and cell viability in engineered cardiac tissue. *Biotechnology and Bioengineering*, 93(2):332–343.

Radisky, E. and Radisky, D. C. (2010). Matrix metalloproteinase-induced epithelial-mesenchymal transition in breast cancer. *Journal of Mammary Gland Biology and Neoplasia*, 15:201–212.

Rajan, N., Habermehl, J., Cote, M.-F., Doillon, C. J., and Mantovani, D. (2006). Preparation of ready-to-use, storable and reconstituted type I collagen from rat tail tendon for tissue engineering applications. *Nature Protocols*, 1(6):2753–2758.

Ram, H., Mohammad, S., Husain, N., , and Gupta, P. N. (2011). Ameloblastic carcinoma. *Journal of Maxillofacial and Oral Surgery*, 9:415–419.

Rattner, A., Sabido, O., Le, J., Vico, L., Massoubre, C., Frey, J., and Chamson, A. (2000). Mineralization and alkaline phosphatase activity in collagen lattices populated by human osteoblasts. *Calcified Tissue International*, 66:35–42.

Reichart, P. A., Philipsen, H. P., and Sonner, S. (1995). Ameloblastoma - biological profile of 3677 cases. *Oral Oncology - European Journal of Cancer Part B*, 31B(2):86–99.

Rhee, S. and Grinnell, F. (2007). Fibroblast mechanics in 3D collagen matrices. *Advanced Drug Delivery Reviews*, 59:1299–1305.

Ribeiro, B. F., Iglesias, D. P. P., Nascimento, G. J. F., Galvao, H. C., Medeiros, A. M. C., and Freitas, R. A. (2009). Immunoexpression of MMPs-1, -2, and -9 in ameloblastoma and odontogenic adenomatoid tumor. *Oral Diseases*, 15(7):472–477.

Richardson, N., Mordan, N. J., Figueiredo, J. A. P., Ng, Y. L., and Gulabivala, K. (2009). Microflora in teeth associated with apical periodontitis: a methodological observational study comparing two protocols and three microscopy techniques. *International Endodontic Journal*, 42(10):908–921.

Rimann, M., Laternser, S., Gvozdenovic, A., Muff, R., Fuchs, B., Kelm, J. M., and Graf-Hausner, U. (2014). An in vitro osteosarcoma 3d microtissue model for drug development. *Journal of Biotechnology*, 189:129–135.

Rizzardi, C., Leocata, P., Ventura, L., Zweyer, M., Brollo, A., Schneider, M., and Melato, M. (2009). Apoptosis-related factors (TRAIL, DR4, DR5, DcR1, DcR2, apoptotic cells) and proliferative activity in ameloblastomas. *Anticancer Research*, 29:1137–1142.

Roth, A. and Singer, T. (2014). The application of 3D cell models to support drug safety assessment: Opportunities & challenges. *Advanced Drug Delivery Reviews*, 69:179–189.

Sahai, E. (2005). Mechanisms of cancer cell invasion. *Current Opinion in Genetics & Development*, 15(1):87–96.

Sampson, D. E. and Pogrel, M. A. (1999). Management of mandibular ameloblastoma: The clinical basis for a treatment algorithm. *Journal of Oral and Maxillofacial Surgery*, 57(9).

Sandra, F., Hendarmin, L., Kukita, T., Nakao, Y., Nakamura, N., and Nakamura, S. (2005a). Ameloblastoma induces osteoclastogenesis: a possible role of ameloblastoma in expanding in the bone. *Oral Oncology*, 41(6):637–644.

Sandra, F., Hendarmin, L., and Nakamura, S. (2006a). Osteoprotegerin (OPG) binds with tumor necrosis factor-related apoptosis-inducing ligand (TRAIL): Suppression of TRAIL-induced apoptosis in ameloblastomas. *Oral Oncology*, 42(4):415–420.

Sandra, F., Hendarmin, L., Nakao, Y., Nakamura, N., and Nakamura, S. (2005b). TRAIL cleaves caspase-8,-9 and-3 of AM-1 cells: A possible pathway for TRAIL to induce apoptosis in ameloblastoma. *Tumor Biology*, 26(5):258–264.

Sandra, F., Hendarmin, L., Nakao, Y., Nakamura, N., and Nakamura, S. (2006b). Inhibition of Akt and MAPK pathways elevated potential of TNF alpha in inducing apoptosis in ameloblastoma. *Oral Oncology*, 42(1):39–45.

Sandra, F., Nakamura, N., Mitsuyasu, T., Shiratsuchi, Y., and Ohishi, M. (2001). Two relatively distinct patterns of ameloblastoma: an anti-apoptotic proliferating site in the outer layer (periphery) and a pro-apoptotic differentiating site in the inner layer (centre). *Histopathology*, 39(1):93–98.

Sanjay, C. J., Chaya, D. M., Rachna, K., Ramnarayan, B. K., and Prashanth, R. (2011). Intraosseous ameloblastoma masquerading as exophytic growth: a case report. *Imaging Science in Dentistry*, 41:89–93.

Santini, M. T. and Rainaldi, G. (1999). Three-dimensional spheroid model in tumor biology. *Pathobiology*, 67:148–157.

Sathi, G. A., Inoue, M., Harada, H., Rodriguez, A. P., Tamamura, R., Tsujigiwa, H., Borkosky, S. S., Gunduz, M., and Nagatsuka, H. (2009). Secreted frizzled related protein (sFRP)-2 inhibits bone formation and promotes cell proliferation in ameloblastoma. *Oral Oncology*, 45(10).

Sathi, G. A., Tsujigiwa, H., Ito, S., Siar, C. H., Katase, N., Tamamura, R., Harada, H., and Nagatsuka, H. (2012). Osteogenic genes related to the canonic WNT pathway are down-regulated in ameloblastoma. *Oral Surgery Oral Medicine Oral Pathology Oral Radiology*, 114(6):771–777.

Sathi, G. S. A., Nagatsuka, H., Tamamura, R., Fujii, M., Gunduz, M., Inoue, M., Rivera, R. S., and Nagai, N. (2008). Stromal cells promote bone invasion by suppressing bone formation in ameloblastoma. *Histopathology*, 53(4):458–467.

Schott, S., Vallet, S., Tower, R. J., Noor, S., Tiwari, S., Schem, C., and Busch, C. (2015). In vitro and in vivo toxicity of 5-FdU-alendronate, a novel cytotoxic bone-seeking duplex drug against bone metastasis. *Investigational New Drugs*, 33(4):816–826.

Shen, L.-C., Chen, Y.-K., Lin, L.-M., and Shaw, S.-Y. (2010). Anti-invasion and anti-tumor growth effect of doxycycline treatment for human oral squamous-cell carcinoma - in vitro and in vivo studies. *Oral Oncology*, 46(3):178–184.

Siar, C. H., Ishak, I., and Ng, K. H. (2015). Podoplanin, E-cadherin, beta-catenin, and CD44v6 in recurrent ameloblastoma: their distribution patterns and relevance. *Journal of Oral Pathology & Medicine*, 44:51–58.

Sikavitsas, V. I., Temenoff, J. S., and Mikos, A. G. (2001). Biomaterials and bone mechanotransduction. *Biomaterials*, 22(19):2581–2593.

Siqueira, A. S., Carvalho, M. R. D., Monteiro, A. C. D., Freitas, V. M., Jaeger, R. G., and Pinheiro, J. J. V. (2010). Matrix metalloproteinases, TIMPs and growth factors regulating ameloblastoma behaviour. *Histopathology*, 57(1):128–137.

Smalley, K. S. M., Lioni, M., Noma, K., Haass, N. K., and Herlyn, M. (2008). In vitro three-dimensional tumor microenvironment models for anticancer drug discovery. *Expert Opinion on Drug Discovery*, 3(1).

Sonoda, A., Iwamoto, T., Nakamura, T., Fukumoto, E., Yoshizaki, K., Yamada, A., Arakaki, M., Harada, H., Nonaka, K., Nakamura, S., Yamada, Y., and Fukumoto, S. (2009). Critical role of heparin binding domains of ameloblastin for dental epithelium cell adhesion and ameloblastoma proliferation. *Journal of Biological Chemistry*, 284(40):27176–27184.

Stechmiller, J., Cowan, L., and Schultz, G. (2010). The role of doxycycline as a matrix metalloproteinase inhibitor for the treatment of chronic wounds. *Biological Research for Nursing*, 11(4):336–344.

Stevens, B., Yang, Y., Mohanda, S. A., Stucker, B., and Nguyen, K. T. (2008). A review of materials, fabrication to enhance bone regeneration in methods, and strategies used engineered bone tissues. *Journal of Biomedical Materials Research Part B-Applied Biomaterials*, 85B(2).

Stevens, M. M. (2008). Biomaterials for bone tissue engineering. *Materials Today*, 11(5).

Sutherland, R. M. (1988). Cell and environment interactions in tumor microregions - the multicell spheroid model. *Science*, 240(4849):177–184.

Sweeney, R. T., McClary, A. C., Myers, B. R., Biscocho, J., Neahring, L., Kwei, K. A., Qu, K., Gong, X., Ng, T., Jones, C. D., Varma, S., Odegaard, J. I., Sugiyama, T., Koyota, S., Rubin, B. P., Troxell, M. L., Pelham, R. J., Zehnder, J. L., Beachy, P. A., Pollack, J. R., and West, R. B. (2014). Identification of recurrent SMO and BRAF mutations in ameloblastomas. *Nature Genetics*, 46(7):722–725.

Szot, C. S., Buchanan, C. F., Freeman, J. W., and Rylander, M. N. (2011). 3D in vitro bioengineered tumors based on collagen I hydrogels. *Biomaterials*, 32:7905–7912.

Takata, T., Zhao, M., Uchida, T., Kudo, Y., Sato, S., and Nikai, H. (2000). Immunohistochemical demonstration of an enamel sheath protein, sheathlin, in odontogenic tumors. *Virchows Archiv-an International Journal of Pathology*, 436(4):324–329.

Tan, S., Pollack, J. R., Kaplan, M. J., Colevas, A. D., and West, R. B. (2016). BRAF inhibitor treatment of primary BRAF-mutant ameloblastoma with pathologic assessment of response. *Oral Surgery, Oral Medicine, Oral Pathology and Oral Radiology*.

Tao, Q., LV, B., Qiao, B., Zheng, C.-Q., and Chen, Z.-F. (2009). Immortalization of ameloblastoma cells via reactivation of telomerase function: Phenotypic and molecular characteristics. *Oral Oncology*, 45(12):E239–E244.

Tapety, F. I., Amizuka, N., Uoshima, K., Nomura, S., and Maeda, T. (2004). A histological evaluation of the involvement of Bio-Oss in osteoblastic differentiation and matrix synthesis. *Clinical Oral Implants Research*, 15(3):315–324.

Tay, J. Y. Y., Bay, B. H., Yeo, J. F., Harris, M., Meghji, S., and Dheen, S. T. (2004). Identification of RANKL in osteolytic lesions of the facial skeleton. *Journal of Dental Research*, 83(4):349–353.

Tekkesin, M. S., Mutlu, S., and Olgac, V. (2011). The role of RANK/RANKL/OPG signalling pathways in osteoclastogenesis in odontogenic keratocysts, radicular cysts, and ameloblastomas. *Head and neck pathology*, 5(3):248–53.

Tsuda, Y., Shimizu, T., Yamato, M., Kikuchi, A., Sasagawa, T., Sekiya, S., Kobayashi, J., Chen, G., and Okano, T. (2007). Cellular control of tissue architectures using a three-dimensional tissue fabrication technique. *Biomaterials*, 8:4939–4946.

Ulrich, T. A., Jain, A., Tanner, K., MacKay, J. L., and Kumar, S. (2010). Probing cellular mechanobiology in three-dimensional culture with collagen-agarose matrices. *Biomaterials*, 31(7).

Vacanti, C. A., Kim, W., Upton, J., Vacanti, M. P., Mooney, D., Schloo, B., and Vacanti, J. P. (1993). Tissue-engineered growth of bone and cartilage. *Transplantation Proceedings*, 25(1):1019–1021.

Vandesompele, J., Preter, K. D., Battyn, F., Poppe, B., Roy, N. V., Paepe, A. D., and Speleman, F. (2002). Accurate normalisation of real-time quantitative RT-PCR data by geometric averaging of multiple internal control genes. *Genome Biology*, 3.

Veirman, K. D., Rao, L., Bruyne, E. D., Menu, E., Valckenborgh, E. V., Riet, I. V., Frassanito, M. A., Marzo, L. D., Vacca, A., and Vanderkerken, K. (2014). Cancer associated fibroblasts and tumor growth: Focus on multiple myeloma. *Cancers*, 6:1363–1381.

Villasante, A. and Vunjak-Novakovic, G. (2015). Tissue-engineered models of human tumors for cancer research. *Expert Opinion in Drug Discovery*, 10:257–268.

Wall, I. B., Bhadal, N., Broad, S., Whawell, S. A., Mudera, V., and Lewis, M. P. (2009). Force generation and protease gene expression in organotypic co-cultures of fibroblasts and keratinocytes. *Journal of Tissue Engineering and Regenerative Medicine*, 3.

Walsh, P. J., Clarke, S. A., Nelson, J., Maggs, C. A., Walker, G. M., and J, B. F. (2011). An in vitro study to assess the potential of a unique micro-porous algal-derived cap bone void filler in comparison with clinically-used bone void fillers. *Journal of Tissue Science and Engineering*, S:1.

Wan, P. T. C., Garnett, M. J., Roe, S. M., Lee, S., Niculescu-Duvaz, D., Good, V. M., Jones, C. M., Marshall, C. J., Springer, C. J., Barford, D., Marais, R., and Cancer Genome, P. (2004). Mechanism of activation of the RAF-ERK signaling pathway by oncogenic mutations of B-RAF. *Cell*, 116(6):855–867.

Wang, A., Zhang, B., Huang, H., Zhang, L., Zeng, D., Tao, Q., Wang, J., and Pan, C. (2008). Suppression of local invasion of ameloblastoma by inhibition of matrix metalloproteinase-2 in vitro. *Bmc Cancer*, 8.

Wang, L. and Stegeman, J. P. (2010). Extraction of high quality RNA from polysaccharide matrices using cetlytrimethylammonium [sic] bromide. *Biomaterials*, 31(7):1612.

Weaver, V. M., Petersen, O. W., Wang, F., Larabell, C. A., Briand, P., Damsky, C., and Bissell, M. J. (1997). Reversion of the malignant phenotype of human breast cells in three-dimensional culture and in vivo by integrin blocking antibodies. *Journal of Cell Biology*, 137(1).

Weigelt, B., Ghajar, C. M., and Bissell, M. J. (2014). The need for complex 3D culture models to unravel novel pathways and identify accurate biomarkers in breast cancer. *Advanced Drug Delivery Reviews*, 69:42–51.

Williams, A., Datar, R., and Cote, R. (2010). Technologies and methods used for the detection, enrichment and characterization of cancer stem cells. *National Medical Journal of India*, 23(6).

Wolfenden, A., Hall, K. D., and Lerch, B. A. (1996). The effect of heat treatment on Young's modulus, damping and microhardness of SiC / Ti-15-3. *Journal of Materials Science*, 31:1489–1493.

Woods, T. and Gratzer, P. F. (2005). Effectiveness of three extraction techniques in the development of a decellularized bone-anterior cruciate ligament-bone graft. *Biomaterials*, 26:7339–7349.

Xavier, S. P., Faria, A. C., de Mello Filho, F. V., Silva, E. R., and de Santana Santos, T. (2013). Recurrence of ameloblastoma in soft tissue. *The Journal of craniofacial surgery*, 24(5):1866–7.

Xouri, G. and Christian, S. (2010). Origin and function of tumor stroma fibroblasts. *Seminars in Cell & Developmental Biology*, 21(1):40–46.

Yasuda, K., Nakanishi, A., Satomura, K., Nagayama, M., and Hayashi, Y. (1991a). The behavior of human ameloblastoma tissue in collagen matrix invitro - an immunohistochemical study. *Journal of Oral Pathology & Medicine*, 20(4):187–190.

Yasuda, K., Satomura, K., and Nagayama, M. (1991b). Behavior of human ameloblastoma cells in collagen matrix invitro - an ultrastructural-study. *Journal of Oral Pathology & Medicine*, 20(9):438–442.

Zaman, M. H., Trapani, L. M., Siemeski, A., MacKellar, D., Gong, H., Kamm, R. D., Wells, A., Lauffenburger, D. A., and Matsudaira, P. (2006). Migration of tumor cells in 3D matrices is governed by matrix stiffness along with cell-matrix adhesion and proteolysis. *Proceedings of the National Academy of Sciences of the United States of America*, 103(29):10889–10894.

Zamaraeva, M. V., Sabirov, R. Z., Maeno, E., Ando-Akatsuka, Y., Bessonova, S. V., and Okada, Y. (2005). Cells die with increased cytosolic ATP during apoptosis: a bioluminescence study with intracellular luciferase. *Cell Death and Differentiation*, 12:1390–1397.

Zhang, B., Zhang, J., Huang, H.-Z., Chen, W.-L., Tao, Q., Zeng, D.-L., Zhang, L.-T., and Xu, J.-H. (2009a). Inhibition of ameloblastoma invasion in vitro and in vivo by inhibitor of metalloproteinase-2 activity. *Journal of Oral Pathology & Medicine*, 38(9):731–736.

Zhang, B., Zhang, J., Huang, H.-Z., Xu, Z.-Y., and Xie, H.-L. (2010a). Expression and role of metalloproteinase-2 and endogenous tissue regulator in ameloblastoma. *Journal of Oral Pathology & Medicine*, 39(3).

Zhang, B., Zhang, J., Xu, Z.-Y., and Xie, H.-L. (2009b). Expression of RECK and matrix metalloproteinase-2 in ameloblastoma. *Bmc Cancer*, 9.

Zhang, L., Chen, X. M., Sun, Z. J., Bian, Z., Fan, M. W., and Chen, Z. (2006). Epithelial expression of SHH signaling pathway in odontogenic tumors. *Oral Oncology*, 42(4):398–408.

Zhang, L., Sun, Z. J., Chen, X. M., and Chen, Z. (2010b). Immunohistochemical expression of SHH, PTC, SMO and GLI1 in glandular odontogenic cysts and dentigerous cysts. *Oral Diseases*, 16(8):818–822.

Zhang, L., Zeng, D., Huang, H., Wang, J., Tao, Q., Pan, C., Xu, J., Zhang, B., and Wang, A. (2010c). Tissue inhibitor of metalloproteinase-2 inhibits ameloblastoma growth in a new mouse xenograft disease model. *Journal of Oral Pathology & Medicine*, 39(1).

Appendix A

Publications and conference abstracts

Publications based on this project

Eriksson T M, Day R M, Fedele S, Salih V (2016) *The regulation of bone turnover in ameloblastoma using an organotypic in vitro co-culture model* Journal of Tissue Engineering; *in print*
Eriksson T M, Day R M, Fedele S, Salih V (2016) *Invasion inhibition in an organotypic soft tissue model of ameloblastoma manuscript in preparation*
Eriksson T M, Day R M, Fedele S, Salih V (2016) *The bisphosphonate alendronate inhibits ameloblastoma growth in an organotypic in vitro model*; *manuscript in preparation*
Eriksson T M, Day R M, Fedele S, Salih V (2016) *The molecular pathways of ameloblastoma development*; *Review; manuscript in preparation*

Conference abstracts based on this project

Mechanical properties of tissue engineered bone-like tumour models
Tissue and Cell Engineering Society (TCES) Annual Meeting, London, July 2016
poster presentation.

Modelling ameloblastoma behaviour with bone-like co-culture scaffolds
British Society for Oral and Dental Research Annual Meeting (BSODR), Cardiff, September 2015 - *oral presentation*. Travel Grant from BSODR Johnson & Johnson (£200).

Examining tissue invasion in an organotypic ameloblastoma model
TCES Annual Meeting, Southampton, July 2015 - *poster presentation*.

Bone turnover in an organotypic *in vitro* model of ameloblastoma
International Association for Dental Research General Session and Exhibition, Boston, US, March 2015 - *poster presentation*. Travel Grant from TCES (£150).

Novel organotypic bone scaffold for ameloblastoma modelling
IADR Pan-European Research (IADR PER) Meeting, Dubrovnik, Croatia, September 2014 - *oral presentation*. Travel Grant from BSODR Johnson & Johnson (£200).

Development of a soft tissue *in vitro* model for ameloblastoma
UK Society for Biomaterials (UKSB) and the European Society of Biomaterials (ESB) annual conference, Liverpool, September 2014 - *poster presentation*.

Development of a three-dimensional model for ameloblastoma
TCES Annual Meeting, Newcastle, July 2014 - *poster presentation*.

Towards 3D *in vitro* models of ameloblastoma
UCL Graduate School annual poster competition, 2014.

Appendix B

Standard curves and routine cell measurements

Figure B.1 shows an image of the fluorescent qRT-PCR amplification curve plotted as delta normalised reporter (ΔRn) vs cycle number. ΔRn is the ratio of fluorescence emission of the reporter dye in the samples to the fluorescence emission of the passive reference (Rox) dye. Based on this curve, the ddC_t values for each of the samples were calculated. Here, the baseline would be set as approximately cycle number 22, which is at the start of the exponential phase of amplification. The baseline value is set in order to remove background levels of fluorescence. The threshold value is set at a point in the middle of the exponential part of the curves. The point at which the amplification curve crosses the threshold is the C_t value for that sample (as indicated by the dotted arrow). The samples towards the left of the exponential phase of the run in fig. B.1 amplified as expected, and these samples can be used for further analysis. In these samples, the PCR reaction also reached a plateau before the run ended, indicating that all reagent had been used up. However, on the right-hand side of the exponential curves, the reactions failed (blue and brown lines). These samples did probably not contain enough mRNA to successfully amplify in the specified 40-cycle run, and therefore failed to reach a plateau. These samples require to be run again.

To the right of the exponential curves, some of the control samples (as indicated by the arrows), did not amplify, as expected. These controls were a water-only control to check for contamination, as well as a mastermix control with no mRNA added.

Specter cell count histograms

Figure B.2 shows a representative image of the results obtained when using the Specter automatic cell counter for counting cells in suspension. The histogram on the top shows the cell diameters in the 1ml suspension, and the lower histogram is the cell volume. The lower and upper limits (in the M1 range) can be tailored to the known cell sizes and to exclude e.g. large particles and dying cells (or cell particles). This count was carried out using the 60μm sensors (used for HOS and GF cells). The blue highlighted area in the 'group stats' box

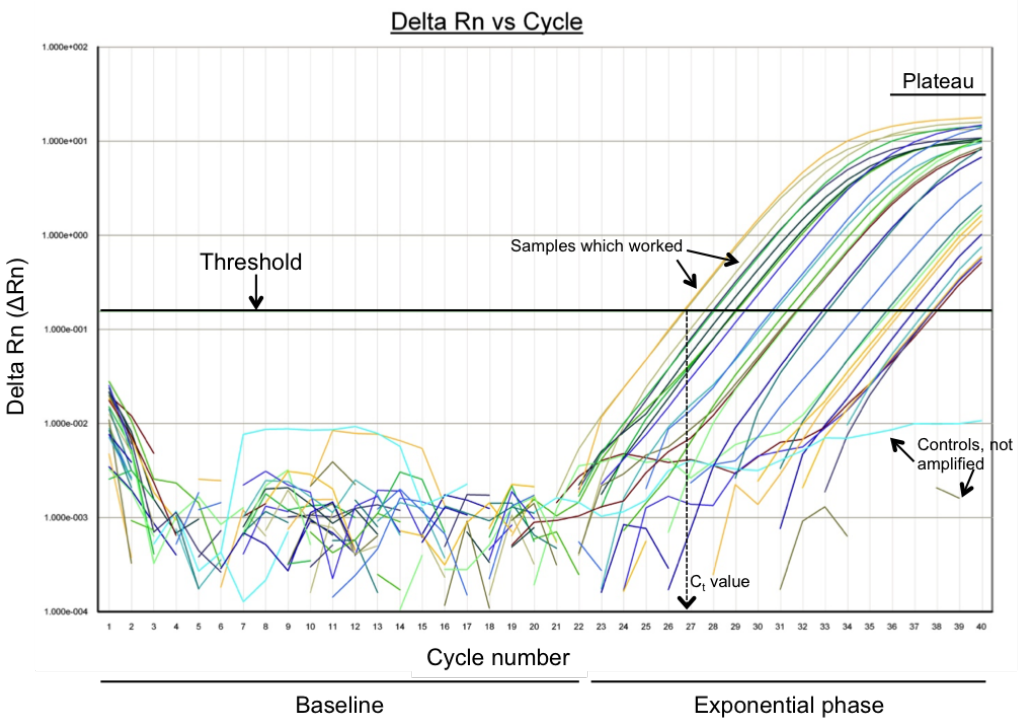

Figure B.1: Representative image of qRT-PCR amplification curve. This linear view curve displays the normalised reporter dye fluorescence (ΔRn) as a function of PCR cycle number for determining the threshold, baseline and C_t values from the qRT-PCR reaction.

on the right shows the size of cells which were counted using this method in this particular count (6-27.3μm). As can be see from other counts, the 40μm sensors count cells sized between 3μm and approximately 8μm. The cell count for this particular sample as seen in column 'M1 Conc. (count/mL)' was 431,000 cells/ml media-PBS solution. This value was then multiplied by the dilution factor 10, as the cell suspension, when preparing for the count was diluted 1:10 (100μl of cell suspension in 900μl PBS), to determine the actual cell number.

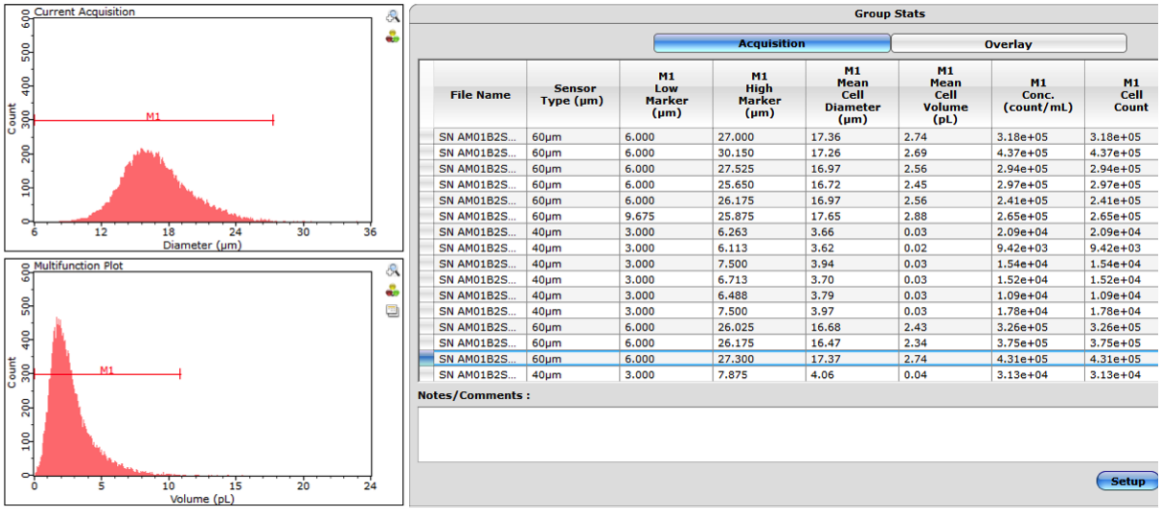

File Name	Sensor Type (µm)	M1 Low Marker (µm)	M1 High Marker (µm)	M1 Mean Cell Diameter (µm)	M1 Mean Cell Volume (pL)	M1 Conc. (count/mL)	M1 Cell Count
SN AM01B2S...	60µm	6.000	27.000	17.36	2.74	3.18e+05	3.18e+05
SN AM01B2S...	60µm	6.000	30.150	17.26	2.69	4.37e+05	4.37e+05
SN AM01B2S...	60µm	6.000	27.525	16.97	2.56	2.94e+05	2.94e+05
SN AM01B2S...	60µm	6.000	25.650	16.72	2.45	2.97e+05	2.97e+05
SN AM01B2S...	60µm	6.000	26.175	16.97	2.56	2.41e+05	2.41e+05
SN AM01B2S...	60µm	9.675	25.875	17.65	2.88	2.65e+05	2.65e+05
SN AM01B2S...	40µm	3.000	6.263	3.66	0.03	2.09e+04	2.09e+04
SN AM01B2S...	40µm	3.000	6.113	3.62	0.02	9.42e+03	9.42e+03
SN AM01B2S...	40µm	3.000	7.500	3.94	0.03	1.54e+04	1.54e+04
SN AM01B2S...	40µm	3.000	6.713	3.70	0.03	1.52e+04	1.52e+04
SN AM01B2S...	40µm	3.000	6.488	3.79	0.03	1.09e+04	1.09e+04
SN AM01B2S...	40µm	3.000	7.500	3.97	0.03	1.78e+04	1.78e+04
SN AM01B2S...	60µm	6.000	26.025	16.68	2.43	3.26e+05	3.26e+05
SN AM01B2S...	60µm	6.000	26.175	16.47	2.34	3.75e+05	3.75e+05
SN AM01B2S...	60µm	6.000	27.300	17.37	2.74	4.31e+05	4.31e+05
SN AM01B2S...	40µm	3.000	7.875	4.06	0.04	3.13e+04	3.13e+04

Figure B.2: Representative histograms and cell counts obtained from the Scepter automated cell counter.

Cell-based assay standards

Figure B.3 shows two standard curves constructed for determining cell numbers using the Alamar Blue assay. Here, the known cell numbers seeded in the wells are plotted against the corresponding fluorescent reading obtained using the Alamar Blue assay at 16 hours post-seeding. The line function was then calculated by applying a line of best fit through the points in the plot. The constant obtained from the equation was then used for calculating the cell numbers in experimental samples. A standard curve was constructed for each separate cell line used for this particular assay.

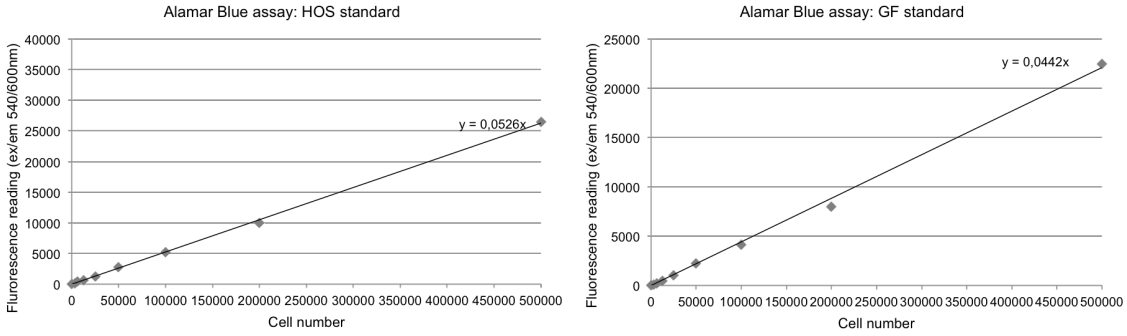

Figure B.3: Representative Alamar Blue standard curves for HOS and GF cells with associated line functions.

Figure B.4 shows two standard curves for known amounts of ATP diluted in OM and KSFM and plotted against the luminescence reading obtained from a Cell Titre Glo 3D assay. Similarly, fig. B.5 shows two standard curves plotted of a known quantity of cells against the resulting luminescence readings.
The constant obtained by calculating the line of best fit was used to deduce the amounts of ATP or cells present in experimental samples with unknown ATP or cell quantities. The standard curves in fig. B.5 made it possible to obtain cell numbers and proliferation information using the luminescence readings.

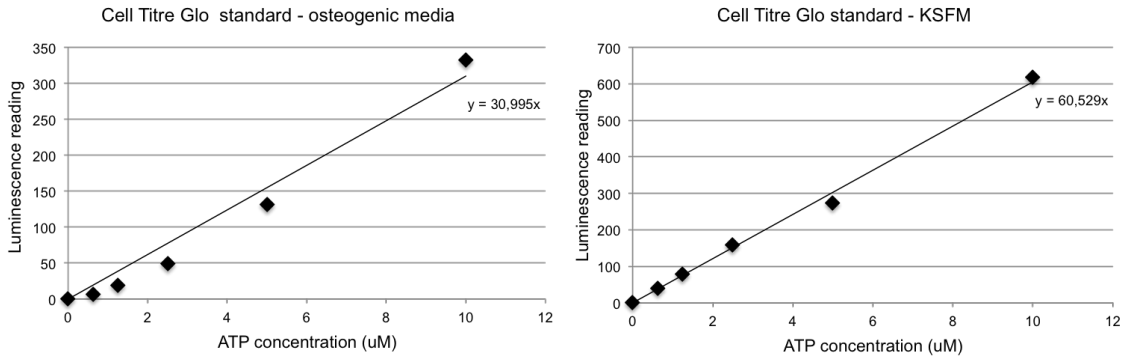

Figure B.4: Standard curves plotted for known amounts of ATP in two different media types used for the Cell Titre Glo 3D proliferation assay. Similar standards were also plotted for each cell type with a known quantity of cells to enable later quantification of cell numbers based on the luminescence reading obtained.

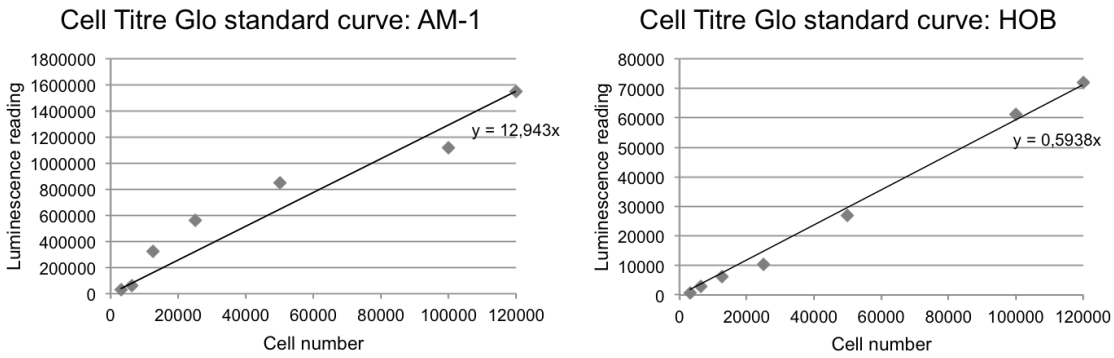

Figure B.5: Known quantities of cell numbers measured for emitted ATP luminescence. Using the resulting values, the cell quantities were plotted on the x axis and the corresponding luminescence reading on the y axis. The constant from the equation for the line of best fit was then used to calculate cell numbers in experimental samples with unknown cell numbers.

Figure B.6 shows the standard curve constructed for the ALP activity assay. The absorbance value at 405nm was measured for known amounts of ALP. A line of best fit was then plotted through the points, and the resulting equation was used to determine ALP amounts in the experimental samples.

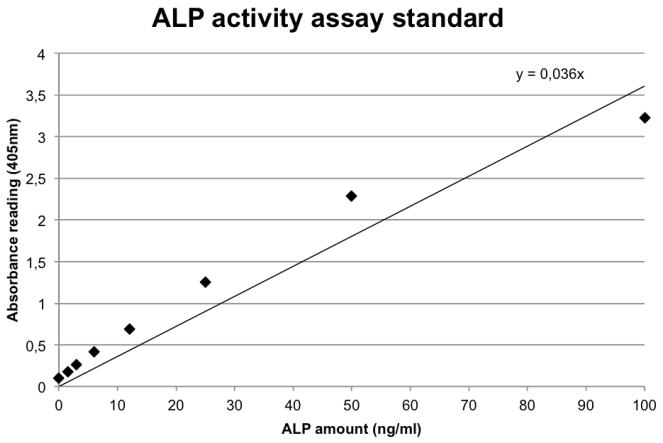

Figure B.6: Standard curve plotted for known amounts of pNPP substrate against the absorbance reading obtained at 405nm.

The concentration of ALP (ALP activity) in the samples was calculates as follows:

$$A/V \div T = U/ml$$

where A is the amount of pNPP (ng/ml) in the samples, calculated based on the standard curve, V is the volume of the sample added per assay well in ml (here 0.1ml) and T is the reaction time in minutes (here 45min).

Mechanical analysis curves

Two representative DMA output graphs are shown in the image in fig. B.7. The frequency used is plotted against the modulus of the material obtained. Fig. B.7A shows a successful elastic region measurement with a linear elastic region, and fig. B.7B shows a failed test, where the curve obtained is not linear.

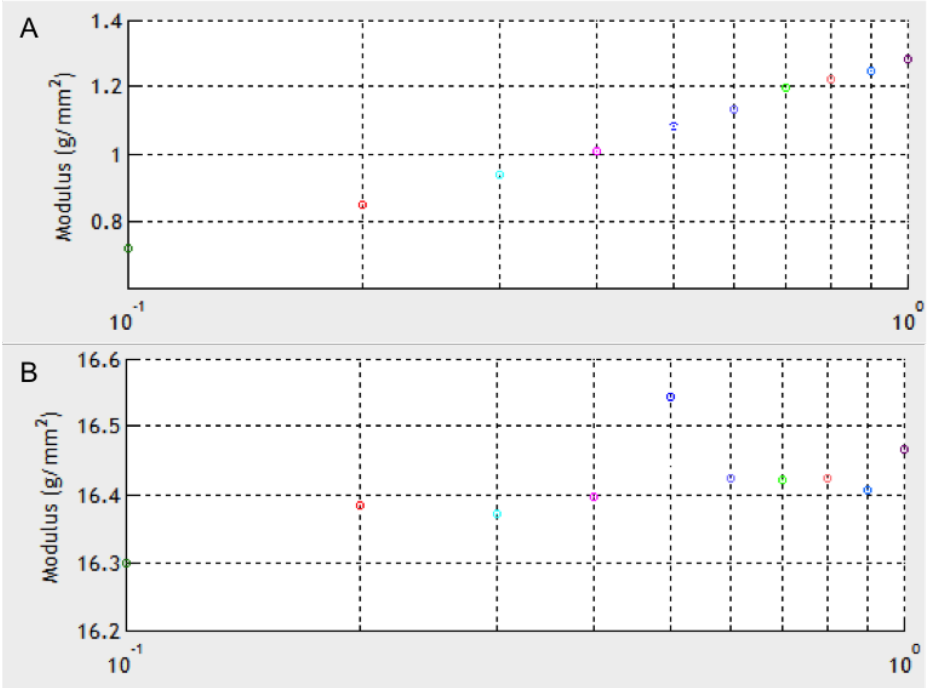

Figure B.7: Representative images of the elastic region of the stress-strain graph obtained using DMA. The coloured dots represent the stiffness measurement obtained at different frequences during the sweep. A) The resulting curve from a successful mechanical test with the measurements within the elastic region; B) A DMA curve from a sample which failed during testing. The curve is no longer linear half way through the frequency sweep, and so this set of results cannot be used to determine material stiffness.

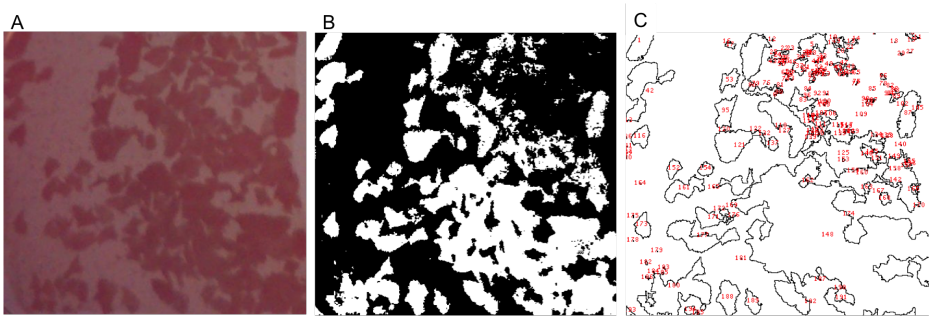

Figure B.8: Measuring the area of the bone-like construct to quantify total amount of Bio-Oss in constructs.

Measuring Bio-Oss content in constructs using ImageJ

Bio-Oss area measurement was carried out as detailed in fig B.8, and as follows:

1. Image of collagen + Bio-Oss construct (square) was first straightened (angle tool in 'Photos' programme) so the whole construct fit within the square.

2. The image was opened up in image J (as RGB; fig. C.8A).

3. Image → Type → 8-bit to get grayscale image; keeping the RGB image open for reference.

5. Image → Adjust → Threshold.

6. Manually adjust the sliders until the image obtained (in B&W) and the granules highlighted are equivalent to the original RGB image (fig. C.8B).

7. Analyze → Analyze particles → Show outlines → OK to obtain image (fig. C.8C).

8. Analyze → Measure → area fraction as percentage of total area of image (in pixels or unit of measurement previously calibrated to).

Immunocytochemistry control staining

Representative images of control samples for immunocytochemical staining are shown in fig. B.9. Control staining was carried out for all different cell types and antibodies used for ICC. Samples fig. B.9A-C were stained with both the EthD-1 nuclear stain (red) and the primary antibody (green). Samples in fig. B.9D and E were only stained with the primary antibody (green) without the nuclear counterstain. Samples in fig. B.9F, H, I and J were only stained with the nuclear counterstain (EthD-1, red), and the secondary AF antibody, but the primary antibody was omitted. Similarly, the sample in fig. B.9G was counterstained with the nuclear stain Sytox green, and the primary antibody was omitted.

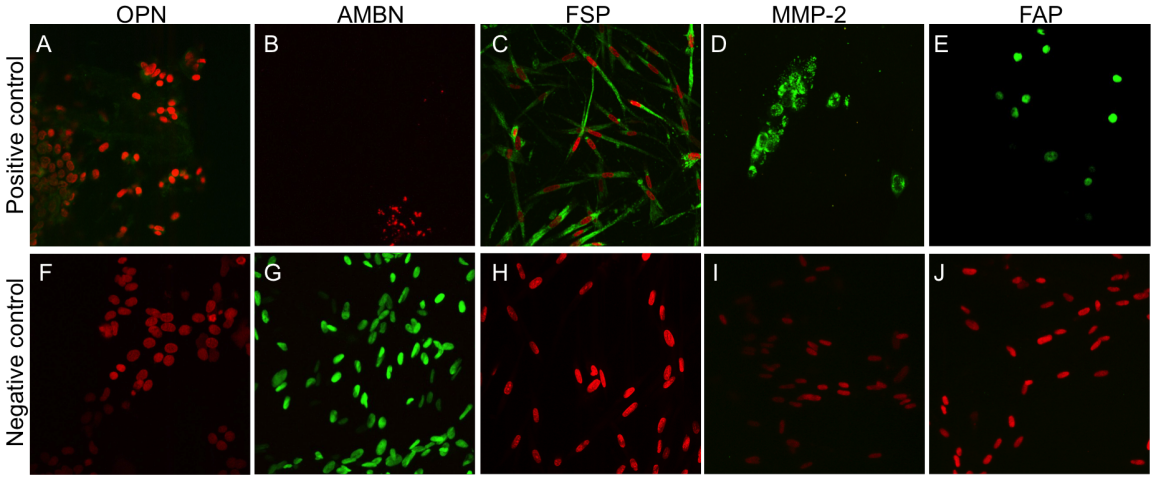

Figure B.9: Representative images of positive and negative controls stained for ICC. Positive controls (A-E) were single-cell type samples which were stained with both the primary and secondary antibodies according to the protocol. Note here A and C are stained with both an antibody and the nuclear counterstains, whereas B, D and E are only stained with the antibody. Negative controls (F-J) were samples where the primary antibody was omitted during staining.

Measuring gel area in ImageJ

Measuring the construct area in ImageJ was carried out for the contraction assays as shown in B.10 and described in the caption.

Therapeutic agent cytotoxicity studies

A brief 72 hour cytotoxicity study was carried out on both HOS and AM-1 cells plated on tissue culture plastic to assess the cytotoxic effects of alendronate (ALN) application on both cell types prior to applying it to the co-culture models. As seen in fig. B.11, HOS cells did not remain viable in the conditions with the higher amounts of added ALN. AM-1 cell viability was found to remain similar in all treatment groups. Based on HOS survival, the two lower amounts of ALN (10nM and 100nM) were used for further studies.

A brief 72 hour cytotoxicity study was also carried out on both GF and AM-1 cells in 2D to assess the cytotoxic effects of Doxycycline on these cells prior to application on the organotypic models. As seen in fig. B.12, GF cells remained mostly viable with up to 80% cell viability in the samples with 5 - 20μg/ml Dox added, whereas cell death was markedly increased in the 50μg/ml Dox-treated samples. AM-1 cell death was found high in all Dox-treated samples. However, as this was in 2D, the drug kinetics were assumed to change in the 3D models. As AM-1 survival was not significantly different in any condition, 10 and 20μg/ml were decided as suitable for Dox testing on the organotypic GF + AM-1 models.

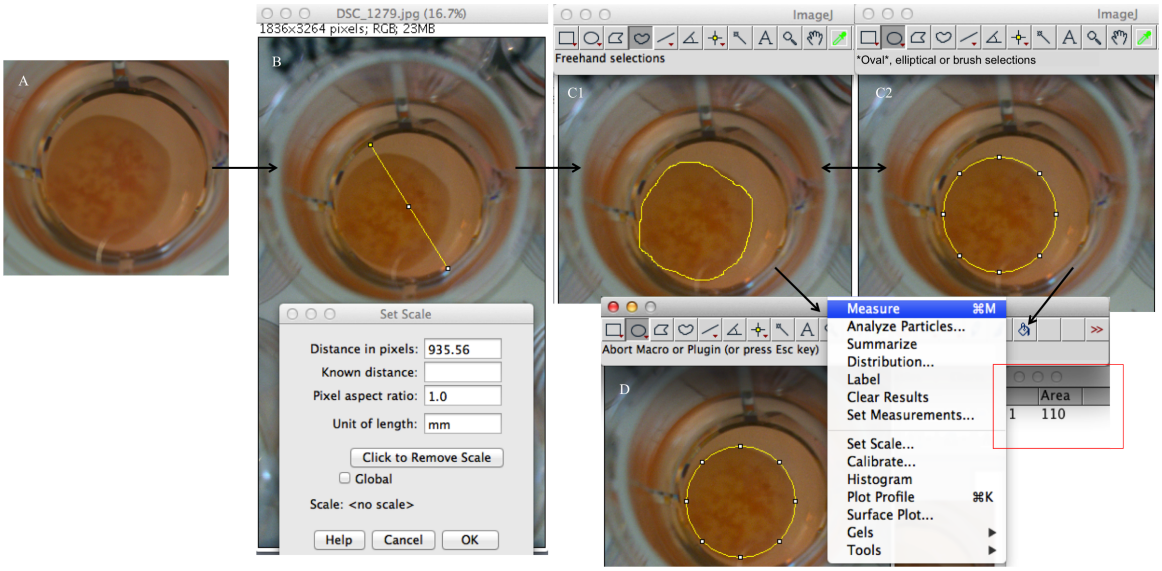

Figure B.10: A) Image of a typical gel opened up in ImageJ. B) The scale of the image was set using the 'set scale' tool and the known diameter of the bottom of the well (16.9mm, with mm set as the 'unit of length'). The scale was set separately for all images to ensure that the measurements were correct for all images. C) Either step C1 or C2 was performed to trace the outside of the gel. The free-hand trace tool in step C1 was useful for gels which did not remain rounded, whereas step C2 was used for rounded, contracted gels. D) Here, the area of the traced part of the image was measured using the 'measure' tool. The resulting area was displayed in a new window as indicated by the red box, with the value in this window corresponding to the value of the area in mm. This value was then normalised to day 0 values to obtain the amount the sample had contracted by.

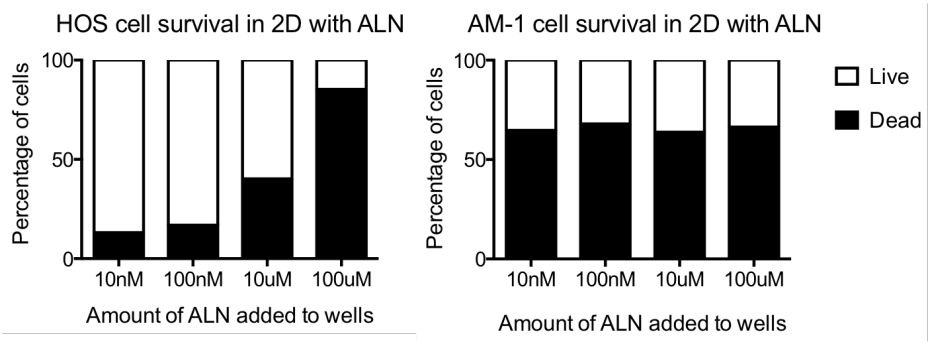

Figure B.11: Cell viability shown as a percentage of HOS and AM-1 cells after a 72hr culture with alendronate. The percentage of viable cells is shown in the white bars, and dead cells in the black bars. Average values of n = 3 are shown.

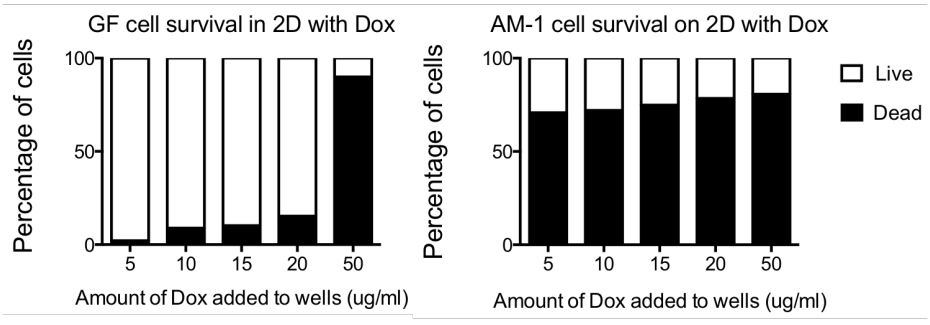

Figure B.12: Cell viability shown as a percentage of GF and AM-1 cells after a 72hr culture with various concentrations of Doxycycline. The percentage of viable cells is shown in the white bars, and dead cells in the black bars. Average values of n = 3.